Institut National Polytechnique de Lorraine

THESE

présentée à l'INPL
pour l'obtention du grade de

Docteur de l'Institut National Polytechnique de Lorraine
Spécialité : Mécanique et Energétique

par

Jérôme JONNET
Ingénieur ENSEM
(Ecole Nationale Supérieure d'Electricité et de Mécanique)

A CONTRIBUTION TO THE UNDERSTANDING OF THE HIGH BURN-UP STRUCTURE FORMATION IN NUCLEAR FUELS

soutenue publiquement le 09/01/2007 devant le jury constitué de :

Rapporteurs :		
Michel Beauvy	Directeur de Recherches,	CEA, Cadarache
Samuel Forest	Directeur de Recherches,	CNRS / Ecole des Mines de Paris, Evry
Examinateurs :		
Daniel Baron	Ingénieur-Chercheur,	Electricité de France, Les Renardières
Alain Degiovanni	Professeur,	INPL-LEMTA, Nancy
Etienne Patoor	Professeur,	Laboratoire de Physique et Mécanique des Matériaux, Metz
Benjamin Rémy	Maître de Conférences	INPL-LEMTA, Nancy
Paul Van Uffelen	Ingénieur-Chercheur,	ITU, Karlsruhe
Invités :		
Rachid Rahouadj	Maître de Conférences	INPL-LEMTA, Nancy
Claudio Ronchi	Chargé de Recherches,	ITU, Karlsruhe
Dragos Staicu	Ingénieur-Chercheur,	ITU, Karlsruhe

Laboratoire d'**E**nergétique et de **M**écanique **T**héorique et **A**ppliquée
CNRS UMR 7563
2, avenue de la Forêt de Haye - BP 160 - 54504 Vandoeuvre-lès-Nancy

Acknowledgements

This PhD work, sponsored by the European Commission, has been made possible by the collaboration between LEMTA, directed by Prof. C. Moyne and the Materials Research group of ITU, directed by Dr. C. Ronchi followed by Dr. R. Konings. I would like to thank all of them.

I wish to express my gratitude to Prof. M. Beauvy and Prof. S. Forest who accepted to report on my thesis, and to Prof. E. Patoor who chaired my defence.

I am indebted to my thesis director, Prof. A. Degiovanni who told me about the opportunity to carry out a PhD at the ITU, and to Dr. C. Ronchi who made it possible. Special thanks are due to Dr. C. Ronchi for his confidence and for letting me dig some theories. I wish I can have the same vision as him on sciences.

Although not being in LEMTA, I benefited of the supervision of Dr. Benjamin Rémy, my thesis co-director. He did not only help me in solving non-trivial equations but also tought me subtle things on the resolution methods. Besides this, I would like to thank him for his time, encouragement and interest in my work, even sometimes late in the afternoon (evening would be more appropriate).

I am greatly indebted to Dr. Paul Van Uffelen. During my PhD, I had the privilege to benefit from his supervision and knowledge: he helped me in understanding many mechanisms related to the fission process, his pragmatism was essential in the realization of this thesis and his scientific approach is a model. I also thank him for correcting my English. I hope that I have retained all his advice, because they are of great value. Thank you very much Paul.

I am grateful to Dr. Dragos Staicu who was always present, from my first day at ITU till an on-line repetition of my defence via Skype. Dragos tought me so many tricks for programming with Matlab or in Fortran, it seemed to me that he had created them himself. I really appreciated to work with him, always motivating and supporting me. Thank you also for the moments that I have shared with you apart from work.

Many thanks to Dr. Thierry Wiss and Dr. Vincenzo Rondinella for all these discussions we had on my research topic. I would like to thank particularly Dr. Thierry Wiss for his support, encouragement and time. He was always present to answer my questions about the experimental results and to teach me basics on electron microscopy. He should have been one of my official supervisors. I am also thinking of these last moments of my thesis where he found the right words to help me in taking the step.

I am grateful to Dr. R. Rahouadj who helped me so much with his comments on my thesis

and for the preparation of my defence. It is a pity that we have not collaborated earlier but I do hope, that this will now continue with ITU on this research topic.

The Directors of ITU, Prof. G.H. Lander followed by Prof. T. Fanghänel are acknowledged for their interest in my work. It is to some extent important to feel that one's work was recognized on all the levels.

Dr. D. Baron is also greatly acknowledged for having accepted to be a member of my jury, and for his comments and discussions we had since our first meeting at the HBS workshop in 2004 at ITU.

Generally speaking, I would like to address a sincere acknowledgement to the unit of Materials Research of ITU. I have spent such great moments in your company, these are engraved forever in my memory.
Special thanks are due to Petra Strube, the essential secretary of the unit, who can arrange things in a flash.
During these years, I could share the office with Jean-Yves Colle who raised me with the rank of his personal secretary. Besides this, this office was frequently the place of everlasting discussions with Franco Capone and Dr. Jean-Pol Hiernaut on topics where nobody agrees together. Believe me, this office is very valuable.
I would like to greatly acknowledge Franco who made me benefit from his wisdom and experience of life. With the time, he considered me as his reference mark for being present at the office with such assiduity. Thank you.

A special thought goes to Franck Delvart and the "Euratom Tischtennis Mannshaft": Denis Wojnowski, Aurélien Pitois, Ernest Ferring, Werner Karle, Christoph Meier, Kalman Körmendi, Matthias Schulz, Daqing Cui ... To play table-tennis once or twice a week was for me the opportunity to change my mind and to live something different. I have so many souvenirs, it would be inappropriate to state them one by one right now. Thank you so much and good luck for the championship.

I would like to make a wink to the ITU Badminton Club, especially to Michael Joergensen, Ian Farthing, Louise Abson, Jörg Rosenbruch and Marcus Walter. Thanks to Michael, I was elected (or constrained to be) chairman of the club. This will remain a very good souvenir.

Many thanks to the Research Fellows from ITU, especially Rachel Pflieger, Frédéric Jutier, Aurélien Pitois, Juliette van der Meer, Paula Juntunen, Petronela Gotcu, Ceren Kuetahyali, Cédric Cozzo. I wish you all the best for the future.
Many thanks to Jean Galy, Caroline Scheppler, Sylvain Morel, Stéphane Birk, Dario Manara, Jean-Luc Arnoult, Marta Munoz Nieto Sandoval, Rino Di Troia & Co ... (I am pretty sure that I have forgotten someone, I am really sorry) for the moments we have shared.

Many thanks to Gertrud Weber and her colleague of FZK (Forschungszentrum Karlsruhe), Doris Stern, who always answered perfectly to my requests and were incredibly quick in providing me with very old books and articles.

Without the help of Vincent Magnenet for handling the formatting and font commands with LaTeX, this thesis would not look so nice. Thank you very much for your time.

I would like to thank Valérie Reichhart for her help in dealing with all these papers related

to the end of a PhD thesis. I was told that this was an additional burden, but it was not in my case, thanks to Valérie.

I am also grateful to Cédric and Caroline Cozzo who accepted to lodge me for the last weeks of my stay in Karlsruhe. During this time, I did not only finish my thesis and prepare my defence, but also learnt a few recipes. I really enjoyed it. Thanks again.
Dr. Jean-Pol Hiernaut is also acknowledged for his help in allowing me to have a smooth departure from Germany.

All my childhood and school friends are acknowledged for their support and understanding in that I could not be present as often as I should have been. They are real friends.

Sincere thoughts go to my brother Sylvain, my sister-in-law Ghislaine and my niece Grâce. Although I was far from them during my PhD, I have had the privilege to be a witness to their union. This was a wonderful moment, thank you so much.

How would it be possible that I do not thank my parents, Roberte and Gil. During all these years (also before my PhD), though not understanding what I did exactly, they always supported me in letting me and giving me the means to do what I wanted to. Seeing in my parents' eyes how proud of me they were after my defence was the most important result of this experience. This thesis is dedicated to them.

The last but not least. Uta, the one of my life, my coach for facing all these daily life problems of a doctorant: doubt, discouragement, stress and so on. Without her, this would simply not be. I am forever grateful to her to have let me go and live this exceptional experience, although far from her. We have spent a lot of time in the trains, just to see each other one or two days during these too short week-ends. But now, everything is over and we can finally live together.

Contents

Résumé

Une contribution à la compréhension de la formation de la structure à haut taux de combustion dans les combustibles nucléaires

1. Le contexte industriel

La production d'électricité d'origine nucléaire est une option qui connaît un fort regain d'intérêt principalement suite à la raréfaction prévue des ressources fossiles et aux préoccupations environnementales liées à l'utilisation de celles-ci. L'optimisation de la consommation des ressources en matériaux fissiles et la réduction de la production des déchets sont des objectifs importants pour assurer une politique énergétique durable. Dans ce but, une option à court terme consiste à augmenter le taux de combustion du combustible nucléaire, principalement l'UO_2, en réacteur. Ceci permettrait de recharger le coeur du réacteur en combustible vierge moins fréquemment, et représente un moyen efficace de réduire le nombre de procédures dans le cycle même du combustible nucléaire, et également de réduire considérablement les coûts d'exploitation.

2. Revue sur les observations et caractérisations de la structure à "haut taux de combustion"

Le taux de combustion des combustibles utilisés dans les réacteurs est augmenté régulièrement et excède la gamme prévue pour ce type de combustible lors des études faites dans les années 60. Un nouveau phénomène, une restructuration cristallographique, est maintenant observé au niveau de la périphérie des pastilles de combustible utilisé à de forts taux de combustion dans des réacteurs commerciaux. Cette restructuration avait déjà été mise en évidence lors de tests d'irradiations, et également dans certains surrégénérateurs, mais elle ne fut pas plus amplement étudiée étant donné que le taux de combustion de déchargement du combustible des réacteurs commerciaux était bien au-dessous du seuil de transformation.

Cependant, autour du milieu des années 80, le même phénomène fut observé dans plusieurs cellules chaudes dans des combustibles utilisés en réacteur de puissance; un des premiers rapports fut établi par D. Baron en 1986 dans le cadre du programme international sur les effets des hauts taux de combustion sur le relâchement des gaz de fission (HBEP) concernant des observations de crayons irradiés pendant cinq cycles (55 MWd/kgU) à la centrale nucléaire de Fessenheim et de crayons semblables irradiés dans le réacteur Zion. Quelques années plus tard, un microscope de type FESEM (microscope électronique à balayage à émission de champ), avec une résolution nanométrique, fut introduit au Japon afin d'étudier plus en détails les combustibles nucléaires. Le microscope a révélé une structure en forme de choufleur et baptisée "Cauliflower" par Hj. Matzke, à cause de son apparence. Cette structure fut ensuite appelée structure "rim" (car apparaissant à la périphérie des pastilles de combustible) et est aujourd'hui plus connue sous le nom HBS pour "High Burn-up Structure". La HBS est caractérisée par une très petite taille de grain (de l'ordre de 0.15-0.30 μm, à comparer à une taille initiale de 10 μm avant la restructuration), par une porosité micrométrique et par une faible quantité de gaz de fission contenue dans le cristal.

Suite à ces observations et premiers résultats, des questions ont surgi au sujet de la possible dégradation des performances du combustible aux hauts taux de combustion, principalement en raison de la porosité élevée dans la partie restructurée qui aurait comme conséquence une augmentation volumique du combustible, une dégradation de sa conductivité thermique et un dégagement potentiel des gaz de fission. En conséquence, la HBS a été le sujet de divers programmes de recherche. Des irradiations expérimentales ont permis d'identifier les conditions spécifiques d'irradiations, en température et taux de combustion, à partir desquelles la restructuration se déclencherait. De même, des analyses issues d'irradiations commerciales ont permis de quantifier l'impact de cette restructuration sur diverses propriétés thermophysiques et mécaniques telles que la conductivité thermique, le module d'Young, la dureté du combustible et sa résistance aux fissures, ainsi que le potentiel en oxygène. La formation de la HBS est alors considérée comme une restauration de ces diverses grandeurs.

3. Bilan de la modélisation de la HBS

Parallèlement aux caractérisations expérimentales dédiées à identifier les mécanismes de formation de la structure à haut taux de combustion, de nombreux chercheurs ont entrepris la modélisation de cette structure. Outre les codes de performance du combustible incluant la présence de la structure à haut taux de combustion sous une forme plus ou moins empirique et les modèles concernant le développement lui-même de la structure dans la pastille, le type de modèle le plus répandu vise à modéliser certains mécanismes et phénomènes identifiés par certaines expériences ou sur base de considérations purement théoriques. Une étude bibliographique des différents modèles développés à ce jour a permis de mettre en évidence les phénomènes jouant un rôle important dans la formation de la HBS. Parmi ceux-ci, une grande majorité des théoriciens s'accordent sur le fait que cette restructuration est le fruit de l'accumulation des défauts d'irradiation et/ou, selon le modèle, des produits de fission gazeux et solides qui créent un état de contrainte interne que le combustible relaxe en formant la HBS.

4. Approche adoptée dans cette thèse

Ce type de relaxation ne peut généralement s'opérer que grâce à un certain type de défauts que sont les dislocations. Dans les métaux subissant une polygonisation, les dislocations sont indispensabes à la formation de nouveaux sous-joints de grain. La transposition de ce phénomène classique dans les métaux au combustible nucléaire irradié à de forts taux de combustion est une option qui ne fut jamais entièrement exploitée. En effet, l'étude bibliographique montre également que les études précédentes ne tiennent pas compte de la présence des dislocations dans les mécanismes de restructuration du combustible nucléaire, ou alors de manière phénoménologique ou erronée. L'approche adoptée dans cette thèse consiste donc en l'étude de la contribution des défauts de type dislocation (ligne de dislocation et boucles d'interstitiels) sur les mécanismes de formation de la HBS.

4.1. Calcul des contraintes induites par diverses configurations de dislocations

L'étude des contraintes induites par la présence des dislocations est d'abord conduite. L'objectif est de calculer l'énergie de déformation emmagasinée dans différentes configurations de dislocations afin de comprendre leur effet sur l'évolution de la microstructure. Un outil

mathématique permettant de calculer les contraintes induites par n'importe quelle configuration périodique de dislocations a donc été développé. Cet outil repose sur la théorie de Kröner proposée à la fin des années 50, et établissant une loi générale entre la source d'incompatibilité (ou de plasticité) et fonction de contraintes (plus connue sous le nom de fonction d'Airy) à partir de laquelle les contraintes élastiques sont dérivées. Cet outil, bien que mathématiquement lourd, s'avère puissant et permet ainsi le calcul de configurations périodiques de dislocations par combinaison, linéaire et/ou matricielle, des solutions calculées pour les empilements et murs de dislocations de type coin. Des caractérisations expérimentales supplémentaires sont nécessaires pour identifier le type des différentes configurations.

4.2. Evolution des défauts dans un échantillon auto-irradiant

Une étude de l'évolution des défauts d'irradiation, de type boucle d'interstitiels, a également été réalisée. Contrairement aux lignes de dislocation précédemment présentées, les boucles de dislocation de type boucle d'interstitiels (également appelées "SIA loops" pour Self-Interstitial Atom loops) se forment par précipitation des atomes qui ont été déplacés de leur site initial dans le cristal. Etant donnée la complexité de l'étude d'un réseau cristallin soumis à des fissions dans des champs de température et de contrainte non-nécessairement uniformes, un système "simplifié" a été choisi afin de déterminer clairement les mécanismes importants gouvernant la nucléation et la croissance des boucles d'interstitiels. Ce système consiste en du combustible UO_2 dopé avec 10% en masse de ^{238}Pu. L'isotope ^{238}Pu est un émetteur α, et chaque décroissance α (un noyau d'hélium $^4_2$He) crée également un atome de recul ^{234}U. Cet atome va alors engendrer la majorité des défauts ponctuels d'uranium et d'oxygène de type lacunes et interstitiels. Par diffusion dans le réseau cristallin, ces défauts ponctuels vont s'agglomérer et créer des défauts dits étendus de type boucles d'interstitiels et "trous" (dus aux lacunes). Des résultats expérimentaux ont été obtenus pour cet échantillon stocké pendant 4 et 7 ans, durées pendant lesquelles les défauts ont été générés de manière continue et homogène. La microscopie électronique à transmission et l'analyse d'images permettent de construire la distribution expérimentale en taille des boucles d'interstitiels. Des équations basées sur la théorie de cinétique chimique sont alors proposées afin de reproduire l'évolution expérimentale de la taille des boucles. Le modèle, basé sur le travail de Hayns, permet d'étudier l'influence de phénomènes physiques supplémentaires, à savoir la remise en solution d'interstitiels contenus dans une boucle due à un impact avec l'atome de recul ^{234}U, ainsi que la coalescence de deux boucles de dislocation due à leur diffusion en surface ou en volume. L'application du modèle montre que les deux processus ont un effet important et positif sur les distributions en taille des boucles. Le premier permet d'atteindre un régime stationnaire et est en compétition avec un mécanisme de croissance basé sur la capture des interstitiels uniquement. Le second permet de simuler une queue orientée vers les plus grandes tailles de boucle, typique du mécanisme de coalescence et semblable à celle observée sur les histogrammes expérimentaux.

5. Conclusions

Cette thèse a permis de faire un bilan conséquent des travaux expérimentaux et théoriques réalisés durant les 20 dernières années afin de comprendre les mécanismes de formation de la structure dite à haut taux de combustion. Se basant sur les observations expérimentales

et sur les modèles développés à ce jour, l'évolution de la microstructure est interprétée comme résultant de la contribution des défauts de type dislocation. Dans ce sens, un outil mathématique permettant de calculer les contraintes induites par n'importe quelle configuration périodique de lignes de dislocations a été développé. Enfin, un modèle d'évolution des défauts d'irradiation et des boucles d'interstitiels, permettant de prendre en compte la remise en solution des atomes constituant les boucles ou leur coalescence par diffusion en surface ou en volume, a également été développé. Ces deux contributions permettent d'avoir une meilleure compréhension des phénomènes liés à la formation de la structure à haut taux de combustion dans les combustibles nucléaires.

Notations

Abbreviations

BMI	
BNFL	British Nuclear Fuels Limited (United Kingdom)
BWR	Boiling Water Reactor
CEA	Commissariat à l'Energie Atomique (France)
CSL	Coincidence site lattice
CRIEPI	Central Research Institute of Electric Power Industry (Japan)
EOS	Equation Of State
EPMA	Electron-Probe Micro-Analysis
FBR	Fast Breeder Reactor
FGR	Fission Gas Release
FP	Fission Products
HBEP	High Burn-up Effects Program
HBRP	High Burn-up Rim Project
HBWR	Halden Boiling Water Reactor
HBS	High Burn-up Structure
IAEA	International Atomic Energy Agency
IFE	Institute for Energy Technology (Norway)
ITU	Institute for TransUranium elements (Karlsruhe, Germany)
JRC	Joint Research Centre
KWU	Kraftwerk Union (Germany)
LEMTA	Laboratoire d'Energétique et de Mécanique Théorique et Appliquée
LWR	Light Water Reactor
MOX	Mixed OXide fuel (mixture of UO_2 and PuO_2)
MX	Ionic solid in which M is the cation and X the anion
M&C	Migration & Coarsening
NFIR	Nuclear Fuel Industry Research
ODE	Ordinary Differential Equation
OR	Ostwald Ripening
PCMI	Pellet-Cladding Mechanical Interaction
PIE	Post-Irradiation Examinations
PWR	Pressurised Water Reactor
SEM	Scanning Electron Microscopy
SIA	Self-Interstitial Atom
TEM	Transmission Electron Microscopy
TEPCO	Tokyo Electric Power COmpany
XRD	X-Ray Diffractometry
XRF	X-Ray Fluorescence
%FIMA	Percent of Fission per Initial Metallic Atom
%TD	Percent of the UO_2 Theoretical Density

Notations associated to a quantity x

x	Scalar quantity
$\underline{x}$	Vectorial quantity
x_i	Indice i component of a vectorial quantity $\underline{x}$
	Scalar quantity associated to the interstitial-type defect
x_v	Scalar quantity associated to the vacancy-type defect
x_l	Scalar quantity associated to the interstitial-type dislocation loop
x_d	Scalar quantity associated to the shear dislocation loop
x_c	Central value of a scalar quantity x
x_s	Surface value of a scalar quantity x
$\underline{\underline{x}}$	Tensorial quantity of order equal to or greater than 2
x_{ij}	Indice (i,j) component of a matricial quantity $\underline{\underline{x}}$
$\bar{x}$	Mean value of a scalar quantity x
$\left(\underline{\underline{x}}\right)_{sym}$	Symmetrization of a matricial quantity $\underline{\underline{x}}$
$\underline{x}^t$	Transposition operation of a vectorial quantity $\underline{x}$
$\underline{\underline{x}}^t$	Transposition operation of a matricial quantity $\underline{\underline{x}}$
x^P	Plastic value of a scalar, vectorial or matricial quantity
x^T	Total value of a quantity

Physical constants and mathematical symbols

a	UO_2 lattice parameter [m]
A	Specific activity [Bq.g^{-1}]
$\underline{b}$	Burgers vector
c_{cell}	Area per UO_2 Schottky trio in an interstitial loop [m^2]
c_{ni}	Fractional concentration of interstitial loops containing n interstitials
$\underline{\underline{C}}$	Elasticity constant tensor (order 4)
D_i	Uranium interstitial diffusion coefficient [cm^2.s^{-1}]
D_v	Uranium vacancy diffusion coefficient [cm^2.s^{-1}]
E	Young's Modulus [N.m^{-2}]
e_{ijk}	Permutation tensor
F	α-particle production rate [m^{-3}.s^{-1}]
H(x)	Heaviside step function
H_V	Vickers hardness [Pa]
J_{res}	Rate of re-soluted interstitials into the matrix [m^{-3}.s^{-1}]
k	Boltzmann's constant (=1.3807$\times$10^{-23} J.K^{-1})
K	Bulk modulus [Pa]
K_{UFP}	Uranium Frenkel pair production rate [s^{-1}]
K_{Ic}	Fracture toughness [MPa.m$^{1/2}$]
K_2	Rate constant for the production of di-interstitials [s^{-1}]

$\mathrm{Li}_n(\mathrm{z})$	Polylogarithm function of order n
L_n	Reaction rate constant of an interstitial loop containing n atoms with a vacancy
N_A	Avogadro's number (=6.0220×10^{23} mol^{-1})
R	Universal gas constant (=k N_A=8.3144 $\mathrm{J.mol}^{-1}.\mathrm{K}^{-1}$)
R_n	Reaction rate constant of an interstitial loop containing n atoms with an interstitial
r_n	Radius of an interstitial loop containing n interstitials
T	Temperature [K]
$\underline{u}$	Displacement field
$u_{i,j}$	Partial derivative of u_i over x_j
$\mathrm{W}_{i,j}$	Collision rate between interstitial loops with radii r_i and r_j [s^{-1}]
x_i^2	Factor in the pre-exponential diffusion coefficient for the deviation from stoichiometry
z_i	Bias factor of interstitial to a specific defect
z_v	Bias factor of vacancy to a specific defect
α_r	Uranium Frenkel pair recombination coefficient
α_3	Skewness value of a data distribution
α_4	Kurtosis value of a data distribution
$\underline{\underline{\alpha}}$	Dislocation density tensor (order 2)
$\underline{\underline{\beta}}$	Distortion tensor (order 2)
$\underline{\underline{\delta}}_{ij}$	Kronecker's symbol
$\delta(x)$	Dirac delta function
ϵ_{im}	Uranium interstitial migration enthalpy [eV]
ϵ_{vm}	Uranium vacancy migration enthalpy [eV]
$\underline{\underline{\varepsilon}}$	Strain tensor (order 2)
ϕ	Prandtl's stress function or stress function of torsion
Γ_l	Jump frequency of an interstitial-type dislocation loop [m]
$\underline{\underline{\eta}}$	Kröner's incompatibility tensor (order 2)
$\underline{\underline{\psi}}$	Stress function tensor (order 2)
$\underline{\underline{\psi}}'$	Modified stress function tensor (order 2)
$\underline{\underline{\lambda}}$	Lamé modulus [Pa]
λ_l	Jump distance of an interstitial-type dislocation loop [m]
μ	Shear modulus [Pa]
μ_α	Depth range in UO_2 of the ^{234}U recoil atom produced by an α-decay [m]
ν	Poisson's ratio
ν_i	Uranium interstitial jump frequency [s^{-1}]
ν_v	Uranium vacancy jump frequency [s^{-1}]
ρ	Density
σ^2	Variance of a data distribution
$\underline{\underline{\sigma}}$	Cauchy stress tensor (order 2)
Ω	Atomic volume of UO_2 [m^3]
$\underline{\underline{\omega}}$	Rotation tensor (order 2)
Δ	Laplacian operator

$\nabla\cdot$ Divergence operator
$\nabla\times$ Left curl operator

Part 1

Introduction

I

Background

Today, most of the nuclear power stations produce between 900 MW and 1300 MW of electricity. This nuclear power initially comes from the recovered heat produced by the fission reaction of fissile atoms, which most known are ^{233}U, ^{235}U, ^{239}Pu and ^{241}Pu, by thermal neutrons. In Fig. I.1, the main elements of a Pressurized Water Reactor (PWR) are shown. The PWR, as well as the BWR (Boiling Water Reactor), belongs to the family of LWRs (Light Water Reactors).

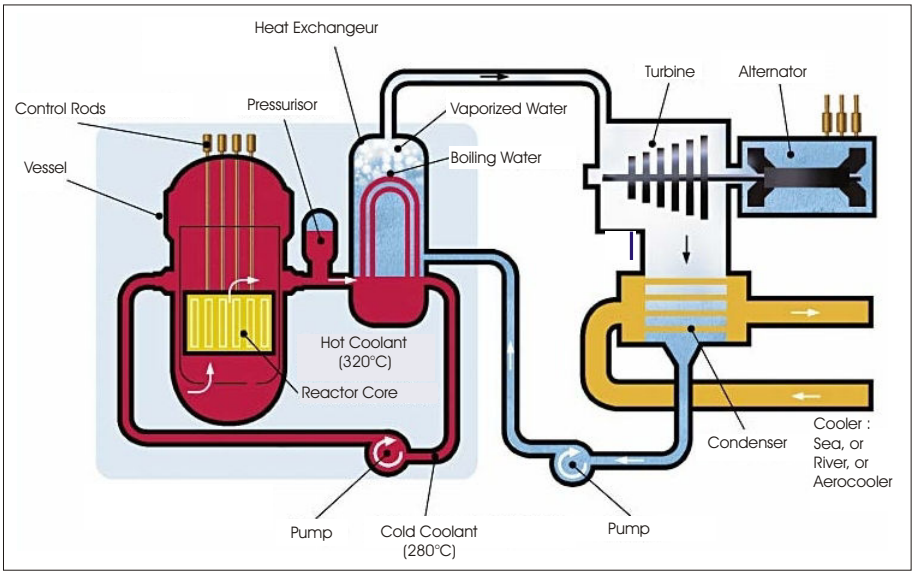

Figure I.1: Main elements of a PWR.

The chain-reaction proceeds in the reactor core, of approximately 4 meters high and made up of assemblies of 264 rods. Each rod contains pellets of fuel (enriched uranium oxide or mixed plutonium and uranium oxides); these pellets are piled-up in a cladding material and form the fuel rod, as shown in Fig. I.2. The assemblies - from 157 up to 205 depending on the reactor power - are surrounded by pressurized-water (155 bars) which is used at the same time as a coolant and as a moderator by slowing down the neutrons to make more

effective the fission reaction. The water flows in the (closed) primary circuit of the reactor, where its temperature increases from approximately 280 to 320°C while circulating accross the fuel rod assemblies before yielding its heat to a secondary circuit in the steam generator. In several tens of assemblies (48 to 73), 24 control rods made of neutron absorbing materials and gathered in bunches can be inserted (Fig. I.2), at the control of the operators to vary the reactivity and thus the core power. This can also be done by introducing boric acid in the primary circuit which also presents the property of absorbing neutrons.

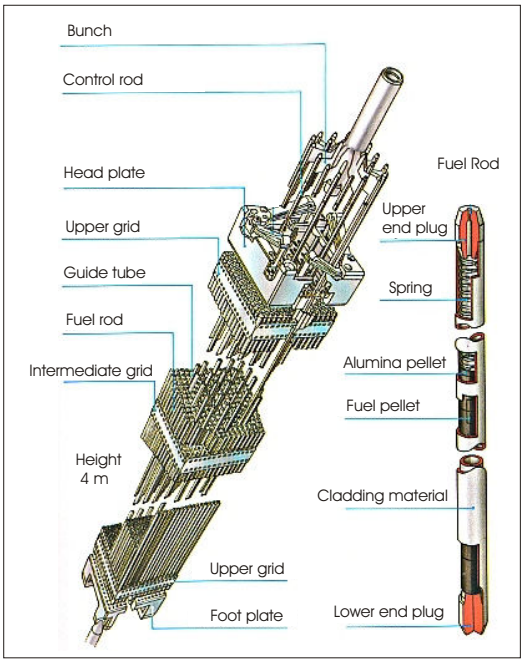

Figure I.2: Fuel rod assembly of a PWR.

To produce nuclear electricity seems to be simple but this is in reality a very sophisticated process which involves many phenomena on an atomic scale.

In particular, the fission process not only generates heat, but also many fission products. These latter are mostly radioactive and we thus understand why they must remain in the fuel rod. This is possible because the fuel pellets themselves inhibit this release, and due to the cladding which constitutes a barrier. The release of gaseous fission products from the pellet can lead to unwanted effects: for instance, the effect of the internal gas pressure may reduce the contact at the cladding/fuel interface, thus reducing the heat transfer from fuel to coolant. Since the fission gas diffusion process is strongly temperature-dependent, any increase in fuel temperature may amplify the situation and eventually lead to the cladding failure, what would be unacceptable from the point of view of radiological safety, if accompanied by a serious reactor accident.

Although the current nuclear power stations demonstrate that this is a safe way to produce electricity, there is thus still strong need for Research and Development. Contrary to the fuel vendors, whose short-term research is mainly directed towards addressing the immediate needs of utilities, principally improved reliability and performance, maximising output and minimising fuel cost [36], the main priority of the long-term research institutions is to provide

the safest conditions for producing nuclear energy as well as to limit the consumption of nuclear resources and generation of nuclear waste. The latter two goals can be achieved by:

- extending the maximum discharge burn-up of the current commercial fuels (mainly UO_2 fuels) beyond the average burn-up of 60 MWd/kgHM (Mega-Watt day per kilogram of Heavy Metal, i.e. U+Pu+MA (Minor Actinides)): with a longer fuel life, more energy is produced for the same volume of fuel, slowing down the increase of spent fuels.
- transmuting the Plutonium and the Minor Actinides in less harmful short-lived elements.

High burn-up extension of LWR fuel is a valuable means to reduce the amount of processes in the nuclear fuel cycle and to reduce total costs of the fuel cycle. Presently, the local burn-up of LWR fuel is exceeding the anticipated range for the UO_2 fuel that was investigated in the 1960's [16]. A "new phenomenon", a crystallographic restructuring called the High Burn-up Structure, is now commonly observed at the rim area of high burn-up fuel pellets in commercial reactors.

Before presenting the state-of-the-art about the High Burn-up Structure, an overview of the basic effects of radiation damage and experimental conditions encountered in a reactor are detailed in the present first part.

II

Basic effects of radiation damage in UO_2 fuels

Contents

II.1 The fission process

Fission was discovered in 1934 when Enrico Fermi irradiated uranium with neutrons and believed he had produced the first transuranic element. In 1938 Otto Hahn and Fritz Strassmann split the uranium atom by bombarding it with neutrons and showed that the elements barium and krypton were formed. Fermi, Hahn and Strassmann did, however, not realize that they had in fact induced a fission reaction. Only later research by others established the necessary knowledge about the nuclear fission process.

Elemental isotopes that undergo induced fission when struck by a free neutron are called "fissionable"; isotopes that undergo fission when struck by a thermal, slow moving neutron are also called "fissile". Not all fissionable isotopes can sustain a chain reaction. For example, ^{238}U, the most abundant form of uranium, is fissionable but not fissile: it undergoes induced fission when impacted by an energetic neutron with over 1 MeV of kinetic energy. But the neutrons produced by ^{238}U fission are not, themselves, energetic enough to induce further fissions in ^{238}U, so no chain reaction is possible with this isotope. Instead, bombarding ^{238}U with slow neutrons causes it to absorb them (becoming ^{239}U) and decay by β emission to ^{239}Pu; that process is used to manufacture ^{239}Pu in breeder reactors. Alternately ^{238}U may be fissioned with an external fast neutron source, causing energy generation.

The fission of uranium is achieved by the neutron capture of isotope 235. From this fission, 2 fission products (FP) as well as neutrons and β- and γ-rays are generated (Fig. II.1):

$$^{235}_{92}U + n \longrightarrow {}^{A_1}_{Z_1}FP_1 + {}^{A_2}_{Z_2}FP_2 + xn + \gamma + \beta \tag{II.1}$$

where A_i and Z_i are the mass and atomic numbers of the two fission products, respectively. x is the average number of emitted neutrons and is equal to 2.43. Several reactions defined by Eq. II.1 are possible. The latter are distinguished by their fission products and respect the conservation of mass-energy. A typical fission products distribution of thermal neutron of ^{235}U is shown in Fig. II.2.

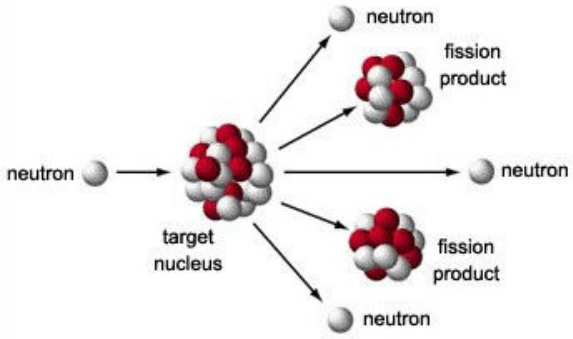

Figure II.1: Fission process.

Fission of one uranium or plutonium atom into two fission products releases about 200 MeV of energy. 80% of this energy is transfered in kinetic energy of the fission products, 65 MeV for the heavy FP and 95 MeV for the light FP in average; the remaining energy is mainly contained in β- and γ-rays. With the exception of 10 MeV carried by the neutrinos, almost all this energy is recovered as heat in the fuel pellets. The strongly ionized fission fragments cover

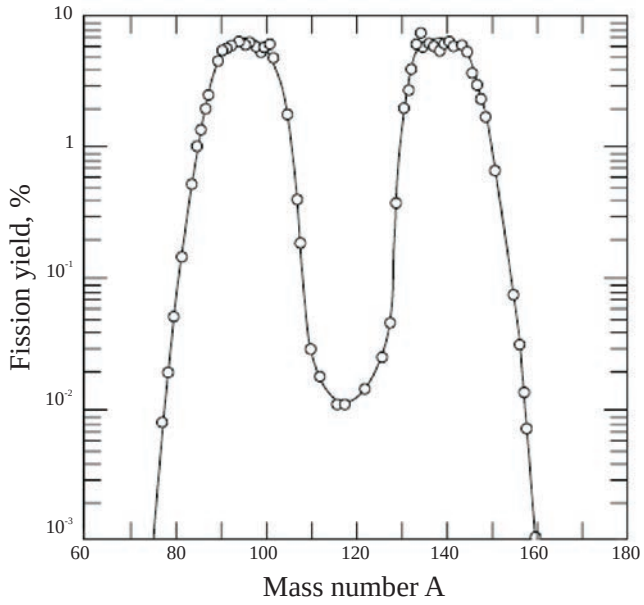

Figure II.2: Fission product distribution of thermal neutron fission of ^{235}U.

a distance of about 8 μm before being stopped; the major part of this energy is dissipated by electronic excitation: over this distance, called "fission spike", and on a diameter of about 10 nm, the atoms from the fuel lattice are strongly excited (temperature can locally exceed the melting temperature). When fission fragments have dissipated the greatest part of their energy, the residual energy (about 7 MeV in total) causes elastic shocks, displacing the atoms from their initial site: each fission thus creates about 25000 Frenkel pairs (vacancy-interstitial pairs, as detailed in II.2) of uranium or plutonium. The majority of these Frenkel pairs recombine almost instantaneously in 10^{-11} s, and a few 5000 Frenkel pairs (at least at low temperature) remain in the lattice.

The next two sections of this chapter present the main various point and extended defects which can occur in a crystal, as illustrated in Fig. II.3.

II.2 Point defects

II.2.1 Classification of point defects

Contrary to the perfect lattices, all real crystals contain defects differentiated according to their dimension. The one-dimensional defect is called a point defect, implying that it involves only one atom surrounded by an otherwise perfect lattice. However, the presence of a point defect may affect the properties of its nearest neighbors, and by elastic or electric interactions, a sizable spherical region of the lattice around the defect. Two point defects are intrinsic to the material, meaning that they form spontaneously in the lattice without any external intervention. These two are the vacancy and the self-interstitial, shown schematically in Fig. II.3 and referenced (d) and (c) respectively. The vacancy is simply an atom missing from a lattice site, which would be occupied in a perfect lattice. The self-interstitial is

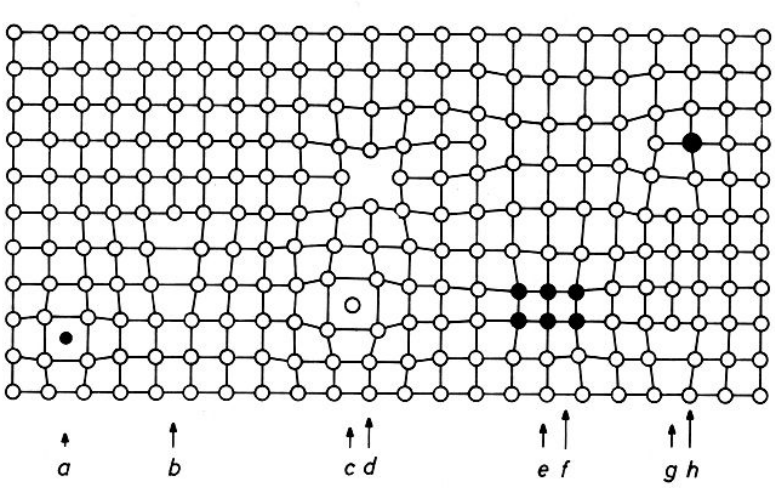

Figure II.3: Various crystal lattice defects: (a) interstitial impurity atom, (b) edge dislocation, (c)self-interstitial atom, (d) vacancy, (e) precipitate of impurity atoms, (f) vacancy-type dislocation loop, (g) interstitial-type dislocation loop, (h) substitutional impurity atom

an atom lodged in a position between normal lattice atoms; that is in an interstice. The qualification "self" indicates that the interstitial atom is the same type as the normal lattice atoms.

The defect referenced (h) and (a) in Fig. II.3 show the two basic mechanisms by which a foreign or impurity atom exists in the crystal lattice of a host element. Large impurity atoms, usually of the same category as the host atoms (e.g., both metals, as nickel in iron), replace the host atoms on regular lattice positions. These are called substitutional impurities. The structure of the lattice is not disturbed, only the identity of the atoms occupying the lattice sites are different. Small atoms that are also chemically dissimilar from the host atoms occupy interstitial positions and do not appreciably distort the surrounding host crystal. They are termed interstitial impurities.

II.2.2 Point defects in ionic crystals

Self-interstitials and vacancies occur naturally in ionic crystals as well as in elemental solids. However, because the cations (M) and anions (X) carry electrical charges, vacancy and interstitial formation are not independent processes. To create a vacancy on the anion sublattice by moving the anion to the surface, for example, would leave the surface negatively charged and the interior around the vacancy with a net positive charge. This violation of local electrical neutrality prevents such a process. Similar arguments apply to cation vacancies or self-interstitials of either ionic type.

Point defects that produce local electrical neutrality are shown in Fig. II.4 in a simplified two-dimensional representation. For simplicity, an MX type ionic solid is depicted. The Schottky defect involves simultaneous movement of a cation and an anion to the surface. In an MX_2 type crystal, two anion vacancies would have to be created for each cation vacancy. The other important point defect in ionic crystals is called a Frenkel defect. It can occur either

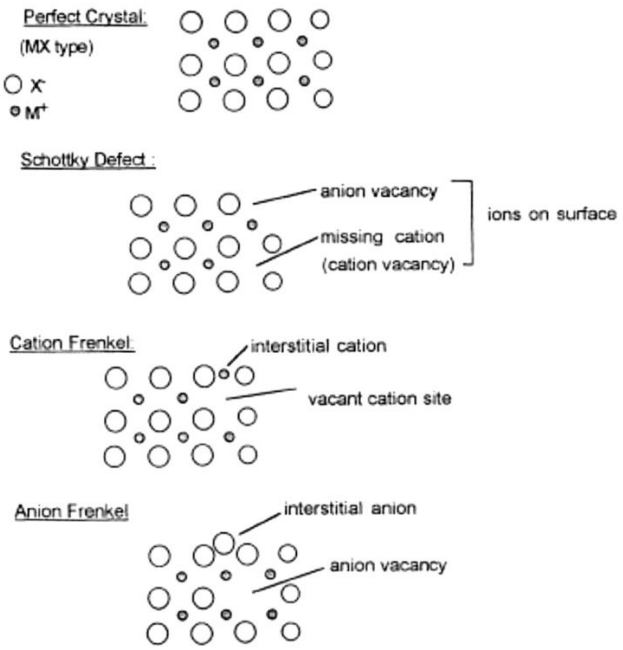

Figure II.4: Point defects in an MX-type ionic crystal.

on the cation sublattice or on the anion sublattice. As shown in Fig. II.4, an ion is moved from a regular lattice site to an nearby interstitial site, thereby maintaining local electrical neutrality[1] Schottky and Frenkel defects are created independently. In any particular crystal, one will dominate, while the other will either be absent or a minor contributor.

II.2.3 Point defects in stoichiometric UO_2

Stoichiometric uranium dioxide crystallizes in the CaF_2 fluorite structure, as depicted in Fig. II.5. Its unit cell can be described in two equivalent ways:

- the U^{4+} ions form a face-centered cubic cell, in which the O^{2-} ions occupy the tetrahedral positions (Fig. II.5).
- the O^{2-} ions form a simple cubic cell in which the U^{4+} ions occupy one cube center out of two.

The UO_2 lattice parameter is: a=0.547 nm (5.47 $\mathring{A}$). The distances between atoms, as well as the number and type of closest neighbours in the UO_2 cell have been proposed by Goldschmidt and Thomassen in 1923 [31] and are shown in Tab. II.1.

Uranium dioxide is a complicated material insofar as point defect formation is concerned. First, the uranium cation can assume oxidation states of 3+, 4+, 5+ and 6+. The mixture

[1]The interstitial ion that charge-compensates a nearby vacant site need not have originated from that site. All that is required is a distribution of vacancies and interstitials of the same type so as to maintain local electrical neutrality.

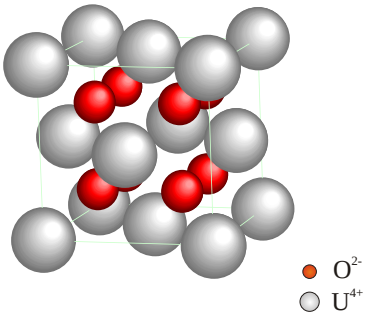

Figure II.5: UO_2 unit cell.

Atome	Ionic radius	First neighbour	Distance
U^{4+}	0.97 $\mathring{A}$	12 U^{4+} 8 O^{2-}	U^{4+}-U^{4+}: a$\sqrt{2}$/2=3.868 $\mathring{A}$ U^{4+}-O^{2-}: a$\sqrt{3}$/4=2.369 $\mathring{A}$
O^{2-}	1.4 $\mathring{A}$	4 U^{4+} 6 O^{2-}	O^{2-}-U^{4+}: a$\sqrt{3}$/4=2.369 $\mathring{A}$ O^{2-}-O^{2-}: a/2=2.735 $\mathring{A}$

Table II.1: Distances between atoms in UO_2.

of oxidation states depends upon the prevailing oxygen pressure. Thus, the nature and concentrations of the point defects in UO_2 depend on a gas-solid equilibrium as well as on the point defect equilibria. The dominant point defects in ideally pure stoichiometric UO_2 are anion Frenkel defects [58], O^{2-} vacancies and O^{2-} interstitials as shown in Fig. II.4. Indeed, despite the cations are smaller than the anions, U^{4+} is less mobile than O^{2-} because it has a greater atomic mass. Nevertheless, because of this low mobility, uranium diffusion in UO_2 is rate-controlling, since for true mass transport to occur all atomic species have to be transported [71]. UO_2 Schottky defects (1 uranium vacancy and 2 oxygen vacancies) occurs to a lesser extent, but can play an important role in fission gas diffusion in stoichiometric UO_2.

II.3 Extended defects

Once point defects start diffusing within the solid, they can interact with each other and form extended defects (linear, planar or 3-dimensional defects) so as to reduce the total energy. These extended defects are the following:

- dislocation-type defects: In general, dislocation-type defects are loops which can exhibit edge, screw and mixed dislocation character within a single loop, or can be prismatic (interstitial- or vacancy-type dislocation loop). The latter is a direct consequence of production and diffusion of interstitials and vacancies of the U and O sublattices. The former is a plastic deformation under external loading and is not a direct product of the fission process. However, it will be shown in the following parts that these dislocations play a central role in this study. The general characteristics and differences between these dislocations are thus presented in this section, as well as the data concerning the polycrystalline

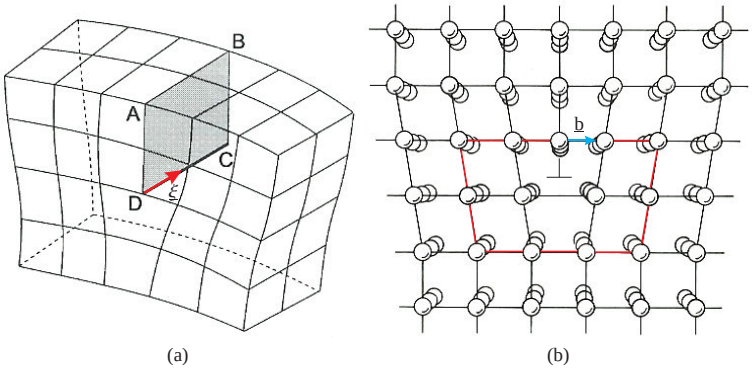

Figure II.6: Perspective view of an edge dislocation in a cubic lattice.

UO_2.

- voids: These are formed by vacancies absorption and are more stable than vacancy loops [94].

II.3.1 Shear dislocation loops and lines

Properties of dislocation loops

Dislocations (of edge type) are usually introduced and thought of as extra lattice planes inserted in the crystal that do not extend through all of the crystal, but end in the dislocation line: dislocation lines mark the boundary between slipped and un-slipped regions. This is shown in the schematic three-dimensional view of an edge dislocation in a cubic lattice (Fig. II.6). This picture shows very clearly the inserted half-plane; it serves as the quintessential illustration of what an edge dislocation looks like.

The Burgers vector of a dislocation, $\underline{b}$, defines the closure failure: the circuit made in counter clockwise direction in material surrounding the dislocation line would close in a "perfect" crystal, but connecting the beginning to the end defines $\underline{b}$, as shown in Fig. II.6(b).

A dislocation is a one-dimensional defect because the lattice is only disturbed along the dislocation line. The dislocation line thus can be described at any point by a line vector $\underline{\xi}$ (Fig. II.6(a)). In the dislocation core the bonds between atoms are not in an equilibrium configuration, i.e. at their minimum enthalpy value; they are heavily distorted. The dislocation thus possesses energy (per unit of length) and entropy.

There is a second basic type of dislocation, called screw dislocation (Fig. II.7). Its atomistic representation is somewhat more difficult to draw - but a Burgers circuit is still possible.

General properties of edge and screw dislocation lines can be presented now:

- The Burgers vector for a given dislocation is always the same, i.e. it does not change with coordinates, because there is only one displacement for every cut.
- Edge and screw dislocations (with an angle of 90° or 0° respectively, between the Burgers and the line vectors) are just special cases of the general case of a mixed dislocation, which

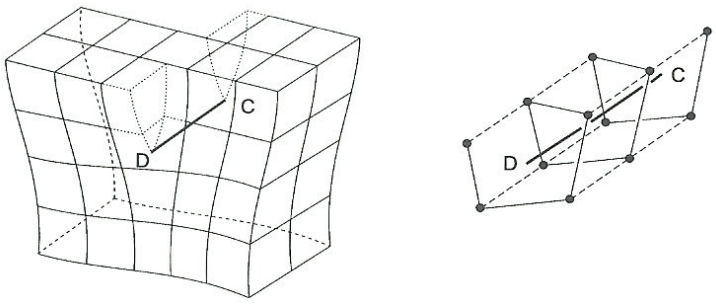

Figure II.7: Perspective view of a screw dislocation in a cubic lattice.

has an arbitrary angle between $\underline{b}$ and $\underline{\xi}$ that may even change along the dislocation line. Fig. II.8 shows the case of a curved dislocation that changes from a pure edge dislocation to a pure screw dislocation.

- A dislocation cannot end in the interior of an otherwise perfect crystal, but only at a crystal surface, an internal surface or interface (e.g. a grain boundary), a dislocation knot or on itself - forming a dislocation loop (Fig. II.9).

- The Burgers vector $\underline{b}$ must be in the plane of the cut which has two consequences: the cut plane must be planar, defined by the line vector and the Burgers vector, and the cut plane is the glide plane of the dislocation; a dislocation loop can move only in this plane without the help of interstitials or vacancies.

- At a dislocation knot the sum of all Burgers vectors is zero ($\sum \underline{b} = 0$), provided all line vectors point into the knot or out of it.

- Dislocation lines can interact with point defects: dislocations climb upward from the slip plane by vacancy absorption or downward from the slip plane by self-interstitial absorption or vacancy emission.

Ionic configurations of dislocations in UO_2

The geometry of slip in a single crystal is fully defined by the slip system, which designates the slip plane (reticular plane in which surface atomic density is maximum) and the slip direction (reticular direction in which linear atomic density is maximum). The dislocation is generally a mixture of screw and edge components in the shape of a loop of type shown in Fig. II.9. However, important deformation properties, such as the creep rate and the yield stress (or usually called the critical resolved shear stress), are controlled primarily by the edge components of the dislocation. Consequently, the nature of edge dislocations in UO_2 have received the most attention in the literature. In 1960, Rapperport and Huntress [99] examined the macroscopic slip of UO_2 monocrystals deformed in compression between 700°C and 1900°C. The most active slip system, highlighted by the analysis of slip trace and the Laue stereotypes, is {100}<110>. The planes {110} and {111} become active when the temperature increases, the slip direction remaining <110>. The planes {111} are often activated

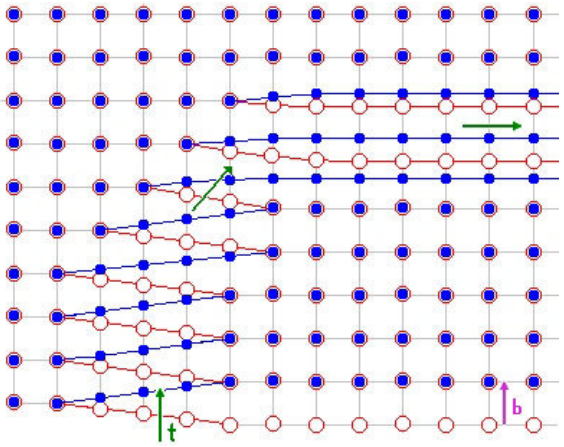

Figure II.8: A curved dislocation.

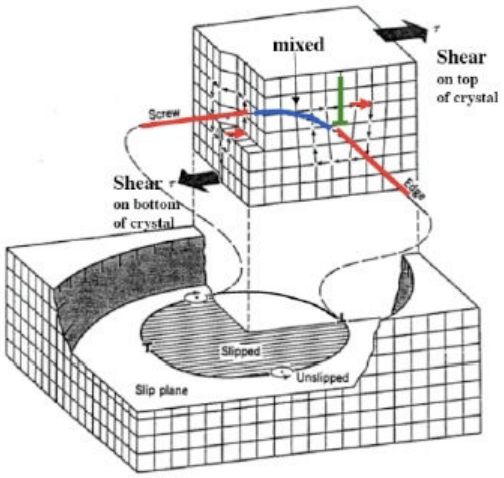

Figure II.9: A dislocation loop.

by cross-slip. In 1963, Ashbee confimed these results, by means of TEM observations, and defined the Burgers vector as a/2 <110> [3]. The distance a/2 <110> effectively corresponds to the shortest period of the fluorite network.

Primary slip planes in UO_2 are not the most dense ones, i.e. {111} planes as classically observed in fcc metals. Other important differences are ascribable to the ionic structure, compared to a simple fcc structure in metals. For instance, an edge dislocation consists of introducing two adjacent extra half-planes in order to keep the electrical neutrality of the crystal. The effective charge of such a dislocation, if any depending on the slip system as shown later, can be assessed by counting the attached bonds of all ions around the dislocation core. In fact, the most important slip system in UO_2 is the one which rather confers on the crystal a minium electrostatic energy than a minimum elastic energy. The easy slip along {100}<110> tends to minimize the intense repulsive force between cations. The anions then screen during such translations.

The ionic configurations of dislocations in UO_2 have been investigated by Evans [29] in order to identify the peculiarities that may influence the deformation characteristics of this material. The cases of the edge dislocation in the primary and secondary slip systems, as well as the screw dislocation, are presented here:

(a) Edge dislocation on the primary system {100}<110>: an examination of this configuration given by Amelinckx shows that there are excess positive charges along the length of the dislocation. This is shown in a three-dimensional model of the dislocation (Fig. II.10). In every Burgers vector length there are four free bonds and this represents a net charge equivalent to the charge on a proton. When a dislocation loop is created from the perfect lattice this positively charged dislocation forms at one end of the loop whilst a negatively charged dislocation forms at the other end. The negatively charged form is shown in Fig. II.11, and this differs from Fig. II.10 only by the omission of the row of calcium ions at the bottom of the left-hand extra half-plane. Again, there are four free bonds within a Burgers vector length of dislocation and this represents a net charge equivalent to the charge on an electron.

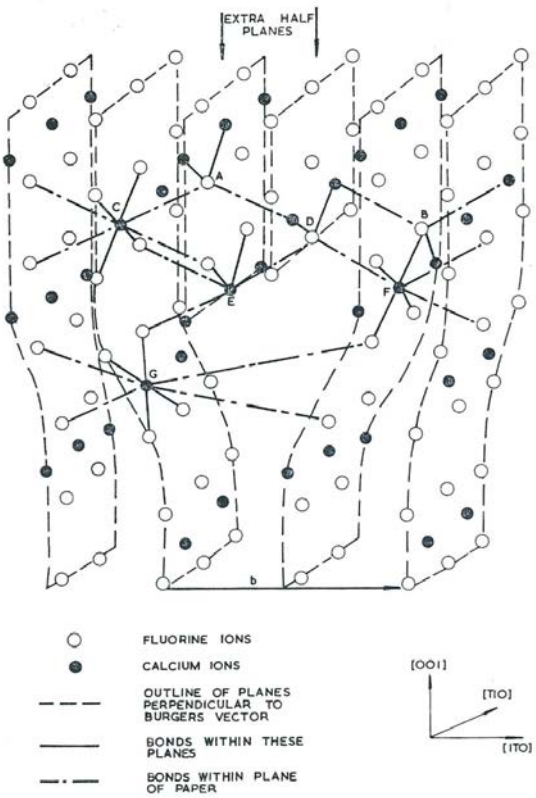

Figure II.10: The positively charged configuration [29].

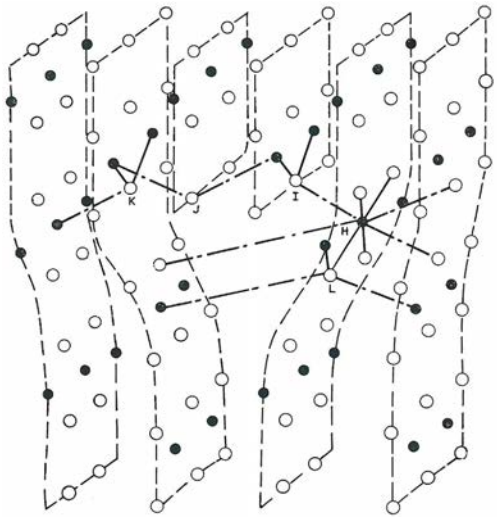

Figure II.11: The negatively charged configuration [29].

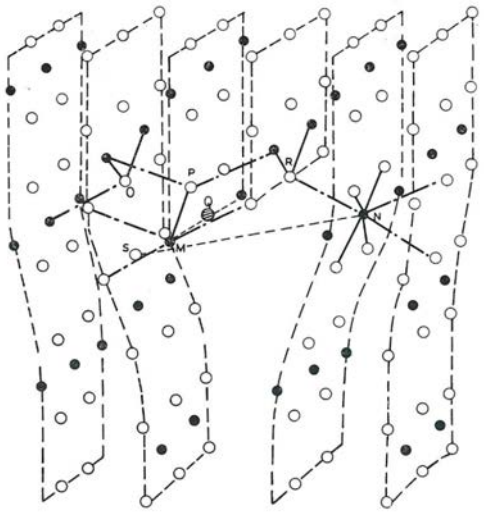

Figure II.12: The uncharged configuration [29].

The case of the uncharged configuration is shown in Fig. II.12. It is considered that this dislocation is the most likely mobile uncharged configuration.

(b) Edge dislocation on the secondary system {110}<$\bar{1}$10>. This is somewhat similar to the edge dislocation on the primary system in rock-salt crystals with positive and negative charges alternating along the length of the dislocation; it is thus uncharged [115]. A comparison of the atomic configuration of an edge dislocation in both primary and secondary slip systems are shown in Fig. II.13

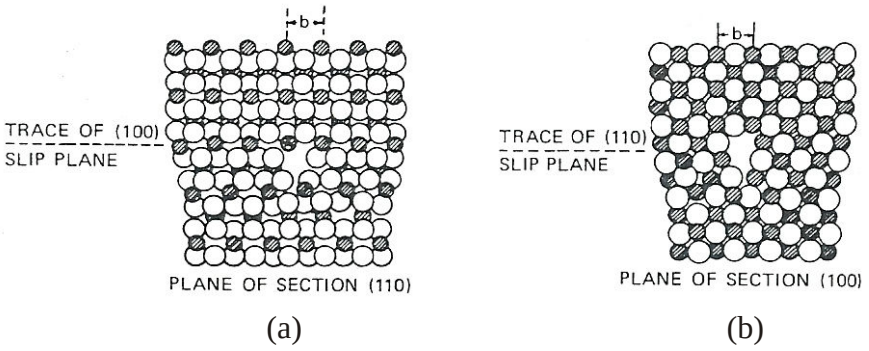

Figure II.13: Atomic configurations around edge dislocations in UO_2 on (a) the primary slip system {100}<110>, (b) the secondary slip system {110}<110> [116]. The U atoms are in black and the O ones in white.

(c) Screw dislocation (primary slip system {100}<110>): This is uncharged and the configuration on the primary planes is shown schematically in Fig. II.14.

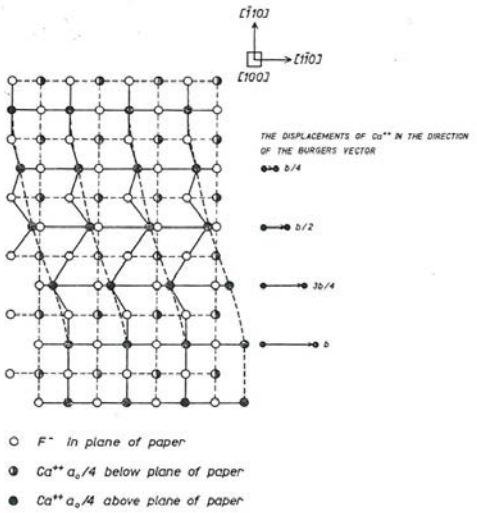

Figure II.14: A screw dislocation on {100}<011> [29].

Ashbee [3] has reported to have observed dissociated dislocations into partial dislocations. However, these stacking faults might have been identified in non-stoichiometric UO_2 due to

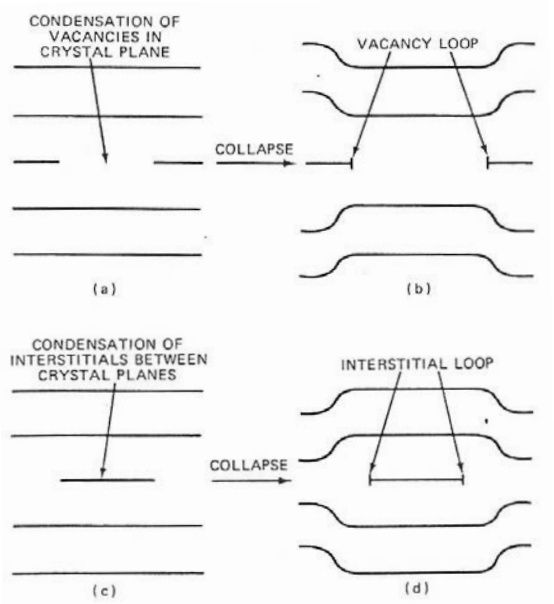

Figure II.15: Formation of vacancy and interstitial loops.

the TEM observation conditions which induced a local reduction of the oxide. This excess uranium ions could stabilize stacking faults according to calculations based on an ionic model [54]. The same calculations showed that the stacking fault energy were much too high to consider the dissociation of dislocations into partial dislocations in UO_2.

II.3.2 Prismatic loops

The second type of loop is called a prismatic loop. This type is fundamentally different from the shear loop; the only features the two types have in common is their circular shape and their ability to expand or contract radially. The more numerous differences between shear and prismatic loops are summarized in Tab. II.2.

Characteristic	Shear loop	Prismatic loop
Location	on slip plane	between close-packed planes
Peripheral dislocation type	mixed	edge
Central portion of loop	perfect crystal lattice	stacking fault
Mechanism of growth	shear stress	absorption of point defects
Orientation of Burgers vector	parallel to loop	perpendicular to loop

Table II.2: Differences between shear and prismatic loops.

Corresponding to the two types of point defects, vacancies and interstitials, there are two types of prismatic loops. These are shown in Fig. II.15. The interstitial loop consists of a disk-shaped layer of atoms formed by assembling free interstitial atoms from the bulk solid. The atom-layer agglomeration is thermodynamically more stable than the same number of atoms dispersed in the lattice as self-interstitials. In structures other than the simple cubic type depicted in Fig. II.15, formation of the interstitial loop disrupts the regular ordering of

planes in the perfect lattice, creating a stacking fault. Interstitial loops form only in solids bombarded by high energy radiation (e.g., neutrons) because only this environment produces sufficient quantities of self-interstitials. The top-part sketch in Fig. II.15 shows a prismatic loop formed by the collapse of a disk of vacancies on a close-packed plane. In common with the interstitial loop, the periphery of the vacancy loop is a circular edge dislocation with a Burgers vector perpendicular to the plane of the loop. However, the Burgers vectors of the two types are of opposite sign.

The study of the nucleation and growth of interstitial loops is further detailed in part 4 in which a UO_2 sample doped with α-emitters homogeneously produces point defects and thereafter interstitial-type dislocation loops.

The interaction of irradiation-produced point defects with these two types of loops provides a mechanism for the phenomenon of irradiation growth in fuel elements containing uranium metal or zirconium alloys [93]. By definition, an interstitial loop grows/shrinks by absorption of interstitials/vacancies, whereas the vacancy loop grows/shrinks by absorption of vacancies/interstitials. However, vacancy loops shrink by self-interstitial atom absorption at all temperatures and shrink by vacancy emission at high temperatures [94]. This means that vacancy loops are intrinsically unstable at all temperatures. Rather than forming loops in the shape of a disc, vacancy condensation results in voids, which are in turn a perfect trap for fission gas atoms.

II.3.3 Void nucleation and growth

Because of preferential absorption of self-interstitials at dislocations, a slight excess of vacancies is left in the solid to first nucleate and then grow voids (a void does not contain gas).

Nucleation refers to the rate at which tiny embryos of these defect clusters appear in the solid. Voids, as well as prismatic loops, can nucleate homogeneously or heterogeneously. Homogeneous nucleation refers to the build-up of small clusters by chance encounters of individual point defects executing random walks in the solid. The stability of these clusters relative to the individual point defects of which they are composed (i.e., voids contain vacancies and perhaps gas atoms whereas loops contain interstitials) is the driving force for nucleation. None of the structural features of the solid are needed to cause agglomeration of the point defects. Heterogeneous nucleation refers to the appearance of voids on distinct structural features of the solid. These features can be prexisting gas bubbles, incoherent precipitate particles, dislocations. The depleted zone created in the collision cascade can also act as heterogeneous nucleation sites for void formation. The latter is considered to be the most important nucleation mechanism in irradiated UO_2 fuels.

Nucleation and growth are often treated as sequential steps in the overall process of void formation. During the nucleation period, the number density of cavities increases with time, but the sizes remain small. During the growth period that follows, the number density stabilizes and the void size increases with time. The void is assumed to be spherical and its growth is controlled by diffusion of vacancies and interstitials from the bulk of the solid to the void surface.

In most situations, gas atoms will stabilize the voids/cavities. The analysis is sensitive to the

equation of state of gas in the cavity, non-ideality is accounted for by the modified Van der Waals Equation of State (EOS) in which the pressure correction has been ommited:

$$p = \frac{mkT}{\frac{4}{3}\pi R^3 - mB} \tag{II.2}$$

where m is the number of gas atoms in the cavity (likely time-dependant) and B the exclusion volume of gas atoms. More details about the effect of gas atoms are given in section III.3.3.

III

Effects of irradiation conditions in a nuclear fuel rod

Contents

During the irradiation in the reactor, the fuel is subjected to many transformations. Different physical, mechanical and physico-chemical phenomena take place, all linked either to the high temperature and to the strong radial temperature gradient within the pellet, or to the disturbances of the crystal lattice induced by the fissions, or to the increasing quantity of fission products which form other phases and are likely to migrate both radially and axially.

All these phenomena interact all together, but are presented separately, as much as possible, for the sake of clarity.

III.1 The temperature distribution

III.1.1 Formation of transuranium elements and plutonium distribution

In parallel with the fission of ^{235}U by thermal neutrons, the fuel is also subjected to transmutation reactions of uranium by neutron captures followed by β-decays. Indeed, absorption of a thermal neutron by a fissile nucleus like ^{235}U or ^{239}Pu does not always lead to the fission of this nucleus. The neutron can simply be captured by the nucleus, which happens for 16% of total fissions of ^{235}U and for 27% of ^{239}Pu. The main part of the neutron captures in UO_2 fuel takes place with ^{238}U (25% of the incidental neutrons are captured by this isotope); these captures are of particular importance because they lead to the formation of fissile isotopes of plutonium (^{239}Pu, and then ^{241}Pu):

$$^{238}_{92}U \xrightarrow{(n,\gamma)} {}^{239}_{92}U \xrightarrow{\beta-} {}^{239}_{93}Np \xrightarrow{\beta-} {}^{239}_{94}Pu \xrightarrow{(n,\gamma)} {}^{240}_{94}Pu \xrightarrow{(n,\gamma)} {}^{241}_{94}Pu \qquad \text{(III.1)}$$

The heavy nuclei resulting from uranium by neutron capture or radioactive decay, typically β-decays, are called *transuranium elements*. Among them, the two fissile isotopes of plutonium (^{239}Pu and ^{241}Pu) play, because of their relative abundance, a particular role in the fuel evolution during irradiation. Indeed, a considerable part of fissions result from these two isotopes. For instance, in UO_2 fuel enriched to 3.25% with ^{235}U, proportion of fissions resulting from plutonium is 30% at a burn-up of 12 MWd/kgU (which corresponds more or less to one irradiation cycle); at 60 MWd/kgU (after 5 irradiation cycles), this reaches 80%.

The evolution of the total concentrations in uranium, plutonium and the fission product neodymium in a fuel pellet as a function of the local burn-up is presented on Fig. III.1. The neodymium concentration increases linearly with burn-up. This is a marker of the fission number and is used as a basis for the analysis of the plutonium concentration evolution. Up to 40 MWd/kgU (which corresponds to about 3 irradiation cycles in a PWR), the production rate of plutonium increases more quickly than that of neodymium. At higher burn-ups, the formation and consumption of plutonium tend to compensate.

In a reactor, the high concentration of plutonium at the pellet periphery is due to a non-uniform distribution of the neutron flux along the pellet diameter. The power generated at the periphery is, as a consequence, higher than in the other parts of the pellet and this effect is all the more high as the initial enrichment is low (because this results from neutron captures of ^{238}U). The digging of the power radial profile in a fuel enriched to 3.25% with ^{235}U, as presented in Fig. III.2 for different values of burn-up, shows that the power profile quickly

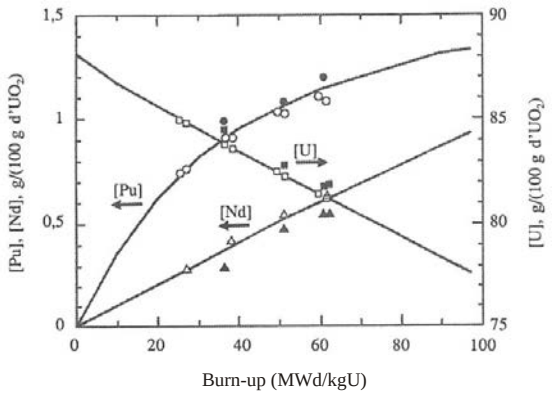

Figure III.1: Evolution of total concentration in U, Pu and Nd as a function of burn-up [5].

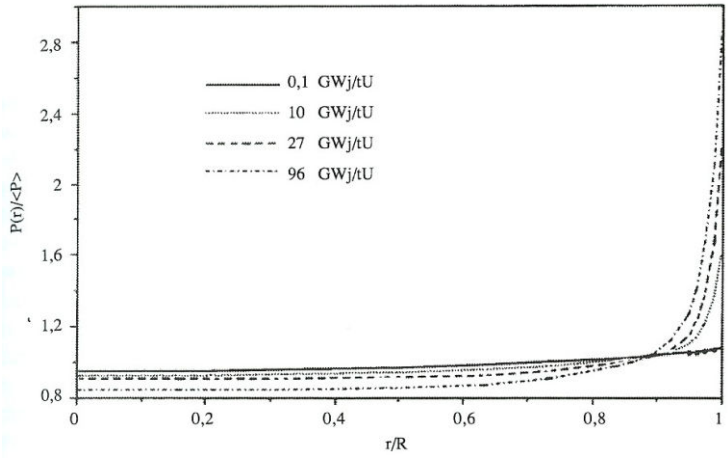

Figure III.2: Relative radial distribution of power in a PWR fuel pellet as a function of burn-up [5].

digs during the first two irradiation cycles and that this evolution is then slower during the following cycles. As burn-up is defined by the integral of the energy, the former shows a similar but less marked variation.

III.1.2 Heat production and transfer

When the chain reaction is starting, the first consequence of the uranium or plutonium fission is heat production. This heat then diffuses to the coolant. To this aim, heat will have to diffuse through the fuel pellet, to cross the gap between the fuel and the cladding, to cross the cladding by conduction and possibly the external oxide layer, and finally to pass in the coolant by diffusive and convective thermal transfers.

The coolant temperature can be easily determined and calculating the thermal transfer through the cladding is quite basic under normal operating conditions. The calculation of the temperatures in any point of the fuel is thus made by:

(a) A calculation of conductive heat flow in an infinite rod in which heat is not homogeneously produced, as shown in Fig. III.2.

(b) A calculation of thermal transfer between the outer part of the fuel pellet and the inner part of the cladding. This calculation depends on whether the gap is open or closed.

The temperature profile within the fuel pellet is determined by solving the heat equation. The most simple solution can be obtained by considering that, in a first approximation, the thermal conductivity of the oxide λ is independent of the temperature and that the power density P_v is also independent of the radial position within the pellet. The temperature in any point of the pellet is given by [55]:

$$T = T_s + \frac{1}{4}\frac{P_l R^2}{\lambda}\left(1 - \frac{r^2}{R^2}\right) \tag{III.2}$$

where R is the pellet radius, λ the thermal conductivity of UO_2, T_s the surface temperature, and P_l the linear power density.

The increase of the central temperature is proportional to the linear power and inversely proportional to the fuel thermal conductivity.

In the case of a real rod, the temperature dependance of the thermal conductivity must be considered. In addition, the approximation of a constant power density is not suitable as shown in Fig. III.2: The power density is lower in the central part of the pellet than at the periphery.

Typical temperature profiles are shown in Fig. III.3 for different constant linear power and a constant gap thickness.

III.1.3 Effects of the temperature

Because of high thermal gradients within the pellet (a few hundreds kelvins per centimeter), internal thermal stresses are developping in the fuel. The latter can be calculated by means of finite elements codes, but a good approximation can be obtained with an analytical solution. With the assumption of constant thermal power, thermal conductivity and thermal expansion coefficient, maximum tensile stresses $\sigma_{\theta\,max}$ are located at the pellet surface and are:

$$\sigma_{\theta\,max} = \frac{E\,\alpha}{2(1-\nu)}(T_c - T_s) \tag{III.3}$$

where E is the Young modulus, ν Poisson's ratio, α the thermal expansion coefficient and T_c the centerline temperature. In common with most other ceramics, polycrystalline UO_2 fuel is a brittle material at temperature less than approximately 0.5 T_{fusion} (about 1400°C). The oxide pellet will crack as soon as $\sigma_{\theta\,max}$ exceeds the fracture stress σ_{fract}, i.e. when:

$$T_c - T_s > 2\frac{1-\nu}{E\,\alpha}\sigma_{fract} \tag{III.4}$$

The rupture stress, such as it is determined from bending tests, can vary notably according to the surface quality. By choosing an average value of 130 MPa, it is shown that the pellet starts fracturing when T_c-T_s >100°C, i.e. during the first power increase to nominal

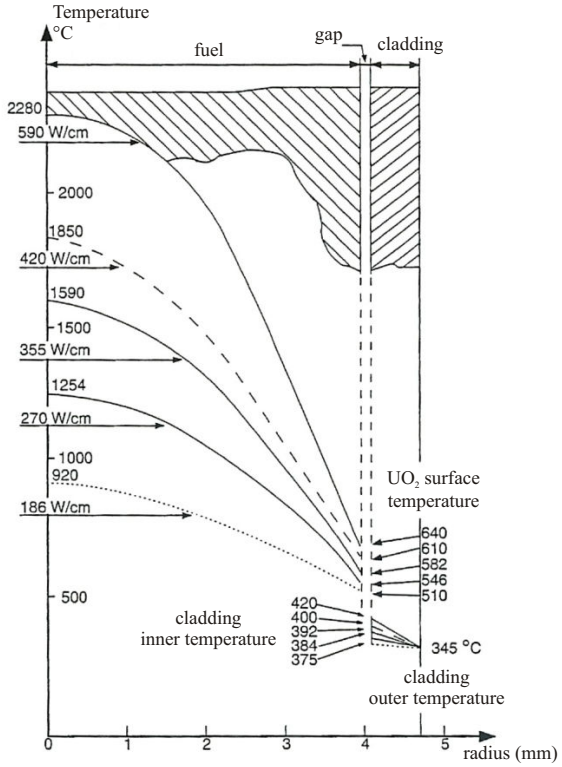

Figure III.3: Temperature distribution in a PWR fuel pellet as function of linear power [55].

conditions where the linear power is only about 50 W.cm^{-1}. At the end of the first power increase, the pellets are thus systematically fractured (Fig. III.4). Transverse sections on PWR fuel pellets generally highlight about ten cracks. These cracks are mainly radial, but transverse ones (perpendicular to the axis) also appear.

In addition, the fuel pellet is subject to thermoelastic deformation. This is due to the fact that the pellet has a finite length (between 10 and 14 mm). This means that the approximation of plane deformation is not valid anymore in the vicinity of the pellet faces: the axial stress becomes zero on these faces. It can be shown that under the effect of thermal stresses, the pellet initially orthocylindric tends to a "hourglassing" shape with convex faces (Fig. III.5).

III.2 The stress distribution

At the beginning of the irradiation, the cladding is subjected to the differential pressure (coolant pressure minus internal gas pressure) and creeps in compression due to this loading. Progressively the pellet-cladding gap closes under the combined effect of the cladding creep and the pellet swelling induced by fission product accumulation (see below). Due to the hourglass pellet shape, the first contact occurs at the inter-pellet level where the gap is the lowest. Between the inter-pellet planes, the cladding continues to creep down to take the exact pellet shape. This mechanism has been correlated with the primary ridges identified on the cladding diametral measurements after irradiation (Fig. III.6(c)).

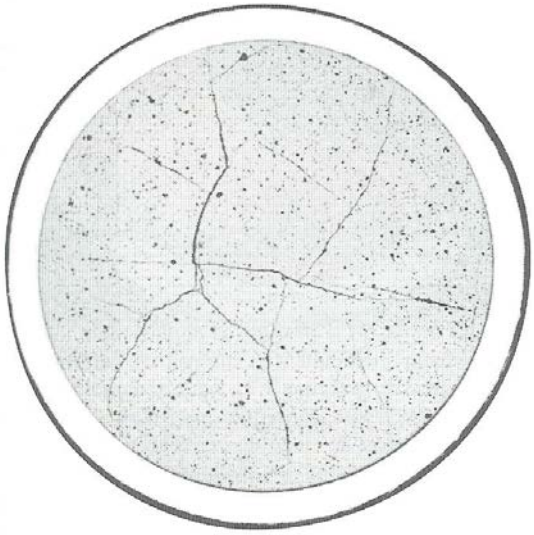

Figure III.4: Macrography of a PWR fuel pellet cracked by the thermal gradient [5].

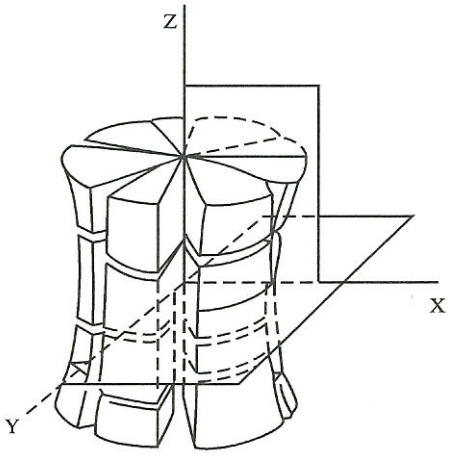

Figure III.5: Fuel pellet with a "hourglassing" shape due to the effect of thermal stresses [5].

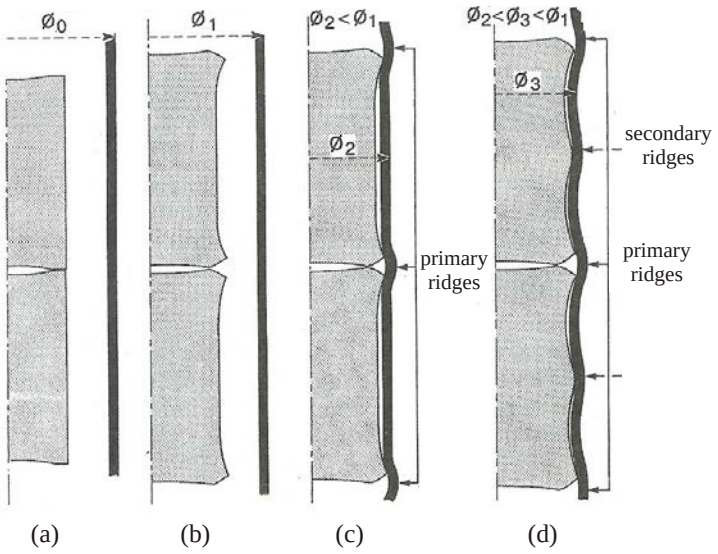

Figure III.6: Evolution of the gap between the cladding and the fuel pellet during irradiation. (a) start of irradiation, (b) first cycle and start of second irradiation cycle, (c) second half of second cycle: first cladding-pellet contact and appearance of primary ridges, (d) in case of power ramp: appearance of secondary ridges [5].

While the gap closes, the cladding, initially loaded in compression, progressively gets in contact with the pellet and becomes loaded in tension. The tensile stress increases slowly up to about 20 to 30 MPa, which corresponds to an equilibrium value, according to the cladding creep rate and the pellet swelling rate. So, in nominal conditions, the cladding easily accommodates the pellet swelling kinetics by a neutron flux activated creep deformation: the cladding is loaded by low PCMI.
During transients (power ramps), the thermal gradient largely and quickly increases to reach within a few minutes a value almost three times higher than the nominal value (1200°C for 4 mm in radius). The corresponding pellet dilatation leads to a strong pellet thrust on the cladding. So, high tensile stresses are induced in the cladding, which cannot easily accommodate such a thermal expansion.
In addition, due to the high temperatures, the fuel viscoplasticity is also activated in the pellet centre and leads to a progressive filling of the transversal cracks. The fuel creep is correlated with the formation of "secondary" ridges at the median pellet plane level (Fig. III.6(d)). In such strong PCMI conditions, the mechanical state of the pellet-cladding system is no more governed by the pellet deformation alone. In fact, the stiffness of the fragmented pellets and the cladding are not so different anymore and the strong cladding mechanical pre-stressing contributes to unbend the fragmented pellets.

III.3 Burn-up and fission product accumulation

III.3.1 Chemical state of fission products

Fission products (FP) are generated in a large number with typical distributions depending on the neutron energy and the respective fissile nuclide. Kleykamp [44] provided a specific

classification scheme based on the chemical state of the fission products. The four different classes are:

1. fission gases and other volatile fission products: Kr, Xe, Br, I;
2. fission products forming metallic precipitates: Mo, Tc, Ru, Rh, Pd, Ag, Cd, In, Sn, Sb, Te;
3. fission products forming oxide precipitates: Rb, Cs, Ba, Zr, Nb, Mo, Te;
4. fission products dissolved as oxides in the fuel matrix: Sr, Zr, Nb and the rare earths Y, La, Ce, Pr, Nd, Pm, Sm.

There are continuous transitions between groups 2 and 3 due to similar oxygen potentials of some fission product oxides and the fuel which changes its composition during the fission process. Transitions also occur between the groups 3 and 4 due to the burn-up dependent distribution coefficients of the respective cations in both of the oxide phases.

The classification provided by Kleykamp can be used to calculate, for instance, the contribution of each group in the swelling rate of the fuel pellet.

III.3.2 Swelling due to solid fission products

Accurate estimation of the dimensional changes of ceramic fuels during irradiation is of the utmost importance in predicting the mechanical performance, especially of fast reactor fuel elements. Fuel swelling due to replacement of heavy metal atoms by fission product atoms is commonly considered as the sum of a contribution due to fission gases and another arising from all other fission products. The former is treated separately because the inert gases xenon and krypton coalesce into bubbles within the fuel (due to their very low solubility), whereas most of the remaining fission products are solid. At low temperatures (<1000°C) the fission gases may not be sufficiently mobile in the fuel to permit coalescence into bubbles, in which case the swelling due to these species is treated in the same manner as is that due to the other fission products.

The physico-chemical parameter which characterizes solid swelling is the volume associated with each atom of fission products in their expected states in the irradiated fuel. This volume includes the oxygen atoms associated with the fission products (if any) and is referred to as the partial volume v_i of the fission product.

The swelling due to solid fission products is found to be [2]:

$$\left(\frac{\Delta V}{V}\right)_{\text{solid FP}} = \frac{V - V^\circ}{V^\circ} = \left(\sum_{\text{solid FP}} Y_i \frac{v_i}{v_U} - 1\right)\beta \qquad \text{(III.5)}$$

where v_i is the partial volume of the fission product, Y_i is the sum of the elemental yields of all fission products in group i and β is the burn-up in at%. The swelling due to solid fission products can be calculated by using the partial volumes estimated in Eq. III.5. The results are shown in Tab. III.1 for uranium fission, but Anselin [2] has shown that the swelling is

Fission product group	Y_i	v_i/v_U	$Y_i.v_i/v_U$
Nb + soluble Zr	0.149		
Y + rare earths	0.534		
Total soluble fission products	0.683	1.00	0.683
Mo	0.240		
Ru + Tc + Rh + Pd	0.263		
Total metallic inclusions	0.503	0.36	0.181
Ba + Sr (as zirconates)	0.149	1.74	0.258
Cs + Rb + I + Te	0.238	0.76	0.181
Other fission products	0.027	0.76	0.021
		Total	1.324

Table III.1: Swelling due to solid fission products in pure UO_2.

essentially the same for mixed uranium-plutonium oxides. The first column in Tab. III.1 lists the fission products in groups of the same physical state (i.e., with the same partial volume), the second column gives the elemental yields, and the third column gives the ratio of the partial volume of the group to that of pure UO_2. Solid fission product swelling in oxide fuels is found to be 0.32% per atom percent burn-up. This figure, however, is subject to large uncertainties for the following reasons:

1. It is based on the assumption that each region of the fuel acts as a closed system for all fission products (except xenon and krypton) and the heavy metals. The complications introduced by fission-product migration are not considered. The general tendency for the hotter regions of the fuel to lose fission products by a variety of mechanisms means that the solid swelling calculated in Tab. III.1 is an overestimate near the fuel center. Conversely, swelling in the zone near the fuel surface where some of the volatile fission products condense is underestimated.

2. The assignment of the physical and chemical states of some of the fission products is subject to considerable uncertainty. For example, in Tab. III.1 all the molybdenum was assumed to exist as metal, where it contributes a partial volume approximately one-third that of UO_2. If this element was present in the fuel as soluble MoO_2, its partial volume would have been equal to that af UO_2. Transfer of molybdenum from the metallic inclusions to the fuel matrix adds $0.240\times(1.00 - 0.36) = 0.15$ to the solid swelling, which would then be 0.47% per atom percent burn-up instead af 0.32%. Since the previous analysis on the chemical state of fission products showed that molybdenum transfers from metal to oxide as irradiation proceeds, the solid fission product swelling should also increase with irradiation.

Moreover, in Tab. III.1, cesium, rubidium, iodine, and tellurium have been assumed to be solids. It has been reported in [93] that these fission products are more likely to be present in gaseous form over most of the fuel and are incorporated into the solid at the fuel surface only if the oxygen potential is sufficiently high. Thus, it would be reasonable to exclude this

category of fission product from solid swelling, which would reduce the latter from 0.32% to 0.14%. The best that available knowledge of the physico-chemical states and migration characteristics of the fission products allows is a band af solid swelling coefficients between 0.15 to 0.45% per atom percent burn-up. In initially hypostoichiometric fuel, the lower figure is probably appropriate, but, for hyperstoichiometric fuel or heavily irradiated fuel of any initial stoichiometry, solid swelling is more likely to be close to the larger number.

III.3.3 Swelling due to gaseous fission products

If the gas is released from the fuel, the pressure within the fuel pin is correspondingly increased, and the cladding is subject to stresses that can ultimately result in failure. In addition, the extent to which the fission gases are freed from the fuel determines in large part the potential hazard of a reactor core in the event of an accidental cladding breach, which can occur either at the reactor site or during transportation of the spent fuel to a reprocessing plant.

On the other hand, if the fission gases are retained in the fuel, they nearly always precipitate as bubbles. Inasmuch as the density of the gas in such bubbles is considerably lower than that of the solid fuel, gas atoms residing in bubbles occupy more volume than either the fissile atoms they replaced or fission-product atoms that segregate as solid phases (e.g., the noble metals). The precipitation of fission gases thus leads to swelling of the fuel to a larger degree than the volume expansion that would occur if the xenon and krypton had remained dispersed on an atomic scale in the fuel matrix (in which case they can be treated as other solid fission products). Swelling adversely affects fuel performance because it promotes fuel-cladding contact, and the resultant stress on the cladding can shorten its lifetime. In addition, the bubbles of low-conductivity gas decrease the thermal conductivity of the fuel in the same manner as the fabricated porosity and thereby lead to fuel temperatures higher than exhibited by fully dense fuel at the same heat rating.

Fission gas swelling and release are complementary phenomena. A piece of fuel that releases a large portion of its fission gases exhibits low swelling because there is little gas remaining in the fuel to form bubbles. Conversely, complete retention of the fission gases in a section of fuel is usually accompanied by significant swelling. These effects can be illustrated by examining the behavior of the fission gases as a function of radial position in a fuel rod. Near the cool periphery of the fuel, the fission gases are quite immobile in the solid (because of the low temperature), and, consequently, they are not released in large quantities, and the expansion they cause is comparable to that of other solid fission products. In this region both release and swelling are low. At intermediate radial positions in the fuel (corresponding roughly to the region of equiaxed-grain growth), release is appreciable, but large swelling can occur because a significant fraction of the gases is retained in the fuel as bubbles. In the hot inner region, nearly all fission gases are released as soon as they are formed, and the swelling is quite small.

Many individual physical processes contribute to the behavior of fission gases in nuclear fuels:

1. Nucleation of gas bubbles: either homogeneously by chance encounters of wandering gas atoms or heterogeneously on fission-fragment tracks or dislocation lines.

2. Growth of gas bubbles by atomic migration of fission gas atoms to existing bubbles. Bubble growth can be affected by the availability of vacancies to permit the bubble to expand as gas is accumulated and by the effects of surface tension and the stress state of the surrounding fuel matrix, which determine the stable size of the bubble.

3. Re-solution of the gas atoms in the matrix.

4. Migration of the bubbles, either as a random-walk process in the absence of directed forces acting on the bubble or as biased motion when such forces are present. The forces that act on gas bubbles in solids are generally believed to be those due to the temperature or stress gradients, or restraining forces due to dislocations and grain boundaries. The former forces always cause the bubble to move in a particular direction. The forces due to crystal defects can act either to pin the bubble if the defects are immobile or to drag the bubbles if the defects are themselves in motion (i.e., dislocations move along glide planes in the crystal in response to mechanical stresses, and grain boundaries move in the process of grain growth). Thus, bubble motion can occur by dislocation-line sweeping or grain-boundary sweeping.

5. Coalescence of bubbles moving either in a random or directional fashion.

6. Interaction of bubbles with the crystal defects (dislocations and grain boundaries).

7. Release of the fission gases, either to external surfaces such as the central void, cracks in the fuel, or the fuel-cladding gap or to internal surfaces such as grain boundaries. When the bubbles on grain boundaries become sufficiently large and numerous, they can link up and release gas to one of the external surfaces.

8. Release of fission gas by direct flight of the energic fission fragments out of an external surface. This mode of release is small and is significant only at low temperatures.

Part 2

State-of-the-Art about the High Burn-up Structure in nuclear fuels

IV

Observations and characterisations of the High Burn-up Structure

Contents

IV.1 Neutronic origin and early observations of the High Burn-up Structure

During irradiation, the strong resonance absorption of epithermal neutrons in ^{238}U leads to the production of the isotope ^{239}U which successively decays by β-emissions to ^{239}Np and ^{239}Pu. For fuel in the form of cylindrical pellets, maximum neutron absorption takes place at the pellet surface, hence the plutonium concentration so formed exhibits a maximum at this outer surface and decreases exponentially towards the pellet centre. Subsequent fissioning of this plutonium results in a near surface enhancement of burn-up compared to that throughout the rest of the pellet. At a pellet average burn-up $\geq$60 MWd/kg, the local burn-up within $\sim$100 μm of the pellet surface is increased by a factor 2 or 3 depending on the flux spectrum of the reactor. The resulting re-crystallized structure is best observed by scanning electron microscopy (SEM) of a fractured specimen where the surface morphology takes on a distinctive "cauliflower" like appearance as illustrated in Fig. IV.1(a). Fig. IV.1(b) shows a micrograph of the same fuel for comparison, but at a different radial position where this structure has not formed. Because of its location at the pellet surface, this structure has first been called "rim effect".

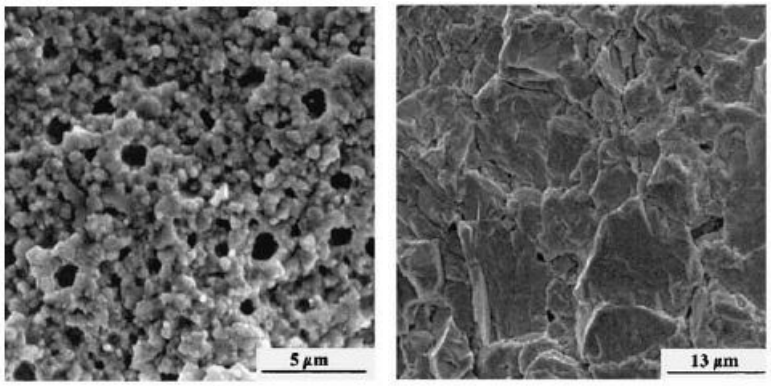

Figure IV.1: SEM micrographs showing the microstructure of a 98 MWd/kg average burn-up fuel at different radial positions (a) r/r_0=1.0, (b) r/r_0=0.5 [66].

With the introduction of 4 and 5 irradiation cycles, there was a renewed interest in this phenomenon in the late 1980's and early 1990's [141, 65, 6]. At first it was thought that the restructuring and enhanced porosity was a direct result of the production of plutonium in the rim region of the pellet. However, electron-probe micro-analysis (EPMA) studies on high burn-up LWR fuel by Walker et al. [142] showed that the restructuring extended much further from the pellet surface than the extent of the plutonium concentration. From these studies it was clear that the restructuring was a result of the local high burn-up and not the generation of plutonium. This conclusion was supported further by Kameyama et al. [40] who investigated the threshold for rim structure formation as a function of burn-up in fuels of different initial enrichment in the High Burn-up Effects Program HBEP (more details about this program can be found in [26, 84]). They found that the threshold, which occurred at a local burn-up of 70-80 MWd/kgU, was independent of the enrichment which varied in their study from 1.38 to 8.25 wt% ^{235}U. The contribution of plutonium to the local burn-

up becomes larger in the lower enriched pellets at high burn-up. They concluded that the plutonium/uranium burn-up ratios did not change the threshold burn-up for rim structure formation. In addition, the different enrichments ensured that the fuels operated at different power densities during irradiation. Thus the invariance of the threshold with enrichment also implied that it was insensitive to power or fission rate.

Further support for the onset of the rim structure depending only on local burn-up and not on the U/Pu fission ratio, hence on plutonium concentration and heat rate, comes from the High Burn-up Rim Project (HBRP) [119, 43, 118]. Here, UO_2 disks fabricated with a ^{235}U enrichment of 26 wt% were irradiated in the Halden reactor, and discharged with a range of burn-up levels up to 100 MWd/kgU. Despite the extreme uranium enrichment and short time irradiation of 2-2.5 years, the onset of the rim structure occurred at burn-up levels very similar to those found in lower enriched LWR fuel as discussed above by Walker et al. [142] and Kameyama et al. [40]. In the highest burn-up disks, this restructuring occurred throughout the whole volume of the disk. As a consequence, there is a tendency to re-name the 'rim' structure as the "High Burn-up Structure", HBS, because such a modification of the microstructure can occur anywhere within the pellet at temperatures less than 1000°C and depends solely on the local burn-up. This is also supported by observations of HBS surrounding Pu-rich regions in some types of MOX fuels whose burn-up is in excess of the surrounding matrix [141].

This restructuring was first observed in very high burn-up fuel in the late 1950's [8] and is described in the book on uranium dioxide by Belle [13]. At that time, there was a substantial study of uranium bearing fuels for use in naval reactors. One characteristic of such an application of nuclear power was the very high burn-up expected before the power unit was serviced or replaced. As a consequence, one subject of research was the possibility of a high burn-up limit to fuel integrity. It was found that UO_2 irradiated to high burn-up, ∼10%FIMA at relatively low temperatures, did experience a change of crystalline state. This was particularly evident in experiments reported by Barney et al. [8] where highly enriched UO_2 particles, 94-95% of the UO_2 theoretical density (%TD), were embedded in a stainless steel matrix and irradiated to exposures up to 30%FIMA (Fig. IV.2). Examination of the fuel particles after irradiation lead the authors to make the following observations:

- Appearance of large pores clearly visible by optical microscopy
- Apparent plasticity of the oxide
- Tendency towards swelling and healing of cracks; the swelling was readily restrained by the imposition of external pressure
- X-ray diffraction showed little or nonexistent peaks but an increase in background scattering; from this it was inferred that the material became amorphous

This "new phenomenon" was also reported by Bleiberg [16] to be observed at the rim area of high burn-up fuel pellets in commercial reactors. The restructuring had already been found in special test irradiations in the early days, and also to some extent in FBRs, but it was not further investigated since the concerned burn-ups for commercial LWR reactors were well below the transformation threshold. However, around the mid-1980's the phenomenon

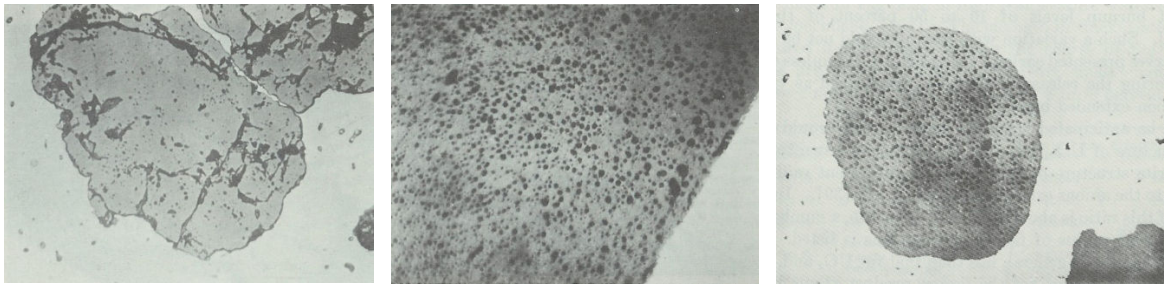

(a) (b) (c)

Figure IV.2: Metallographs of (a) unirradiated UO_2 particle of 95%TD in stainless-steel matrix, as-etched, (b) irradiated to 25 at%, as-polished, (c) irradiated to 30 at%, as-polished. All pictures are ×500, reduction factor 1/2 [8].

was observed again at several hot cells in power reactor fuel; one of the first reports was made at the 1986 meeting of the HBEP program by D. Baron based on observations on Fessenheim Fragema rods irradiated to five cycles (55 MWd/kgU) [10] and similar rods irradiated in the Zion reactor [7]. There, reduction of EPMA signal for xenon was first observed at the rim area of the pellets. Nearly at the same time ceramographic observations were reported by other hot laboratories, e.g., BMI for C-E fuel reported by S.R. Pati [95], and also Windscale for KWU fuel [7]. A few years later, FESEM (Field Emission SEM), with its ultimate sub-nanometer resolution, was introduced in Japan to investigate nuclear fuels [45]. The microscope revealed a structure named by Hj. Matzke "Cauliflower-like", which has an appearance similar to the complex biological morphology of the vegetable [74, 100]. After these observations and findings, some concern arose about the possible degradation of fuel performance at high burn-up, mainly due to the high porosity in the restructured fuel which would result in volumetric increase, thermal conductivity degradation and potential fission gas release (cf chapter V).

IV.2 Characterisations of the HBS

Fuels with higher discharge burn-ups have then been extensively studied in order to investigate in detail this new structure (now known as rim structure or HBS). In 1996, a complete description of the HBS was proposed. As a rule, this zone is characterised by:

(1) Xe depletion from the matrix of newly formed small grains, as measured by EPMA (e.g. [79, 26, 53]),

(2) coarsened fission gas pores of micrometric size [129],

(3) sub-division of the initial grains from typically 10 μm to 0.15-0.30 μm (e.g. [79, 91]).

It was already considered at that time that the grain subdivision and the formation of the new fission gas bubble and pore structure were correlated. Moreover, general agreement existed that the HBS was caused by a combination of the high burn-ups reached in the rim region and its low operating temperatures [131, 26, 141, 142]. The threshold local burn-up for this effect has been reported in the range 70-80 MWd/kgHM [26, 142].

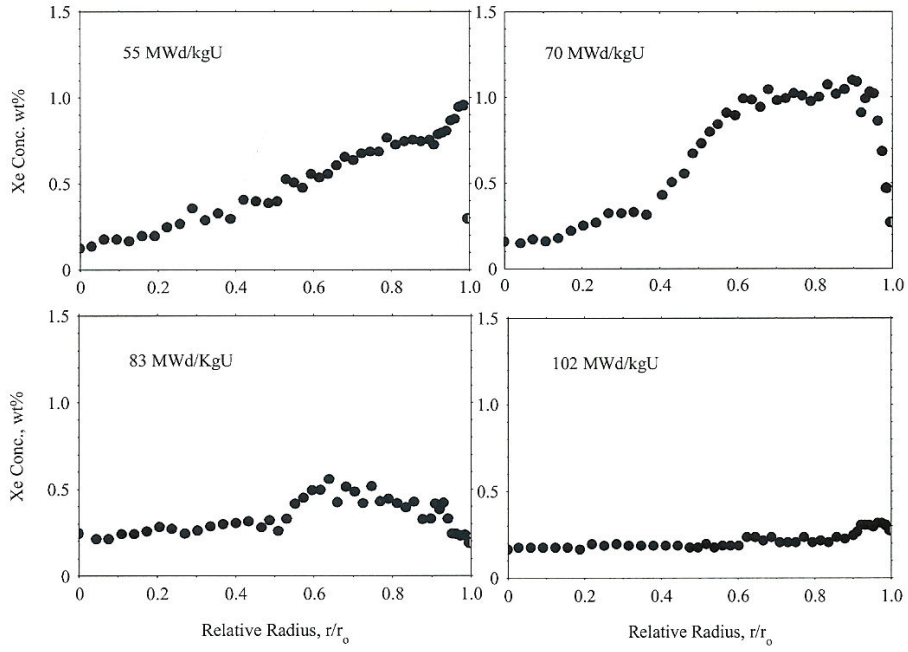

Figure IV.3: EPMA concentration profiles for the radial distribution of Xe retained in the UO_2 grains of 4 PWR fuels [20].

These 3 characteristics are now presented in more detail.

IV.2.1 Measurement of Xe-depletion from the restructured UO_2 matrix

The investigation of Xe-depletion from the matrix in high burn-up fuels started in the beginning of the 1990's with the post-irradiation examinations of the HBEP fuel rods. EPMA has then been widely used to estimate the radial extent of the HBS by measuring the distance over which Xe depletion occurs in the outer region of the fuel.

Figs. IV.3 and IV.4 show typical results obtained by means of EPMA and produced by Walker et al. [141, 142, 140], Une et al. [137], Mogensen et al. [84], Brémier et al. [20], Manzel and Walker [66].

As an example, EPMA concentration profiles for the radial distribution of Xe retained in the UO_2 grains of four PWR fuel pellets with burn-ups of 55, 70, 83 and 102 MWd/kgU are shown in Fig. IV.3.

It can be seen that at 55 MWd/kgU the concentration of Xe drops sharply at the pellet surface showing that the high burn-up structure has begun to form. Between this point and r/r_0=0.7, where thermally activated release begins, there is complete retention. Between r/r_0= 0.7 and the pellet centre the concentration of retained gas gradually decreases from 0.7 to 0.2 wt%. At 70 MWd/kg, the concentration of retained gas in the region between r/r_0=0.6 and 0.9 has increased markedly. In this region the fission gas created during the irradiation is completely retained. The HBS penetrates to r/r_0=0.9 and as a result the concentration of retained Xe falls steeply in the interval between this radial position and the pellet surface.

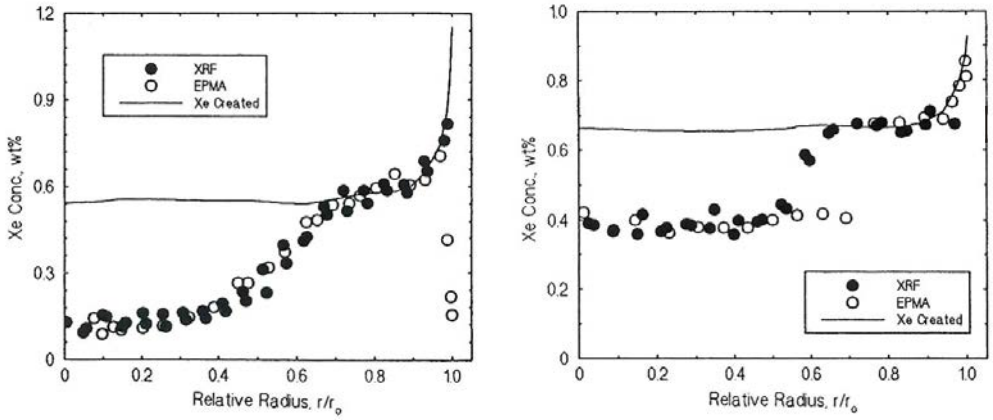

Figure IV.4: Radial distributions of xenon of different fuel sections with average burn-up (a) 54.9 MWd/kg and (b) 62.5 MWd/kg [84].

Between r/r_0=0.6 and the pellet centre the effect of thermal release is clearly visible. In this region the concentration of retained gas drops from about 1 wt% at r/r_0=0.6 to 0.3 wt% at r/r_0=0.4 and then levels off. At 83 MWd/kg, over the whole fuel radius a large percentage of fission gas is missing from the fuel grains. Between r/r_0=0.6 and the pellet surface, the observed Xe depletion is due to the presence of the HBS. In the central region of the pellet, thermal gas has progressed further and low concentrations of retained Xe are measured out to r/r_0=0.5. At the highest burn-up of 102 MWd/kgU, a low Xe concentration of 0.1 to 0.3 wt% is measured over the entire fuel radius. In the outer part of fuel the low concentration suggests that the HBS is fully developed; that is to say, no un-transformed UO_2 grains exist. In the central region of the fuel, the low concentration of Xe is a consequence of the fact that thermally activated release is everywhere complete.

The X-ray fluorescence (XRF) technique can also be used in the analysis of understanding the fission gas behavior in irradiated fuels. In contrast to EPMA, which measures the concentration of gas retained in the UO_2 lattice and in gas bubbles smaller than 0.1 μm, XRF gives the total amount of gas locally retained in a nuclear fuel, which includes the concentration trapped on grain boundaries and in large intergranular bubbles. Thus, by using both XRF and EPMA to measure the radial distribution of xenon in nuclear fuel, a detailed picture of fission gas behavior can be obtained. An example is shown in Fig. IV.4. As seen in Fig. IV.4(a) a near perfect match exists between the XRF and EPMA profiles. Only in the rim region between r/r_0=0.97 and the pellet surface do the profiles deviate significantly. The inflexion in the EPMA profile at r/r_0=0.97 marks the limit of penetration of the HBS. The fact that the XRF profile follows closely the increase in burn-up in the vicinity of the fuel rim is taken as evidence that most, if not all, of the xenon missing from the new grains was contained in the pores of the high burn-up structure. This remark is very important in understanding the effect of the HBS on fission gas release, as detailed in section V.3. It is seen from Fig. IV.4(b) that in the central region of the fuel and in the outer part of the fuel between r/r_0=0.75 and 0.97 there is a good match between the XRF and EPMA profiles. In the central region of the fuel thermal gas release had occurred and in the zone between r/r_0= 0.5 and 0.75 XRF measured far higher concentrations of retained xenon than EPMA

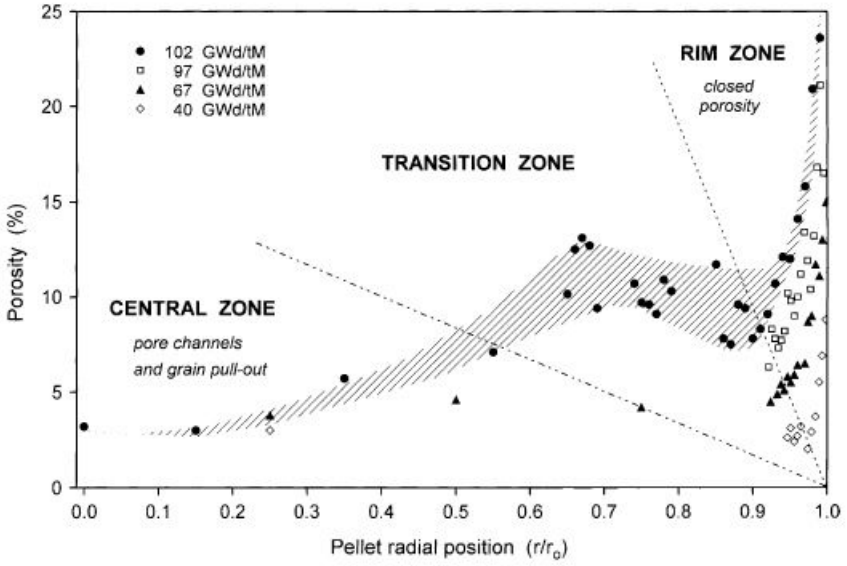

Figure IV.5: Variation of the fuel porosity with the pellet radius and burn-up [127].

showing that fission gas was trapped in the grain boundary porosity in this region. At the pellet rim the EPMA profile does not fall, but increases with the local burn-up indicating that the HBS has not formed although the local burn-up at the pellet rim had exceeded 80 MWd/kgU. The HBS did not form in this case due to the possible large grain size of this fuel (78 μm).

IV.2.2 Characteristics of the HBS porosity

From standard PWR UO_2 fuel samples irradiated in a commercial power reactor with burn-ups in the range of 40-67 MWd/kg, Spino et al. [129] performed a quantitative analysis of the evolution of the HBS porosity towards the pellet interior as the average burn-up increases. The maximum average burn-up was 66.6 MWd/kg but the data have recently been completed with fuel pellets irradiated up to 102 MWd/kg [127].

The main results of this analysis are shown in Figs. IV.5 and IV.6. Fig. IV.5 shows the typical variation of the fuel porosity with the pellet radius and burn-up, revealing the different zones with different porosity types that are manifested in the fuels, and the usual spread of the results. As a rule, the central zone is typically characterised by grains decorated with intergranular bubbles, abundant pore channels and a marked trend to grain pull-out. The peripheric zone is rather characterised by closed porosity and lesser propensity to grain pull-out. For all the samples measured, a similar exponential porosity increase on approaching the pellet edge is observed. The width in which this exponential growth occurs, and the maximum value at the edge, increase with the average burn-up of the sample. The level of porosity at which the exponential growth starts increases gradually as well with the average burn-up.

Fig. IV.6 displays the volume pore size distributions obtained for the samples with burn-ups

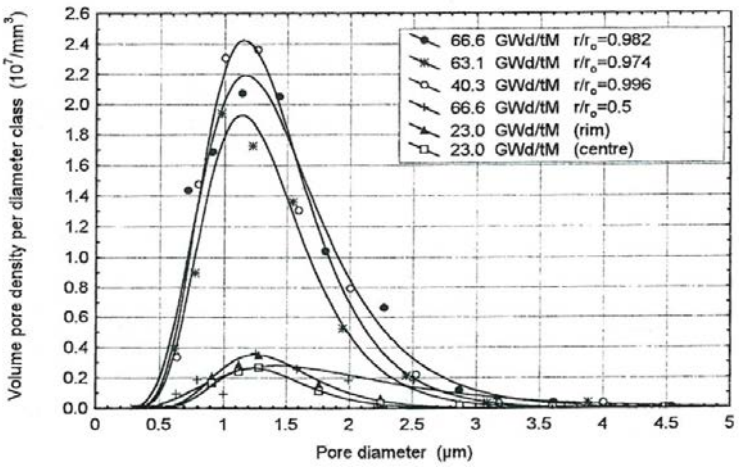

Figure IV.6: Pore size distributions at the peripheric and intermediate regions at different average burn-ups [129].

40.3, 63.1 and 66.6 MWd/kg. The latter are compared with results at lower burn-ups (23 MWd/kg) [4]. It is shown [4] that there is no significant difference at low burn-up between the pore densities at the fuel centre and peripheric region. On the contrary, the results of Spino et al. [129] clearly show that at burn-ups around 40 MWd/kg and above, the pore densities in the region affected by the HBS increase by about one order of magnitude relative to those of intermediate fuel regions (Fig. IV.6). This increase in porosity causes an increase in the total fuel swelling. This is shown in Fig. IV.7 in which the relative immersion densities of fuel samples with average burn-ups up to 100 MWd/kg have been plotted. It is seen that after the initial in-pile densification step, the fuel density steadily decreases with burn-up, with a clear increase in slope at burn-up >70 MWd/kg. In Fig. IV.7, the equivalent density loss attributed to the total matrix swelling $(1 - \Delta V^{matrix}/V_0^{matrix})$ is shown, according to the measurements of [4] (in which the range of determinations was limited to 40 MWd/kg). As indicated, this corresponds to a swelling rate of 1% per 10 MWd/kg. Brémier et al. [20] consider that above 65-70 MWd/kg, this swelling rate increases to 1.5 % per 10 MWd/kg. For comparison, Spino et al. [127] reasonably reproduced the density loss with an expression of the type $(\rho/\rho_{th})^2 = (a + b.BU^{3/2})$.

IV.2.3 Investigation of sub-divided HBS grains

Scanning Electron Microscopy (SEM) at high magnification and Transmission Electron Microscopy (TEM) have been extensively used in order to achieve progress in the characterisation and understanding of the HBS formation mechanisms.

The reference to a sub-division of the initial grains of 10 μm to new small grains in the size range 0.15-0.30 μm is in fact a simplified view of the process. First, the appearance of sub-grains depends on where the observation is performed. Indeed, two sub-grain populations have been highlighted by Lozano [62, 63]: polyhedral and round sub-grains (Fig. IV.8). Polyhedral sub-grains, with a size of 0.5-0.8 μm, are observed only inside the HBS, and thereby are characteristic of the HBS effect. Round sub-grains, 0.1 μm in size, are essentially located around pores with micrometric sizes. Moreover, Lozano has shown that these round

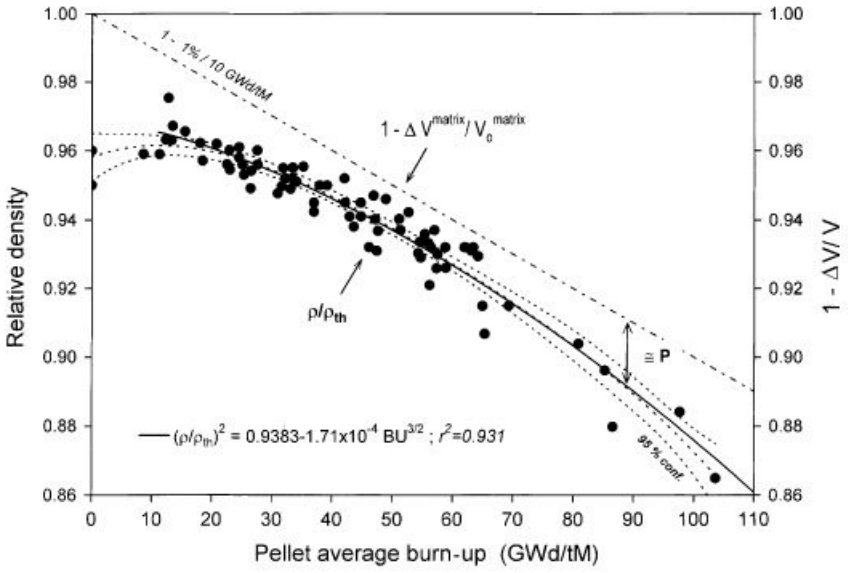

Figure IV.7: Measured relative immersion density as a function of the average pellet burn-up [127]. ρ is the bulk fuel density, ρ_{th} the theoretical density of UO_2 (10.96 g.cm^{-3}), and $\Delta V^{matrix}/V_0^{matrix}$ represents the fuel matrix swelling (split into the contributions of solid and gaseous fission products).

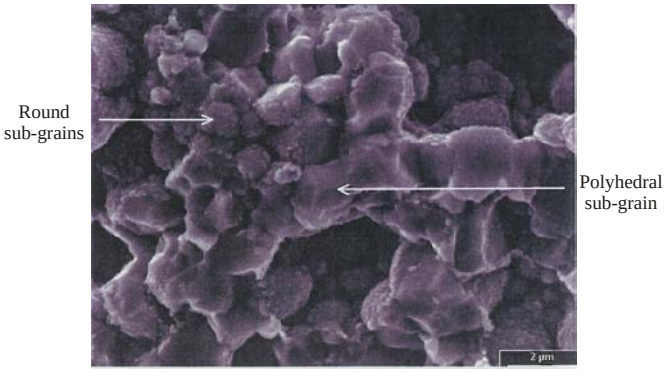

Figure IV.8: SEM micrograph showing the two different types of grains observed in the HBS. The HBS has been observed in the PuO_2 agglomerates of a MOX fuel [62].

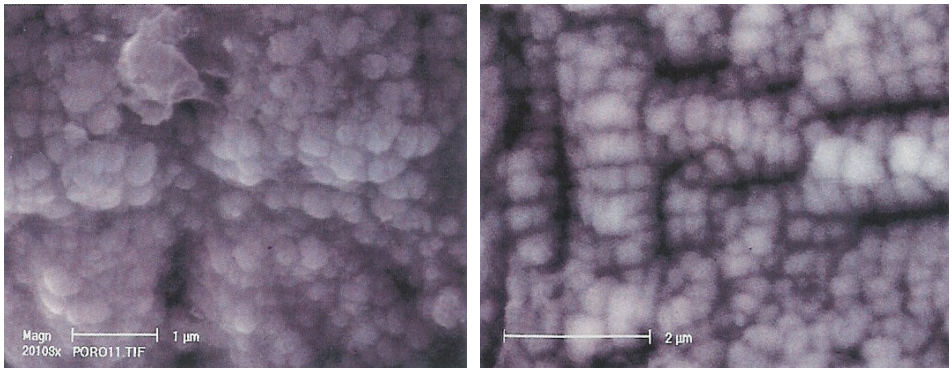

(a) (b)

Figure IV.9: SEM micrographs showing round sub-grains: (a) disordered round grains at the surface of a pore, and (b) grain surface sub-division on rolls, which are sub-divided on ordered round grains [63].

sub-grains are either disordered (Fig. IV.9(a)), or ordered and form rolls (Fig. IV.9(b)).

Second, depending on the HBS formation is the result of polygonization or recrystallization, this completely changes the mechanisms by which the new sub-grains have been produced. Indeed, recrystallization refers to the following sequential steps: formation of subgrains, growth of the subgrains into recrystallization nuclei, and growth of the recrystallized grains. On the contrary, polygonization is a dividing process to small grains and intermediate grain sizes can be observed during the subdivision [146].

On a UO_2 fuel specimen irradiated up to a pellet average burn-up of 49 MWd/kg in a BWR, Nogita and Une [91] performed microstructural observations by means of TEM. The maximum irradiation temperature at the pellet edge has been estimated by a fuel performance code to be about 400°C. Moreover, EPMA data indicated Xe depletion at the pellet periphery due to the formation of coarsened bubbles. The Ce concentration profile obtained by EPMA also permitted to assess the locally enhanced burn-up (due to the Pu build-up) to be about 100 MWd/kg.

From magnified bright-field TEM micrographs, Nogita and Une identified three different microstructures: (1) accumulated damage clusters of dislocations and small intragranular bubbles, (2) recrystallized grains, and (3)coarsened bubbles of about 0.5 μm in size. In the diffraction pattern of region A (Fig. IV.10), the main spots of {220} of the UO_2 single crystal from the [111] orientation are seen, which indicates the presence of a perfect crystal. On the other hand, the diffraction pattern from region B shows uniform rings of spots from UO_2, indicating the absence of a preferred grain orientation. From these observations, Nogita and Une concluded that recrystallized grains with high angle boundaries were present in region B.

From the dark-field image of the same region, the surface of the coarsened bubble showed an intricately bright image, indicating the presence of an extremely high density of dislocations and/or finely sub-divided grains. These results suggested that coarsened bubbles contained FP gases of Xe and Kr at very high pressures. Since the irradiation temperature at the pellet periphery is too low for thermally activated vacancies to contribute to coarsened bubble

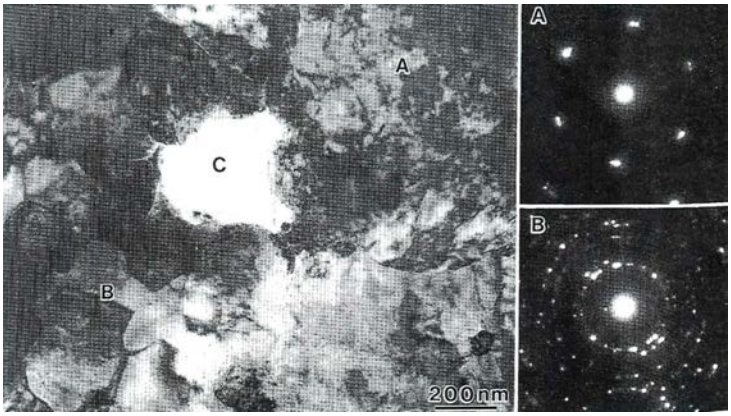

Figure IV.10: Bright-field TEM image of the HBS structure and selected diffraction patterns showing a defect cluster accumulated region A, a recrystallized region B, and a coarsened bubble C [91].

growth, Nogita and Une considered that the dislocations were produced by the dislocation loop punching mechanism. According to Spino [122], this is possible but not very probable.

Later in 2002, the first results of HBRP were published in the open literature by Sonoda et al. [118]. High resolution SEM examinations were performed in order to clarify the transition from original grains to sub-divided grains of the HBS. Fig. IV.11 shows the typical SEM images in the test matrix of burn-up and temperature.

It is seen that, before restructuring, most of the specimens have a structure characterised by original grains whose average size is 9.7±0.8 μm. In the restructured specimens, polyhedral grains with sizes ranging between 0.5 and 2 μm were observed away from the coarsened bubbles, while rounded grains in the size range 150-300 nm were only observed on the inner surface of coarsened bubbles. It was also observed that the size of the polyhedral grains decreases as burn-up increases. This can be explained by assuming that a homogeneous grain sub-division process takes place in the grains, forming smaller and smaller polyhedral grains as burn-up increases. The formation of rounded grains might be due to the effect of free surfaces. This important remark, in turn, would suggest that the HBS formation is independent from the existence of pores. This feature has never been explained theoretically (see chapter VI).

The same burn-up and temperature matrix can be built with TEM images [119]. A clear difference in the microstructure is shown in Fig. IV.12 for the restructured and non-restructured specimens. The four specimens from the UO_2 disks irradiated at a burn-up higher than 75 MWd/kgU and at a temperature below than 1100°C contain the new polyhedral sub-grains which are typical of the HBS, compared to the other specimens in which dislocation lines are anchored by fission gas bubbles and precipitates. The latter feature is clearly seen on the micrographs at low temperature (in the range 450-530°C) when the burn-up is increasing from 55 to 82 MWd/kgU. Fig. IV.13(a) and (b) show micrographs of a disk irradiated to 75 MWd/kgU at 1000°C. Fig. IV.13(a) shows small grains with low angle boundaries, as demonstrated by the electron diffraction pattern in the inset. In the sub-grain, a high density of small fission gas bubbles is present, with bubble diameter in the range 3-8 nm. These bubbles also decorate sub-grain boundaries in the same size range. Fig. IV.13(b) illustrates some

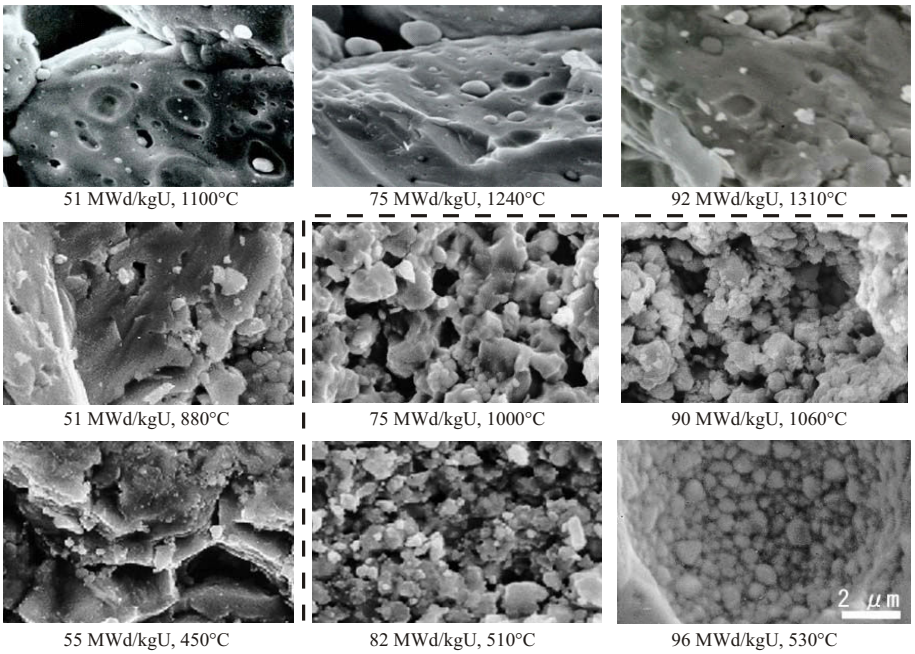

Figure IV.11: SEM observations on the fracture surfaces of specimens irradiated at different burn-ups and temperatures. All pictures have same magnification. The dashed line shows the threshold for the HBS formation [118].

dislocation pile-ups that may act as a possible start of sub-grain boundary (the lack/white dots mean that the dislocations are perpendicular to the micrograph plane). The latter two figures actually show typical micrographs of restrucured samples in which most of the sub-grain boundaries are observed to be low angled and the boundaries strongly decorated by fission gas bubbles.

Another typical feature of samples that are not restructured are shown in Fig. IV.14. In the case of a low temperature and a moderate burn-up sample (Fig. IV.14(a), 55 MWd/kgU, 450°C), a high density of fission gas bubbles and precipitates of solid FPs are observed, and many of the bubbles have formed strings along dislocation lines. In the case of a high irradiation temperature and at high burn-up as shown in Fig. IV.14(b) (92 MWd/kgU, 1310°C), dislocation networks are observed and the configuration seems to be similar to that of low burn-up commercial fuels [118]. The latter results brought Sonoda et al. to the conclusion that the correlation between dislocations and FP precipitates could be the trigger of piling-up of dislocations and resultant formation of low angled sub-grains.

From that study, it was also proposed that the HBS forms when the following specific conditions are fulfilled:

1. Local threshold burn-up: ≈70 MWd/kg [119]
2. Temperature limit: < 1000°C [42]

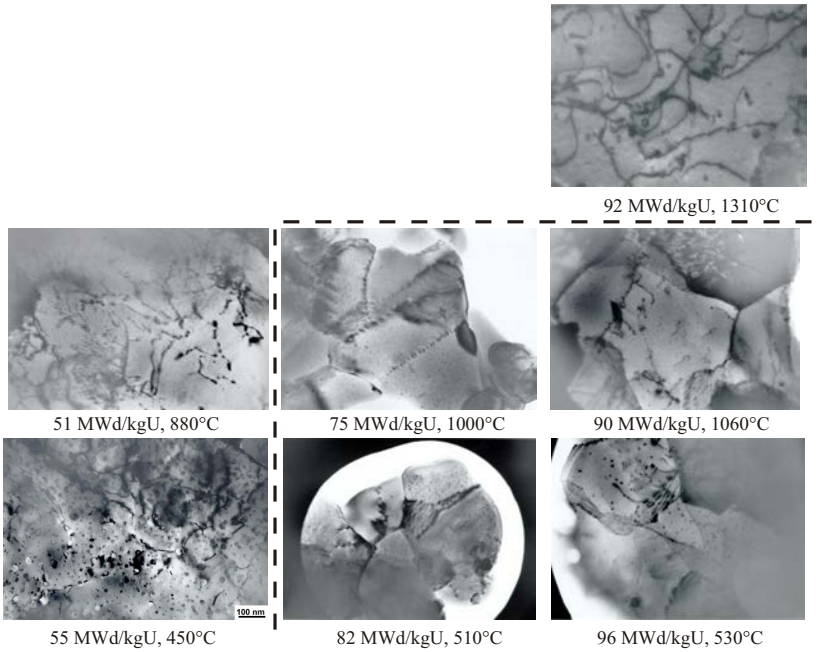

Figure IV.12: TEM micrographs of specimens irradiated at different burn-ups and temperatures. All pictures have same magnification [119].

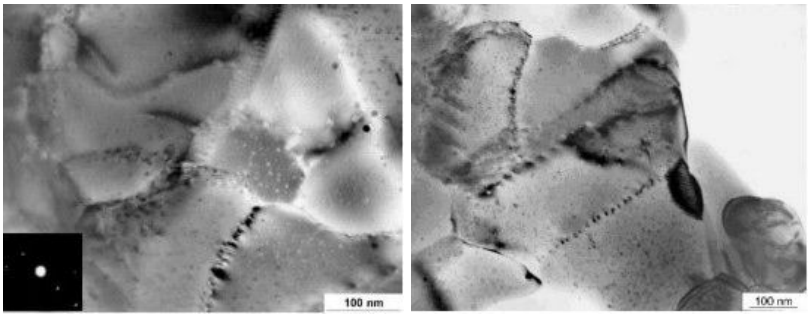

Figure IV.13: TEM micrographs of the sample of 75 MWd/kgU, 1000°C [119].

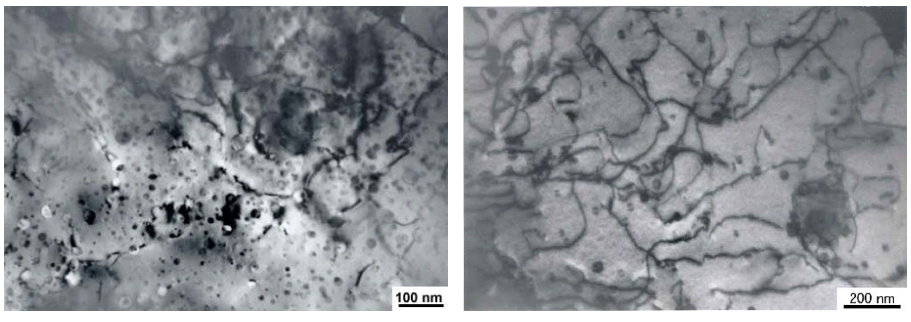

Figure IV.14: TEM micrographs of non-restructured UO_2 of (a) 55 MWd/kgU, 450°C and (b) 92 MWd/kgU, 1310°C [119].

V

The Effects of the HBS on fuel performance

Contents

The formation of the high burn-up structure has consequences on various parameters. After the first observations presented in the preceding chapter, it was initially tought that the HBS could deteriorate fuel performance at high burn-up, mainly due to the high porosity in the restructured fuel which would result in volumetric increase, thermal conductivity degradation and potential fission gas release. The effects on various properties are further analysed in this chapter.

V.1 Effect on mechanical properties

The radial variation of the Vickers hardness H_V and the fracture toughness K_{Ic} in high burn-up fuels have been widely investigated by Spino and co-workers in [129, 81, 124]. For this purpose, micro-indentation tests were performed in hot-cells at room temperature and under protective N_2-atmosphere, using the indentation device of a remote-controlled microscope equipped with a standard Vickers diamond pyramid.

The Vickers hardness test method consists of indenting the test material with a diamond indenter, in the form of a right pyramid with a square base and an angle of θ=136° between opposite faces, subjected to a load. The two diagonals of the indentation left in the surface of the material after removal of the load are measured using a microscope and their average is calculated. The area of the sloping surface of the indentation is calculated. The Vickers hardness is the product obtained by dividing the kgf load by the area of indentation:

$$H_V = \frac{2F \sin\left(\frac{\theta}{2}\right)}{d^2} \tag{V.1}$$

where F is the Load in kgf and d the arithmetic mean of the two diagonals in mm. H_V can be converted in GPa:

$$H_V = 1.8544 \times 10^{-9} \frac{F}{(2a)^2} \qquad \text{[GPa]} \tag{V.2}$$

where F is the indentation load in N, and a the imprint half-diagonal length in m.

The fracture toughness can be then calculated via the relationship [28]:

$$K_{Ic} = 0.057\, H_V\, a^{1/2} \left(\frac{E}{H_V}\right)^{2/5} \left(\frac{c}{a}\right)^{-3/2} \qquad \text{[MPa.m}^{1/2}\text{]} \tag{V.3}$$

K_{Ic} is the critical stress intensity factor and is defined to be the value at which critical crack extension occurs. Both quantities are in MPa.m$^{1/2}$ and the designation I in K_{Ic} originates from the nomenclature of the different types of crack opening. Type I (Fig. V.1) is the technologically most important type.

Spino et al. observed that the Vickers Hardness H_V remained relatively constant along most of the pellet radius, with the exception of a peripheric region showing the rim zone in which the Hardness reduced of up to 30% of the average. Similarly to this profile, the crack lengths remain relatively constant along the pellet radius (r/r_0=0 to 0.8) until they start to decrease on approaching the outer part of the fuel as shown in Fig. V.2. This indicates a smaller propensity to crack propagation of the outer fuel regions, and thus an increase of the fracture toughness (up to 100%). An important feature is the fact that the shortening of the crack lengths started well before any hardness decrease could be measured, suggesting that the

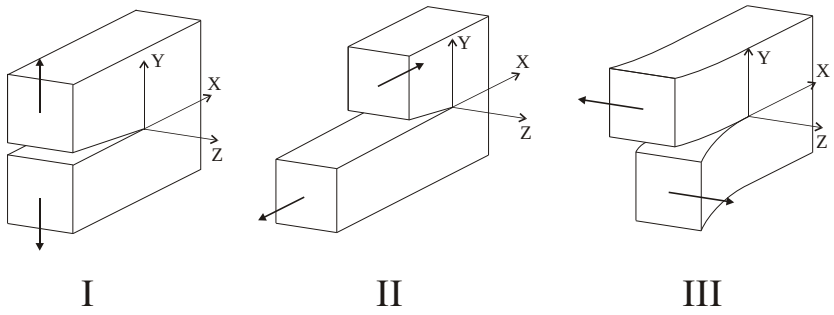

Figure V.1: The three fundamental types of crack opening.

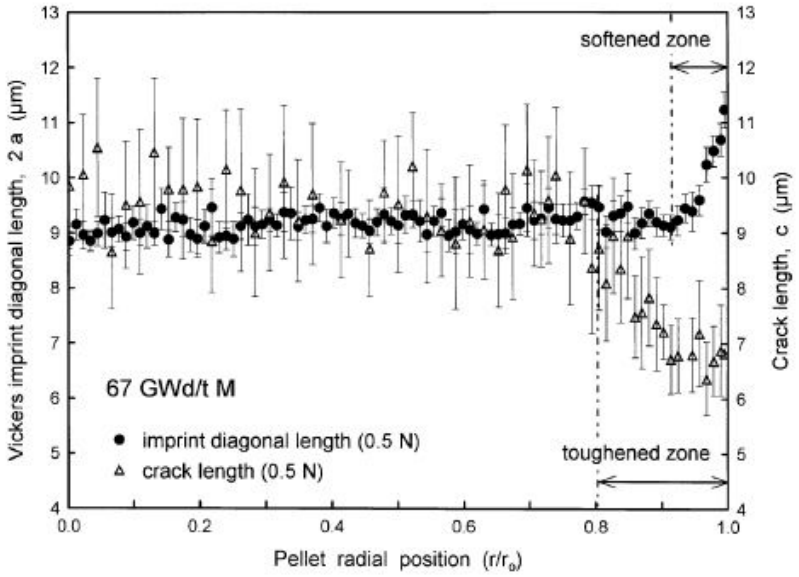

Figure V.2: Typical indentation response of LWR fuels showing the Vickers print diagonal and crack lengths dependence as a function of the pellet radius [124].

toughening effect associated with the rim zone extended beyond the region defined by the porosity increase or by the hardness reduction. Spino et al. [129] had previously observed the increase of the fracture toughness and proposed this was caused by the grain refinement occuring in the rim zone.

Matzke and Spino [81] also found that the width of the toughened zone and the degree of toughening clearly increased with the average burn-up.

Recently, Spino and Papaioannou [125] have correlated the UO_2 lattice parameter with the HBS formation of a 80 MWd/kg average burn-up fuel. Fig. V.3 shows that three different radial zones can be established in terms of the lattice parameter, showing a maximum plateau of it at r/r_0=0.62-0.78. The decrease of the lattice constant towards the pellet center was attributed to thermal healing effects. In contrast, the decrease towards the pellet edge was attributed to the HBS formation, for which temperature effects are basically excluded. This was also corroborated in principle by the radial profiles of the other properties plotted in Fig. V.3. Among the many paramaters intervening in the lattice parameter profile (α- and

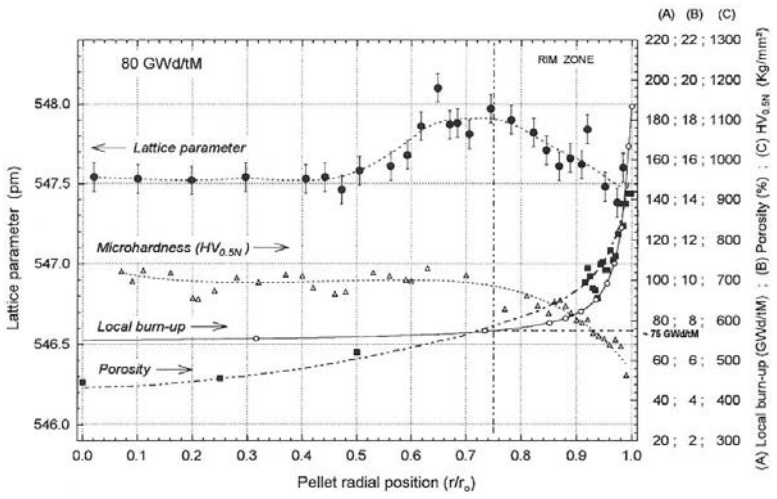

Figure V.3: Lattice parameter as a function of radial position of a 80 MWd/kg fuel. Comparison with radial profiles of burn-up (calculated), micro-hardness and porosity is also shown [125].

fission damage, thermal healing effects, lattice dimension changes due to dissolution of fission products and actinides, and finally the local burn-up effect associated to the HBS formation), the observed expansion-contraction behavior was explained by Spino and Papaioannou [125] alternatively by a saturation of primary interstitials (with subsequent recombination with excess vacancies), or by a saturation of interstitial-type dislocation loops. The latter explanation via dislocation loops could give a possible formation mechanism of the HBS, assuming a growth of these loops with burn-up, until saturation is reached when a stable dislocation cell structure is formed [125].

V.2 Effect on thermophysical properties

Knowledge of the radial temperature distribution in UO_2 fuel during irradiation is essential to the successful prediction of fuel performance at high burn-up. This is because the fuel operating temperature affects, amongst other things, fission product migration, fission gas release, grain growth and swelling. Moreover, the thermal stresses that are associated with steep radial temperature gradients can cause the fuel to plastically deform at the centre or crack at the outside during a reactor power transient. Of the various factors affecting the fuel operating temperature one of the most important is the fuel thermal conductivity. This is not constant during irradiation but decreases with burn-up due to a combination of the build-up of fission products, the formation of porosity and radiation damage in the UO_2 lattice.

Recently, Ronchi et al. [112] measured, by using the laser flash method, the thermal diffusivity of UO_2 disc fuel from the High Burn-up Rim Project (HBRP). As detailed in [119, 43], the disc fuel differed from power reactor fuel in three main ways. First, it was highly enriched to enable the target burn-up to be reached rapidly. Second, the radial burn-up profile was relatively flat and the radial temperature gradient was less than 100°C during irradiation. Third, and perhaps most importantly, cladding constraint was absent during irradiation.

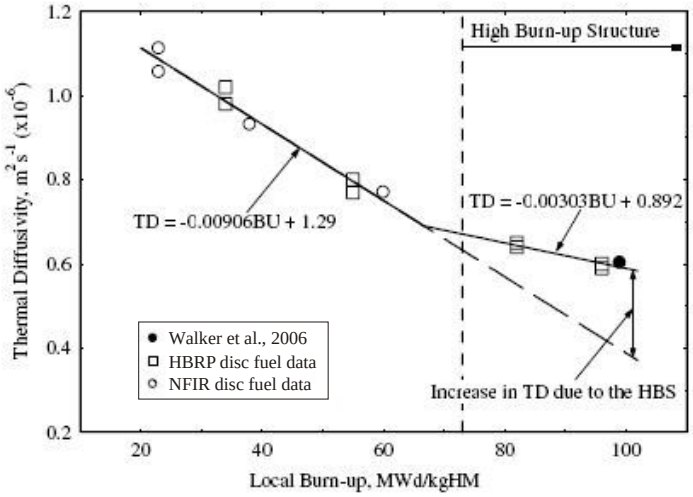

Figure V.4: Influence of the presence of the HBS on the thermal diffusivity of the high burn-up fuel. The vertical broken line marks the burn-up at which the HBRP disc fuel had fully transformed to the HBS [144].

Ronchi et al. [112] found that the thermal diffusivity of the irradiated discs decreased with increasing burn-up. The largest decrease was observed in a fuel disc that had been irradiated to a burn-up of 92 MWd/kgU at a temperature of 450°C. Most significantly, Ronchi observed that the thermal diffusivity of the irradiated fuel discs recovered during annealing and that the degree of recovery increased with the annealing temperature.

Recently, Walker et al. [144] studied the thermal conductivity of a commercial PWR fuel with an average section burn-up of 102 MWd/kgHM. The thermal conductivity data reported were derived from thermal diffusivity measurements made using the laser flash method. The thermal diffusivity at r/r_0=0.81 of this high burn-up fuel is plotted in Fig. V.4 together with the thermal diffusivity results for the irradiated discs from the NFIR and HBRP programmes. Kinoshita et al. [43] showed that the good agreement between the thermal diffusivity data generated by the NFIR programme and HBRP clearly reflects the broad similarities that exist in the fuel disc and rod design characteristics and between the histories of the two irradiations that were performed in the Halden boiling water reactor (HBWR). On plotting the measured thermal diffusivity as a function of the disc burn-up, Kinoshita et al. observed that the thermal diffusivity decreased only slightly at a burn-up of 60 MWd/kgHM, which is the local burn-up threshold commonly accepted for the formation of the high burn-up structure [53, 84]. They deduced from this that the HBS formation is not accompanied by a significant degradation in fuel thermal conductivity. If it is accepted that the regression line for the data below 60 MWd/kgHM represents the changes in the thermal diffusivity of the fuel due to the build-up of fission products and in-pile irradiation damage with burn-up, then it is apparent that if the HBS had not formed, the thermal diffusivity at 100 MWd/kgHM would have fallen to 3.8×10^{-7} $m^2.s^{-1}$. As a consequence of the formation of the high burn-up structure, however, the thermal diffusivity of the fuel at 100 MWd/kgHM is actually 5.9×10^{-7} $m^2.s^{-1}$; that is, 55% higher than the value expected to result from the degradation caused by the build-up of fission products and point defects in the fuel lattice at this burn-up. Clearly, the increase in thermal diffusivity and conductivity caused by the HBS formation is

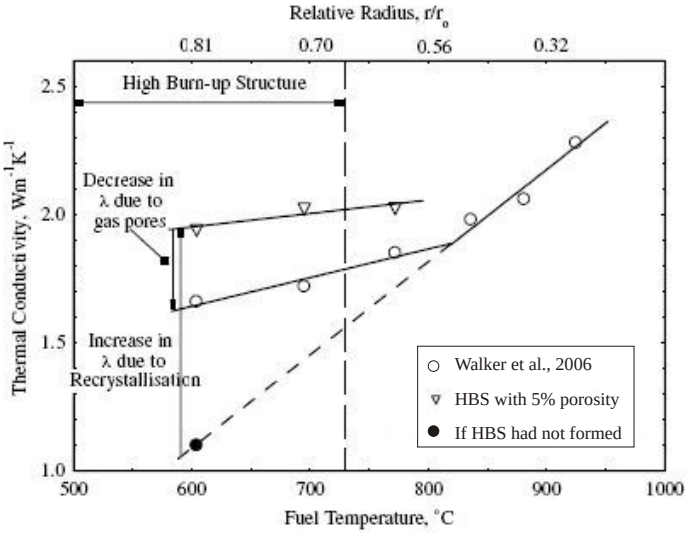

Figure V.5: Thermal conductivity of the high burn-up fuel at 217°C as a function of the local radial temperature during the last irradiation cycle [144].

a consequence of the removal of fission product atoms from the fuel lattice and healing of radiation defects that accompanies restructuring of the fuel grains (part of the HBS formation mechanisms).

Moreover, the role of the pores of the high burn-up structure as sinks for the fission gas expelled from the fuel lattice during restructuring is more important than their effect as barriers to heat transport. In Fig.V.5 the local thermal conductivity of the commercial high burn-up fuel is plotted against the local radial temperature during the last irradiation cycle. Regression lines are drawn through the data points lying between the fuel centre and r/r_0=0.5 and through the data points in the outer region of the fuel at r/r_0=0.6, 0.7 and 0.81. The former line represents the effect of temperature on the thermal conductivity of the fuel at a burn-up of about 90 MWd/kgHM and a porosity of 3-6%. It reveals that if the high burn-up structure had not formed the thermal conductivity of the fuel would have fallen to at least 1.1 $W.m^{-1}.K^{-1}$ at r/r_0=0.81. Also shown in Fig. V.5 is the thermal conductivity of the recrystallised fuel in the outer region of the pellet assuming it to contain 5% porosity instead of the higher measured values of 8 and 10.3% [144]. It can be seen that the thermal conductivity of the less porous, recrystallised fuel is substantially higher than that calculated from the measured local thermal diffusivity and the measured local porosity. The thermal conductivity of the recrystallised fuel at 5% porosity was calculated using Eq. V.4, which is recommended by Brandt and Neuer [19] for this purpose:

$$\lambda_0 = \frac{\lambda_P}{1 - \alpha P}\,, \qquad \alpha = 2.6 - 0.5t \tag{V.4}$$

where P is the porosity fraction, λ_P is the thermal conductivity of UO_2 with porosity P, λ_0 is the thermal conductivity of UO_2 of theoretical density, and t = T(°C)/1000.

From Fig. V.5, it is clear that restructuring increased the thermal conductivity in the outer region of the fuel at 217°C by between 29% and 77%, whereas the porosity created by the gas swept out of the grains resulted in a decrease of 11-15%. It will be noted that the inflection in

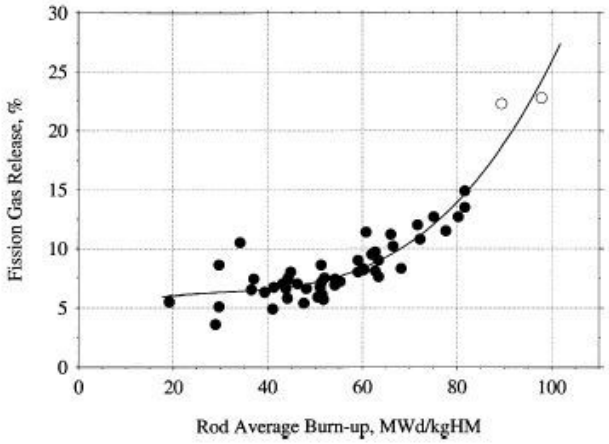

Figure V.6: Percentage of fission gas release to the rod free volume [66].

the radial thermal conductivity profile does not occur at r/r_0=0.66, which is the penetration limit of the high burn-up structure reported by Manzel and Walker [66], but deeper in the fuel at r/r_0=0.51. Between r/r_0=0.51 and 0.66, the fuel microstructure is closely related to the HBS (see Fig. 9, Ref. [66]) where both untransformed and sub.divided UO_2 grains coexist. The increase in thermal conductivity found between r/r_0=0.51 and 0.66 is undoubtedly a consequence of the occurrence of restructuring in this region.

As a conclusion of these studies, the formation of the high burn-up structure has a positive effect on the thermal conductivity in the outer region of the fuel. The thermal conductivity in this region of the fuel is much higher than would be the case if the HBS was not present. This increase in thermal conductivity caused by the HBS formation is a consequence of the removal of fission product atoms and radiation defects from the fuel lattice during restructuring of the fuel grains. There is indeed broad agreement that the fission products are principally responsible for the degradation of the thermal conductivity of UO_2 with increasing burn-up. It is pointed out that the role of the pores of the high burn-up structure as sinks for fission gas expelled from the fuel lattice during restructuring is more important than their effect as barriers to heat transfer.

V.3 Effect on fission gas release

During normal conditions, it was first thought that the HBS porosity induced an enhanced mobility of the fission gases and that there was a new fission gas release process occuring directly from the restructuring at high burn-up. This assumption was supported by EPMA studies which showed that there was indeed a decrease in xenon concentration in the vicinity of the pellet surface when measured by this technique. This new process could explain why the fission gas release can reach 25% in high burn-up fuel [66], this value increasing exponentially with the formation of the HBS, even in the presence of a high porosity in the HBS (Fig. V.6).

However, other authors think that the majority of the gas is located within the pores. Indeed,

there was no reduction in xenon concentration when measuring larger volumes with XRF (X-Ray Fluorescence). The reason for this is that in XRF, information is collected from a much greater depth within the fuel than in EPMA and consequently, the gas contained in intergranular bubbles and pores is also included in the measurements. Thus, the difference in the local concentration of Xe measured by XRF and EPMA should correspond to the amount of Xe retained on the grain boundaries [143]. This difference between the two measurement techniques can thus be used to precisely study the radial distribution of xenon and the width of the HBS.

As shown in section IV.2.1, Mogensen et al. [84] determined the radial xenon concentration profiles by XRF and EPMA of commercial low enriched BWR fuel with burn-ups of 44.8-54.9 GWd/tU and high enriched PWR fuel with burn-ups from 62.5 to 83.1 GWd/tU. It was found that the percentage of gas released from the UO_2 grains in the outer region of the fuel was generally small compared with the percentage released from the pellet cross-section. This is consistent with the current understanding that most of the fission gas released from the fuel when the high burn-up structure forms is retained in the new pore structure. This has been also confirmed by Spino et al. [126] who showed that at least up to 250 MWd/kg local burn-up and 25% local porosity, no relevant interconnecting paths between pores were present in the HBS.

Thus, the conclusion of these studies was that there was no appreciable loss of fission gas from the pellet rim to the gap and that the majority of the gas was located within the pores which were surrounded by a "depleted" matrix (with a constant xenon concentration at around 0.25 wt%). The large amount of the gas which has been released would come from the inner part of the fuel. Indeed, in the rim zone, there is a little, but non-negligible, decrease of the thermal conductivity due to the increased porosity (see previous section). Thus, the central temperature may increase, leading to an enhanced thermally activated release process from the inner part of the fuel pellet.

VI

Modelling of the High Burn-up Structure

Contents

VI.1 Introduction

In addition to the various experimental characterisations summarized above, extensive theoretical work has been performed as well in order to model the HBS, mechanistically or empirically.

In order to discuss the existing knowledge on polygonization processes and the attempts to model the High Burn-up Structure formation in UO_2 fuels, Matzke et al. [80] have indexed the different mathematical models of the structure formation. These models can be divided into three categories, depending on their point of view:

(1) The process of initiating the restructuring : the aim of such models is to describe the mechanism of the restructuring and precisely determine the conditions for HBS nucleation (burn-up threshold, influence of temperature and fission rate, preferential sites).

(2) The development and growth of the restructured region, as a function of parameters such as burn-up, temperature, mechanical stresses, grain size, etc.

(3) The performance of fuel, taking into account the material properties changes due to the HBS, during transient, accident and steady operating conditions.

The first HBS models appeared around 1994. With the growing number of characterisations of the HBS, more and more models have been developed, starting from various assumptions and depending on the mechanisms adopted by the researchers. The main scenarios for the HBS formation are first presented, followed by the models, all mixed categories, which were developed.

VI.2 Proposed scenarios for the HBS formation

Three main scenarios have been proposed so far by Nogita and Une [91], Spino et al. [129, 123] and later by Sonoda et al. [118] on the basis of the HBRP results.

From the results of the TEM micrographs, Nogita and Une proposed a formation mechanism of the HBS (Fig. VI.1(a)), which is directly related to the accumulation of radiation damage. Tangled dislocation networks are formed by the inhomogeneous accumulation of dislocations after the development of interstitial-type dislocation loops. On the other hand, intragranular FP gas bubbles are formed by the clustering of vacancies and FP gases of Xe and Kr. With increasing burn-up, tangled dislocations are organized into sub-divided grains with high angle boundaries [90]. Then, some of them are recrystallized, sweeping out small intragranular bubbles.

This interpretation has been recently opposed to the results from the HBRP program. As indicated before, recrystallization refers to a series of steps, i.e. formation of subgrains, growth of the subgrains into recrystallization nuclei, and growth of the recrystallized grains. However, according to the TEM observations of the HBRP specimens [118] presented in section IV.2.3, it seems clear today that the initial grains are polygonized (dividing process to small grains

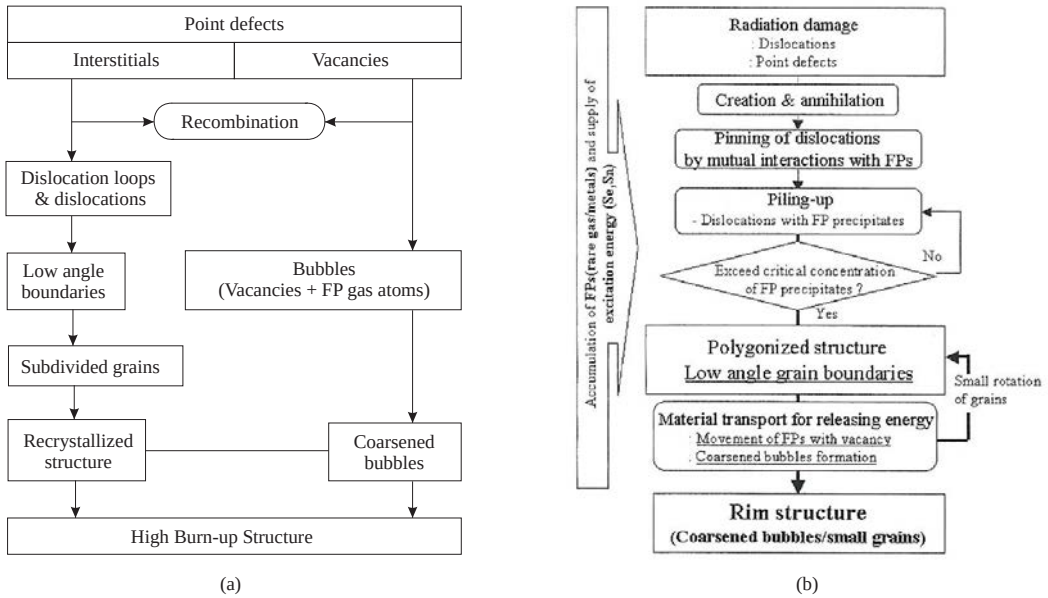

Figure VI.1: Diagram of the HBS formation mechanisms as proposed by (a) Nogita and Une [91] and (b) Sonoda et al. [118].

with low angle boundaries with the neighboring grains, both large and small ones) instead of a pure recrystallization process. Moreover, Matzke [77] draw important conclusions about the recrystallization process: there is no instantaneous recrystallization due to the accumulation of gas and radiation damage, an increased temperature is needed for recrystallization, and recrystallization, if occuring, does not necessarily sweep gases. The latter three facts totally disagree with the formation mechanisms proposed by Nogita and Une in Fig. VI.1(a).

Sonoda et al. [118] proposed a mechanism diagram for the HBS formation, based on the accumulation and mutual interaction of (1) radiation damage including point defects and dislocations, (2) FPs including gas bubbles and metal particles, and (3) stored energy caused by electronic excitation and nuclear collision which may cause radiation-enhanced diffusion of interstitials and vacancies, and the growth of dislocation loops. This diagram is shown in Fig. VI.1(b).

Meanwhile, Spino [129] proposed an interpretation of his results on the HBS porosity. In this interpretation, the modification of the original grain structure leads to the formation of two typical regions: a narrow band of fully recrystallized-porous material at the pellet periphery, and a rather wide adjacent transition zone where partially recrystallized-porous areas appear dispersed within the original matrix structure, with a decreasing concentration towards the pellet interior. Moreover, from the SEM observations on the same samples (not shown here), the pores were observed to become more separated from each other towards the pellet interior, with localised recrystallized regions around the pore surface. Based on these findings, an idealised representation of the HBS and adjacent zones was proposed and is shown in Fig. VI.2. The material is sub-divided in cubic cells with the center of each cell being occupied by a single pore with its associated recrystallized surrounding. The characteristic cell size is related to the measured volume pore density through the relationship $L = (1/N_V)^{1/3}$. For simplicity, a mean diameter was assigned to each pore and was calculated through the

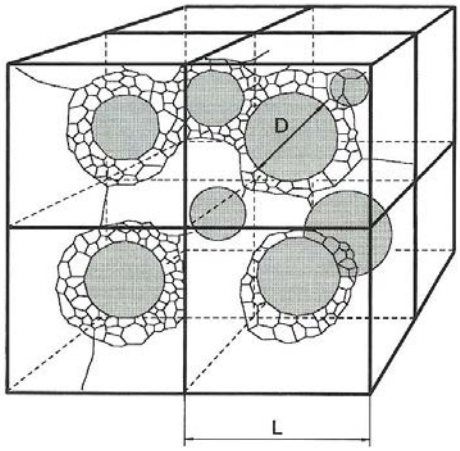

Figure VI.2: Cellular representation of the HBS as proposed by Spino et al. [129].

expression $D = (6P/\pi N_V)^{1/3}$, where P is the local porosity and N_V the local volume pore density.

It was shown that for a given average burn-up the mean pore size remained in the range 1.2-1.6 μm at all radial positions, while the cell size decreased towards the pellet edge from 5 to $\sim$2 μm in the range $0.75 \leq r/r_0 \leq 1$, for the average burn-up of 40.3 MWd/kg. These dimensions were found to agree well with the SEM observations. Moreover, for the sample with a burn-up of 66.6 MWd/kg, the calculated critical pore-to-pore distance below which the material is fully recrystallized was found to be 1.5 μm. At this distance, and according to the representation of Spino, complete overlapping of the localised recrystallized areas around pores occurs.

VI.3 Models developed so far

Most of the models proposed so far are of category (1). Among them, the first model of Rest and Hofman [106, 107] is based on the stored energy which is concentrated on a network of sink-like nuclei (walls of a cellular dislocation network). This model is based on the following assumptions:

1. A cellular dislocation structure evolves relatively early in the irradiation period. The incubation time required for this substructure to evolve is ignored.

2. Some impurities formed during fissioning on the material diffuse as vacancy-impurity complexes to cell walls.

3. The impurities effectively pin the wall, i.e. dislocation movement to and from the wall is retarded.

4. Not all cell walls are uniformely affected by impurities; the walls containing no impurities continue to undergo subgrain coalescence.

The latter nuclei diminish with dose due to their interaction with mobile radiation-induced defects. Grain subdivision is induced when the energy per nucleus, also calculated in the model in terms of fission density, is high enough that the creation of grain-boundary surfaces is offset by the creation of strain-free volumes, with a resultant net decrease in the free energy of the material. However, whereas it is accepted that dislocations interact and tend to cluster into arrangements of high dislocation density that are separated by regions with relatively low dislocation density, the process assumed concerning the diffusion of vacancy-solute atom pairs has not been well established experimentally.

The model of Lemekhov [56] (category (1)) is based on the saturation of fission gas in the matrix related to atomic mixing in fission tracks. When the local fission gas concentration exceeds a certain threshold, a very fine capillary can form along the track's axis. The stability of these capillaries is the criterion chosen for the grain degradation: when the pressure of the lattice gas in the capillary-shaped mixing volume is higher than the limit of the surface energy, the capillary becomes unstable:

$$P_L = \frac{kT}{\Omega}\left(\frac{\partial S}{\partial N}\right)_{G,\,N} \geq \frac{\gamma}{2a}$$

where Ω is the UO_2 atomic volume, S the entropy function at constant heat energy W and constant number G of gas atoms in the lattice, γ the specific energy and a the UO_2 lattice parameter. Despite this description is physically acceptable for the release of fission gas to extended defects (e.g. dislocations and grain boundaries), the HBS formation in UO_2 can not be explained alone by a temperature dependent parameter (kT in P_L) and entropy may not be burn-up dependent.

The analysis of different Xe profiles measured by EPMA in LWR fuels from different sources was used by Lassmann et al. [53] to prove the concept of a threshold burn-up and to derive an equation for the xenon depletion. For this purpose, it was assumed that the loss term of Xe from the matrix to the pores is proportional to the Xe concentration, which leads to:

$$Xe(bu) = \dot{c}_{Xe}\left[\frac{1}{a} + \left(bu_0 - \frac{1}{a}\right)\exp(-a(bu - bu_0))\right] \qquad \text{with } bu \geq bu_0 \tag{VI.1}$$

where a is a fitting parameter and bu_0 the threshold burn-up. $\dot{c}_{Xe}$ is the xenon creation rate and is obtained from the equation shown on Fig. VI.3. As already mentioned, the Xe concentration does not fall below 0.25wt%, from which the fitting parameter a is obtained. The threshold burn-up were estimated to range from 60 to 75 GWd/tU. The lower value was attributed to the beginning of the transition from the normal UO_2 structure towards the formation of the HBS whereas the higher value was the threshold for the homogeneous HBS zone. Fig. VI.3 shows the experimental data together with the solution for different threshold burn-up values of Eq. VI.1.

The Xe depletion in the transition zone and the HBS described by Eq. VI.1 has been implemented in the TRANSURANUS code. This model, of category (3), predicts reasonably well the thickness of the HBS zone and the corresponding Xe depletion up to cross section average burn-ups of approximately 70 GWd/tU. Although Eq. VI.1 did not reveal the mechanisms of the HBS formation, it was considered as a first empirical approximation for describing the

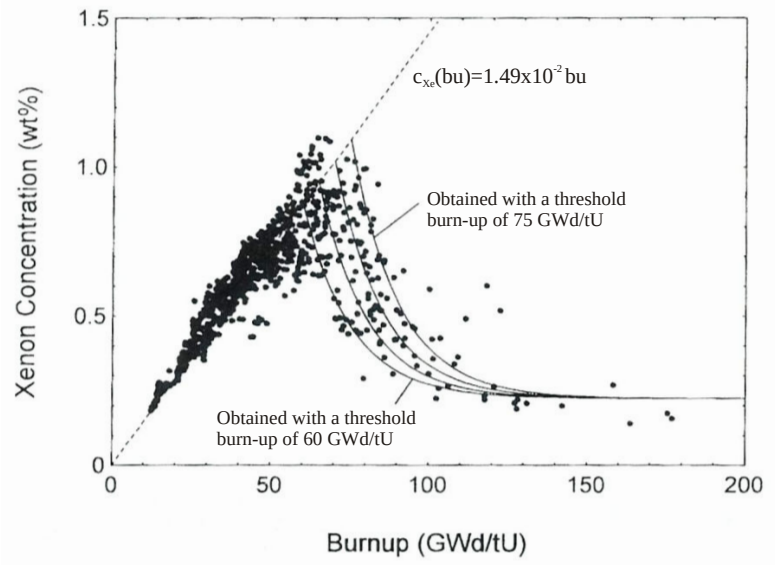

Figure VI.3: Comparison between predicted and measured local xenon concentrations as a function of the local burn-up; the threshold burn-up was varied between 60 and 75 GWd/tU by steps of 5 GWd/tU [53].

formation of a HBS zone.

Chkuaseli and Matzke [23] proposed that the fission product bubbles were the main source of stress. These bubbles may be highly over-pressurised due to the shortage of thermal vacancies at low temperatures. Therefore, the material under irradiation will be characterised by the formation of non-uniform stress fields with the maximal stress near the inclusion. Such inhomogeneity of the stress distribution, in principle, may be the cause of the spatial partitioning and eventually inhomogeneous distribution of vacancies and interstitials in the material. Interstitials may be concentrated mainly in the regions between inclusions where the stress level is minimal, leading to the formation of a high density of dislocation walls, and eventually, at a definite threshold burn-up, of subgrain boundaries.

Concerning the modelling of the formation of the coarsened bubbles, it is considered that during irradiation some large bubbles are less subjected to the radiation-induced re-solution process, even in the presence of a surrounding subgrain boundary. Therefore, such bubbles can survive and act as nuclei of the coarsened bubbles, which continue to capture fission gas atoms and point defects due to the mass transport along grain boundaries.

However, although their model, of both category (1) and (2), is based on precise experimental observations, grain boundary diffusion is only effective at very low burn-up [135]. Moreover, interstitial-type dislocation loops that can form in a region of minimal stress field are mixed up with Orowan-type dislocation loops, which may form by loop punching for instance. These two kinds of dislocation loops are fundamentally different as presented in chapter II.

The model of Baron et al. [11] is also of category (1) and (2). This model assumes that the lattice accumulates energy induced by fission products. When this lattice energy exceeds an

empirical temperature and burn-up dependent threshold value, the excess energy is converted into newly created boundaries of the sub-divided grains. The extent of the sub-divided area is calculated as a function of the accumulated energy and the size of the new sub-grains. For the evaluation of the HBS pore volume fraction and mean size, heterogeneous nucleation of bubbles and preferential diffusion of gas atoms to dislocation lines and network are considered. For this purpose, the fuel pellet consists of two zones: the original matrix where the xenon diffusion coefficient is negligible at low temperatures (classic diffusion), and the restructured zone characterised by a higher xenon diffusion coefficient. Two bubble populations are considered: the nanometric bubbles in the original matrix, able to be completely destroyed by fission spikes, and the bubbles on dislocation surfaces able to grow, thanks to the preferential diffusion in this zone.

This model is the first which evaluates the onset of the HBS formation by the internal energy accumulated in the lattice. However, this threshold energy is not physically calculated and is implemented as a fitting parameter, as well as the size of the HBS sub-grains. Moreover, the xenon diffusion coefficient in the perturbed fuel zone could not be evaluated and has been calculated by multiplying the classical diffusion coefficient by a fitting factor (equal to 100).

Actually, the latter scenario is very close to Nogita and Une's interpretation [91], which is represented in Fig. VI.1. According to Nogita and Une, the HBS formation is directly related to the accumulation of radiation damage. Tangled dislocation networks are formed by the inhomogeneous accumulation of dislocations after the development of interstitial-type dislocation loops. However, the mix-up of interstitial loops with dislocation loops needed to form sub-grain boundaries is also here reiterated, or the passage from one dislocation type to the other is not clearly expressed.

The second model of Rest [102, 101] is also of category (1). His first model [106, 107] for ion-induced crystallization and amorphisation of U_3Si has been generalized to include U_3Si_2 and UO_2. However as stated above, the idea that vacancy-solute atom pairs formed during irradiation can migrate to cell walls was not based on direct experimental evidence. For this reason, Rest proposed an alternative theory based on the assumption that bombarding ions can produce clusters of amorphous material that are considered as centers of expansion (CE), or excess free volume zones, and also propagating compressed waves, called centers of compression (CC). The rate-equations of CE and CC have lead the author to think it was possible that the primary mechanism available to form recrystallized grain nuclei was the CC-CE annihilation.

However, the recrystallization of U_3Si under ion bombardment appears to involve low damage doses compared to those in high burn-up UO_2 fuel and may be related to the tendency to become amorphous under ion bombardment, which is not the case of UO_2 [132].

Kinoshita [41] proposed a mathematical description of open reaction-diffusion processes of defects produced by irradiation and UO_2 fission product mixture. In this model, of category (1), the vacancy is considered as the primary defect that contributes to the restructuring. Indeed, the growth of pores after restructuring indicates that extensive amounts of vacancies were transported during the process. However at temperatures lower than 1000 K, defects such as dislocations can not be moved by thermal activation, but could become mobile as a

result of interactions with vacancies.

Although this model is not complete for the whole process (the incubation period of the structure formation is not modeled and the fission gas release from bubbles to grain boundaries is not included), Kinoshita's calculations confirmed the presence of a possible spatial instability which destroys the uniform distribution of point defects. However, this instability is shown to exist only if the interstitial diffusion coefficient was modified between two spatial segments during the calculation and under the condition of considering a dislocation density one order of magnitude higher than the observed values at a burn-up of 7% FIMA. No physical process was proposed at that time to explain the difference of the diffusion coefficients.

In order to interpret the observations of Spino [123] that xenon depletion, pore formation and grain subdivision occur successively at increasing local burn-ups, Rest and Hofman [108] proposed another rate-theory based model. In this model, also of category (1), the nucleation and growth of cavities during low-temperature irradiation of UO_2, in the presence of irradiation-induced interstitial-loop formation and growth, were investigated. This model consists of a set a coupled equations, which take into account the impact of the accumulation of interstitial loops on the growth and loop size distribution. They concluded, contrary to the conclusion of their previous work [106], that the fission gas atom was a possible candidate as an impurity. This model also assumes that the dislocation loops grow and accumulate until a cellular dislocation microstructure forms, according to the following equation:

$$C_A C_\rho \sqrt{\frac{\pi}{f(\nu)}} - d_l(t)\sqrt{\rho_l(t)} = 0 \qquad \text{(VI.2)}$$

where C_A, C_ρ and $f(\nu)$ are parameters which are functions of crystallographic and mechanical values of the materials, as initially applied for metals in [33]. d_l(t) and ρ_l(t) are the dislocation loop diameter and density, respectively. However, there is a confusion between Rest's description of dislocation loops (interstitial-type dislocation loops) and shear-type dislocation loops as it is in [33].

Later on, Rest [103] proposed to calculate the triggering event for irradiation-induced recrystallization and to determine the exact role of gas bubbles in this process. This model, based on the same ideas that the previous models in [102, 101, 108], considers the evolution of a cellular dislocation network upon which not only impurity atoms, as first considered in [108], but also fission gas bubbles can nucleate and grow. The model assumes that precipitates that are greater than a critical size pin triple-point nodes of the resulting sub-grain network, thus eliminating them as potential recrystallization nuclei. Contrary to the previous models, Rest used calculations based on thermodynamics for the triggering of recrystallization. The resulting expression for the fission density is shown to be athermal and weakly dependent on fission rate. Moreover, this model shows that materials with $\varepsilon_i > \varepsilon_v/2$ (interstitial and vacancy migration enthalpies, respectively) are precluded from irradiation-induced recrystallization. However, the confusion between shear dislocation loops (used in [33]) and interstitial-type dislocation loops is here reiterated.

In line with the previous model, Rest proposed a model [104], of category (2), for the progression of recrystallization. Based on the same assumptions of [103], the volume fraction of

recrystallized fuel is calculated as a function of time, initial grain size d_g and a coefficient ν_{df} which is proportional to the strain induced by the change in lattice parameter:

$$V_r = 1 - \left[1 - \frac{2\,\nu_{df}\,t}{d_g}\right]^3 \tag{VI.3}$$

The gas-bubble swelling in UO_2 is calculated, both before and after the recrystallization occured and is, respectively:

$$\left(\frac{\Delta V}{V}\right)_g = \frac{3c_g a^3}{4} + \frac{4\pi}{3}\left(r_b^3 c_b + \frac{3R_b^3 C_b}{d_g}\right) \tag{VI.4}$$

$$\left(\frac{\Delta V}{V}\right)_{gx} = 4\pi R_{bx}^3\left(\frac{C_b}{d_g} + \frac{C_{bx}}{d_{gx}} + \frac{1}{3d_{gx}^3}\right) \tag{VI.5}$$

R_{bx} and C_{bx} are the radius and density, respectively, of the new population of bubbles in the recrystallized zone, in which the grain size is calculated to be d_{gx}. In Eqs. VI.4 and VI.5, $\{c_b, r_b\}$ and $\{C_b, R_b\}$ are the intra- and intergranular fission gas bubble density and radius, respectively. The latter quantities have been calculated and measured by Spino et al. [127].

In 2004 at the international workshop on the HBS in nuclear fuels that we organized at ITU, Likhanskii et al. [60] proposed a model (category (1)) to determine a possible mechanism leading to the spatial instability introduced by Kinoshita [41]. This model was then improved in [61] by considering that the dislocation anisotropy and motion, which were not taken into account in [59, 60], play a role in the stability analysis. It is shown [61] that under fuel irradiation conditions a peak in the vacancy concentration can form near the core of an edge dislocation, thus enhancing the uranium Frenkel pair recombination. This modification in the uranium interstitial diffusion coefficient could be a possible explanation to Kinoshita's instability development. However, the re-solution of interstitials from the loops introduced in the behavior of point defects has been applied to the mean size of loops, which leads to an over-estimation of the number of interstitials driven back into the matrix and does not reproduce the exact effect of the re-solution process. The role of gaseous fission products is completely disregarded as well, although their reactions with vacancies are known to be important. Moreover, in the model presented during the HBS workshop [60], Xe diffusion was suggested to occur via an interstitial mechanism, which is in contradiction with Matzke's observations [72].

Very recently, Rest [105] proposed to gather all the main results from his previous models. The fission density at which recrystallization occurs, the volume fraction of recrystallized fuel as a function of density, the size of recrystallized grains and the change in the lattice parameter are all given as functions of material properties and can be applied to any materials undergoing recrystallization. Nevertheless, the same confusion has been reiterated through all the models developed so far by Rest: an interstitial-type dislocation loop (or also called prismatic loop) is a direct consequence of production and diffusion of interstitials, whereas shear-type or Orowan-type dislocation loop (or line) is a plastic deformation under external loading and is not a direct product of the fission process (see section II.3). Moreover, Rest considers that the HBS formation is a recrystallization process whereas it is widely agreed that the grain-subdivision of high burn-up UO_2 fuel is a micro-polygonization process.

VI.4 Summary and conclusions

Many models have been developed up to now in order to understand the HBS formation and propagation and to take into account its effects on fuel performance. Most of them are dedicated to the understanding of the formation mechanisms.

Despite the numerous attempts, no scenario is able today to explain how the HBS forms, let alone a model to determine the role of various parameters which can affect the formation conditions. There is clearly room for improvement in this direction. Moreover, every model is based on assumptions that differ from a model to another, depending on the scenario considered.

Our approach has not been to develop another model, but rather to study the influence of mechanisms which were identified to play an important role in the restructuring in order to contribute to the understanding of the HBS formation scenario. As soon as it was agreed that the internal energy of the system, stored as elastic energy, increases with time (or burn-up) with the production of many defects up to certain irradiation conditions which trigger the HBS formation, the main first step would be to calculate this energy or to describe the stress fields responsible of such a change in the microstructure. The idea of considering the evolution of the crystal energy with burn-up was first used in the model developed by Hermitte and Baron [35, 11] but was at that time an adjustable coefficient. An attempt in calculating the various contributions of the stored energy is here carried out. The details of our approach are given in the next chapter after a conclusion of this part.

VII

Conclusions and objectives of this study

High burn-up fuel is a very complex system. Given the potential impact of the HBS on the discharge burn-up limit of nuclear fuel rods, this feature has been the subject of various research programmes. As a result, the HBS has been relatively well characterised: There is a general agreement that the HBS is characterised by Xe-depletion from the matrix, pore formation and grain sub-division. Moreover, the irradiation conditions which must be fulfilled simultaneously for the HBS formation are also well determined: the local burn-up should exceed 70 MWd/kg and the local temperature should remain below 1000°C. The HBS formation is not a fission rate effect and is athermal below the temperature limit. In addition, the HBS is not a negative feature of high burn-up fuel and does not seem to be a handicap to achieve higher burn-ups [12]: limited amount of gas is released from the HBS, some properties are restored (lattice parameter, thermal conductivity) with the HBS formation and the pellet-cladding interaction is reduced thanks to a softer HBS [113].

Nevertheless, there is no universal consensus on the exact mechanisms of the HBS formation and further development within the fuel pellet during irradiation. A number of questions still remain open, among them:

- What is the driving force for the nucleation of the HBS? The role played by the accumulation of fission products is dominating according to Chkuaseli and Matzke [23], whereas Une et al. [137, 90, 61] consider that the accumulation of radiation damage is more important. It is also considered that both accumulations are needed [11].

- What are the nucleation centers? Depending on whether the HBS forms on the pore surface, or in the bulk, the nucleation centers are considered to be the over-pressurised bubbles [129, 11, 123], or cellular dislocation networks [106], grain boundaries [136], or the so-called "recrystallization nuclei" [91, 103].

- What is the scenario of the formation process? Despite the fact that some authors [141, 132, 91, 103] consider that the HBS formation is due to a recrystallization process, the appropriate process is rather considered to be a microscopic polygonization of the initial grains by Matzke [77, 78] whose conclusions were supported by work performed with suitable insoluble fission products (Xe and I) implanted in UO_2 at high energy (including fission energy).

- What are the parameters affecting the HBS formation? One of them refers to the pressure induced by the pellet-cladding mechanical interaction. According to the results from the HBRP program in which the HBS has been observed in UO_2 fuel disks irradiated at high burn-up without any external constraint (from the cladding), it seems likely that this parameter is not decisive but may rather accelerate or delay the HBS formation. According to Baron [9], the pore size and density depend on the hydrostatic stress and the further HBS propagation depends on the pore density. Une et al. [138] on the other hand consider that the only effect of a strong PCMI is the suppression or reduction of the HBS porosity increase at higher burn-ups, though the HBS is propagating towards the pellet center.

  Another feature whose role is not yet determined is the initial grain size. According to Une et al. [136], large grains, in which Xe-depletion from the matrix was measured by EPMA to be lower than in standard grains, offer a higher resistance to the formation of the high burn-up structure, whereas Baron [9] considers that the pore size distribution is changed, compared with standard grains, resulting in limited HBS propagation. The difference lies in the nucleation center of the HBS: according to Une [136], the HBS nucleates at the grain-boundaries, instead of at the over-pressurised bubbles according to Baron [11, 9].

Assuming that, in line with Matzke [78], the HBS formation is a polygonization of the initial grain structure, the relaxation occuring with the HBS can only take place through the dislocations. In metals undergoing polygonization, dislocations are necessary to form new sub-grain boundaries. The transposition of this traditional phenomenon in metals to nuclear fuel irradiated up to high burn-up is an option which has not yet been exploited. Indeed, the bibliographical study also shows that the previous studies either do not take into account the presence of dislocations in the restructuring mechanisms, or in a phenomenological or wrong way. The approach adopted in this thesis thus consists in the study of the contribution of the dislocation-type defects (both dislocation line and interstitial-type loop) on the HBS formation mechanisms.

The first dislocation-type defect considered is the dislocation line. It can be a perfect line extending through the crystal or a portion from a dislocation loop (the line ending on itself) considered as linear when the loop radius is large.

Once produced, the dislocations are assumed to move and to form different structures or networks as observed in metals. The study of the stresses associated with the presence of dislocations is therefore carried out in part 3. The objective is to calculate the strain energy stored in various dislocation configurations in order to understand their effect on the evolution of the microstructure. A mathematical tool for the calculation of the stresses induced by any periodic configuration of dislocations has been developed for this purpose. Such a tool proves to be necessary since the experimental data concerning the dislocations in irradiated UO_2 fuels do not provide the information needed to analyze a single configuration. The type of the newly produced dislocations may be only of screw type, or of edge type, or also a mixture of both types. Afterwards, the new sub-grain boundaries appearing in the HBS may be flexion boundaries (involving edge dislocations) or torsion boundaries (involving screw dislocations). The theory on which the tool is based as well as the application to periodic configurations are presented in the next part. The perspectives of such a tool are also discussed, in particular its applicability to calculations to demonstrate the role of the porosity and the initial grain

size in the HBS formation.

In part 4, a study of the evolution of irradiation defects, with particular attention to the interstitial-type dislocation loops, was carried out. As shown in the previous chapters, these interstitial loops are considered by many researchers, both theorists (e.g. [23, 11, 103] and experimentalists (e.g. [91, 125]), to play a role in the build-up of the HBS. Moreover, the microstructure observation of any irradiated nuclear fuel is only possible once the fuel has been cooled for at least 3 years, time during which the additional interstitial loops have been produced due to the fuel α-activity. The latter is the most important source of defects after the fuel discharge from the reactor. Since sub-microscopical characterisation of irradiated fuel is very complex, a simpler system reproducing some of the features observed in the HBS, was chosen in the form of UO_2 sintered pellets, doped with $\sim$10 wt% ^{238}Pu and stored for different times, during which α-damage resulting from the decay of ^{238}Pu was produced. In this way, the single effect of interstitial-type dislocation loops can be studied, as these loops are directly formed by precipitation of interstitials, produced by the self-irradiation. The experimental loop size distributions were obtained by means of transmission electron microscopy and image analysis for this sample stored during 4 and 7 years. Equations based on the chemical rate theory are then proposed in order to reproduce the experimental size distribution of interstitial loops. The model is based on that of Hayns [34] and features additional phenomena in addition to the classical diffusion of point defects, namely the resolution process of interstitial atoms from the loops back into the matrix due to the impact with the recoil atom ^{234}U, as well as the coalescence of two dislocation loops by surface or volume diffusion. The effects of the latter two phenomena on the interstitial loop formation are also discussed.

Part 3

Towards the modelling of the effect of stress on the HBS formation

VIII

Introduction

Whether the accumulation of fission products or of radiation damage, or even both, is the trigger of the HBS formation, the previous part on the HBS characterisation and modelling has highlighted that dislocation lines may play a role in the build-up of the HBS. From the experimental point of view, it was qualitatively observed that the dislocation lines accumulated during irradiation may have reordered themselves to form a low energy configuration of dislocations (under the assumption that the HBS formation is a polygonization of the initial grain structure, as proposed by Matzke [78]), namely the new sub-grain boundaries. From the theoretical side, the dislocation is also regarded as a defect to be accounted for in the HBS formation mechanisms [61, 108, 105, 35, 11].

In the present part, the dislocations, once produced, are assumed to move and to form different structures or networks. The latter are very well known in metals where their evolution can be monitored and observed much more easily than in nuclear materials, as a function of the applied stress or measured strain. Despite the different dislocations which can appear in the UO_2 fluorite structure were already studied in 1969 by Evans and Pratt [29], no detailed experimental study on the evolution of dislocation configurations in irradiated nuclear fuels are so far available. This is clearly due to the radioactivity of these specific samples which limits the observation of the microstructure and the number of observations as well. As a consequence, no calculation of the strain energy contained in the UO_2 material for given dislocation configurations could be performed. The study of the stresses induced by the presence of dislocations in irradiated UO_2 is therefore the main objective of this part. To this end, a tool is developed which enables the calculation of the strain energy induced by any (periodic) configuration of dislocations.

The theory developed by Kröner on which the tool is based, is presented in chapter IX together with the necessary knowledge of compatible and incompatible elasticity and plasticity.

In chapter X, Kröner's theory has been applied to well known periodic configurations of dislocations: edge dislocation pile-up and wall, screw dislocation pile-up and symmetrical tilt-boundary. In each case, the stress function tensor, from which the stress tensor is derived, is calculated under the form of an analytical expression. A comparison of the elastic energy contained in such configurations is also performed, from which low and high energy configurations of dislocations can be distinguished.

IX

Linear continuum theory of dislocations

Contents

IX.1 Elastic and plastic distortion

In this section, a qualitative description of elastic and plastic distortion is presented. Following Kröner [51], figures are widely used in order to give a simple illustration of how materials are deformed.

It is convenient and does not restrict the validity of the physical laws to be formulated in cartesian coordinates x_1, x_2 and x_3. In this coordinate system, a volume element which is small but finite is denoted by $\Delta V = \Delta x_1 \Delta x_2 \Delta x_3$. The undeformed volume element ΔV is sketched in Fig. IX.1 with its lattice structure which, for simplicity, is taken as cubic.

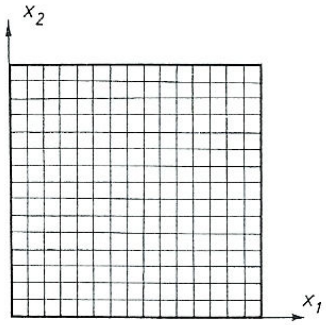

Figure IX.1: Lattice plane of a crystal of small volume ΔV in its reference state [51].

In the following, two types of deformations are distinguished, namely elastic and plastic deformations. The point to be stressed here is that during the elastic deformation the lattice is dragged along into a new configuration. This is shown in Fig. IX.2 where a few homogeneously distorted states of the original undeformed volume element ΔV of Fig. IX.1 are sketched. The geometric situation of the elastically deformed volume element is described by the elastic distortion tensor $\underline{\underline{\beta}}$ with cartesian components β_{ij} (i, j=1, 2, 3). $\underline{\underline{\beta}}$ is an asymmetric tensor which in the linear theory can be decomposed into the symmetric elastic strain tensor $\underline{\underline{\varepsilon}}$ and the antisymmetric elastic rotation tensor $\underline{\underline{\omega}}$ so that:

$$\beta_{ij} = \varepsilon_{ij} + \omega_{ij} \qquad \left(\underline{\underline{\beta}} = \underline{\underline{\varepsilon}} + \underline{\underline{\omega}}\right) \tag{IX.1}$$

The elastic strain tensor, $\underline{\underline{\varepsilon}}$, describes a change of the shape of ΔV and the corresponding strain of the lattice. The elastic rotation tensor $\underline{\underline{\omega}}$ on the other hand, describes a rigid rotation of the element whereby the lattice structure is rigidly rotated too through the same angle ("dragged along") as shown in Fig. IX.2(d).

In Fig. IX.3, the corresponding plastic distortions are shown. A superscript, P, has been applied in order to distinguish the plastic distortion tensor, $\underline{\underline{\beta}}^P$, from the elastic distortion tensor, $\underline{\underline{\beta}}$. The equations analogous to Eq. IX.1 are:

$$\beta_{ij}^P = \varepsilon_{ij}^P + \omega_{ij}^P \tag{IX.2}$$

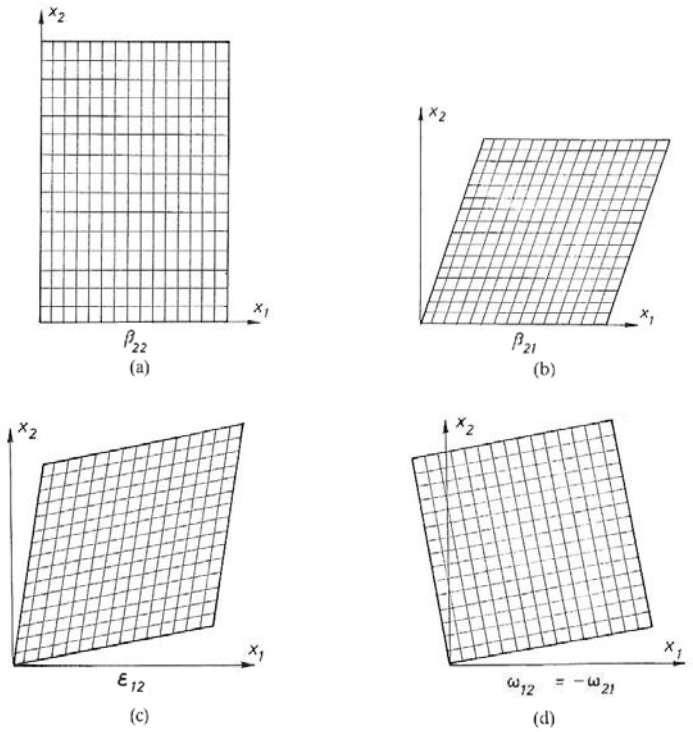

Figure IX.2: Examples of homogeneous elastic and rigid transformations of the crystal in Fig. IX.1 [51].

The plastic distortion β_{22}^P $(=\varepsilon_{22}^P)$ in Fig. IX.3(a) corresponds to the climb in x_1-direction of a set of edge dislocations where the dislocation lines are parallel to the x_3-axis whereas the Burgers vectors, all equal, point in the x_2-direction.

The plastic distortion β_{21}^P of Fig. IX.3(b) can similarly be thought to be produced by edge dislocations gliding in x_1-direction and having their lines parallel to the x_3-direction with Burgers vector pointing in x_1-direction. Since $\varepsilon_{21}^P = \varepsilon_{12}^P = (\varepsilon_{12}^P + \varepsilon_{21}^P)/2$, the plastic strain ε_{21}^P in Fig. IX.3(c) implies a glide along two sets of planes, as does also the plastic rotation $\omega_{12}^P = -\omega_{21}^P = (\omega_{12}^P - \omega_{21}^P)/2$ of Fig. IX.3(d). Note that the elastic and the plastic distortions of the volume element ΔV always lead to the same changes of the shape. The difference in the corresponding configurations shown in Figs. IX.2 and IX.3 is rather a change in the lattice structure. Whereas elastic distortion always means the same distortion of the shape and the lattice, the lattice structure is not at all changed during the (purely) plastic deformation. This means that, whereas the internal state of ΔV is changed during an elastic deformation which results in an elastic strain, this is not the case with the corresponding plastic distortion because changes of the shape are not considered to change the internal state of ΔV.

So far a qualitative picture of the elastic and plastic distortion has been presented, as well as their decomposition into their respective elastic and plastic strains and rotations. A quantitative description is possible if elastic and plastic displacement (vector) fields $\underline{u}$ and $\underline{u}^P$ are introduced, which describe how the points of the undeformed element ΔV are transferred to the points of the distorted element during the deformation. Clearly they determine the

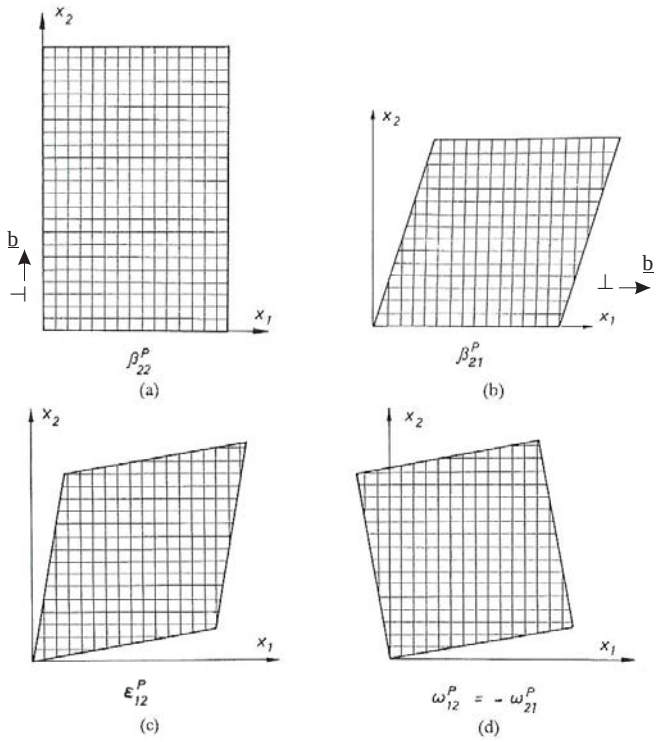

Figure IX.3: Examples of macroscopically homogeneous plastic distortions of the crystal in Fig. IX.1 [51].

distortions according to the gradient relations $\beta_{ij} = u_{j,i}$[1] and $\beta^P_{ij} = u^P_{j,i}$. Both distortions add up the total distortion $\underset{=}{\beta}^T$, in case of small plastic deformations, given by:

$$\beta^T_{ij} = \beta_{ij} + \beta^P_{ij} \tag{IX.3}$$

Since only the very small volume element ΔV was investigated, over which the distortion was assumed to be constant, the distortion can be considered as well defined by the gradients of the corresponding displacement fields. This definition works even in a larger volume in which the distortions are no longer constant, provided these distortions can be described in terms of a global rather than local displacement field, i.e. provided such a global displacement field does exist. It is shown in section IX.2 that such a field does not exist if the distortion is incompatible. The total, elastic and plastic distortion tensors in differential form are:

$$du^T_i = \beta^T_{ij} dx_j \tag{IX.4}$$
$$du_i = \beta_{ij} dx_j \tag{IX.5}$$
$$du^P_i = \beta^P_{ij} dx_j \tag{IX.6}$$

In situations in which one of the forms IX.4, IX.5 or IX.6 is integrable, the corresponding displacement function does exist and its gradient is the pertaining distortion.

[1] $f_{,k}$ is the partial derivative of f over x_k and is defined as $f_{,k} = \frac{\partial f}{\partial x_k}$.

IX.2 Compatibility and incompatibility

The distortions of isolated small volume elements ΔV were first analysed. Now the problem of combining many such volume elements with the aim to build up a macroscopic body is investigated. The following steps are then performed: the undeformed continuum is cut into many small pieces ΔV, which are numbered in order to identify them later. Every volume element is plastically deformed. In order to treat non-trivial but macroscopically continuous situations, it is assumed that the impressed plastic distortion varies slowly from one element to its neighbours. Two cases can then be distinguished:

In the first case, all volume elements (now taken to be infinitesimal) fit well together. Then all elements can be welded together without being further strained or rotated. The same deformed state can now be achieved when the undeformed body is not cut into pieces but when under the applied stress dislocations are formed which then deform the body in such a way that at the end they have all disappeared, partly through the surface and partly by annihilation in the interior. To every point of the body can be assigned a plastic displacement field $\underline{u}^P$ which describes how the points are transferred from the initial to the final state during the deformation. The corresponding plastic distortion is $\underline{\underline{\beta}}^P = \nabla \underline{u}^P$. There is no elastic distortion so that for this special situation the total and plastic distortions and displacements are equal. An important feature of this deformation is that, although the shape of the body may change remarkably, its internal state remains unchanged. Clearly, this is a highly idealized situation.

In the second case, the volume elements (though infinitesimal) do not fit together. This is shown in Fig. IX.4 which represents a cross section through various configurations of the body. Fig. IX.4(a) gives the initial state, Fig. IX.4(b) the disconnected state after a small plastic deformation (which here is assumed to lead to a pure strain) is performed. In order to come back to a compact configuration, the elements can be elastically deformed in such a way that they fit together again. The simplest way of doing this is to superimpose on the plastically deformed elements an elastic distortion $\underline{\underline{\beta}}' = -\underline{\underline{\beta}}^P$ which brings the element back to the position just before they were deformed plastically (Fig. IX.4(c)). Now they can be welded together and the forces which have produced the elastic distortion $\underline{\underline{\beta}}'$ can be removed. This allows the body to relax into the low energy configuration of Fig. IX.4(d) by a second elastic distortion $\underline{\underline{\beta}}''$. The total distortion is

$$\underline{\underline{\beta}}^T = \underline{\underline{\beta}}' + \underline{\underline{\beta}}'' + \underline{\underline{\beta}}^P = \underline{\underline{\beta}}'' \tag{IX.7}$$

and can be represented by the total displacement field $\underline{u}^T$. The same is not true for the plastic and elastic distortion. In fact, the non-fitting of the elements after the plastic deformation implies that the plastic displacement, defined in the isolated elements, jumps through one boundary to the next, non-fitting element. This means that in the limit of volume elements going to zero, there is a quasi-continuous distribution of displacement jumps so that the displacement field is no longer unique. The same consideration can be applied to the elastic distortion $\underline{\underline{\beta}}'$. Since $\underline{\underline{\beta}}'$ cannot be derived from a displacement field, this is the same situation for the whole elastic distortion $\underline{\underline{\beta}}' + \underline{\underline{\beta}}''$. The result is that both $\underline{\underline{\beta}}$ and $\underline{\underline{\beta}}^P$ are incompatible distortions, i.e. distortions which are not compatible with the existence of a unique displacement field. Generally speaking, a compatible distortion is understood as a distortion following

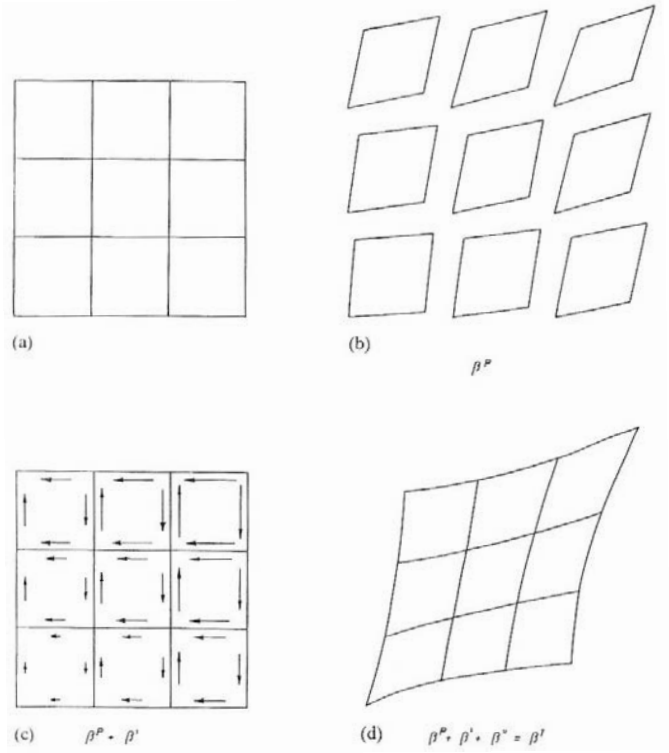

Figure IX.4: Incompatibility of elastic and plastic strains [51].

from a deformation which transforms a compact (i.e. connected) body into another compact body. An incompatible distortion is then a distortion following from a deformation which transforms a compact body into a non-fitting, i.e. non-compact (disconnected) collection of small elements.

A similar process can be considered by applying a plastic deformation which leads to a pure plastic rotation of the elements. The operations involved are shown in Fig. IX.5. In order to obtain a non-trivial situation, a plastic rotation $\underline{\underline{\omega}}^P$ was chosen, which varies from one element to the other thus giving rise to a misfit of the elements (Fig. IX.5(b)). A rigid elastic rotation $\underline{\underline{\omega}} = -\underline{\underline{\omega}}^P$ can be applied, so that the elements occupy the same volume as in the initial state (Fig. IX.5(c)). Nevertheless, the body is not in its initial state after welding together the now-fitting elements, because during the elastic rotation the lattice was rotated together with the volume elements. Since the described operation does not lead to the appearance of stresses, there is in contrast to the case of plastic strain, no relaxation process necessary to bring the body into a low energy configuration. This means that the shape of the body is unchanged although the lattice orientation now varies from point to point. In the limit of volume elements going to zero, a continuous curvature of the lattice structure is observed, which is called Nye's curvature [92] or contortion, the latter name because this curvature always accompanies the torsion, i.e. dislocation in polycrystalline materials.

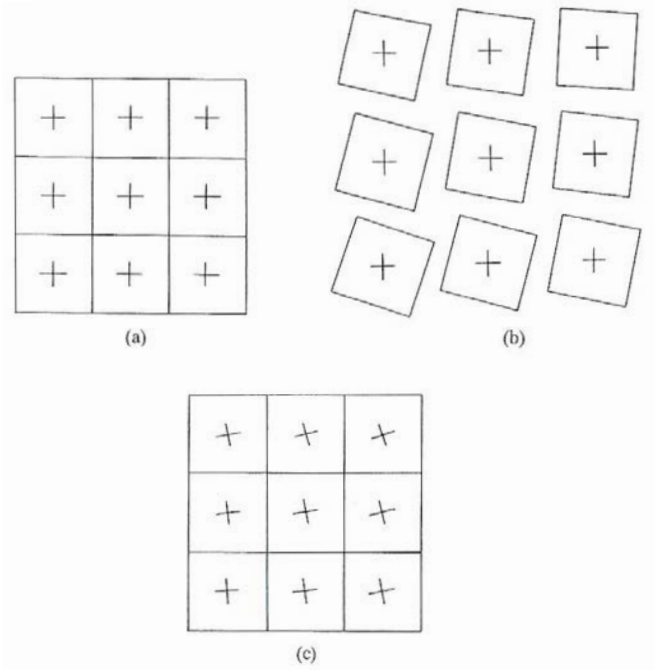

Figure IX.5: Strain-free lattice curvature [51].

IX.3 The tensor of incompatibility

IX.3.1 First order differential form of the incompatibility law

A quantitative description of incompatibility is now proposed. For this purpose, it is necessary to translate into the mathematical language of the compatibility equations the presence of strain singularities, like dislocations as previously introduced. The first approach to this problem has been made by Ney [92]. Bilby et al. [15] and Kröner [49, 47, 48] derived the fundamental equation (see Eq. IX.10 below) that underlies the continuum theory of dislocations, as it has been extensively developed afterwards by Kröner [50]. The latter has recently gathered the main equations presented below in [52].

Each point in the material has an initial and a final position which can be related by the total displacement field $\underline{u}^T$. Therefore, Eq. IX.4 must be integrable, the two others, Eqs. IX.5 and IX.6, are not. The integrability condition satisfied by the differential form IX.4 has the shape:

$$e_{ikl}\,\beta^T_{lj,k} = 0 \qquad \left(\text{curl } \underline{\underline{\beta}}^T = 0\right) \tag{IX.8}$$

where e_{ijk} is the permutation tensor. Since $\underline{\underline{\beta}}^T$ is the sum of its elastic and plastic part, we also have:

$$e_{ikl}\,\beta_{lj,k} = -e_{ikl}\,\beta^P_{lj,k} = -\alpha_{ij} \tag{IX.9}$$

Here, a new tensor $\underline{\underline{\alpha}}$ is introduced and is interpreted as a tensor of dislocation density. Whereas the relation curl $\underline{\underline{\beta}}^P = \underline{\underline{\alpha}}$ has the status of a definition, the other relation contained

in Eq. IX.9, namely

$$e_{ikl}\,\beta_{lj,k} = -\alpha_{ij} \qquad \left(\nabla \times \underline{\underline{\beta}} = -\underline{\underline{\alpha}}\right) \tag{IX.10}$$

is a fundamental field equation of the (linear) continuum theory of dislocations. It states that a continuum can be in an incompatible distortion state $\underline{\underline{\beta}}$ provided there exists a dislocation density according to Eq. IX.10 which guarantees that the body does not break into pieces. The interpretation of Eq. IX.10 together with the appearance of first order derivatives suggests the name "first order compatibility law" or also "first order incompatibility law". The first name is suitable from the point of view that the fulfilment of Eq. IX.10 guarantees that the total distortion is compatible; the second name refers to the fact that the elastic distortion, which as a state quantity has a more profound significance than the total distortion, is incompatible. For this reason, the situation in which Eq. IX.10 is non-trivial, i.e. $\underline{\underline{\alpha}} \neq 0$, is rather preferred and therefore also speaking of incompatibility equations is preferable.

An immediate consequence of the definition of $\underline{\underline{\alpha}}$ in Eq. IX.9 is the equation:

$$\alpha_{ij,j} = 0 \qquad \left(\mathrm{div}\ \underline{\underline{\alpha}} = 0\right) \tag{IX.11}$$

which means that dislocations cannot end inside the medium. Any dislocation density given a priori must satisfy this equation. This feature was already proposed in section II.3, although without any demonstration.

IX.3.2 Integral form of the incompatibility law

It is interesting to consider the integral form of the incompatibility law which is obtained by multiplying both sides of Eq. IX.10 with the oriented area element dS and performing an integration over an arbitrary internal surface S with edge line C:

$$\iint_S e_{ikl}\,\beta_{lj,k}\,dS_i = -\iint_S \alpha_{ij}\,dS_i \tag{IX.12}$$

With the help of Stokes' theorem and Eq. IX.5, we obtain

$$\iint_S e_{ikl}\,\beta_{lj,k}\,dS_i = \oint_C \beta_{lj}\,dx_l = \oint_C du_j \tag{IX.13}$$

It is found that:

$$\oint_C du_j = -\iint_S \alpha_{ij}\,dS_i = -b_j \tag{IX.14}$$

The equation

$$\oint_C du_j = -b_j \tag{IX.15}$$

has been used by Burgers [22] in order to define the single dislocation line as the singularity of the elastic displacement field $\underline{u}$ with which it surrounds itself. Clearly, the vector $\underline{b}$ results only when the circuit C encompasses the dislocation line. In this case $\underline{b}$ is independent of the particular choice of C provided it encompasses just one dislocation. $\underline{b}$ is called the Burgers vector of the dislocation. As mentioned before, $\underline{b}$ and $\underline{t}$, the tangential vector of the dislocation line, define together the dislocation completely.

When establishing the basic field equations of dislocation theory, Kröner considered continuous distributions of dislocations rather than single dislocations. In this way, Kröner interpreted $\underline{b}$ in Eq. IX.16 as the resulting Burgers vector of all dislocations which pierce through the surface S introduced above. With this understanding, $\underline{b}$ can be written as

$$\underline{b} = \iint_S \underline{\underline{\alpha}}\, d\underline{S}$$

and the interpretation of $\underline{\underline{\alpha}}$ as a line density of dislocations is now proposed. In particular, the first subscript in α_{ij} indicates the average line direction of the dislocations piercing through the area element dS_i whereas the second subscript gives the direction of the Burgers vector. Thus the diagonal components describe dislocations which have coinciding directions of their lines and Burgers vectors whereas these directions are perpendicular for the dislocations described by the non-diagonal elements of α_{ij}. In other words, the diagonal and non-diagonal components correspond to screw and edge dislocations respectively. It is important to note that screw and edge dislocations are not invariant notions in this theory because the diagonal and non-diagonal components of a tensor do not form an invariant decomposition. This is related to the fact that dislocations can change their edge-screw character along the line. But it also reflects the fact that the description of dislocation distributions in terms of continuous distributions is less detailed than the crystallographic description: knowledge of the tensor $\underline{\underline{\alpha}}$ does not allow to determine the crystallographic dislocations uniquely.

Similarly to Eq. IX.16, the following equation can be obtained from Eq. IX.9 when starting from the plastic, rather than the elastic, distortion:

$$\oint_C du_j^P = b_j \tag{IX.16}$$

which now becomes the definition equation for the Burgers vector as a dislocation is by nature a plastic deformation.

IX.3.3 Second order differential form of the incompatibility law: tensor of incompatibility

A second order differential form of the incompatibility law is now determined, which is of great use for the calculation of the internal stress state. For this, the elastic strains, ε_{ij}, are directly used. The latter are defined in terms of a displacement field, u_j, by the following relation, under the assumption of small deformations:

$$\varepsilon_{ij} = \frac{1}{2}\left(u_{j,i} + u_{i,j}\right) \qquad \left(\underline{\underline{\varepsilon}} = \text{def}\ \underline{u}\right) \tag{IX.17}$$

where "def $\underline{u}$" holds for "deformation of $\underline{u}$". This definition of the elastic strains is less general than their definition as the symmetric part of the elastic distortion tensor defined by Eq. IX.5 because it implies that the differential form IX.5 is integrable, under the condition curl $\underline{\underline{\beta}} = 0$. The problem of finding an integrability condition, not for $\underline{\underline{\beta}}$, but rather for its symmetric part $\underline{\underline{\varepsilon}}$ has been solved by de St. Venant who found that the tensor field $\underline{\underline{\varepsilon}}$ can be represented in the special form given by Eq. IX.17 if, and only if, $\underline{\underline{\varepsilon}}$ satisfies the differential equations:

$$-e_{ikm}\, e_{jln}\, \varepsilon_{mn,kl} = 0 \qquad \left(\text{inc}\ \underline{\underline{\varepsilon}} = 0\right) \tag{IX.18}$$

where "inc f" holds for "incompatibility of f", which is better known as:

$$\text{inc } \underline{\underline{\varepsilon}} = \nabla \times \underline{\underline{\varepsilon}} \times \nabla$$

Eqs. IX.18 are called the de St. Venant compatibility equations, where the term "compatibility" refers to the fact that there is a compatibility between the tensor field $\underline{\underline{\varepsilon}}$ and the idea that this field can be represented in terms of only a vector field which then has the meaning of a displacement field.

The symbolic notation "inc" has been introduced by Kröner [49, 47, 48, 50] for two reasons. Firstly, a tensor field is compatible if its incompatibility vanishes. The notation inc $\underline{\underline{\varepsilon}}$ for the incompatibility therefore allows a convenient characterisation of situations which are not compatible. Secondly, in the theory of symmetric tensor fields the differential operators def, inc and div play a role which is analogous to the role played by the operators grad, curl and div in the theory of vector fields. In particular, there exist two important identities, namely:

$$\text{div inc } \equiv 0 \tag{IX.19}$$

$$\text{inc def } \equiv 0 \tag{IX.20}$$

which are analogous to the often used identities div curl $\equiv 0$, curl grad $\equiv 0$ and permit to decompose any symmetric tensor field into a deformation field and an incompatibility field, just analogous to the well-known decomposition of a vector field into a gradient and a curl part, as shown by Kröner in [50]. In particular, any symmetric tensor field with vanishing divergence can be represented as an incompatibility field whereas it is a deformation field of type IX.17 if its incompatibility vanishes. These considerations strongly suggested Kröner to introduce second order incompatibility equations of the form:

$$-e_{ikm}\, e_{jln}\, \varepsilon_{mn,kl} = \eta_{ij} \qquad \left(\text{inc } \underline{\underline{\varepsilon}} = \underline{\underline{\eta}}\right) \tag{IX.21}$$

where the incompatibility tensor field $\underline{\underline{\eta}}$ is a quantitative measure of incompatibility, i.e. of the deviation from compatibility. It was already pointed out that the incompatibility arises from the presence of the dislocations. The next task is then to express the formal incompatibility equations IX.21 with the tensor of dislocation density.

Eq. IX.10 can be derived and decomposed into symmetric and antisymmetric parts, according to Eq. IX.1:

$$\nabla \times \underline{\underline{\beta}} \times \nabla = -\underline{\underline{\alpha}} \times \nabla \tag{IX.22}$$

$$\nabla \times \underline{\underline{\varepsilon}} \times \nabla + \nabla \times \underline{\underline{\omega}} \times \nabla = -\underline{\underline{\alpha}} \times \nabla \tag{IX.23}$$

Since the incompatibility operator "inc" transforms symmetric tensors into new symmetric tensors and antisymmetric tensors to new antisymmetric tensors, the incompatibility tensor defined by Eq. IX.21 can be immediately obtained as a function of the tensor $\underline{\underline{\alpha}}$ of dislocation density:

$$\underline{\underline{\eta}} = -\left(\underline{\underline{\alpha}} \times \nabla\right)_{sym} \tag{IX.24}$$

where the suffix "sym" indicates that the symmetric part of $\underline{\underline{\alpha}} \times \nabla$ is to be taken.

IX.4 Incompatibility as the fundamental source of internal stresses

IX.4.1 The basic equations of the internal stress problem

The problem to be treated in this section consists in the calculation of the internal stress and strain fields due to a given distribution $\underline{\underline{\eta}}$ of incompatibilities. Like in the previous section, the body will be considered as infinite.

The force equilibrium conditions on the medium are given by the equations:

$$\sigma_{ij,j} = 0 \qquad (\text{div } \underline{\underline{\sigma}} = 0) \tag{IX.25}$$

$$\sigma_{ij} = \sigma_{ji} \qquad (\underline{\underline{\sigma}} = \underline{\underline{\sigma}}^t) \tag{IX.26}$$

that are to be satisfied. The superscript "t" means that a transposition operation is performed.

Besides Eqs. IX.25 and IX.26, the incompatibility law in the form given by Eq. IX.21 is taken into account.

The law of elasticity (generalized Hooke's law) to be used contains fully the elastic anisotropy and is written as:

$$\sigma_{ij} = C_{ijkl}\,\varepsilon_{lk} \tag{IX.27}$$

$$C_{ijkl} = C_{jikl} = C_{ijlk} = C_{klij} \tag{IX.28}$$

Eqs. IX.25, IX.26, IX.21, IX.27 and IX.28 form the system of equations to be solved for the infinite body for a prescribed incompatibility tensor function $\underline{\underline{\eta}}$.

IX.4.2 The second order stress function tensor

In the following, the solid is assumed to be isotropic. Under these conditions, Eqs. IX.25, IX.26, IX.21, IX.27 and IX.28 can be rearranged to give the final equations to be solved:

$$\Delta\sigma_{ij} + \frac{1}{1+\nu}\left(\sigma_{kk,ij} - \Delta\sigma_{kk}\,\delta_{ij}\right) = 2\mu\,\eta_{ij} \tag{IX.29}$$

where ν is the Poisson's ratio, $\mu = \frac{E}{2(1+\nu)}$ the shear modulus, δ_{ij} the Kronecker's symbol. $\Delta = \nabla^2$ is the laplacian and $\sigma_{kk} = \sigma_{11} + \sigma_{22} + \sigma_{33}$.

The latter equation is not used practically to solve the internal stress problem. However, an inspection of the basic Eqs. IX.25, IX.26, IX.21, IX.27 and IX.28 shows that we are dealing with a field theory involving symmetric tensor fields. The analogy of such a theory with the well-known vector field theories has been already emphasized in section IX.3 where the identities div inc $\equiv 0$ and inc def $\equiv 0$ were compared with the corresponding identities of the differential operations div, curl, grad appearing in the vector field theories, but also in field theories with non-symmetric tensors. In this way, the form IX.25 of the equilibrium law together with Eq. IX.19 suggested Kröner to introduce analogously an auxiliary symmetry

tensor field, $\underline{\underline{\psi}}$, called the tensor field of second order stress functions. The diagonal stress function components have been considered already by Maxwell [83], the non-diagonal ones by Morera [86] and both together by Beltrami [14] in a representation given later in Eq. IX.42 which here reads:

$$\sigma_{ij} = -e_{ikm}\, e_{jln}\, \psi_{mn,kl} \qquad \left(\underline{\underline{\sigma}} = \text{inc}\ \underline{\underline{\psi}}\right) \tag{IX.30}$$

Since a symmetric tensor field is determined only by its incompatibility and divergence, Kröner concluded that, just as in the vector field theories, the tensor potential $\underline{\underline{\psi}}$ can be subject to a gauge condition which, for the elastic isotropic medium with shear modulus μ and Poisson's ratio ν, is most conveniently introduced via another auxiliary tensor potential $\underline{\underline{\psi}}'$ defined as:

$$\psi'_{ij} = \frac{1}{2\mu}\left(\psi_{ij} - \frac{\nu}{1+2\nu}\psi_{kk}\delta_{ij}\right) \tag{IX.31}$$

$$\psi_{ij} = 2\mu\left(\psi'_{ij} + \frac{\nu}{1-\nu}\psi'_{kk}\delta_{ij}\right) \tag{IX.32}$$

If $\underline{\underline{\psi}}'$ is inserted in Eq. IX.30 and the resulting expression for $\underline{\underline{\sigma}}$ introduced into the incompatibility equations IX.21 via Hooke's law (Eqs. IX.27 and IX.28), it is found that the resulting equations and thus all Eqs. IX.25, IX.26, IX.21, IX.27 and IX.28 are satisfied if the ψ'_{ij} obey the equations:

$$\nabla^4\psi'_{ij} = \eta_{ij} \qquad \left(\nabla^4\underline{\underline{\psi}}' = \underline{\underline{\eta}}\right) \tag{IX.33}$$

$$\psi'_{ij,i} = 0 \qquad \left(\text{div}\ \underline{\underline{\psi}}' = 0\right) \tag{IX.34}$$

Eqs. IX.33 and IX.34 are the final equations of the internal stress problem for a given incompatibility $\underline{\underline{\eta}}$. The general solution and a direct application to the case of singles dislocations are given in the next subsection.

IX.4.3 General and special solutions of the internal stress problem

The general solution

From the theory of bipotential equations, it is known that in the case of an infinite medium, the solution of Eq.IX.33 is given by:

$$\psi'_{ij}(\underline{r}) = -\frac{1}{8\pi}\iiint_V \eta_{ij}(\underline{r}')\parallel \underline{r} - \underline{r}'\parallel dV' \tag{IX.35}$$

where $\underline{r}$ and $\underline{r}'$ are the observation and position vectors respectively, as shown in Fig. IX.6.

Once $\underline{\underline{\psi}}'$ is calculated, the stress field $\underline{\underline{\sigma}}$ can be obtained with the following expression:

$$\sigma_{ij} = 2\mu\left(\Delta\psi'_{ij} - \frac{1}{1-\nu}\left(\psi'_{kk,ij} - \Delta\psi'_{kk}\,\delta_{ij}\right)\right) \tag{IX.36}$$

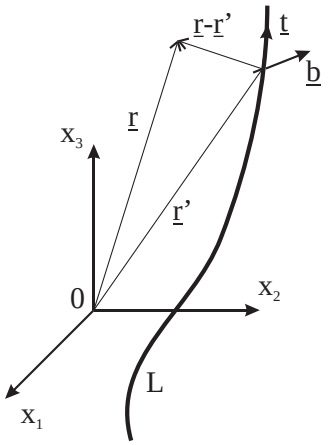

Figure IX.6: Parametrisation of a single dislocation line.

Single dislocations

As a first application of his theory, Kröner proposed to solve the case of single dislocations. In this particular case, the volume integration in Eq. IX.35 can be reduced to a path integration along the dislocation line L with tangential vector $\underline{t}$ (Fig. IX.6). If ρ is the distance of a point from the line L which passes through the points $\underline{r}'$, then the corresponding tensor of dislocation density has the form:

$$\alpha_{il}\left(\underline{r}\right) = t_i\, b_l\, \delta\left(\rho\right) \tag{IX.37}$$

because this form of $\underline{\underline{\alpha}}$ leads to the correct resulting Burgers vector piercing through a small area s perpendicular to the dislocation line.

In fact the integration over s gives:

$$\iint \alpha_{il}\, dS_i = \iint t_i\, b_l\, \delta\left(\rho\right)\, t_i\, dS = b_l \tag{IX.38}$$

where the definition of the δ-function which implies $\iint \delta\left(\rho\right)\, dS = 1$ has been used. Replacing the incompatibility tensor in Eq. IX.35 by the dislocation density tensor according to Eq. IX.24 yields:

$$\psi'_{ij}\left(\underline{r}\right) = \frac{1}{8\pi} \iiint \parallel \underline{r} - \underline{r}' \parallel \, \left[e_{jln}\, \alpha_{il,n}\left(\underline{r}'\right)\right]_{(ij)}\, dV' \tag{IX.39}$$

where the suffix (ij) denotes symmetrization in these subscripts. With $dV = dS\, dl$, $dl_i = t_i dl$, and α_{il} from Eq. IX.37, we obtain:

$$\psi'_{ij}\left(\underline{r}\right) = \frac{1}{8\pi}\left[e_{jln}\, b_l\, \mathcal{J}_i\left(\underline{r}\right)\right]_{(ij)} \tag{IX.40}$$

$$\mathcal{J}_i\left(\underline{r}\right) = \int_L \parallel \underline{r} - \underline{r}' \parallel \, dl'_i \tag{IX.41}$$

Thus the stress functions and the stresses are just derivatives of the line integrals $\mathcal{J}_i$. These integrals lead to elementary functions only for straight or piecewise straight dislocations. The

latter case is important because curved dislocations can be approximated by polygon type dislocations. This feature is widely used in Dislocation Dynamics codes (see [148] and [147]) for the study of plasticity or irradiation-induced hardening from the production of dislocation loops. In such codes, the loop is segmented into straight lines and the approximated stress field of the loop is then deduced by superposition of the self-stresses of all the segments. These approximated calculations turn out to be sufficiently accurate, and Zbib and de la Rubia [147] showed that not so many segments are necessary to reach the exact solution.

Plane problems

The stresses and strains due to single dislocations or due to continuous distributions of dislocations which all extend parallel to the x_3-axis do not depend on the x_3-coordinate. The stress function given by Eq. IX.30, when written in Cartesian coordinates, has the form:

$$\begin{aligned} \sigma_{11} &= -\frac{\partial^2\psi_{22}}{\partial x_3^2} - \frac{\partial^2\psi_{33}}{\partial x_2^2} + 2\frac{\partial^2\psi_{23}}{\partial x_2\partial x_3} \\ \sigma_{12} &= -\frac{\partial}{\partial x_3}\left(-\frac{\partial\psi_{12}}{\partial x_3} + \frac{\partial\psi_{23}}{\partial x_1} + \frac{\partial\psi_{31}}{\partial x_2}\right) + \frac{\partial^2\psi_{33}}{\partial x_1\partial x_2} \end{aligned} \qquad \text{(IX.42)}$$

plus equations arising by cyclic permutation of the subscripts in Eq. IX.42. In the case of the plane problem, $\partial/\partial x_3 = 0$, the latter equations read:

$$\sigma_{11} = -\frac{\partial^2\psi}{\partial x_2^2}\,, \quad \sigma_{22} = -\frac{\partial^2\psi}{\partial x_1^2}\,, \quad \sigma_{12} = \frac{\partial^2\psi}{\partial x_1\partial x_2}\,, \quad \psi = \psi_{33} \qquad \text{(IX.43)}$$

$$\sigma_{23} = -\frac{\partial\phi}{\partial x_1}\,, \quad \sigma_{31} = \frac{\partial\phi}{\partial x_2}\,, \quad \phi = -\frac{\partial\psi_{23}}{\partial x_1} + \frac{\partial\psi_{31}}{\partial x_2} \qquad \text{(IX.44)}$$

$$\sigma_{33} = -\frac{\partial^2\psi_{11}}{\partial x_2^2} - \frac{\partial^2\psi_{22}}{\partial x_1^2} + 2\frac{\partial^2\psi_{12}}{\partial x_1\partial x_2} \qquad \text{(IX.45)}$$

Eqs. IX.43 are the well-known equations containing the Airy's stress function. In Eq. IX.44, ϕ is the stress function of torsion, sometimes called Prandtl's stress function. Apparently, Eqs. IX.43 and IX.44 represent stress states which are independent of each other and also of the stress state σ_{33} in Eq. IX.45. The latter equations are now inserted in the isotropic inverse Hooke's law. Substituting the strain ε_{mn} so obtained in the incompatibility law in order to include the tensor $\underline{\underline{\alpha}}$ of dislocation density, the following equations are obtained:

$$\nabla^4\psi = \frac{\mu}{1-\nu}\left(\alpha_{31,2} - \alpha_{32,1}\right) \qquad \text{(IX.46)}$$

$$\nabla^2\phi = -\mu\,\alpha_{33} \qquad \text{(IX.47)}$$

$$\sigma_{33} = \nu\left(\sigma_{11} + \sigma_{22}\right) \qquad \text{(IX.48)}$$

According to the components of $\underline{\underline{\alpha}}$ in Eqs. IX.46 and IX.47 (non-diagonal and diagonal components), it is seen that Airy's stress function describes edge dislocations and Prandtl's function screw dislocations, all extending parallel to the x_3-direction. The solutions of Eqs. IX.46 and IX.47 for the infinite medium is well known from bipotential and potential theory, and are given for a single edge dislocation defined by $\alpha_{31}(r') = b\,\delta(\rho)$ and for a screw dislocation $\alpha_{33} = b\,\delta(\rho)$:

$$\psi(r) = \frac{\mu\,b}{4\pi(1-\nu)}\left(\rho^2\,\ln\rho\right)_{,2} \qquad \text{(edge dislocation)} \qquad \text{(IX.49)}$$

and

$$\phi(r) = -\frac{\mu}{2\pi} \ln \rho \qquad \text{(screw dislocation)} \tag{IX.50}$$

where ρ is the distance in the plane x_3=0 between the points $\underline{r}$ and $\underline{r}'$. These solutions of the internal stress problem have been determined earlier by Burgers [22].

It will be shown in chapter X that the same formalism can be applied to infinite distributions of dislocations. The solutions will not be obtained by means of Eq. IX.35 but by direct resolution of Eq. IX.33 by using a general method presented in appendix A.

X

Calculation of stress fields induced by dislocation configurations

Contents

X.1 Introduction

In this chapter, typical configurations of periodic dislocation lines are studied. The stress fields induced by an edge dislocation pile-up and wall are first presented, as a direct application of Kröner's theory presented in chapter IX with use of the resolution method of biharmonic equations developed in this thesis and presented in appendix A.

The stress field induced by basic configurations of periodic edge dislocations (i.e. pile-up and wall) is well-known in the literature. The shear stress component of an edge dislocation wall was first given by Burgers [22] and the normal components then by Cottrell [25]. The starting point is the expression of stress induced by a single edge dislocation. The stress field of the dislocation wall is obtained by adding up the individual stresses:

$$\sigma_{ij}(\underline{r}) = \sum_k \sigma_{ij}^k(\underline{r}) \tag{X.1}$$

where $\sigma_{ij}^k(\underline{r})$ is the stress field induced by a single dislocation. As for the cases presented here, the latter expressions of stresses could also be simplified in an analytical form. Later, Li [57] used these results and made a detailed analysis of the interaction between an edge dislocation wall and a single edge dislocation line for the study of growth of an edge dislocation wall.

Contrary to this classical approach, Kröner's theory directly regards the infinite plane of strain sources which are taken into account into the incompatibility tensor $\underline{\underline{\eta}}$. Then, the stress function tensor is determined, from which the stress components are derived.

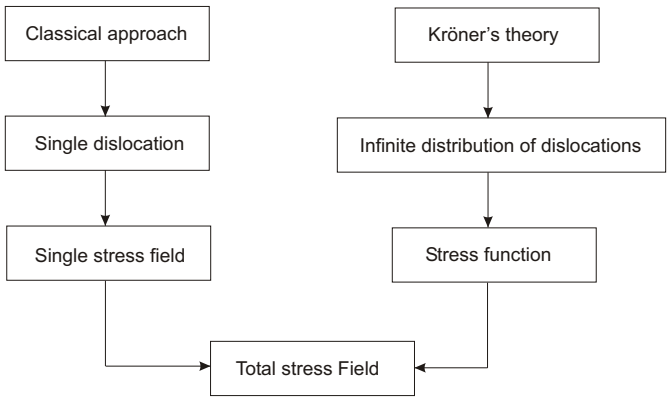

Figure X.1: Stress calculation methods.

Fig. X.1 clearly shows the difference between these two approaches. The main interest in using the heavy formalism of Kröner lies in the possibilities of such a tool. This will be shown for the other cases studied in this chapter: screw dislocation pile-up and symmetrical tilt-boundary. The results presented in the next section have been recently published in [39].

X.2 Application of Kröner's theory to various dislocation configurations

For each dislocation configuration, the following steps are applied, in which the main equations to be solved are pointed out:

1. For a given dislocation configuration, the dislocation density tensor $\underline{\underline{\alpha}}$ is proposed.
2. The incompatibility tensor $\underline{\underline{\eta}}$ is deduced from Eq. IX.24:
$$\underline{\underline{\eta}} = -\left(\underline{\underline{\alpha}} \times \nabla\right)_{sym}$$
3. The solution of the bipotential equation (Eq. IX.33)
$$\nabla^4 \underline{\underline{\psi'}} = \underline{\underline{\eta}}$$
gives the stress function tensor $\underline{\underline{\psi'}}$.
4. The stress field $\underline{\underline{\sigma}}$ is finally deduced from Eq. IX.36:
$$\sigma_{ij} = 2\mu \left(\Delta\psi'_{ij} - \frac{1}{1-\nu} \left(\psi'_{kk,ij} - \Delta\psi'_{kk}\, \delta_{ij} \right) \right)$$
5. In section X.3, the elastic energy of a dislocation configuration is calculated. The elastic strain $\underline{\underline{\varepsilon}}$ is calculated from Eq. IX.27:
$$\underline{\underline{\sigma}} = \underline{\underline{C}} : \underline{\underline{\varepsilon}}$$
and the elastic energy is deduced from:
$$e = \frac{1}{2}\, \underline{\underline{\sigma}} : \underline{\underline{\varepsilon}}$$

X.2.1 Edge dislocation pile-up

The general method to solve Eq. IX.33 when the incompatibility tensor $\underline{\underline{\eta}}$ is given under the form of an infinite and periodic distribution of dislocations is entirely presented in appendix A for the case of an edge dislocation pile-up. The same method is then applied to the case of an edge dislocation wall for which only the final expression is given.

According to Fig. X.2, the dislocation density tensor is reduced to the single component:

$$\forall n \in \mathbb{N}, \qquad \alpha_{31}\left(\underline{x}\right) = \sum_{n=-\infty}^{\infty} b\, \delta\left(x_1 - nh\right) \delta\left(x_2\right) \tag{X.2}$$

which leads to a source term

$$\eta_{33}\left(\underline{x}\right) = \alpha_{31,2}\left(\underline{x}\right) = \sum_{n=-\infty}^{\infty} b\, \delta\left(x_1 - nh\right) \delta'\left(x_2\right) \tag{X.3}$$

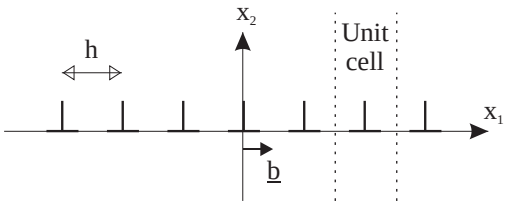

Figure X.2: Edge dislocation pile-up.

The equation to be solved is then:

$$\nabla^4 \psi_{pileup}\left(\underline{x}\right) = \sum_{n=-\infty}^{\infty} b\,\delta\left(x_1 - nh\right)\delta'\left(x_2\right) \tag{X.4}$$

By using the result of Eq. A.25, we obtain the stress function of an edge dislocation pile-up:

$$\boxed{\psi_{pileup}\left(\underline{x}\right) = -\frac{b}{4\pi}\sum_{k=1}^{\infty}\frac{x_2}{k}\cos\left(\frac{2\pi k x_1}{h}\right)\exp\left(-\frac{2\pi k \mid x_2 \mid}{h}\right) + \frac{b}{h}\frac{x_2^2}{4}\mathrm{sign}\left(x_2\right)} \tag{X.5}$$

The latter expression can be simplified if the series can be expressed as an analytical limit. This requires to express $\sum_{k=1}^{\infty} e^{-k\alpha}\cos\left(kx\right)$ (and also $\sum_{k=1}^{\infty} e^{-k\alpha}\sin\left(kx\right)$), as well as its successive indefinite integral, e.g. by mean of Complex Analysis.

The starting point for the calculation of $\sum_{k=1}^{\infty} e^{-k\alpha}\cos\left(kx\right)$ (and later $\sum_{k=1}^{\infty} e^{-k\alpha}\sin\left(kx\right)$) is the following geometric series:

$$\sum_{k=1}^{n} e^{-k\alpha+ikx} = \sum_{k=1}^{n}\left(e^{-\alpha+ix}\right)^k \tag{X.6}$$

This series is convergent if:

$$\mid e^{-\alpha+ix} \mid \leq 1 \quad \Leftrightarrow \quad \mid e^{-\alpha} \mid \leq 1 \tag{X.7}$$

As α is taken to be always greater than 0, the previous condition is verified. Under these conditions, the limit of the series is:

$$\sum_{k=1}^{\infty} e^{-k\alpha+ikx} = \frac{e^{-\alpha+ix}}{1-e^{-\alpha+ix}} \tag{X.8}$$

Taking the real and imaginary parts of Eq. X.8, we obtain the following expressions:

$$\sum_{k=1}^{\infty} e^{-k\alpha}\cos\left(kx\right) = \frac{1}{2}\frac{\sinh\alpha}{\cosh\alpha - \cos x} - \frac{1}{2} \tag{X.9}$$

$$\sum_{k=1}^{\infty} e^{-k\alpha}\sin\left(kx\right) = \frac{1}{2}\frac{\sin x}{\cosh\alpha - \cos x} \tag{X.10}$$

Then, the indefinite integral is calculated:

$$\begin{aligned}\sum_{k=1}^{\infty} -\frac{1}{k} e^{-k\alpha+ikx} &= \int \sum_{k=1}^{\infty} e^{-k\alpha+ikx} d\alpha \\ &= \ln\left(1-e^{-\alpha+ix}\right)+C\end{aligned}$$

where C is a constant of integration. The natural logaritm of a complex number is defined by:

$$\ln z = \ln \mid z \mid + i \arg(z)$$

Here, $z = 1 - e^{-\alpha+ix}$:

$$\ln \mid 1-e^{-\alpha+ix} \mid = \frac{1}{2}\ln(\cosh\alpha - \cos x) - \frac{1}{2}\alpha + \frac{1}{2}\ln 2 \tag{X.11}$$

$C = -\frac{1}{2}\ln 2$ is appropriate and the first indefinite integral is found to be:

$$\sum_{k=1}^{\infty} -\frac{1}{k} e^{-k\alpha+ikx} = \frac{1}{2}\left[\ln(\cosh\alpha - \cos x) - \alpha\right] + i \arg\left(1-e^{-\alpha+ix}\right) \tag{X.12}$$

By taking the real part of Eq. X.12, it is found that:

$$\sum_{k=1}^{\infty} -\frac{1}{k} e^{-k\alpha} \cos(kx) = \frac{1}{2}\left[\ln(\cosh\alpha - \cos x) - \alpha\right] \tag{X.13}$$

The latter expression appears in Eq. X.5, and by writing

$$\alpha = \frac{2\pi \mid x_2 \mid}{h} \geq 0 \qquad and \qquad x = \frac{2\pi x_1}{h} \tag{X.14}$$

a simplified expression for the stress function in the case of an edge dislocation pile-up reads:

$$\boxed{\psi_{pileup}(\underline{x}) = \frac{bx_2}{4\pi}\frac{1}{2}\left[\ln\left(\cosh\left(\frac{2\pi \mid x_2 \mid}{h}\right) - \cos\left(\frac{2\pi x_1}{h}\right)\right) - \frac{2\pi \mid x_2 \mid}{h}\right] + \frac{b}{h}\frac{x_2^2}{4}\mathrm{sign}(x_2)} \tag{X.15}$$

Eq. X.15 is an analytical expression of the stress function which enables to calculate the stress field of the edge dislocation pile-up in a straightforward manner. From this, it is obvious that we can make advantage of Eq. X.15 to calculate the stress field of other configurations involving dislocation pile-ups, like the edge dipolar mat shown in Fig. X.3. This configuration is a well-known dislocation structure in the metals subject to unidirectional deformations [33]. More particularly, it is known that the edge dipolar mat is a stable configuration when the angle between two opposite dislocations is 45°, i.e. :

$$d = \frac{h}{2} \tag{X.16}$$

This condition can be easily checked with the present tool by superposing two edge dislocation pile-ups, with opposite Burgers vector and separated by a distance d. The total stress function can subsequently be obtained from which the elastic energy in a unit cell containing two opposite dislocation lines can be calculated for different sets of values for h and d. However, we are here mainly interested in presenting the results concerning simple dislocation planes and the edge dipolar mat will not be further studied in this part.

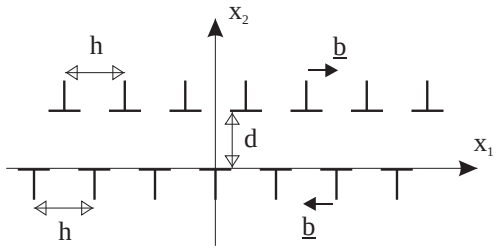

Figure X.3: Edge dipolar mat.

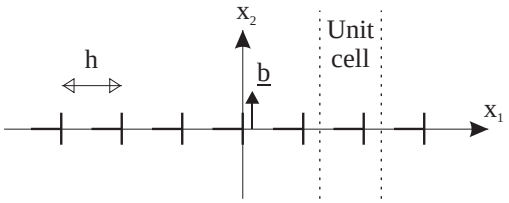

Figure X.4: Edge dislocation wall.

X.2.2 Edge dislocation wall

In the case of an edge dislocation wall as shown in Fig. X.4, the only non-zero component of the dislocation density tensor $\underline{\underline{\alpha}}$ is α_{32}, and the source term is:

$$\forall n \in \mathbb{N}, \qquad \eta_{33}\left(\underline{x}\right) = -\alpha_{32,1}\left(\underline{x}\right) = -\sum_{n=-\infty}^{\infty} b\,\delta'\left(x_1 - nh\right)\delta\left(x_2\right) \tag{X.17}$$

The same method of integration presented in appendix A can be applied, leading to the following solution:

$$\boxed{\psi_{wall}\left(\underline{x}\right) = \frac{hb}{8\pi^2}\sum_{k=1}^{\infty}\left(\frac{1+\frac{2\pi k}{h}\mid x_2\mid}{k^2}\right)\sin\left(\frac{2\pi k}{h}x_1\right)\exp\left(-\frac{2\pi k}{h}\mid x_2\mid\right)} \tag{X.18}$$

By taking the imaginary part of Eq. X.12, it is found that:

$$\begin{aligned}\sum_{k=1}^{\infty} -\frac{1}{k}e^{-k\alpha}\sin\left(kx\right) &= arg\left(1-e^{-\alpha+ix}\right)\\ &= \arctan\left[\frac{e^{\alpha}-\cos x}{\sin x}\right] - \frac{\pi}{2}sign\left(\sin\left(x\right)\right)\end{aligned} \tag{X.19}$$

Now, the second indefinite integral is calculated:

$$\begin{aligned}\sum_{k=1}^{\infty}\frac{1}{k^2}e^{-k\alpha}\sin\left(kx\right) &= \int\sum_{k=1}^{\infty} -\frac{1}{k}e^{-k\alpha}\sin\left(kx\right)d\alpha\\ &= \underbrace{\int\arctan\left[\frac{e^{\alpha}-\cos x}{\sin x}\right]d\alpha}_{I(x)} - \alpha\frac{\pi}{2}sign\left(\sin\left(x\right)\right)\end{aligned} \tag{X.20}$$

The constant of integration has been chosen to be equal to zero. $I(x)$ is not a known integral. However, by performing a change of variable

$$u = \frac{e^{\alpha} - \cos x}{\sin x} \tag{X.21}$$

and an integration by parts, $I(x)$ is expressed as:

$$I(x) = \alpha \arctan\left(\frac{e^{\alpha} - \cos x}{\sin x}\right) - A(x;\alpha) \tag{X.22}$$

where

$$\begin{aligned} A(x;\alpha) &= \frac{1}{2} i \left[\alpha \ln\left(\frac{1 - e^{\alpha}(\cos x + i \sin x)}{1 - e^{\alpha}(\cos x - i \sin x)}\right) \right. \\ &\left. + \mathrm{Li}_2\left(e^{\alpha}(\cos x + i \sin x)\right) - \mathrm{Li}_2\left(e^{\alpha}(\cos x - i \sin x)\right) \right] \end{aligned} \tag{X.23}$$

$A(x;\alpha)$ is a real-valued function with complex variable. $\mathrm{Li}_2(\mathrm{z})$ is a special case of the polylogarithm $\mathrm{Li}_n(\mathrm{z})$ for n = 2, which is the function:

$$\mathrm{Li}_n(z) = \sum_{k=1}^{\infty} \frac{z^k}{k^n} \tag{X.24}$$

$\mathrm{Li}_2(\mathrm{z})$ satifies

$$\mathrm{Li}_2(z) = \int_z^0 \frac{\ln(1-t)}{t} dt \tag{X.25}$$

Then, $\mathrm{Li}_2(\mathrm{z})$ is calculated by using the *dilog* function:

$$\mathrm{Li}_2(z) = dilog(1-z) = \int_1^{1-z} \frac{\ln t}{1-t} dt \tag{X.26}$$

By inserting the results of Eqs. X.22, X.20 and X.19 in Eq. X.18, and by writing

$$\alpha = \frac{2\pi \mid x_2 \mid}{h} \qquad \text{and} \qquad x = \frac{2\pi x_1}{h} \tag{X.27}$$

the final result is:

$$\boxed{\psi_{wall}(\underline{x}) = -\frac{hb}{8\pi^2} A(x_1; x_2)} \tag{X.28}$$

where

$$\begin{aligned} A(x_1;x_2) &= \frac{1}{2} i \left[\frac{2\pi \mid x_2 \mid}{h} \ln\left(\frac{1 - e^{\frac{2\pi|x_2|}{h}}\left(\cos\left(\frac{2\pi x_1}{h}\right) + i \sin\left(\frac{2\pi x_1}{h}\right)\right)}{1 - e^{\frac{2\pi|x_2|}{h}}\left(\cos\left(\frac{2\pi x_1}{h}\right) - i \sin\left(\frac{2\pi x_1}{h}\right)\right)}\right) \right. \\ &+ \mathrm{dilog}\left(1 - e^{\frac{2\pi|x_2|}{h}}\left(\cos\left(\frac{2\pi x_1}{h}\right) + i \sin\left(\frac{2\pi x_1}{h}\right)\right)\right) \\ &\left. - \mathrm{dilog}\left(1 - e^{\frac{2\pi|x_2|}{h}}\left(\cos\left(\frac{2\pi x_1}{h}\right) - i \sin\left(\frac{2\pi x_1}{h}\right)\right)\right) \right] \end{aligned} \tag{X.29}$$

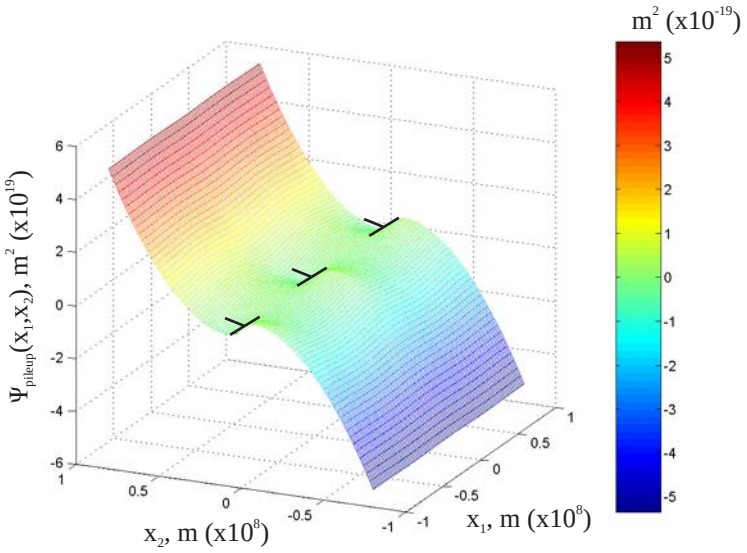

Figure X.5: $\psi_{pileup}\left(x_1, x_2\right)$ for an edge dislocation pile-up.

The stress functions of the edge dislocation pile-up and wall, calculated from Eqs. X.15 and X.28 respectively, are shown in Figs. X.5 and X.6 respectively. In Eqs. X.15 and X.28, the remaining parameter is the Burgers vector modulus. As presented in section II.3.1, Ashbee [3] showed that the Burgers vector in all glide planes in UO_2 is a/2 <110>, from which the modulus can be calculated:

$$b = a\,\frac{\sqrt{2}}{2} = 3.87\mathring{A} \tag{X.30}$$

where a is the UO_2 lattice parameter.

The stress function $\psi_{pileup}\left(\underline{x}\right)$ in Fig. X.5 shows well-known characterics: the dislocation pile-up plane separates two half spaces of opposite sign, which is responsible for stresses at large distances. This is not the case for the edge dislocation wall (Fig. X.6) where $\psi_{wall}\left(\underline{x}\right)$ is in average equal to zero at large distances from the dislocation line plane.

Moreover, $\psi_{wall}\left(\underline{x}\right)$ undergoes important variations located at every dislocation line of the distribution plane. These variations are due to the compensation between compression and tension fields of one dislocation line with its neighbour, as illustrated in Fig. X.15.

The stress field associated with each configuration is derived and the non-zero components are plotted in Figs. X.7 and X.8 for the edge disloaction pile-up and wall respectively.

In these figures, the stress unit is:

$$\sigma_0 = \frac{\mu b}{2\pi\left(1-\nu\right)h} \tag{X.31}$$

where μ is the Shear modulus, ν the Poisson's ratio, b the Burgers vector modulus and h the

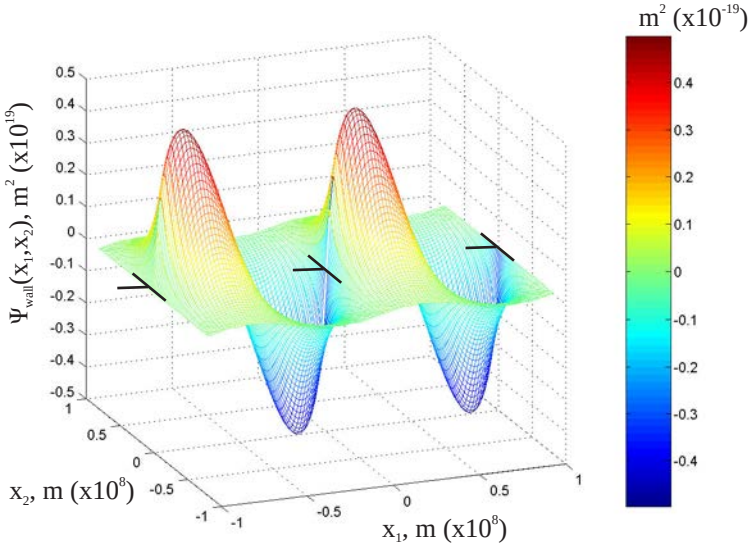

Figure X.6: $\psi_{wall}\left(x_1, x_2\right)$ for an edge dislocation wall.

dislocation interdistance chosen to be 20 nm:

$$\nu = 0.3 \tag{X.32}$$

$$E = 200 \text{ GPa} \tag{X.33}$$

$$\mu = \frac{E}{2(1+\nu)} \tag{X.34}$$

The stress components are plotted at a distance $x_2 = \pm$ 0.6 nm from the dislocation plane.

It is shown that the solutions calculated from the stress functions $\psi\left(\underline{x}\right)$ are in perfect agreement with the solutions given by Cottrell [25], Li [57] and Borisova [17].

Finally it is noticed that, as for the edge dipolar mat, the stress field induced by the edge dipolar wall shown in Fig. X.9 would as well be determined by superposing two edge dislocation walls, with opposite Burgers vector and separated by a distance d.

X.2.3 Screw dislocation pile-up

Another direct application of Kröner's theory is the pile-up of screw-type dislocation, as shown in Fig. X.10. In this case, the dislocation line and Burgers vector are colinear, in the z-direction.

The dislocation density tensor of a screw dislocation pile-up is simply written as:

$$\forall n \in \mathbb{N}, \qquad \alpha_{33}\left(\underline{x}\right) = \sum_{n=-\infty}^{\infty} b\,\delta\left(x_1 - nh\right)\delta\left(x_2\right) \tag{X.35}$$

By using Eq. IX.24, the source term tensor is not reduced to a single component but is given

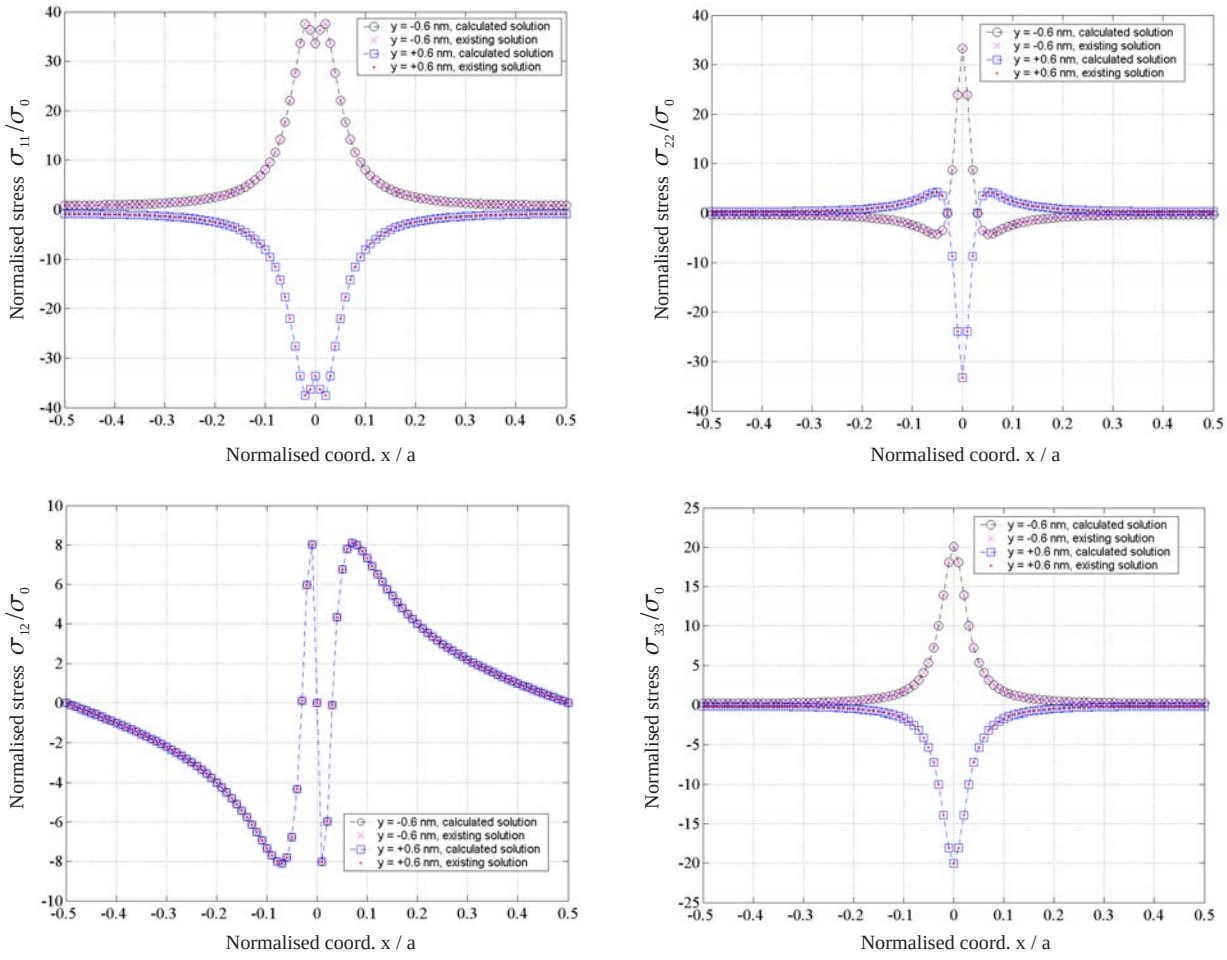

Figure X.7: Comparison of calculated stress components for an edge dislocation pile-up in a unit cell (defined in Fig. X.2) obtained by means of the new tool (Eq. X.15) with the simplified solution provided in the open litterature [22].

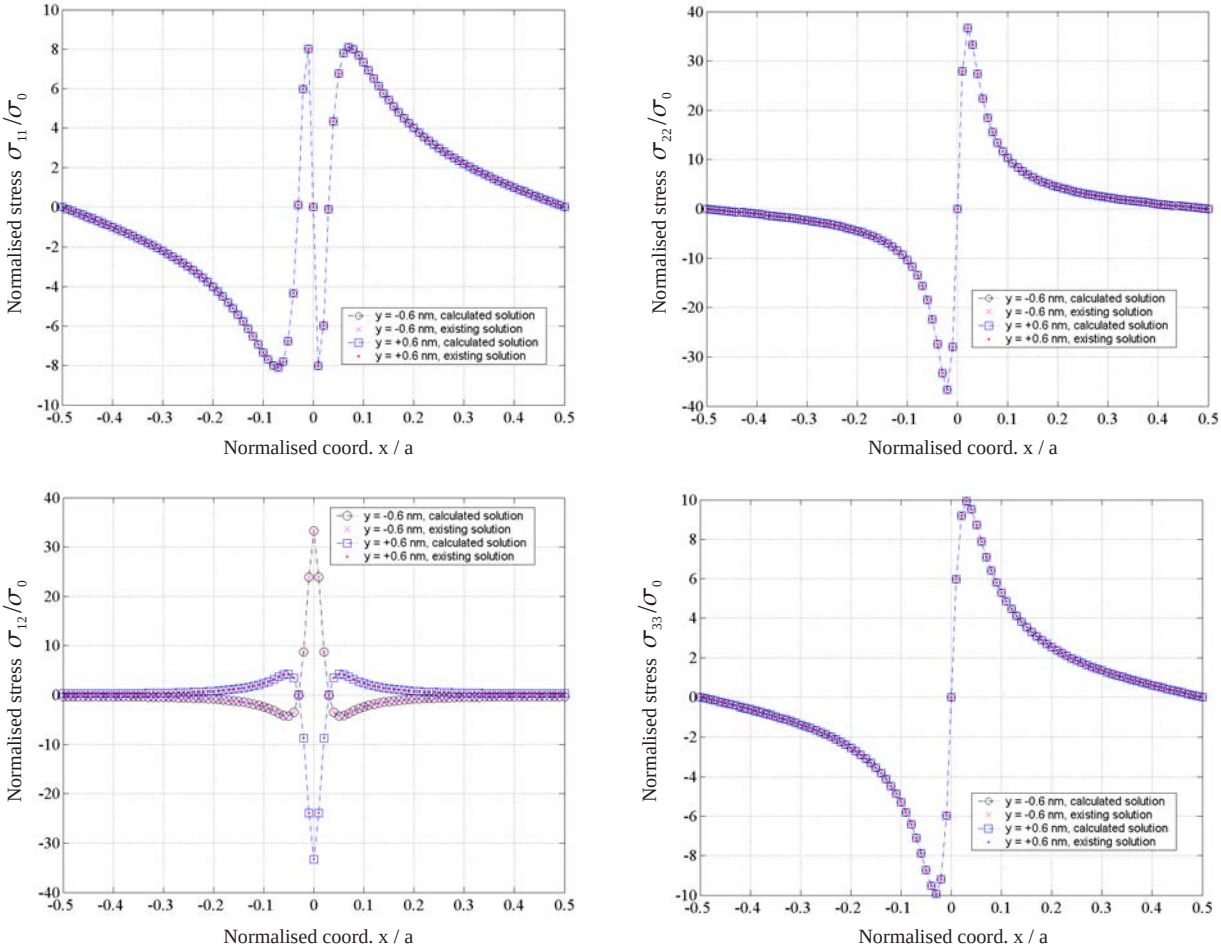

Figure X.8: Comparison of calculated stress components for an edge dislocation wall in a unit cell (defined in Fig. X.4) obtained by means of the new tool (Eq. X.28) with the simplified solution provided in the open litterature [22].

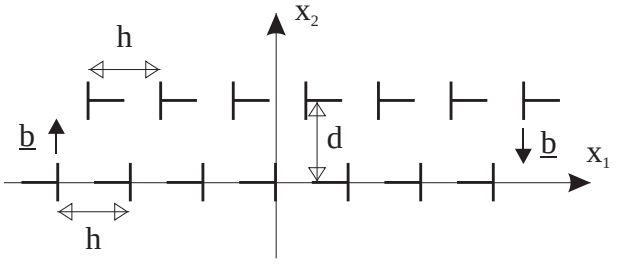

Figure X.9: Edge dipolar wall.

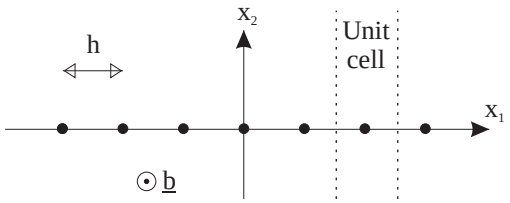

Figure X.10: Screw dislocation pile-up.

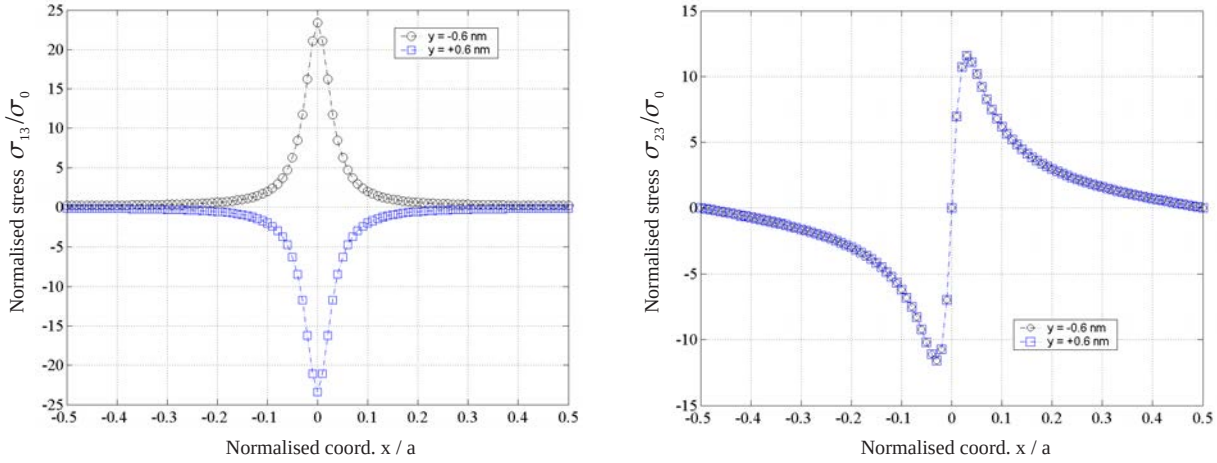

Figure X.11: Calculated solutions of stress components for a screw dislocation pile-up as defined by Fig. X.10.

by:

$$\underline{\underline{\eta}}\left(\underline{x}\right) = \begin{bmatrix} 0 & 0 & \frac{-\alpha_{33,2}(\underline{x})}{2} \\ 0 & 0 & \frac{\alpha_{33,1}(\underline{x})}{2} \\ \frac{-\alpha_{33,2}(\underline{x})}{2} & \frac{\alpha_{33,1}(\underline{x})}{2} & 0 \end{bmatrix} \tag{X.36}$$

Eq. IX.33 can be solved independently for each component of Eq. X.36. It should be emphasized that the terms $\alpha_{33,2}\left(\underline{x}\right)$ and $\alpha_{33,1}\left(\underline{x}\right)$ are comparable to the source terms $\alpha_{31,2}\left(\underline{x}\right)$ of the edge dislocation pile-up and $\alpha_{32,1}\left(\underline{x}\right)$ of the edge dislocation wall. As the solutions of Eq. IX.33 are known for these two cases, noted $\psi_{pileup}\left(\underline{x}\right)$ and $\psi_{wall}\left(\underline{x}\right)$ respectively, the stress function solution for this screw dislocation pile-up is obtained by using he solutions $\psi_{pileup}\left(\underline{x}\right)$ and $\psi_{wall}\left(\underline{x}\right)$:

$$\underline{\underline{\psi}}\left(\underline{x}\right) = \begin{bmatrix} 0 & 0 & \frac{-\psi_{pileup}(\underline{x})}{2} \\ 0 & 0 & \frac{-\psi_{wall}(\underline{x})}{2} \\ \frac{-\psi_{pileup}(\underline{x})}{2} & \frac{-\psi_{wall}(\underline{x})}{2} & 0 \end{bmatrix} \tag{X.37}$$

The latter tensor is then computed to obtain the stress field. As a known characteristic of screw dislocations, only shear stresses in the dislocation line direction are non-equal to zero (Fig. X.11).

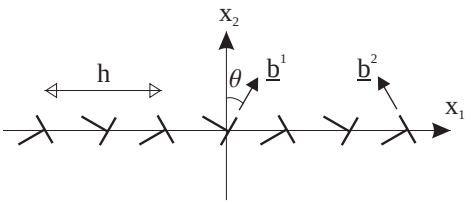

Figure X.12: Symmetrical tilt-boundary.

X.2.4 Symmetrical tilt boundary

The present formalism can also be applied to the case of the symmetrical tilt-boundary. A general representation of such an edge dislocation configuration is shown in Fig. X.12.

In this case, the dislocation density tensor is made of two terms, each one containing two distributions associated with a Burgers vector:

$$\forall n \in \mathbb{N}, \qquad \alpha_{3j}\left(\underline{x}\right) = b_j^1 \sum_{n=-\infty}^{\infty} \delta\left(x_1 - nh\right)\delta\left(x_2\right) + b_j^2 \sum_{n=-\infty}^{\infty} \delta\left(x_1 - nh - h/2\right)\delta\left(x_2\right) \quad \text{(X.38)}$$

where j=1, 2 and b_j^1 and b_j^2 are defined by:

$$\underline{b}^1 = b\begin{pmatrix} \omega \\ \xi \\ 0 \end{pmatrix} \quad and \quad \underline{b}^2 = b\begin{pmatrix} -\omega \\ \xi \\ 0 \end{pmatrix} \quad with\ \omega, \xi > 0\ and\ \sqrt{\omega^2 + \xi^2} = 1 \qquad \text{(X.39)}$$

According to the conditions given in Eq. X.39, ω and ξ can be calculated as a function of the angle θ:

$$\begin{cases} \omega\left(\theta\right) = \sin\theta \\ \xi\left(\theta\right) = \mid \cos\theta \mid \end{cases} \qquad \text{(X.40)}$$

By using Eq. IX.24, it is found that the source term tensor is here reduced to only one component:

$$\underline{\underline{\eta}}\left(\underline{x}\right) = \begin{bmatrix} 0 & 0 & 0 \\ 0 & 0 & 0 \\ 0 & 0 & \alpha_{31,2}\left(\underline{x}\right) - \alpha_{32,1}\left(\underline{x}\right) \end{bmatrix} \qquad \text{(X.41)}$$

It follows that the equation to be solved is:

$$\begin{aligned} \nabla^4\psi_{33}\left(\underline{x}\right) &= \omega b \sum_{n=-\infty}^{\infty} \left[\delta\left(x_1 - nh - h/2\right) - \delta\left(x_1 - h/2 - nh\right)\right]\delta'\left(x_2\right) \\ &\quad - \xi b \sum_{n=-\infty}^{\infty} \left[\delta'\left(x_1 - nh\right) + \delta'\left(x_1 - h/2 - nh\right)\right]\delta\left(x_2\right) \end{aligned} \qquad \text{(X.42)}$$

In this case, we can make use of the solutions calculated for the edge dislocation pile-up and wall:

$$\begin{aligned} \psi_{33}\left(\underline{x}\right) &= \omega\left[\psi_{pileup}\left(x_1; x_2\right) - \psi_{pileup}\left(x_1 - h/2; x_2\right)\right] \\ &\quad + \xi\left[\psi_{wall}\left(x_1; x_2\right) + \psi_{wall}\left(x_1 - h/2; x_2\right)\right] \end{aligned} \qquad \text{(X.43)}$$

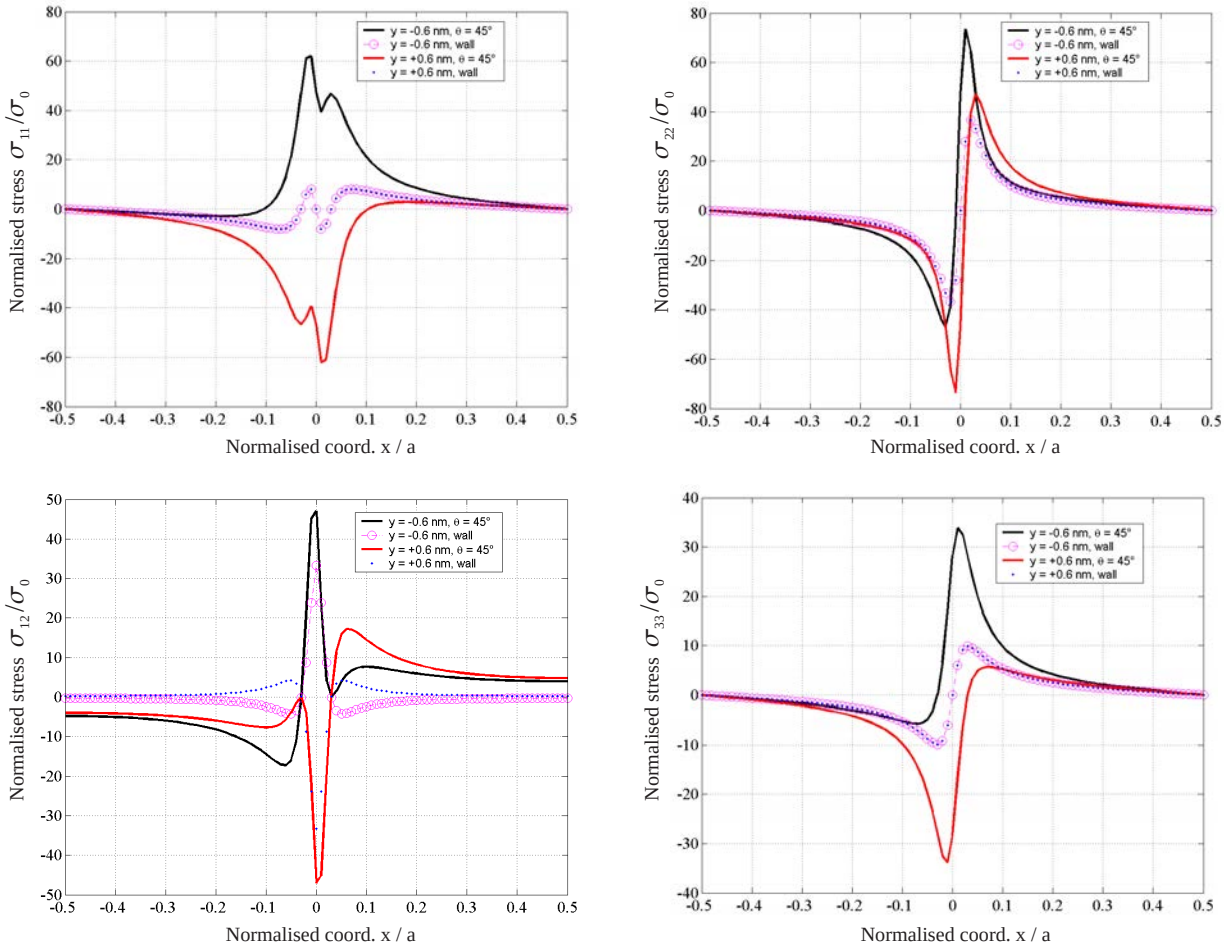

Figure X.13: Calculated stress components for a symmetrical tilt-boundary. The components are plotted for the dislocation line situated in x_1=0. The stress components of the edge dislocation wall are also shown.

The stress field associated with the symmetrical tilt boundary can be derived with Eq. IX.36 and the non-zero components are plotted in Fig. X.13 for an angle θ equal to 45°. For comparison, the non-zero components corresponding to an edge dislocation wall are plotted on the same figure.

It is shown that the normalised stress components of the edge dislocation wall are always lower than the normalised stress components of the symmetrical tilt-boundary with a misorientation of 45°. According to these preliminary results, it seems that the edge dislocation wall is the configuration which minimizes all the stress field in the material.

X.3 High and low energy configurations of dislocations

From the stress fields induced by all configurations studied in this work, the elastic energy contained in such configurations can be calculated. For this purpose and as presented before, the strain tensor for a given dislocation configuration has been calculated by using the law of

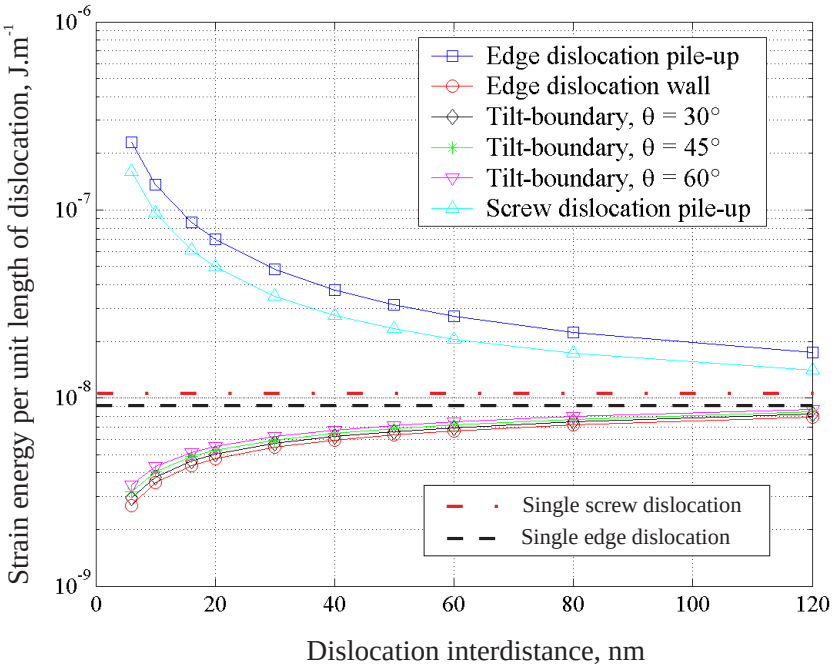

Figure X.14: Elastic energy in a unit cell, per unit length of dislocation. The length of the unit cell along x_2 has been chosen to be constant for all configurations and equal to 320 nm in order to take into account possible long range stresses.

elasticity. The elastic energy is then deduced from the double contracted product of $\underline{\underline{\sigma}}$ and $\underline{\underline{\varepsilon}}$. The elastic energy per unit length of dislocation has been calculated down to the dislocation core radius, below which the assumption of small deformations falls. There does not exist an accurate value for the core radius, which is often set to be greater than or equal to the module of the Burgers vector. In the present work, the dislocation core radius was set to $5\mathring{A}$.

Fig. X.14 shows the variation of the elastic energy contained in a unit cell, as shown in Figs. X.2, X.4, X.10 and X.12, as a function of the interdistance h between the dislocations, for the four configurations studied previously. In the case of the symmetrical tilt-boundary, three different angles have been chosen.

As expected, all cases involving an edge-type dislocation converge towards the solution of a single edge dislocation plotted with the black dash line in Fig. X.14 as the interdistance increases: for an important interdistance, the dislocation does not interact any more with its neighbour, whatever the orientation of the dislocation. This is also the case with the screw dislocation pile-up whose elastic energy is decreasing towards the value referenced by the red dot and dash line and corresponding to the energy of a single screw dislocation, when the interdistance is increasing.

Moreover, in the case of the edge and screw dislocation pile-ups, the energy of a unit cell is always higher than this reference value - whilst the energy of the unit cell is always lower in the case of the edge dislocation wall and tilt-boundaries. To understand this important difference, Fig. X.15 shows, in a simple way, how each stress field can interact with the others. When the interdistance decreases, the compression part of a unit cell is compensated by the

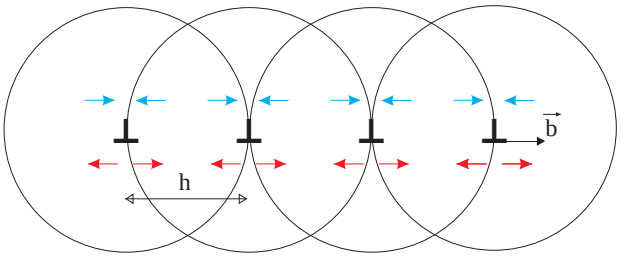

(a) edge dislocation pile-up

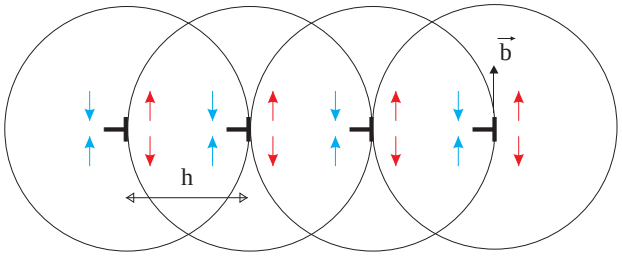

(b) edge dislocation wall

Figure X.15: Simplified representation of tensile and compressive fields in the edge dislocation pile-up and wall configurations.

tension part of its neighbour, in the case of the edge dislocation wall (Fig. X.15(b)). This feature is not observed in the case of the simple pile-up of dislocations, where the stress fields do not compensate but rather add up to those induced by the neighbours (Fig. X.15(a)). From this result, it is clearly shown that some configurations can be considered as high and low energy dislocation structures. The edge and screw dislocation pile-ups are high energy structures, whereas the edge dislocation wall and tilt-boundary are low energy structures. This was already known that pile-up of any dislocation type is not the preferable structure to minimize the elastic energy, but this is clearly shown with the present tool which also enables a direct comparison of the different energies.

The effect of the mis-orientation angle on the elastic energy contained in a unit cell of the symmetrical tilt-boundary is shown in Fig. X.16. It is noticed that for a given interdistance h, the higher the mis-orientation angle, the higher the elastic energy. The minimum of the elastic energy is obtained for the edge dislocation wall, which confirms what was observed in the previous section. According to the configuration in Figs. X.4 and X.12, the edge dislocation wall corresponds to the symmetrical tilt-boundary with a mis-orientation angle equal to zero. It is here important to underline that the mathematical tool developed in this work does not take into account the presence of any coincidence site lattice. A coincidence site lattice (CSL) is a kind of superstructure that develops when, for certain mis-orientation angles, some lattice points of the first lattice (I) coincide exactly with some lattice points of the second lattice (II). This is shown in Fig. X.17 in which a $\Sigma 5$ boundary is illustrated. Σ is by definition the unit cell volume of the CSL in units of the unit cell volume of the elementary

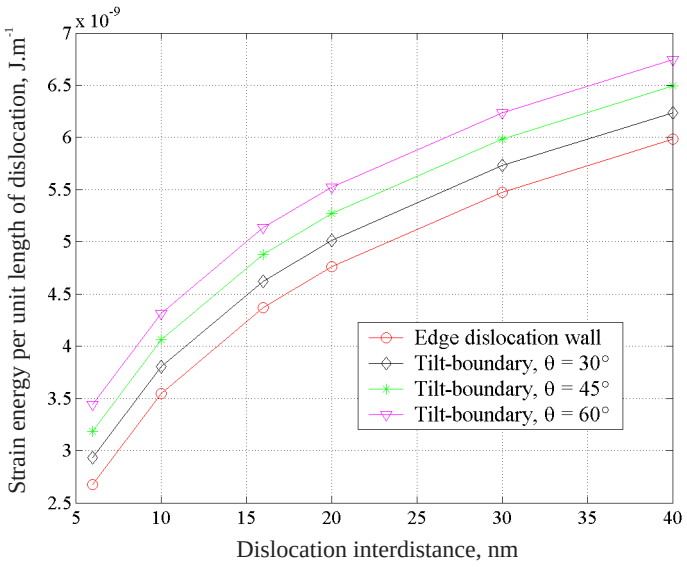

Figure X.16: Comparison of various dislocation configurations.

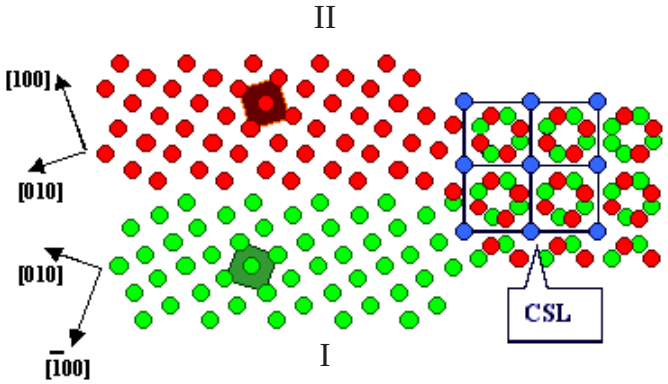

Figure X.17: Example of a coincidence site lattice (in blue).

cells of the crystals, and is more simply calculated as:

$$\Sigma = \frac{A_{CSL}}{A_{crystal}} \tag{X.44}$$

where A_{CSL} and $A_{crystal}$ are the CSL and initial crystal unit cell surfaces, respectively.

It should be emphasized that the tilt-boundary as presented here does not model directly the low-angle sub-grain boundary, as some observed in the HBS (e.g. [100, 118]). In the previous calculations, the values ω and ξ characterising the mis-orientation angle θ were set independently of the interdistance h. In the case of a low-angle grain boundary, there is a relation between the angle Ω seen by two adjacent grains and the distance h between two dislocations with the same Burgers vector in the grain-boundary (Fig. X.18). This relation is given by:

$$\sin\theta = \sin\frac{\Omega}{2} = \frac{b}{h} \tag{X.45}$$

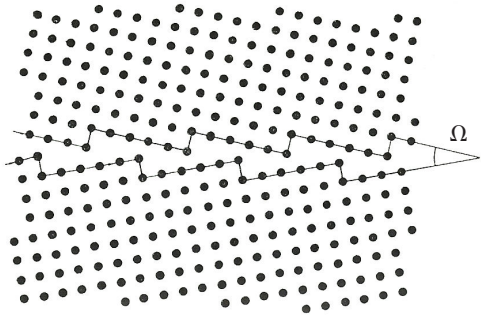

Figure X.18: Lattice representation of a low-angle θ grain-boundary.

By inserting Eq. X.45 in Eq. X.40, it is found that ω and ξ are given by:

$$\begin{cases} \omega = \frac{b}{h} \\ \xi = \sqrt{1 - \left(\frac{b}{h}\right)^2} \end{cases} \tag{X.46}$$

These two coefficients have been inserted in Eq. X.43. The elastic energy of the low-angle grain-boundary has been calculated and is plotted in Fig. X.19, down to very small dislocation interdistance. The elastic energy of the edge dislocation wall is always the lowest, although Fig. X.19 shows that the elastic energy of the low-angle grain-boundary is extremely close. As shown in the inset, the difference is however increasing when the interdistance is reduced. This is explained by the fact that a decreasing interdistance entails an increasing mis-orientation angle (cf Eq. X.45), which means that the stress field compensation between the dislocations is less effective.

Nevertheless, the difference between these two configurations can be neglected, hence the low-angle grain-boundary in Fig. X.18 can be simply represented by the edge dislocation wall in Fig. X.4.

From Fig. X.19, the elastic energy per unit length of dislocation in the case of the new sub-grains in the HBS can be calculated. Ray et al. [100] measured the sub-grain mis-orientation from the diffraction pattern of restructured UO_2 fuel observed by means of TEM to be less than 5°. From Eq. X.45 and Fig. X.19, the interdistance and the elastic energy are deduced: at around 4.5 nm, the energy per unit length of dislocation is $\simeq$2.2 J.m^{-1} for each dislocation in the grain-boundary.

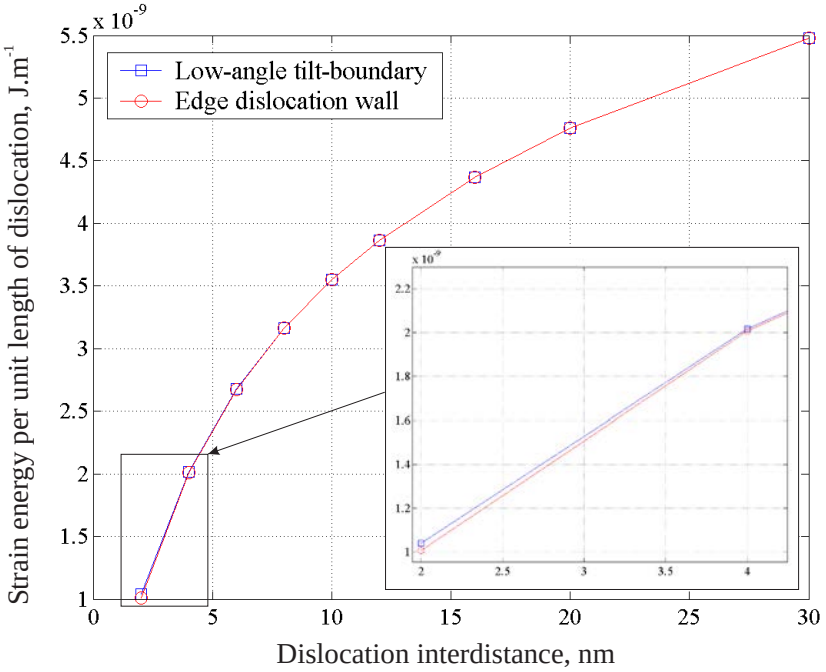

Figure X.19: Elastic energy of the low-angle grain-boundary and the edge dislocation wall.

XI

Summary and conclusions

The formalism of discrete dislocations in a continuum proposed by Kröner [50] has been applied to develop a general tool with which stress distributions associated with all types of periodic dislocation configurations can be analysed. This was impossible with the tools of Cottrell [25], Li [57] and Borisova [17], which are based on the classical theory that only deals with individual dislocations and sums of their stress fields.

In the four configurations studied (edge dislocation pile-up and wall, screw dislocation pile-up and symmetrical tilt-boundary), an analytical expression of the stress function tensor is expressed. The results concerning the edge dislocation pile-up and wall show a perfect agreement with the solutions calculated by Cottrell [25] and Li [57]. The results also underline one of the main strengths of this general tool in that it enables inferring the stress field of periodic configurations of dislocations, based on the solutions calculated for the elementary periodic configurations. In this way, the screw dislocation pile-up and the symmetrical tilt boundary can be easily studied, the resulting stress field in both cases being obtained by a combination of the solutions corresponding to the edge dislocation pile-up and wall.

From the stress fields induced by all configurations studied in this work, a comparison of the elastic energy contained in a unit cell has been examined. It has been concluded that some configurations are qualified as high energy structure, due to an increasing energy with a decreasing interdistance between the dislocations. This is the case of the edge and screw dislocation pile-ups. On the contrary, for the edge dislocation wall and symmetrical tilt-boundary, it has been calculated that the elastic energy is decreasing when the dislocations are closer and closer. These two configurations are therefore called "low energy structures".

The difference between the high and low energy configurations was explained by a compensation (in the case of the low energy configurations) or superposition (in the case of the high energy configurations) of the stress fields of each dislocation in the distribution.

As a general conclusion, the stress distribution can be studied in any isotropic and infinite material with the present tool, as a function of dislocation family, configuration and dislocation density.

Part 4

Radiation damage evolution in UO_2

XII

Introduction

The interstitial-type dislocation loops are considered by many researchers, both theorists (e.g. [23, 11, 103] and experimentalists (e.g. [91, 125]), to play a role in the build-up of the HBS. This was shown in the bibliographic review of the different models developed so far for the onset of the HBS, as presented in chapter VI. It is considered, for instance in [103, 125], that these dislocation loops may grow until saturation is reached when a stable dislocation cell structure is formed. However, the exact mechanisms for the growth of interstitial loops and the subsequent formation of the HBS in irradiated nuclear fuels are still unclear. In most models that take into account the evolution of loops [41, 108, 59], the latter are assumed to grow by trapping single interstitials diffusing in the matrix, and the resulting loop size is not of the same order of magnitude as the observed sub-grain structure of the HBS. Moreover, the role of such interstitial loops in the build-up of new sub-grain boundaries within the material is not clarified. It is also pointed out that these interstitial loops develop in the material during the cooling period after the discharge from the reactor, due to the fuel α-activity.

An analysis of the evolution of interstitial-type dislocation loops in UO_2 submitted to radiation damage is proposed here in order to answer these questions. Nevertheless, since sub-microscopical characterisation of reactor irradiated fuel is very complex, a simpler system reproducing some of the features observed in the HBS, was chosen in the form of UO_2 sintered pellets, doped with $\sim$10 wt% ^{238}Pu and stored for different times, during which α-damage resulting from the decay of ^{238}Pu was produced. By this way, the single effect of interstitial-type dislocation loops can be studied.

In chapter XIII, the fabrication procedure of the α-doped samples is presented. Many experiments have been performed in order to determine the effects of self-irradiation damage produced during the storage time on various properties. The techniques, as well as the experimental results are also presented in chapter XIII. One of the most interesting results is the build-up of the interstitial loop size histograms, obtained for two different storage times. These experimental results constitute the basis of the present study. The question addressed here is: which mechanisms involving the defects produced by the α-decay of the samples can lead to the observed interstitial loop histograms? The knowledge of the mechanisms responsible for the nucleation and growth of interstitial loops in the present self-irradiating samples will contribute to the understanding of the evolution of these defects in UO_2 nuclear fuels under reactor conditions.

For this purpose, a detailed model is being developed and is presented in chapter XIV. Rather than starting from scratch, we chose an existing model which was initially developed to study the nucleation of interstitial loops in irradiated graphite and stainless steel [34], and apply an extended version to nuclear fuel. The set of reaction rate equations enables to consider additional physical phenomena, such as the re-solution process of interstitials back into the matrix due to the impact with a ^{234}U recoil atom (α-decay of ^{238}Pu) and the coalescence of loops which diffuse by surface or volume mechanisms. The theoretical model is presented, the numerical solutions are calculated and a discussion on the role of the mechanisms considered here is proposed.

XIII

Experimental study of α-doped UO_2 samples

Contents

XIII.1 Fabrication of the samples

Pellets of UO_2 containing 0.1 and 10 wt.% of a doping additive consisting mainly of ^{238}Pu were fabricated following the same procedure reported in [117]. Tab. XIII.1 summarizes the specific activity values and the amount of the nuclides in the α-doping oxide. The specific activity value of ^{238}U is also shown for comparison.

Nuclide	Specific Activity (Bq/g metal)	Doping oxide composition (%)
^{238}Pu	6.34×10^{11}	66.7
^{239}Pu	2.30×10^{09}	17.9
^{240}Pu	8.42×10^{09}	3.0
^{241}Pu	3.81×10^{12}	0.1
^{242}Pu	1.45×10^{08}	0.1
^{234}U	2.31×10^{08}	12.1
^{241}Am	1.27×10^{11}	0.1
^{238}U	1.24×10^{04}	

Table XIII.1: Specific activity of the components and composition of the doping powder added to UO_2.

The specific activity of the doping oxide after the fabrication has been calculated to be:

$$A = 3.76 \times 10^{11} \quad \text{Bq/g} \tag{XIII.1}$$

from which the α-activity of the materials were deduced by considering the weight fraction of additive (respectively 0.1 and 10 wt.%):

$$A_{0.1\%} = 3.76 \times 10^{08} \quad \text{Bq/g} \tag{XIII.2}$$
$$A_{10\%} = 3.76 \times 10^{10} \quad \text{Bq/g} \tag{XIII.3}$$

The powders were prepared using a sol-gel method, based on co-precipitation from a nitric acid solution. This method was adopted to ensure an intimate mixing of the doping material with the UO_2 matrix, hence a uniform distribution of the α-activity in the final product. The powders were calcined and then uniaxially pressed into cylindrical pellets. The pressed material was sintered at 1700°C for 8 hours in an $Ar/H_2(6\%)$ atmosphere, obtaining pellets of about 6 mm diameter and 4 mm height, with an average density of 94% of the theoretical value for UO_2 (i.e. 0.94×10.96 g.cm^{-3}).

Two types of specimen were prepared for the experiments: discs, approximately 1 mm thick, cut from the pellets, and crushed materials sieved to obtain 2 different particle size distributions, i.e. smaller and bigger than 125 μm. Before the start of any experiment, the samples were annealed at 1000°C for several hours in the sintering atmosphere, in order to recover damage and alterations caused by the sample preparation procedure and by the α-decays occurring between fabrication and start of the measurements.

XIII.2 Measurement techniques

After the fabrication and at different time intervals, the two α-doped samples have been well characterised in order to monitor the accumulation of α-damage in the materials. The measurement techniques which provide the most important information for the present study are presented here.

Optical microscopy has been used to determine the average grain size of the doped samples, which was also observed on micrographs from SEM examinations.

The build up of α-decay damage in the material was analysed by measuring the lattice parameter change as a function of time (hence of cumulative damage) using X-Ray Diffractometry (XRD). The development of the hardness of the material with time (damage level) was also measured using Vickers indentation.

The oxygen potential of the material was also measured after various time intervals, to monitor the change of the O/M ratio during storage at room temperature in N_2 atmosphere (with $\sim$0.1% O_2). These measurements were performed using a miniaturized galvanic cell under vacuum in a furnace placed in a glove box with a N_2 atmosphere. This cell has been used in previous work to determine the oxygen potential of irradiated fuel, both UO_2-based [76] and (U,Pu)O_2 [69] up to high burn-up values. The specimen is inside a Y_2O_3-doped ThO_2 crucible which acts as electrolyte. The crucible is closed with a Pt lid under pressure. The Pt lid is in contact with the specimen. The Pt wires of a Pt/Pt-l0% Rh thermocouple provide the electrical contacts to the reference electrode and to the Pt lid.

Transmission electron microscopy (TEM) has been performed in order to observe the evolution of the microstructure during the storage time at room temperature.

XIII.3 Experimental results

XIII.3.1 SEM examinations

The mean grain diameter of the sintered material doped with 10 wt.% in ^{238}Pu was measured to vary between 4 and 6 μm. The typical grain structure is shown on the SEM micrographs in Fig. XIII.1. This figure shows the grain-boundaries which were thermally etched (Fig. XIII.1(a)) and grain-boundaries appearing on a transgranular fracture (Fig. XIII.1(b)).

XIII.3.2 Lattice parameter evolution

An overall measurable effect of the α-decays in the material is the increase of the lattice parameter. Fig. XIII.2 shows the results of the XRD measurements for the ($U_{0.9}$, $Pu_{0.1}$)O_2 sample. The absolute values and the fractional variation of the lattice parameter (respectively, on the left and right vertical axes) are plotted as a function of time. The measurements were started 10 hours after annealing, i.e. with essentially no initial damage. The evolution with time of the α-decay for ^{238}Pu is also shown. The expected initial lattice parameter value was calculated assuming that each fluorite type phase (i.e. UO_2 and PuO_2) contributes pro-

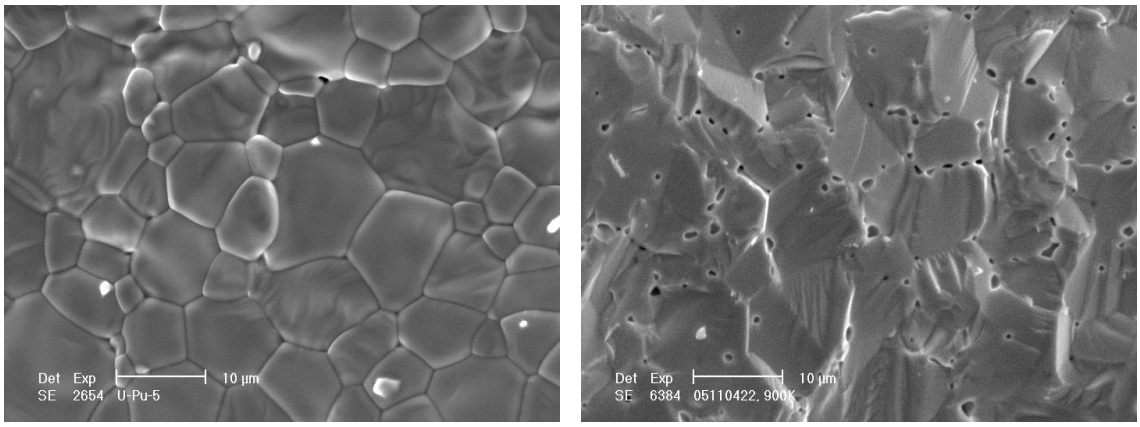

(a) (b)

Figure XIII.1: SEM micrographs of the fabricated $(U_{0.9}, Pu_{0.1})O_2$ sample showing (a) grain-boundaries thermally etched, and (b) a transgranular fracture.

portionally to its concentration to the resulting lattice parameter. The experimental results show an increase of the lattice parameter with time (corresponding to increasing damage). After approximately 2 months, the lattice parameter value had increased by ∼0.25%, similar to reported UO_2 values [145, 70]. The saturation level of the lattice parameter increase for different actinide oxides subject to α-decay is between ∼0.23% and ∼0.35% (see e.g. [30]; for $^{238}PuO_2$ it is ∼0.28% [89]). The 0.1 wt. % UO_2 sample did not show, during the same time interval, appreciable variations of the lattice parameter. This was expected because of the one hundred-fold lower decay rate.

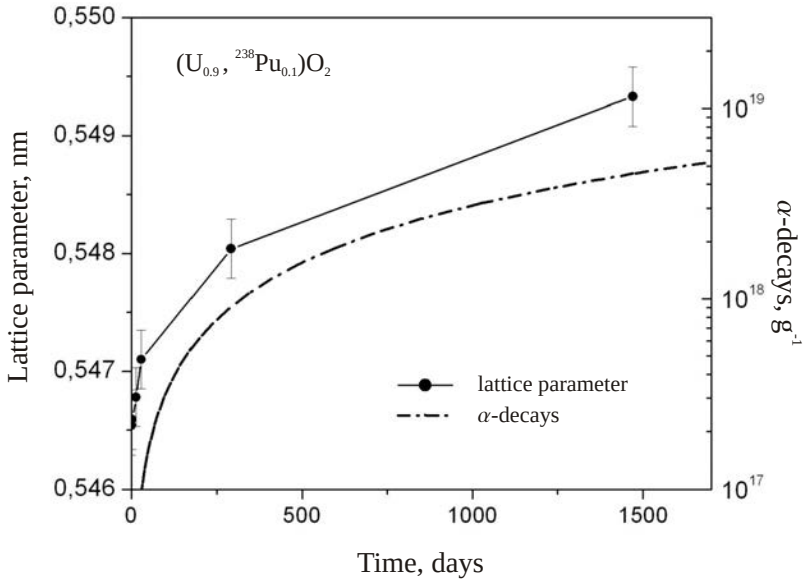

Figure XIII.2: Lattice parameter changes as a function of time [24]. The α-decay evolution with time for ^{238}Pu is also shown.

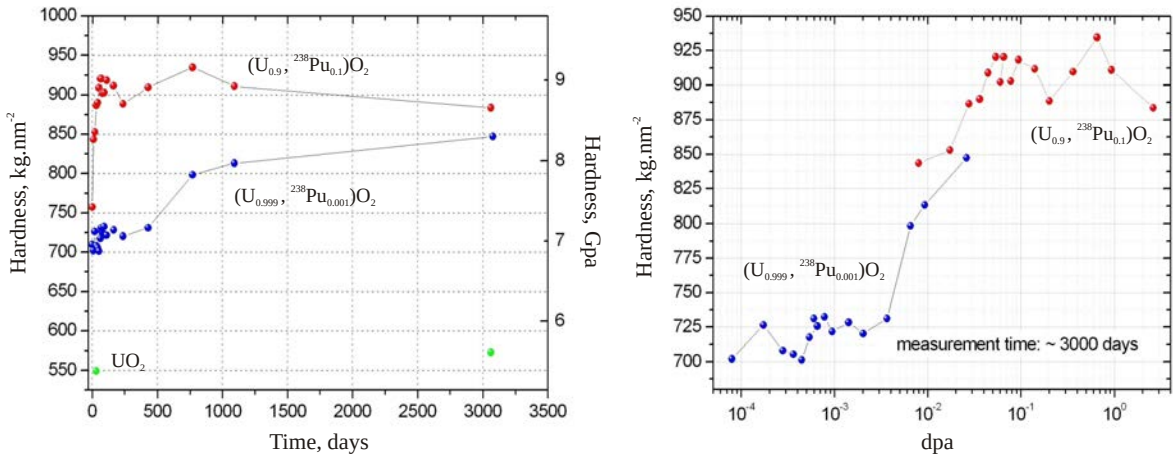

Figure XIII.3: Vickers hardness as a function of time (a), and dpa (b), for the $(U_{0.9}, Pu_{0.1})O_2$ and $(U_{0.999}, Pu_{0.001})O_2$ materials [24].

The α-decay dose accumulated in the $(U_{0.9}, Pu_{0.1})O_2$ sample during six months is 5.3×10^{17} g^{-1}. Each α-particle - of 5.499 MeV energy - creates in average 66 U displacements (displacement energy threshold 40 eV) and 140 O displacements (displacement energy threshold 20 eV), whilst the ^{234}U recoil atom (92 KeV) creates 295 U and 1180 O displacements, according to TRIM [149] code predictions. If no damage overlapping or recombination is considered, the total defect concentrations are 1.9×10^{20} g^{-1} for uranium and 7×10^{20} g^{-1} for oxygen Frenkel pairs. In fact, only a small fraction of damage is effectively present as point defects at these doses. The majority either recombine or interact with other defects to form less energetic extended configurations. With a UO_2 atomic density of 6.7×10^{21} atoms.g^{-1}, the dpa value is finally found to be 1.1 for the 4 year-old sample, and 2 for the 7 year-old one.

XIII.3.3 Vickers hardness

A behavior similar to that observed with the XRD was found by performing periodically repeated Vickers hardness measurements. The results are shown in Fig. XIII.3. While the $(U_{0.999}, Pu_{0.001})O_2$ did not show significant variations of the hardness during the first 250 days, the values measured for $(U_{0.9}, Pu_{0.1})O_2$ increased, and after approximately the same period appeared to have reached a maximum value, corresponding to an increase of hardness of ∼20% (Fig. XIII.3(a)). Despite the up and down behavior of the hardness measured for the $(U_{0.9}, Pu_{0.1})O_2$ sample, the hardness seems to have reached a maximum value after the two first years, then decreasing to an asymptotic level which is not yet determined. Fig. XIII.3(b) shows the same results as Fig. XIII.3(a), but the hardness is plotted as a function of the displacement per atom (dpa). It is shown that the hardness of the $(U_{0.999}, Pu_{0.001})O_2$ sample tends to join the hardness of the $(U_{0.9}, Pu_{0.1})O_2$ sample, but at longer time due to the one hundred-fold lower decay rate.

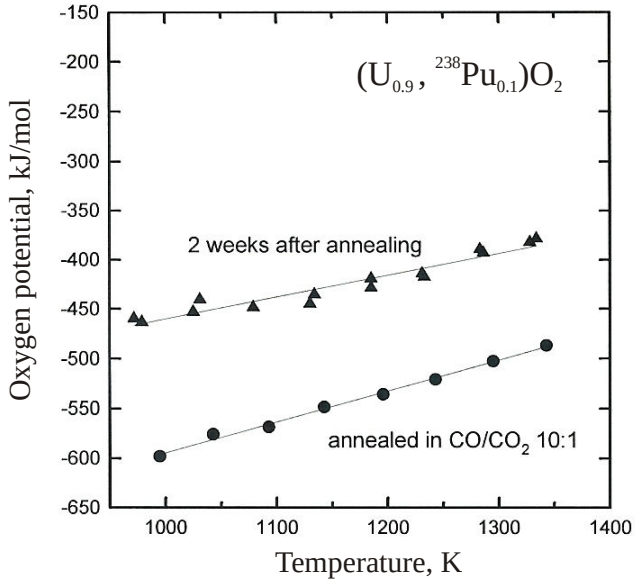

Figure XIII.4: Oxygen potential of the $(U_{0.9},Pu_{0.1})O_2$ sample as a function of temperature, measured immediately after annealing and 2 weeks after [114].

XIII.3.4 Oxygen potential

Fig. XIII.4 shows the results of the oxygen potential measurements. The data for the annealed sample show the condition of the material at the start of each test and correspond to stoichiometric (U,Pu)O_2. After 2 weeks storage under N_2 atmosphere (containing ∼0.1% of O_2), the potential of the material increased slightly. This indicates some small oxidation.

XIII.3.5 TEM examinations

Fragments of a few milligrams of the original $(U_{0.9},Pu_{0.1})O_2$ pellets were crushed in ethanol. The resulting suspension was dropped on a copper grid filmed with carbon. The TEM used in this study is a Hitachi H700 HST operating at 200 kV and modified to handle radioactive materials. More details can be found in [1] in the chapter on Nuclear Materials.

The examinations were carried out on samples of two different ages (i.e. two different damage levels) corresponding to a storage time of 4 and 7 years after fabrication. Fig. XIII.5 shows two bright field pictures of the sample after 4 and 7 years respectively.

The main defect that was observed on both specimens consists of interstitial-type dislocation loops, as the ones simulated by Marian et al. [68] in α-Fe and shown in Fig. XIII.6. The interstitial loops are homogeneously distributed within the material. From 1.1 dpa (4 years) to 2 dpa (7 years), it can be noticed that the loops size has slightly increased and that their overall concentration has increased as well. The dislocation loop size and density has been determined by manual image analysis. The loop size distributions are shown in Fig. XIII.7.

In order to enable a comprehensive comparison with the numerical results in chapter XIV, the experimental distributions are described in terms of statistical values, more precisely the

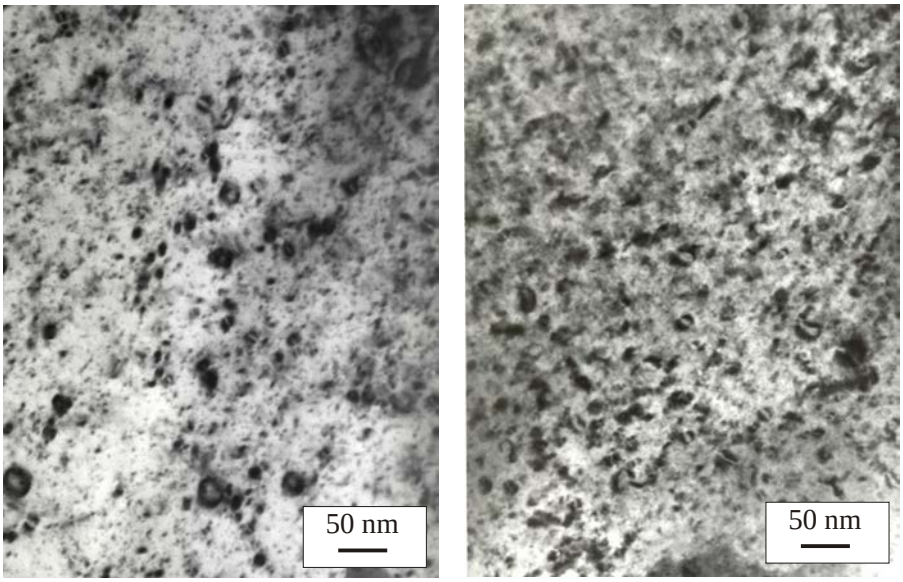

Figure XIII.5: TEM bright field image evidencing the formation of dislocation loops at t=4 years (a) and t=7 years (b), respectively, in the $(U_{0.9},Pu_{0.1})O_2$ sample [38].

first four moments: the loop mean radius, standard deviation, skewness and kurtosis. The mean radius $\bar{r}$ of the interstitial loops of radius r_n with a density c_{ni} is calculated as follows:

$$\bar{r} = \frac{1}{N} \sum_n c_{ni} r_n \tag{XIII.4}$$

where n is the number of size classes in the histogram and

$$N = \sum_n c_{ni} \tag{XIII.5}$$

is the total concentration of loops.

The standard deviation σ represents the "width" or "variability" around the mean value and is calculated as the square root of the variance:

$$\sigma^2 = \frac{1}{N} \sum_n c_{ni} \left(r_n - \bar{r}\right)^2 \tag{XIII.6}$$

The variance is known as the second moment $\sigma^2 = \mu_2$, which is used to calculate the successive moments, and especially the skewness. The skewness (nondimensional quantity) characterizes the degree of asymmetry of a distribution around its mean. The usual definition is [97]:

$$\alpha_3 = \frac{1}{N} \sum_n c_{ni} \left(\frac{r_n - \bar{r}}{\sigma}\right)^3 \tag{XIII.7}$$

Finally, the fourth moment of the size distribution or the kurtosis is calculated. The kurtosis is also a nondimensional quantity and measures the relative peakedness of flatness of a

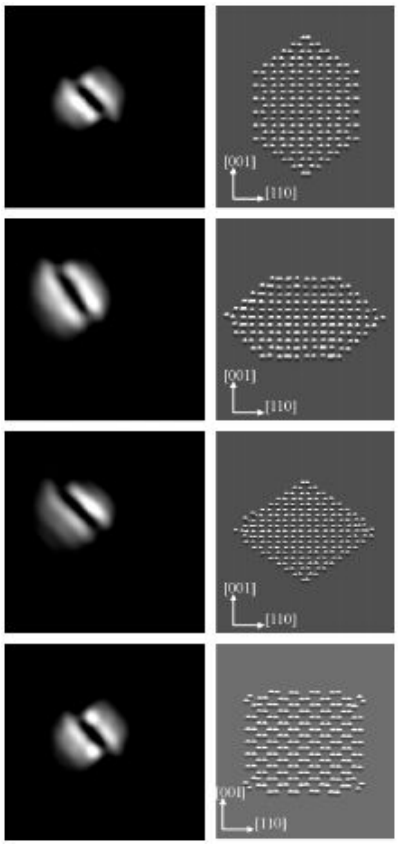

Figure XIII.6: Simulated images (left) of <100>{110} loops with different sizes and shapes (right) in α-Fe. The atomic configurations on the right are viewed from a $[1\bar{1}0]$ direction [68].

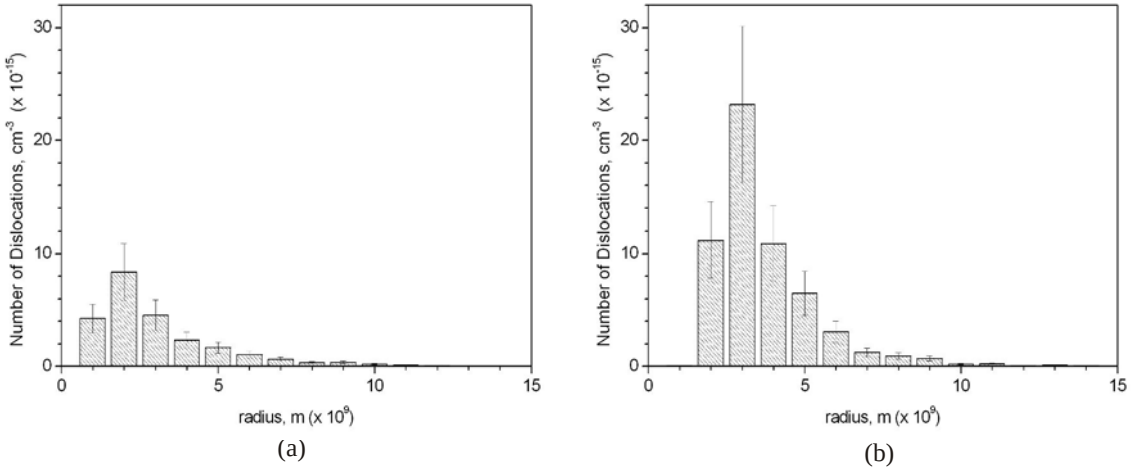

Figure XIII.7: Loop size histograms from the $(U_{0.9},Pu_{0.1})O_2$ sample observed at t=4 years (a) and t=7 years (b), respectively [38].

	4 years old	7 years old
Loop mean radius	3.05 nm	3.71 nm
Standard deviation	2.03 nm	1.69 nm
Modal value	2 nm	3 nm
Corresponding loop density	8×10^{15} cm^{-3} $\pm$ 3×10^{15} cm^{-3}	23×10^{15} cm^{-3} $\pm$ 6×10^{15} cm^{-3}
Skewness	1.65	2.04
Normalised kurtosis	3.01	6.34

Table XIII.2: Statistical values of the experimental distributions

distribution. The conventional definition of the kurtosis is:

$$\alpha_4 = \frac{1}{N}\sum_n c_{ni}\left(\frac{r_n - \bar{r}}{\sigma}\right)^4 \tag{XIII.8}$$

The normalised kurtosis is more used:

$$\gamma = \alpha_4 - 3 \tag{XIII.9}$$

where the "-3" term creates the zero value for a normal distribution. A distribution with positive normalised kurtosis is termed *leptokurtic*, whereas a distribution with negative normalised kurtosis is termed *platykurtic*. Tab. XIII.2 shows the results calculated from the experimental distributions of Figs. XIII.7. A shift of 1 nm in size is observed for the class of the main population (from 2 to 3 nm). According to the histograms in Fig. XIII.7, the other classes remain close to the same value. In addition, the skewness of the distribution is more and more perceptible, which is confirmed by the calculated values.

An experimental uncertainty of 30% is reported on the loop size histograms in Fig. XIII.7. This large uncertainty originates from the determination of the sample thickness. The latter was similar for both specimens, but could not be determined accurately (no thickness fringes could be observed) since it had to be deduced from other contast features. The thickness used for the image analysis was 100 nm, with an error estimated to be 30%. It should be pointed out that applying a constant percentage error on all loop size classes do not modify the values of the first four moments, hence the shape of the histograms. Only the interstitial loop density of the modal value is modified, as indicated in Tab. XIII.2.

XIV

Modelling the evolution of defects in α-doped UO_2

Contents

XIV.1 Introduction

The homogeneous nucleation of any precipitated defect results in a distribution of sizes [34]. In the case of the (U,Pu)O_2 sample, the nucleation and growth of the interstitial-type dislocation loops occurs due to the continuous production of point defects, especially the uranium interstitials, resulting from the α-decay of ^{238}Pu. Once created, the fate of an interstitial may be any of the following:

- recombination with a vacancy or a vacancy cluster.
- trapping by another interstitial, forming a di-interstitial which is assumed to be the nucleus of dislocation loops.
- trapping by grain boundaries.
- trapping by the periphery of an existing dislocation loop, causing the latter to grow.
- survive all previous considered trapping centers.

A differential growth rate between loops of different size leads to a net rate of increase in the concentration of loops in the size range r to $r + dr$ given by:

$$\left[\frac{\partial n(r,t)}{\partial t}\right] dr = -\frac{\partial}{\partial r}\left[n(r,t)\frac{dr}{dt}\right] dr \tag{XIV.1}$$

An analytical solution to Eq. XIV.1 can only be found in particular cases. Among them, Speight [121] calculated the size distribution in irradiated UO_2 of a steady-state population of bubbles subjected to the re-solution into the matrix of gas atoms by fission fragments. However, the main assumption of his study can not be fulfilled, especially since steady-state has not been experimentally observed in the samples under consideration.

Brown [21] proposed a particular solution of Eq. XIV.1 in the case where the net growth rate of dislocation loops does not depend on their size. The solution is the following:

$$n(\mathbf{r},t)\,\Delta r = n_0(t-\tau) \tag{XIV.2}$$

where $\mathbf{r} = r(t) - r(t-\tau)$, n_0 is the di-interstitial loop concentration and Δr is the radius increment corresponding to the addition of one interstitial to a di-interstitial loop. Brown calculated the loop size distribution to be very narrow (very low variance) and with a high negative skewness. Despite his method being very simple to derive a size distribution from the only values $r(t)$ and $n_0(t)$, size-dependent phenomena can not be accounted for with his model.

For non-steady state conditions, the only possibility to solve Eq. XIV.1 is to use numerical methods in order to solve an equivalent system of equations. These equations are based on the chemical rate theory in which the reaction rate constants correspond to the sinks of the real microstructure [18], as outlined in the next sections.

XIV.2 A comprehensive model of defects in α-doped UO_2

XIV.2.1 Initial set of equations

Hayns [34] proposed a set of linear first-order differential equations describing the nucleation and growth of a dislocation loop distribution in irradiated graphite and steel. In this model, the whole size distribution can be calculated as the model consists of a rate-equation for each loop size increment (corresponding to the addition of one interstitial to an existing loop). These equations are as follows:

$$\frac{dc_v(t)}{dt} = K - \alpha_r\, c_v(t)c_i(t) - \sum_{n=2}^{neq} L_n\, c_{ni}(t)c_v(t) - D_v\, \rho_d\, c_v(t) \quad \text{(XIV.3)}$$

$$\frac{dc_i(t)}{dt} = K - \alpha_r\, c_v(t)c_i(t) - K_2\, c_i(t)c_i(t) - \sum_{n=2}^{neq-1} R_n\, c_{ni}(t)c_i(t) + L_2\, c_{2i}(t)c_v(t) - D_i\, \rho_d\, c_i(t) \quad \text{(XIV.4)}$$

$$\frac{dc_{2i}(t)}{dt} = \frac{1}{2}K_2\, c_i(t)c_i(t) + L_3\, c_{3i}(t)c_v(t) - L_2\, c_{2i}(t)c_v(t) - R_2\, c_{2i}(t)c_i(t) \quad \text{(XIV.5)}$$

$$\frac{dc_{3i}(t)}{dt} = R_2\, c_{2i}(t)c_i(t) + L_4\, c_{4i}(t)c_v(t) - R_3\, c_{3i}(t)c_i(t) - L_3\, c_{3i}(t)c_v(t) \quad \text{(XIV.6)}$$

$$\cdots$$

$$\frac{dc_{ni}(t)}{dt} = R_{n-1}\, c_{(n-1)i}(t)c_i(t) + L_{n+1}\, c_{(n+1)i}(t)c_v(t) - R_n\, c_{ni}(t)c_i(t) - L_n\, c_{ni}(t)c_v(t) \quad \text{(XIV.7)}$$

$$\cdots$$

$$\frac{dc_{neqi}(t)}{dt} = R_{neq-1}\, c_{(neq-1)i}(t)c_i(t) - L_{neq}\, c_{neqi}(t)c_v(t) \quad \text{(XIV.8)}$$

In the above equations, c_v, c_i and c_{ni} are the concentrations of vacancies, intertitials and dislocation loops containing n interstitials, respectively; K is the damage rate considered to be constant as previously; α_r the interstitial-vacancy recombination coefficient; K_2 is the rate constant for the production of di-interstitials (interstitial loop nucleus); D_v and D_i are the vacancy and interstitial diffusivities; ρ_d is the density of pre-existing dislocations, neglected in our analysis as almost no dislocation line was observed by means of TEM in the samples studied. L_n and R_n are the reaction rate constants of a loop containing n atoms with a vacancy and interstitial, respectively. neq is the number of equations of the system, which corresponds to the maximum number of interstitials involved in a loop. The rate constants R_n and L_n are defined by [34]:

$$R_n = z_i\, D_i \left(\frac{2\pi}{\Omega}\right) \sqrt{\frac{n\, c_{cell}^2}{\pi}} \quad \text{(XIV.9)}$$

$$L_n = z_v\, D_v \left(\frac{2\pi}{\Omega}\right) \sqrt{\frac{n\, c_{cell}^2}{\pi}} \quad \text{(XIV.10)}$$

where c_{cell}^2 is the area per "atom" in a loop. On the assumption that interstitial-type dislocation loops have formed in the (110) planes, the size c_{cell} of a UO_2 Schottky trio - in order

to keep the electrical neutrality of the material - was simply calculated as:

$$c_{cell}^2 = (2\, d_{O-O})\, d_{U-U} \tag{XIV.11}$$

where d_{O-O} and d_{U-U} are the oxygen-oxygen and uranium-uranium distances, respectively [31].

The temperature dependence of c_v and c_i is contained in the interstitial and vacancy diffusivities. These diffusivities are expressed as [108]:

$$D_v = x_i^2\, a^2\, \nu_v \exp\left(-\epsilon_{vm}/kT\right) \tag{XIV.12}$$

$$D_i = \frac{2}{3} x_i^2\, a^2\, \nu_i \exp\left(-\epsilon_{im}/kT\right) \tag{XIV.13}$$

where the ratio 2/3 between the uranium interstitial and vacancy diffusivities comes from the difference in the number of stable nearest neighbour sites, ϵ_{vm} and ϵ_{im} are the vacancy and interstitial migration enthalpies, respectively. ν_v and ν_i are the vacancy and interstitial jump frequencies, a is the lattice parameter and x_i is a factor that takes into account the deviation from stoichiometry. x_i^2 has been estimated to be in the range 10^{-2} - 1 [58].

Tab. XIV.1 shows the values of the various parameters used in the solution of Eqs. (XIV.3-XIV.8). Not all parameters used in the present model are shown in Tab. XIV.1, due to an

Parameter	Value	Reference
ν_v	5×10^{13} s^{-1}	[108, 109]
ν_i	5×10^{12} s^{-1}	[108, 109]
ϵ_{vm}	2.4 eV	[139, 108, 109]
z_v	1.0	[108, 109]
z_i	1.0005	[108, 109]
a	5.47 $\AA$ (UO_2)	[46]
b_v	$a\sqrt{2}/2$	[46]

Table XIV.1: Values of various parameters used in the calculation for the α-doped UO_2 material.

uncertainty on their exact value. This is the case of x_i^2 and ϵ_{im}. For this reason, their impact on the simulated results will be rather analysed with a sensitivity technique.

XIV.2.2 Re-solution of interstitials from dislocation loops

In addition to the processes presented above, it is considered in the present study that the existing dislocation loops may be subjected to re-solution of their interstitials back into the matrix due to the impact of a ^{234}U recoil atom as illustrated in Fig. XIV.1. In order to take into account this phenomenon, Eq. XIV.4 for the interstitial concentration in the matrix and the generic Eq. XIV.7 for the concentration of (n)-interstitial loops are replaced by

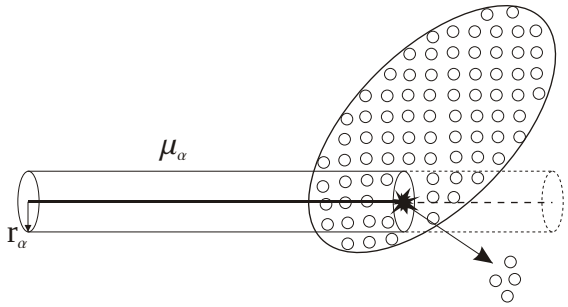

Figure XIV.1: Re-solution of interstitials from a loop back into the matrix.

Eqs. XIV.14 and XIV.15 respectively:

$$\begin{aligned}\frac{dc_i(t)}{dt} &= K - \alpha_r\, c_v(t)c_i(t) - \sum_{n=2}^{n_{eq}} R_n\, c_{ni}(t)c_i(t) + L_2\, c_{2i}(t)c_v(t) \\ &\quad + \sum_{n=2}^{n_{eq}} c_n(t)F\,\mu_\alpha\,(n)\,c_{cell}^2\, min(n, n_\alpha) \qquad \text{(XIV.14)}\\ \frac{dc_{ni}(t)}{dt} &= R_{n-1}\, c_{(n-1)i}(t)c_i(t) + L_{n+1}\, c_{(n+1)i}(t)c_v(t) \\ &\quad - R_n\, c_{ni}(t)c_i(t) - L_n\, c_{ni}(t)c_v(t) \\ &\quad + c_{(n+n_\alpha)i}(t)F\,\mu_\alpha\,(n+n_\alpha)\,c_{cell}^2 - c_{ni}(t)F\,\mu_\alpha\,(n)\,c_{cell}^2 \qquad \text{(XIV.15)}\end{aligned}$$

The additional summation in the right-hand side of Eq. XIV.14 is the sum of all interstitials that were driven back into the matrix. The fifth term in the right-hand side of Eq. XIV.15 represents the creation of a (n)-interstitial loop from a $(n+n_\alpha)$-interstitial loop which has lost n_α interstitials after impact with a recoil atom. The parameter n_α is estimated as follows: each α-particle - of 5.499 MeV energy - creates in average 66 U displacements (displacement energy threshold 40 eV) and 140 O displacements (displacement energy threshold 20 eV), whilst the ^{234}U recoil atom (92 KeV) creates 295 U and 1180 O displacements [149]. If only the number of displacements created by the recoil atom is taken into account, the volume for which the probability that a loop of radius r_α is totally destroyed is equal to 1, is given by:

$$\frac{295\, V_U + 1180\, V_O}{N_A} = \mu_\alpha\, \pi\, r_\alpha^2 \qquad \text{(XIV.16)}$$

where V_U and V_O are the molar volumes of the uranium and oxygen atoms, respectively. N_A is the Avogadro constant. The number of interstitials driven back into the matrix therefore reads:

$$n_\alpha = \lfloor \frac{\pi r_\alpha^2}{c_{cell}^2} \rfloor \qquad \text{(XIV.17)}$$

where $\lfloor x \rfloor$ is the floor function, also called the greatest integer function, and gives the largest integer less than or equal to x.

XIV.2.3 Coalescence of diffusing dislocation loops

The coarsening mechanisms of inert gas bubbles in irradiated materials are known to have important effects on the bubble size distribution. The two main mechanisms usually consid-

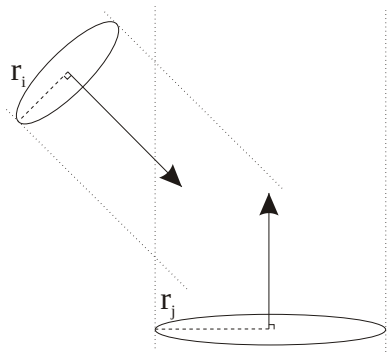

Figure XIV.2: Coalescence of two loops of different radius, diffusing along one of the (110) planes. The resulting loop is assumed to be cylindrical.

ered are the migration and coalescence (M&C), and the Ostwald ripening (OR), i.e. cavities or precipitates grow at the expense of the smaller ones due to concentration gradients in the matrix (diffusional solute segregation). It is here suggested to extend this concept to interstitial-type dislocation loops. The latter are crystal defects that can be subjected to these coarsening mechanisms, just like bubbles, although their diffusion in the matrix are dependent on their crystallographic formation plane. Moreover, the experimental loop size distributions in Fig. XIII.7 show a sknewness typical for a coarsening mechanism. Asymmetric size distributions with positive skewness (tail oriented towards larger sizes), as observed in Fig. XIII.7, constitutes a sign of coarsening process governed by migration and coalescence [128]. The other important coarsening mechanism (Ostwald ripening) usually leads to size distributions with negative skewness (asymmetric tail oriented to smaller sizes).

Migration and coarsening of self-interstitial atom loops has been and is still under investigation in neutron-irradiated metals, due to their importance in materials for fusion reactors. The tool used to study the nucleation and growth of interstitial loops at atomic scale is the molecular dynamics technique. This technique enables to study the detailed structure and shape (assumed to be cylindrical in the present study) of interstitial loops [68] as well as their interactions [67].

In the following it is assumed that the interstitial loops are able to move in the absence of temperature or stress gradients, along the normal of their cylindrical plane as shown in Fig. XIV.2. The aim of this study is to understand the mechanisms involved in the growth of interstitial dislocation loops. The adopted technique using the chemical rate theory is very efficient to consider additional phenomena in the initial set of equations but cannot reproduce the exact shape of loops and their various interactions (see e.g. [67]). As a consequence, it is assumed that whenever two loops are coalescing together, the resulting loop is a cylindrical disc as well.

The generic Eq. XIV.7 for the concentration of (n)-interstitial loops contains two more terms:

$$\begin{aligned}\frac{dc_{ni}(t)}{dt} &= R_{n-1}\, c_{(n-1)i}(t)c_i(t) + L_{n+1}\, c_{(n+1)i}(t)c_v(t) \\ &\quad -R_n\, c_{ni}(t)c_i(t) - L_n\, c_{ni}(t)c_v(t) \\ &\quad +\sum_{j=2}^{n} W_{j,n-j}(t) - \sum_{j=2}^{neq-1} W_{n,j}(t)\end{aligned} \tag{XIV.18}$$

where

$$W_{n,j}(t) = \frac{8(r_n + r_j)(D_n + D_j)}{\Omega}\left[1 + \frac{r_n + r_j}{\sqrt{\pi(D_n + D_j)t}}\right] c_{ni}(t)\, c_{ji}(t) \tag{XIV.19}$$

is the rate of collisions between loops with radii r_n and r_j. The second term between brackets in Eq. XIV.19 can be neglected when migration distance between collisions is large compared to loop radii. The first summation in Eq. XIV.18 represents the creation of a loop containing (n)-interstitials from a $(n-j)$-interstitial loop colliding with a (j)-interstitial loop. The second summation is the loss of (n)-interstitial loops which have collided with any other loop.

The surface diffusion of dislocation loops in the matrix is considered first. For this purpose, the expressions for the atomic mechanism of bubble motion due to surface diffusion [93] have been derived and applied to the case of interstitial-type dislocation loops. The macroscopic parameter describing this process is the surface diffusion coefficient D_s which is related to the parameters characterising the molecular motion by the Einstein equation:

$$D_s = \frac{\lambda_s^2 \Gamma_s}{4} \tag{XIV.20}$$

where λ_s is the jump distance on the solid surface and Γ_s is the total jump frequency of an atom on the surface. The dislocation loop executes motion in the same direction as the diffusing atoms if the loop is assumed to diffuse along the normal direction of its formation plane of family (110):

$$D_l = \frac{\lambda_l^2 \Gamma_l}{4} \tag{XIV.21}$$

where λ_l and Γ_l are the jump distance and jump frequency of the loop, respectively.

The jump distance of a loop is the displacement of the loop which occurs when one atom on its surface moves a distance λ_s. This quantity has been derived for spherical bubbles (see e.g. [32]) and Olander [93] showed how the same result could be obtained by considering a cubical bubble. From this, the calculation for a disc-shaped dislocation loop leads to a jump distance of a loop of radius r_n given by:

$$\lambda_l = \left(\frac{\Omega}{\pi b r_n^2}\right) \lambda_s \tag{XIV.22}$$

The loop jump frequency is the rate at which all atoms on the inner surface of the loop hop. If the area occupied by a surface atom is approximated by c_{cell}^2, the number of molecules on

the inner surface of a loop of radius r_n is $2\pi r_n^2/c_{cell}^2$. Since each of these molecules jumps Γ_s times a second, the frequency of the discrete loop jumps is:

$$\Gamma_l = \left(\frac{2\pi r_n^2}{c_{cell}^2}\right)\Gamma_s \tag{XIV.23}$$

As a consequence, by combining Eqs. XIV.20-XIV.23 the surface diffusion coefficient of an interstitial-type loop with radius r_n reads:

$$D_l^{surface} = \frac{\Omega^2}{\pi r_n^2 b^2 c_{cell}^2} D_s \tag{XIV.24}$$

which can be reasonnably approximated by:

$$D_l^{surface} \simeq \frac{2a^2}{\pi r_n^2} D_s \tag{XIV.25}$$

where D_s is the surface self-diffusion coefficient of UO_2.

The volume diffusion mechanism is also considered to be important in the migration and coalescence of extended defects, especially in materials subjected to a continuous defect production. In this case, the loop jump frequency is now calculated by using the expression in [93] as:

$$\Gamma_l = \left(\frac{2\pi r_n^2}{a^4}\right) D_i \tag{XIV.26}$$

The loop jump distance also reads:

$$\lambda_l = \left(\frac{\Omega}{\pi b r_n^2}\right)\left(\overline{\lambda_i^2}\right)^{1/2} \tag{XIV.27}$$

The characteristic distance required on the right-hand side of Eq XIV.27 is the root-mean-square distance between the point on the surface where an interstitial enters the solid and the point on the surface where it is recaptured by the loop. As a first approximation, $\overline{\lambda_i^2}$ is calculated as $\overline{\lambda_i^2} \simeq r_n a$ (a corresponds to the minimum distance and r_n to the maximum distance). By using the relation between the Burgers' vector length and the lattice parameter in UO_2 ($b = a\sqrt{2}/2$), the volume diffusion coefficient of a loop of radius r_n is:

$$D_l^{volume} \simeq \frac{a}{\pi r_n} D_i \tag{XIV.28}$$

XIV.3 Numerical results and discussion

XIV.3.1 Integration method

The numerical integration of Eqs. XIV.3-XIV.7 has been achieved by a classical forward Euler method:

$$y_{n+1} = y_n + h\, f\,(t_n;\, y_n) \tag{XIV.29}$$

which advances a solution from t_n to $t_{n+1} = t_n + \Delta t$, where Δt is the time-step. Even though this procedure is very economical in terms of computing time and storage, the solution of a

very large number of equations can be costly. As an example, some values are calculated as follows and given in Tab. XIV.2: c_{ni} being the concentration of loops containing n interstitials, the radius of such an interstitial loop can be calculated by using Eq. XIV.17 and replacing r_α by the required radius. Eq. XIV.17 shows that the number of interstitials in a loop is not

Number of equations	Simulated loop radius (nm)
100	∼2.6
200	∼3.7
500	∼5.8
1000	∼8.2
2000	∼11.6
4000	∼16.4

Table XIV.2: Number of equations needed to simulate a given interstitial loop radius.

a linear function of the radius, but is a square root function. As a consequence, more and more equations are necessary to simulate a small radius increment. This problem has been alleviated to a certain extend by optimizing the number of operations in various calculation loops by allowing the number of equations to vary with time. However, even if Eq. XIV.15 for the re-solution process does not introduce so much additional computing time, Eq. XIV.18 for the coalescence of two loops of different radii is more problematic. In particular, the calculation of the two summations in Eq. XIV.18 is extremely costly. As a consequence, the computing time to simulate the 4 and 7 years storage times ranges between a few hours and a few months, and not all solutions could be calculated up to the 7 years storage time (cf below).

The forward Euler method, like any explicit method, is very easy to implement in a fortran code for solving ODEs (Ordinary Differential Equations). The computation of the successive iterations does not require the handling of matrices to be decomposed and inversed, which is typical of implicit methods. The fortran code developed in this work is presented in appendix C. However, contrary to the implicit ones, the explicit methods are not absolutely stable (a-stable), which means that for a given time step, the calculated solution may diverge from the exact solution. Fig. XIV.3 shows a typical solution of the set of equations, calculated for both storage times (4 and 7 years) at different time steps. It is shown that there is no important variation in the solution when varying the time step from Δt=1 s to 20 s, which represents the range used in the present work.

XIV.3.2 Calculation of the interstitial loop size distribution and parameter analysis

The aim of this section is to study the effect of the remaining independent parameters which were not yet set in Eq. XIV.3-XIV.8, as well as the main parameter characterising the re-solution process, μ_α. A parameter analysis was thus performed by applying the Taguchi method on the three following parameters:

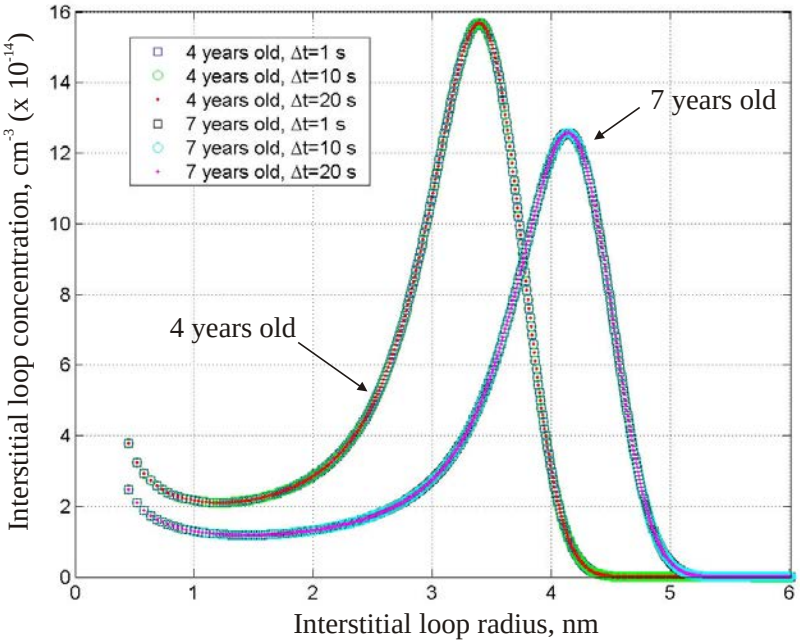

Figure XIV.3: Influence of the time step value on the stability of the solution.

1. Uranium-interstitial migration enthalpy: this parameter is not determined accurately so far and is determinant in studying the effect of interstitial diffusion (see below).

2. Deviation from stoichiometry in the pre-exponential coefficient of the uranium-interstitial diffusivity: this parameter was also chosen because a variation of the interstitial migration enthalpy does not only change the uranium-interstitial migration enthalpy but also the recombination coefficient of uranium Frenkel pairs. The latter is expressed as follows [88]:

$$\alpha_r = \frac{12}{x_i^2 a^2}\left(\frac{3}{2}D_i + D_v\right) \tag{XIV.30}$$

   which, according to Eqs. XIV.12 and XIV.13, simplifies to:

$$\alpha_r = 12\left(\nu_i \exp\left(-\epsilon_{im}/kT\right) + \nu_v \exp\left(-\epsilon_{vm}/kT\right)\right) \tag{XIV.31}$$

   The parameter x_i^2 enables to study the separate effect of the uranium diffusion coefficient on the numerical results.

3. Depth range μ_α of the ^{234}U-recoil atom produced by the α-decay of ^{238}Pu: this parameter was used for analysing the re-solution process of interstitials from the loops back into the matrix. This process is thought to play a role in the growth mechanisms of interstitial loops but the effect of μ_α has never been analysed.

The storage temperature was not a variable parameter as it is known accurately. Moreover, according to the different parameters used, the temperature dependence only appears in the exponential of the point defect diffusion coefficients and will thus have the same effect as varying the migration enthalpy.

Parameter	Minimum value	Maximum value	Reference
ϵ_{im}	0.65 eV	0.8 eV	this work
${x_i}^2$	10^{-2}	1	[58]
μ_α	10 nm	30 nm	$\pm$50% of [75, 82]

Table XIV.3: Minimum and maximum values of the parameters.

The parameters x_i^2 and μ_α have been set to a minimum and a maximum value, which corresponds to extrema of usually used values. The latter are given in Tab. XIV.3.

Concerning the uranium-interstitial migration enthalpy in UO_2, the range of chosen values is very narrow and there is no reference to previous work. Firstly, there is no agreement on the exact value of this parameter. Matzke determined experimentally the uranium-interstitial migration enthalpy in UO_2 to be around 2 eV [73]. Despite this value was established in 1987, no new or reliable experimental value was proposed up to now. Veshchunov et al. [139] used a value of 0.3 eV, Rest and Hofman [106, 108] 0.6 eV, and Morelon et al. [85] calculated the uranium-interstitial migration energy in UO_2, by using an empirical interaction potential in molecular dynamics simulations, to be 5.0 eV. Secondly, the uranium-interstitial diffusivity is very sensitive to the value of the migration enthalpy. For instance, the ratio of the diffusivity calculated with the migration enthalpy given by Veshchunov [139] over the one calculated with the migration enthalpy given by Rest [106] is about:

$$\frac{D_i(\epsilon_{im} = 0.3 \text{ eV})}{D_i(\epsilon_{im} = 0.6 \text{ eV})} \simeq 1.2 \times 10^5 \tag{XIV.32}$$

As a consequence, the time step to allow such differences in the diffusion coefficient may vary considerably. As the aim of the present study is not to determine the exact value of the uranium-interstitial migration enthalpy but to assess its effect, there is no need to consider for the moment a wide range of values (see Tab. XIV.3). The lowest value (0.65 eV) has been chosen in order to reduce the computation time, and the highest value (0.8 eV) in order to have a significant effect of Frenkel pair recombination:

$$\frac{\alpha_r(\epsilon_{im} = 0.65 \text{ eV})}{\alpha_r(\epsilon_{im} = 0.8 \text{ eV})} \simeq 3.5 \times 10^2 \tag{XIV.33}$$

A first set of runs consisting of the initial Eqs. XIV.3-XIV.8, completed by Eqs. XIV.14 and XIV.15 in order to take into account the re-solution process previously introduced, has been performed. Eight numerical runs were carried out employing the orthogonal array $L_8(2^3)$ (Tab. XIV.4) to investigate the effects of the selected parameters on the statistical moments and shape of the loop size distribution. $L_8(2^3)$ means that 8 runs are needed to investigate three different parameters, each of which is set at 2 predetermined levels.

In Tab. XIV.4, the "+" and "-" signs correspond to the maximum and minimum values of a parameter, respectively. The last column will be used in order to study the interaction effect between the parameters ϵ_{im} and x_i^2 on the calculated solutions (see below). The choice of the "+" and "-" signs in the last column has been done according to the following convention: (-)×(-)=(+), (-)×(+)=(-) and (+)×(+)=(+).

Case	ϵ_{im}	${x_i}^2$	μ_α	$\epsilon_{im} \times {x_i}^2$
1	-	-	-	+
2	-	-	+	+
3	-	+	-	-
4	-	+	+	-
5	+	-	-	-
6	+	-	+	-
7	+	+	-	+
8	+	+	+	+

Table XIV.4: Test matrix according to the Taguchi procedure.

Case	Loop mean radius	Standard deviation	Modal radius	Associated concentration	Skewness	Normalised Kurtosis
1	2.73 nm	0.71 nm	3 nm	37×10^{15} cm^{-3}	-0.32	0.09
2	2.65 nm	0.58 nm	3 nm	46×10^{15} cm^{-3}	-0.87	0.45
3	11.07 nm	1.26 nm	11 nm	33×10^{15} cm^{-3}	-3.48	18.89
4	10.76 nm	1.16 nm	11 nm	48×10^{15} cm^{-3}	-4.24	24.75
5	1.53 nm	0.50 nm	2 nm	399×10^{15} cm^{-3}	-0.06	-1.82
6	1.42 nm	0.49 nm	1 nm	511×10^{15} cm^{-3}	0.33	-1.88
7	4.43 nm	0.86 nm	5 nm	595×10^{15} cm^{-3}	-1.05	2.10
8	4.34 nm	0.77 nm	5 nm	583×10^{15} cm^{-3}	-1.44	3.30

Table XIV.5: Results obtained from the loop size histogram for the 4-year-old storage time.

For the sake of clarity and brevity, not all calculated solutions are plotted. As examples, the solutions of cases 3 and 6 in Tab. XIV.4 are shown in Fig. XIV.4 and Fig. XIV.5, respectively, for both storage times. The shape of the interstitial loop concentration distribution in Figs. XIV.4 and XIV.5 can be explained on the basis of simple physical considerations: a fraction of the continuously generated point defects form interstitial loop nuclei , i.e. di-interstitials, whose concentration is therefore lower. The remaining point defects either stay in solution in the UO_2 lattice, form new nuclei, or contribute to their growth. Larger loops have a higher interstitial capture volume and from this point, the interstitial loop distribution fully develops, by taking here the shape of a normal distribution.

The loop size histograms are then build-up from the calculated loop concentrations in the sample. Fig. XIV.6 shows typical histograms from the case 3 and 6, only after t=7 years of storage.

For a quantitative characterisation of the loop size histograms, the same statistical values calculated with Eq. XIII.4-XIII.9 for the experimental distributions are also calculated for all cases and given in Tab. XIV.5 for the simulation of the 4-year-old storage time, and in Tab. XIV.6 for the 7-year-old one.

The results of Tabs. XIV.5 and XIV.6 show that none of the eight runs for both storage times gave results in very good agreement with those of Tab. XIII.2. However, it is pointed out

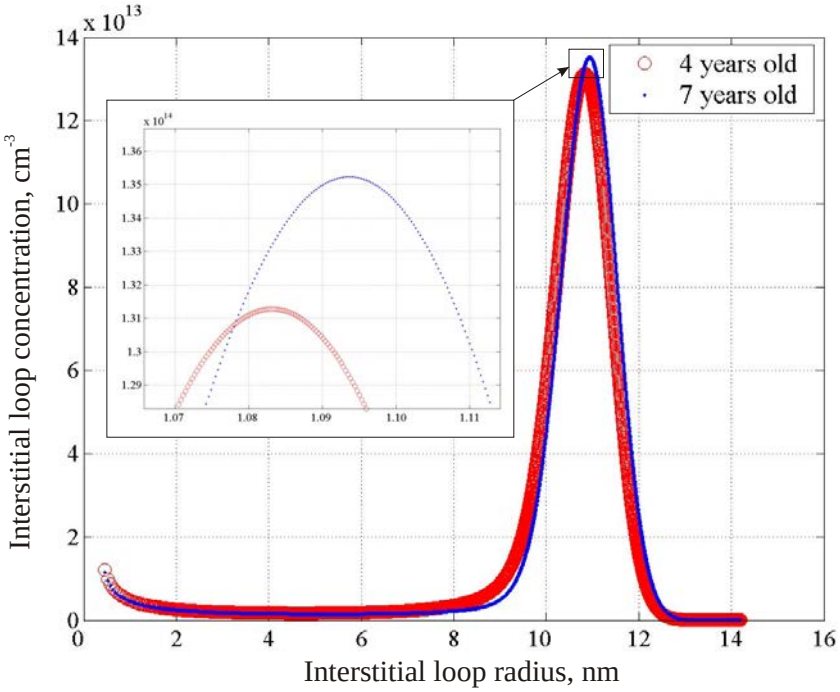

Figure XIV.4: Calculated solution of case 3, for the two storage times.

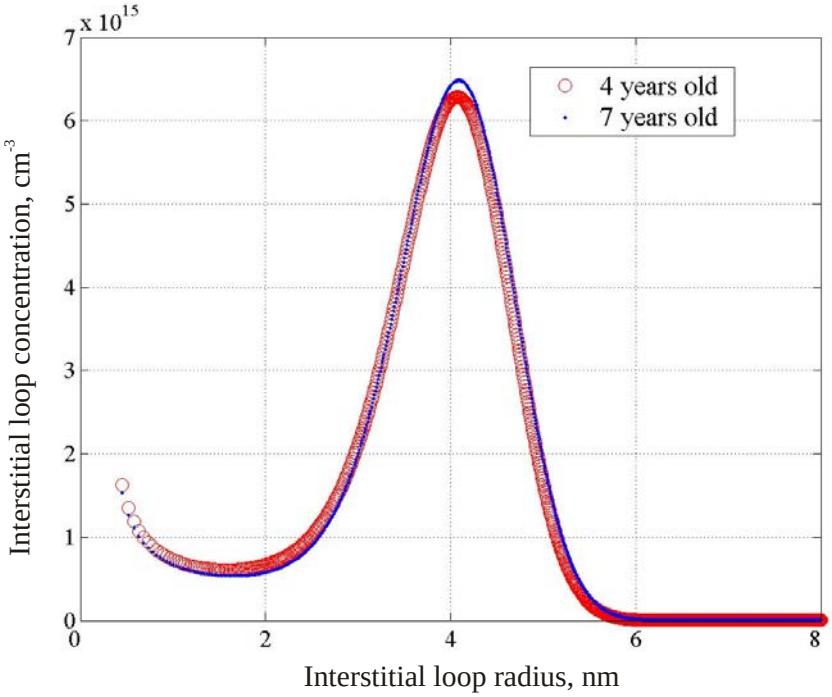

Figure XIV.5: Calculated solution of case 7, for the two storage times.

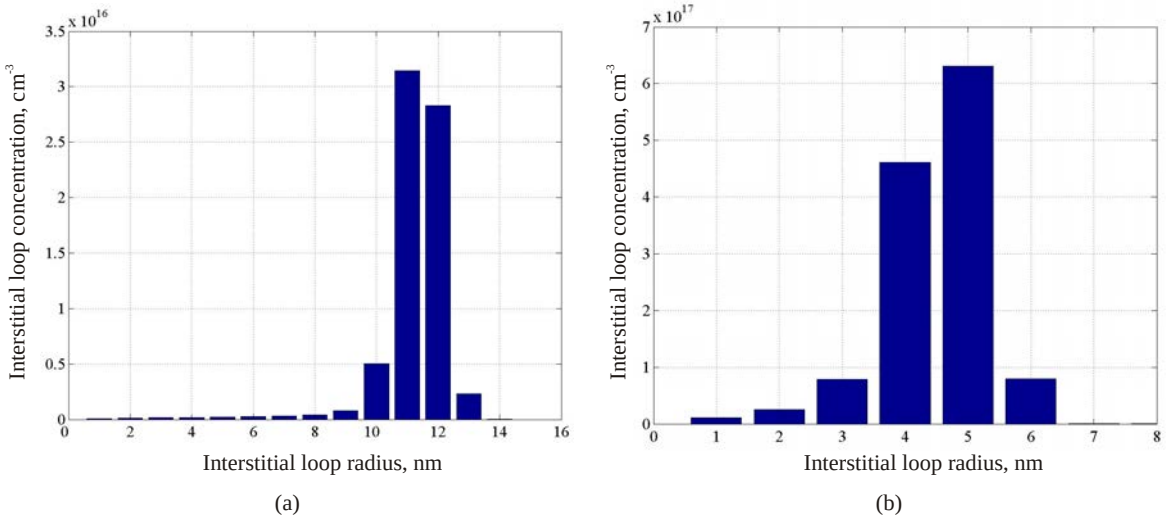

Figure XIV.6: Simulated loop size histograms of (a) case 3 and (b) case 7.

Case	Loop mean radius	Standard deviation	Modal radius	Associated concentration	Skewness	Normalised Kurtosis
1	2.76 nm	0.71 nm	3 nm	37×10^{15} cm^{-3}	-0.29	0.05
2	2.65 nm	0.57 nm	3 nm	49×10^{15} cm^{-3}	-0.87	0.41
3	11.24 nm	1.21 nm	11 nm	31×10^{15} cm^{-3}	-3.79	22.59
4	10.88 nm	1.09 nm	11 nm	52×10^{15} cm^{-3}	-4.80	31.12
5	1.56 nm	0.52 nm	2 nm	365×10^{15} cm^{-3}	0.07	-1.33
6	1.44 nm	0.50 nm	1 nm	483×10^{15} cm^{-3}	0.24	-1.92
7	4.49 nm	0.85 nm	5 nm	631×10^{15} cm^{-3}	-1.03	2.25
8	4.36 nm	0.74 nm	5 nm	616×10^{15} cm^{-3}	-1.48	3.78

Table XIV.6: Results obtained from the loop size histogram for the 7-year-old storage time.

	4 years old				7 years old			
Level	ϵ_{im}	${x_i}^2$	μ_α	$\epsilon_{im} \times {x_i}^2$	ϵ_{im}	${x_i}^2$	μ_α	$\epsilon_{im} \times {x_i}^2$
-	6.80 nm	2.08 nm	4.94 nm	6.19 nm	6.88 nm	2.10 nm	5.01 nm	6.28 nm
+	2.93 nm	7.65 nm	4.79 nm	3.54 nm	2.96	7.74 nm	4.83 nm	3.56 nm
Abs. diff.	-3.87 nm	5.57 nm	-0.15 nm	-2.65 nm	-3.92 nm	5.64 nm	-0.18 nm	-2.72 nm

Table XIV.7: Parameter effect on the loop mean radius.

	4 years old				7 years old			
Level	ϵ_{im}	${x_i}^2$	μ_α	$\epsilon_{im} \times {x_i}^2$	ϵ_{im}	${x_i}^2$	μ_α	$\epsilon_{im} \times {x_i}^2$
-	0.93 nm	0.57 nm	0.83 nm	0.85 nm	0.89 nm	0.57 nm	0.82 nm	0.83 nm
+	0.65 nm	1.01 nm	0.75 nm	0.73 nm	0.65 nm	0.97 nm	0.72 nm	0.72 nm
Abs. diff.	-0.28 nm	0.44 nm	-0.08 nm	-0.12 nm	-0.24 nm	0.40 nm	-0.10 nm	-0.11 nm

Table XIV.8: Parameter effect on the standard deviation.

here that the goal is not to reproduce exactly the experimental distributions in Fig. XIII.7 but to determine the relative importance of various parameters or mechanisms involved in the process leading to these observed loop size distributions in α-doped UO_2 samples. The former case would need more accurate data in order to provide the simulation results with a good basis for the fitting analysis. The latter case, a sensitivity analysis, is treated hereafter.

Based on the results in Tabs. XIV.5 and XIV.6, a level average analysis can be performed. As described by Taguchi in [96], a level average analysis is one of the techniques used to explore the results of the Taguchi method. The name derives from determining the average effect of each parameter on the outcome of the run. The goal is to identify those parameters that have the strongest effects and whether they exert their effect independently or through interacting with other parameters. This level average analysis has been applied in order to identify the effects of ϵ_{im}, x_i^2 and μ_α on the loop mean radius, standard deviation, skewness and normalised kurtosis. The results are reported in Tabs. XIV.7, XIV.8, XIV.9 and XIV.10.

In the following, it is very important to keep in mind that the range for each parameter is very different. As shown in Tab. XIV.3, μ_α fluctuates between 10 and 30 nm, the maximum over the minimum value ratio is a factor 3. There are two orders of magnitude between the minimum and maximum values of x_i^2 hence in the uranium-interstitial diffusion coefficient because x_i^2 is contained directly in the pre-exponential factor of the uranium-interstitial diffusivity. The parameter ϵ_{im} fluctuates by about 20% only, but the effect is more than three orders of magnitude on the uranium-interstitial diffusion coefficient.

Moreover, the following discussion does not take into consideration the positive or negative value of any result. A negative difference between the "+" and "-" levels in the average value of a parameter simply means that an increase of the parameter induces a decrease in the calculated result. This is the case of the uranium-interstitial migration energy for which an increase of its value causes a decrease in the diffusion and recombination coefficients.

A first and direct result of the level average analysis is that the value of μ_α has always the smallest effect on the loop mean radius, standard deviation, skewness and normalised kurtosis,

	4 years old				7 years old			
Level	ϵ_{im}	${x_i}^2$	μ_α	$\epsilon_{im} \times {x_i}^2$	ϵ_{im}	${x_i}^2$	μ_α	$\epsilon_{im} \times {x_i}^2$
-	-2.23	-0.23	-1.23	-1.86	-2.44	-0.21	-1.26	-2.07
+	-0.55	-2.55	-1.55	-0.92	-0.55	-2.77	-1.73	-0.92
Abs. diff.	1.68	-2.32	-0.32	0.94	1.89	-2.56	-0.47	1.15

Table XIV.9: Parameter effect on the skewness.

	4 years old				7 years old			
Level	ϵ_{im}	${x_i}^2$	μ_α	$\epsilon_{im} \times {x_i}^2$	ϵ_{im}	${x_i}^2$	μ_α	$\epsilon_{im} \times {x_i}^2$
-	11.04	-0.79	4.81	9.98	13.54	-0.70	5.89	12.61
+	0.42	12.26	6.65	1.48	0.69	14.93	8.35	1.62
Abs. diff.	-10.62	13.05	1.84	-8.5	-12.85	15.63	2.46	-10.99

Table XIV.10: Parameter effect on the normalised kurtosis.

compared to the ϵ_{im} and x_i^2, and this for both storage times. This does not mean that the re-solution itself has no effect, but that the value of μ_α in the range considered is not so important. As an example, Fig. XIV.7 shows the effect of re-solution on the loop distribution calculated with the initial set of equations. It is shown in Fig. XIV.7 that without the re-solution process, the mean radius would be much higher than the ones reported in Tabs. XIV.5 and XIV.6. Moreover when re-solution is accounted for, the entire distribution is brought back to a level which does not evolve between 4 and 7 years old. This means that there is a competitive effect between the growth of loops by trapping interstitials (due to self-diffusion of interstitials into the matrix) and destruction of loops through the re-solution process.

From Tabs. XIV.7, XIV.8, XIV.9 and XIV.10, it is shown that the loop mean radius, standard deviation, skewness and normalised kurtosis are all very sensitive to the parameter x_i^2. The latter results are also sensitive to the parameter ϵ_{im}, compared to the effect of μ_α. However, contrary to x_i^2, which acts only on the uranium-interstitial diffusion coefficient, ϵ_{im} modifies the Frenkel pair recombination coefficient as well. In order to separate the effect of an enhanced diffusion coefficient from the one of the Frenkel pair recombination coefficient due to the parameter ϵ_{im}, we take advantage of the Taguchi method for studying the interaction between ϵ_{im} and x_i^2. The results are reported in all tables in the column "$\epsilon_{im} \times x_i^2$". For the analysis, the fact that ϵ_{im} and x_i^2 have opposite effects on the uranium diffusivity is also used. By this way, the influence of the uranium diffusivity is more or less compensated (the effect is not zero exactly due to the difference in the range of values for the uranium diffusivity when varying ϵ_{im} or x_i^2), and the final result contains mainly the influence of the uranium Frenkel pair recombination coefficient.

As a result, it is found from Tabs. XIV.7, XIV.8, XIV.9 and XIV.10 that the the single effect of the uranium Frenkel pair recombination coefficient is always less than the effect of x_i^2. However, this difference in the parameter sensitivity is quite relative since the range of values for ϵ_{im} is much smaller than for x_i^2. It is therefore concluded that ϵ_{im} is also a sensitive parameter in the range of values studied here.

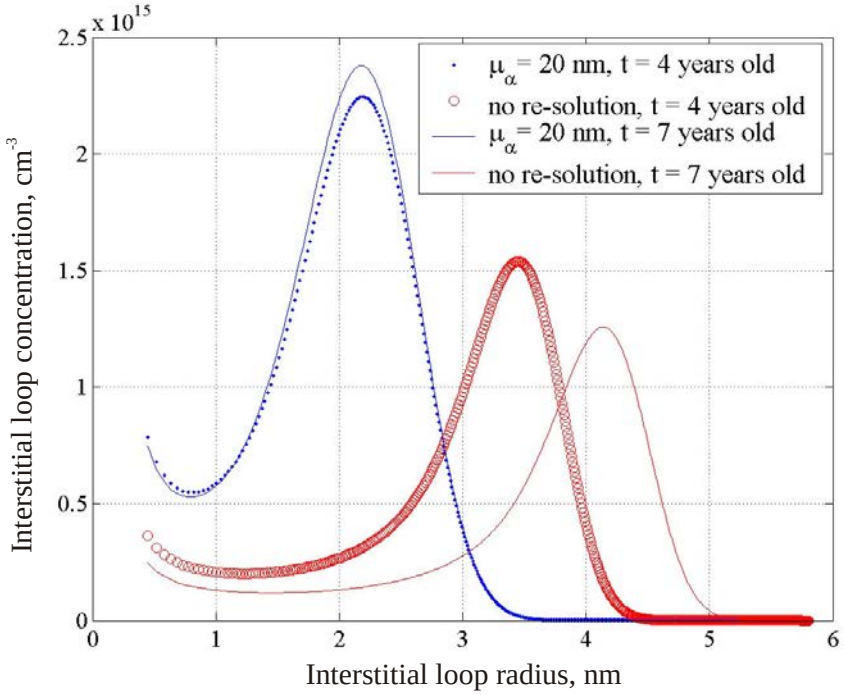

Figure XIV.7: Effect of re-solution process on the interstitial loop concentrations.

As a conclusion of the level average analysis by applying the Taguchi method on Eqs. XIV.3-XIV.8 and Eqs. XIV.14-XIV.15 with the parameters ϵ_{im}, x_i^2 and μ_α, it is shown that:

- The loop mean radius, standard deviation, skewness and normalised kurtosis are all sensitive to the parameters ϵ_{im} and x_i^2. The effect of the uranium-interstitial migration energy is twofold. First, a decreasing value of ϵ_{im} enhances the diffusion of uranium-interstitial, and has therefore the same effect of an increasing value of x_i^2. Second, this enhances the Frenkel pair recombination coefficient as well. It is shown in Tabs. XIV.5 and XIV.6 for cases 5, 6, 7 and 8 that for the highest value of ϵ_{im}, the recombination is very small and a very high peak in the maximum loop concentration is induced, which totally disagrees with the experimental observations in spite of the experimental uncertainties. This gives a tendency in setting the value of ϵ_{im} to lower values. Because ϵ_{im} and x_i^2 have opposite effects on the uranium-interstitial diffusion coefficient, the increase in the latter due to ϵ_{im} can be compensated by using a small value for x_i^2.

- The re-solution process of interstitial back into the matrix due to the collision with the recoil atom ^{234}U has an important effect on the loop mean size, as shown in Fig. XIV.7. Without re-solution, the loop size distribution is growing towards higher and higher radii. With re-solution, the big loops are destroyed and the entire distribution is brought back to a level which does not evolve between 4 and 7 years old when the value of the uranium interstitial diffusion coefficient is not so high. This means that there is a competitive effect between the growth of loops by trapping interstitials (due to self-diffusion of interstitials into the matrix) and destruction of loops through the re-solution process. Moreover, the overall effect of re-solution is that a steady-state is almost achieved, which is not the case

without re-solution. It is important to notice that the experimental loop size histograms shown in Fig. XIII.7 do not evolve obviously between 4 and 7 years old, only the modal radius increased from 2 to 3 nm.

The parameter μ_α characterising the re-solution process has no or little effect compared to x_i^2 and ϵ_{im}. Nevertheless, the standard deviation is always smaller in cases 2, 4, 6 and 8 than in the cases 1, 3, 5 and 7, for both storage times. Therefore, in order to keep constant the total concentration of loops within the distribution for a given set of parameters, the normalised kurtosis increases, in absolute value, with decreasing standard deviation, as shown in Tabs. XIV.5 and XIV.6. This change is small when μ_α varies from 10 to 30 nm. As a result, even if μ_α may be subjected to uncertainties, the overall effect is small and a value of 20 nm, as determined in [82], can be used when re-solution is accounted for.

XIV.3.3 Need for a coarsening mechanism

In order to further analyse the evolution of interstitial loops in the α-doped UO_2 samples, the coarsening mechanism previously introduced, namely the coalescence of interstitial loops, has been introduced in the set of equations. The approach of this section consists in considering the coalescence of loops only, the re-solution process is not taken into account despite, according to the above conclusions, that the loop mean radius will be over-estimated. This approach was first chosen due to numerical difficulties to solve the global system, i.e. the one with the re-solution and coalescence processes. In addition, this is a requirement in this mechanistic approach to study isolated mechanisms in order to draw reliable conclusions.

As presented in section XIV.2, both surface and volume diffusion mechanisms of loops were initially considered. Before running costly calculations (in computing time), the relative values of these mechanisms are assessed.

For the surface diffusion of loops, it is found in Eq. XIV.25 that the surface diffusion coefficient of loop is a function of D_s which is the surface self-diffusion coefficient of UO_2. The data compiled by Maiya [64] and Matzke [37] gave the following relationship for D_s:

$$D_s = 5 \times 10^5 \exp\left(-\frac{450000}{RT}\right) \qquad \text{cm}^2.\text{s}^{-1} \tag{XIV.34}$$

with 1200°C< T <1800°C and R=8.3144 J mol^{-1} K^{-1}. The values of D_s have been estimated by Matzke to be within an experimental scatter band of two orders of magnitude for the temperature range examined. However, no equation for the surface self-diffusion coefficient of UO_2 at room temperature (298 K) was found in the open literature. As a first approximation, Eq. XIV.34 is used to calculate the surface diffusion coefficient in Eq. XIV.25 at the storage temperature of the samples (room temperature). The latter coefficient has been calculated for two different interstitial loop sizes, in order to assess the size effect on the loop mobility (Tab. XIV.11).

In Tab. XIV.11, the results for the volume diffusion of loops are also shown. For this calculation, x_i^2 and ϵ_{im} have been set to the values which give the lowest uranium-interstitial diffusion coefficient.

As a consequence of the results shown in Tab. XIV.11, the surface diffusion mechanism can be considered as negligible at the temperature considered in the present study, and the fol-

Loop radius	1 nm	10 nm
$D_l^{surface}$	1.3×10^{-74} cm^2.s^{-1}	1.3×10^{-76} cm^2.s^{-1}
D_l^{volume}	5.2×10^{-19} cm^2.s^{-1}	5.2×10^{-20} cm^2.s^{-1}

Table XIV.11: Comparison of the surface and volume diffusion coefficient of interstitial loops, for two different loop radii.

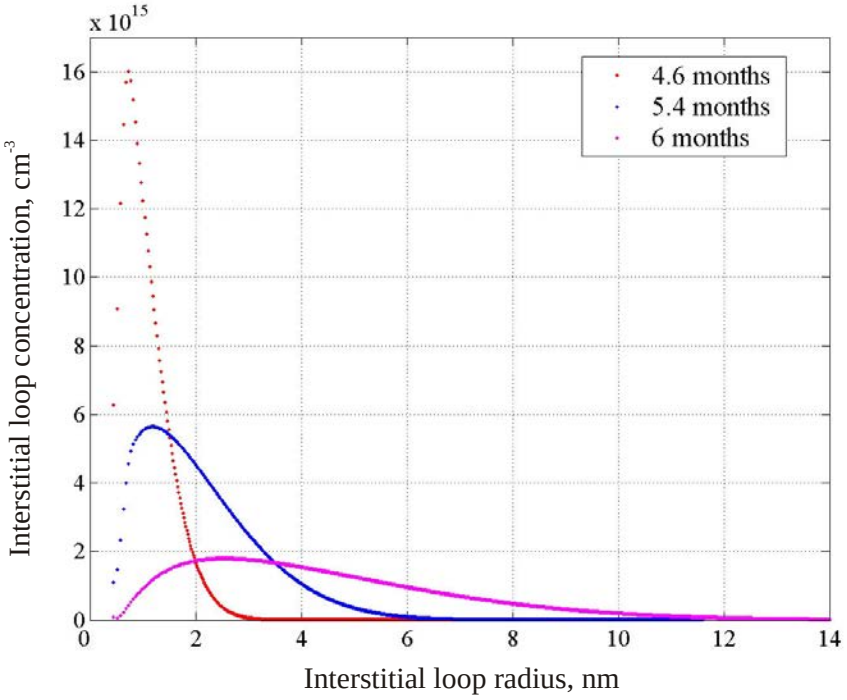

Figure XIV.8: Interstitial loop concentrations at different times. In this calculation, D_i=5×10^{-18} cm^{2}s^{-1}.

lowing calculations involving the coalescence of loops will be limited to the volume diffusion mechanism.

As stated above, the computation time is extremely increasing when the equations for the coalescence are included in the initial set of equations. For this reason, a complete matrix of runs as defined by the Taguchi method could not be performed in the time frame of this PhD. However, as shown by Eq. XIV.28, the volume diffusion coefficient of loops only depends on D_i. The single effect of coalescence can be studied if and only if D_i is the only parameter to vary, which means that x_i^2 is prefered, because ϵ_{im} changes the recombination coefficient as well. Moreover, regarding the previous preliminary conclusions, an adequate value for ϵ_{im} should be chosen in order to avoid both extreme computation time and irrelevant low Frenkel pair recombination coefficient: in the following, ϵ_{im}=0.7 eV.

A first run has been performed with an imposed uranium-interstitial diffusion coefficient of D_i=5×10^{-18} cm^{2}s^{-1}. The result is shown in Fig. XIV.8. The interstitial loop concentrations have not been calculated for the two storage times, but limited to 6 months. The reason

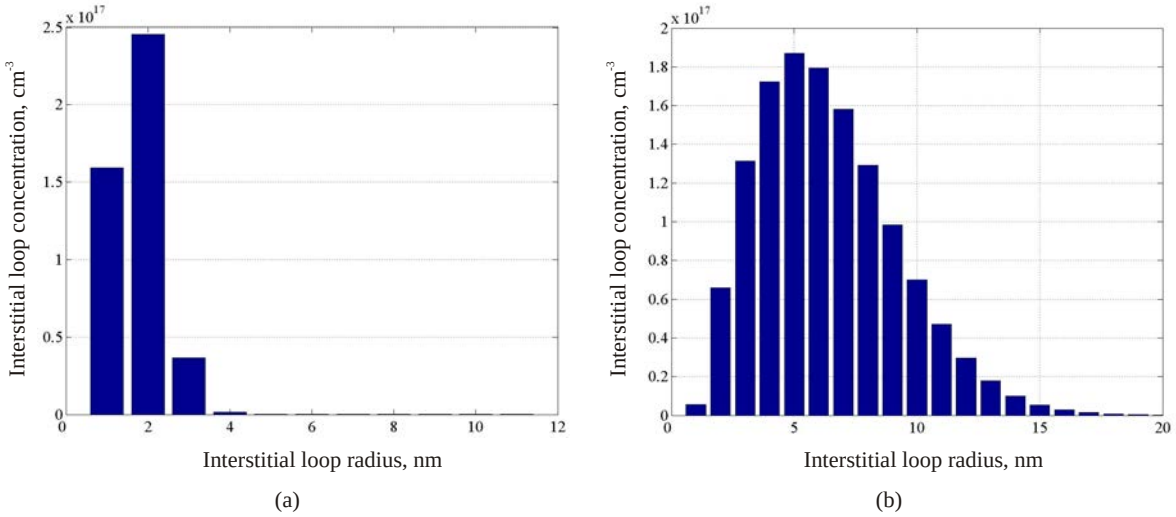

Figure XIV.9: Loop size histograms at (a) 4.6 months and (b) 6 months.

for this short simulated storage time is that further calculations would have given a loop size distribution with a loop mean radius increasing more and more rapidly, which is not observed experimentally. Fig. XIV.8 shows the calculated interstitial loop concentrations after 4.6, 5.4 and 6 months. At t=4.6 months, a distribution of loop concentrations similar to those observed in the previous section, seems to be achieved, but at smaller radii due to the low value of D_i and with a sharp maximum value. After 5.4 months, the effect of interstitial loop coalescence is clearly seen: a tail oriented towards the larger loop radii appears, which is even more visible after 6 months.

The loop size histograms for the storage times of 4.6 and 6 months are plotted in Fig. XIV.9. Between these two storage times (1.4 month), the loop size histogram has evolved very rapidly, due to a very effective effect of the volume diffusion and coalescence of interstitial loops.

As mentioned before, further calculations with this set of values result in an unstable distribution of interstitial loop concentrations. For this reason, the uranium-interstitial diffusion coefficient has been reduced by one order of magnitude, which reduces the effect of volume diffusion and coalescence of loops as well. ϵ_{im} has not been modified in order to keep the same uranium Frenkel pair recombination coefficient. Fig. XIV.10 shows similar results as in Fig. XIV.8, but after much longer simulated storage times due to the reduced diffusion coefficient. After t=4 years, a distribution comparable to the one obtained after 4.6 months in Fig. XIV.8 has formed. As previously observed, the distribution evolves very rapidly again. After 4 years and 5 months, a tail typical of the volume diffusion and coalescence of loops has appeared. As a first conclusion, these results shown that once a distribution of interstitial loops similar to a normal distribution has formed, the coalescence is very effective. Large loops form more rapidly from the small ones by coalescence, than the small ones form from di-interstitial nucleation and trapping interstitials.

Fig. XIV.11 shows the loop size histogram obtained after 4 years and 5 months, from which the statistical values previously introduced are derived (Tab. XIV.12).

Almost all values in Tab. XIV.12 are in good agreement with the values shown in Tab. XIII.2,

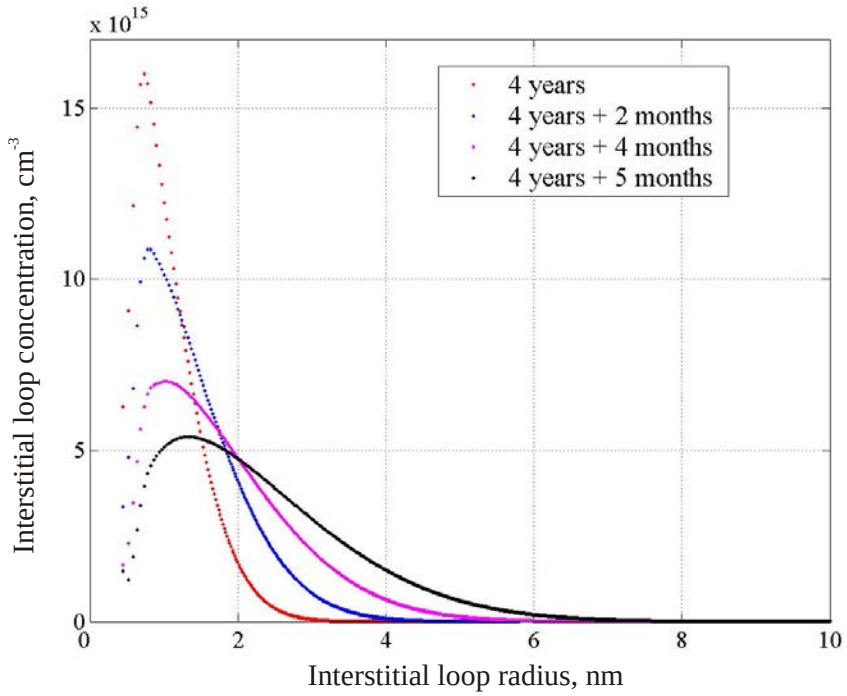

Figure XIV.10: Interstitial loop concentrations at different times. In this calculation, D_i=5×10^{-19} cm^2s^{-1}.

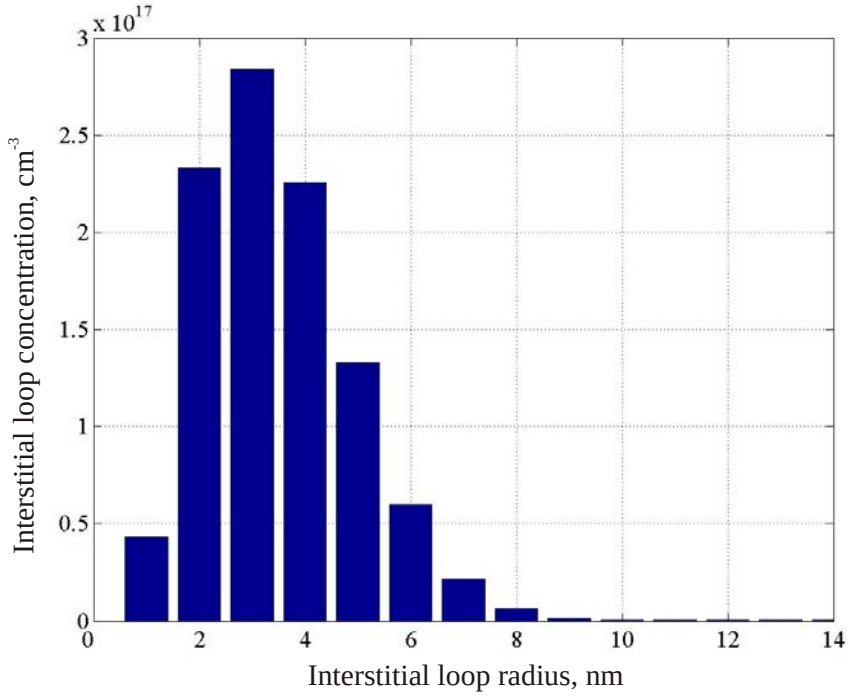

Figure XIV.11: Loop size histograms at 4 years and 5 months.

Loop mean radius	3.52 nm
Standard deviation	1.58 nm
Modal value	3 nm
Corresponding loop density	284×10^{15} cm^{-3}
Skewness	1.69
Normalised kurtosis	8.19

Table XIV.12: Statistical values obtained from the histograms in Fig. XIV.11.

except for the maximum loop concentration which is much higher. As a consequence, and despite that this is not the result of a sensitivity analysis as it was performed for the re-solution process and parameter analysis, the volume diffusion and coalescence of interstitial-type dislocation loops is a mechanism to be accounted for in the behavior of α-produced radiation damage in UO_2 in order to obtain the correct skewness, hence the tail oriented towards larger radii in the loop size histogram.

XIV.4 Summary and conclusions

The model developed initially by Hayns [34] has been extended for the study of radiation damage in α-doped UO_2 samples. The inclusion of additional physical mechanisms which were thought to play an important role in the behavior of defects has been also considered.

The first one is the re-solution process of interstitials driven from the loops back into the matrix due to the impact with the recoil atom ^{234}U. Irradiation-induced re-solution of fission gas is an important mechanism in the behavior of fission gas bubbles in irradiated UO_2 fuel [134, 133], and a similar mechanism has been applied to the case of interstitial-type dislocation loops. This is an innovative contribution in the understanding of the point defect behavior, as it was never applied before on this type of defects.

Equations for the re-solution process have been proposed and complete the initial set of equations. A sensitivity analysis has been performed by use of the Taguchi technique in order to assess the importance of the parameter characterising the re-solution process (μ_α), together with two other independent parameters for the importance of uranium-interstitial diffusion (ϵ_{im} and x_i^2) and of uranium Frenkel pair recombination (ϵ_{im}). From this analysis, it was found that the loop mean radius, standard deviation, skewness and normalised kurtosis are sensitive to the parameters ϵ_{im} and x_i^2, hence are sensitive to the diffusion and recombination coefficients. It was also found that the value of μ_α has almost no effect on the statistical values, despite the re-solution mechanism itself has a strong and positive effect on the loop mean radius and skewness. Finally, the re-solution of interstitials from the loops is a mechanism which enables to achieve a steady-state of the growth of interstitial loops, as observed experimentally. As a consequence, this mechanism is identified to be important for the study of point defects in α-doped materials.

The second mechanism proposed and analysed in this section is the coalescence of diffusing interstitial-type dislocation loops. This type of coarsening mechanism is known to have important effects on the bubble size distribution of inert gases in irradiated materials. It was suggested to extend also this idea to interstitial-type dislocation loops. The latter are crystal defects that can be subjected to a coarsening mechanism, just like bubbles, although their diffusion on the matrix is dependent of their crystallographic formation plane.

The surface and volume diffusion coefficients have been derived for the case of diffusing interstitial loops. It has been shown that the surface diffusion mechanism is negligible compared to volume diffusion. Due to extremely long computation times, the simulated loop size distributions could not be calculated for the two storage times. An analysis of the single effect of volume diffusion coefficient of loops has been performed instead. It is shown that the coalescence mechanism of diffusing interstitial loops is very effective and strongly dependent on the uranium-interstitial diffusion coefficient, and that the simulated loop size histograms show a tail oriented towards the larger loop sizes (positive skewness) which is typical of the present coarsening mechanism and similar to the one observed on the experimental histogram in Fig. XIII.7.

The statistical values in Tab. XIV.12 derived from the last simulated histogram shown a better agreement with the same values in Tab. XIII.2 from the experimental histograms, except for the maximum loop concentration which is much higher. As a result of the previous parameter analysis, this maximum peak is due to a low uranium Frenkel pair recombination. Consequently, much more interstitials are present in the matrix for the nucleation and further growth of di-interstitial loops. In order to correct this value, a higher Frenkel pair recombination coefficient would be needed by decreasing the value of ϵ_{im}. However, this will result in an enhanced diffusion coefficient and therefore in an unstable distribution of interstitial loop concentrations. A very low pre-exponential factor in the diffusion coefficient, in order to correct this phenomenon, can not be experimentally justified. However, the previous analysis has also shown that the re-solution of interstitials from the loops, as proposed in the present work, is a mechanism which reduces the effect of an excessive uranium-interstitial diffusion coefficient and tends to obtain a steady-state distribution of loops. A further analysis must be investigated in order to study the combined effects of re-solution and coalescence of interstitial loops.

Part 5

Conclusions and perspectives of this PhD thesis

The aim of this PhD thesis was to contribute to the understanding of the High Burn-up Structure formation mechanisms in nuclear fuels. For this purpose, a bibliographical review on the characterisation, effects, interpretations and models of the HBS was first achieved. As a result, it is seen that the HBS, characterised by Xe-depletion from the matrix, pore formation and grain sub-division, is not a negative feature of high burn-up fuel and does not seem to be a handicap to achieve higher burn-ups during normal operating conditions. However, there are still many open questions on the exact mechanisms of its formation and further development within the fuel pellet during irradiation.
In order to answer some of these questions, the emphasis has been laid on the role of the nucleation, growth and accumulation of dislocation-type defects, i.e. shear dislocation lines and interstitial-type dislocation loops. The former are necessary in the build-up of new sub-grain boundaries under the assumption that the HBS formation is a polygonization process. The latter are a consequence of the irradiation-produced point defects and their role in the mechanisms of the HBS formation is not yet clarified. The study of these defects is all the more important as the bibliographical study on the HBS models highlighted the possible confusion between these two fundamentally different types of dislocations.

Therefore, the work carried out in this PhD consisted in two distinct parts: (a) a theoretical stress analysis induced by the presence of dislocations which may form various configurations, (b) a study of the evolution of irradiation defects, especially the interstitial-type dislocation loops, was conducted with particular attention to the growth mechanisms.

Stress analysis of periodical dislocation configurations

In metals undergoing polygonization, dislocations are necessary to form new sub-grain boundaries. The transposition of this phenomenon in metals to nuclear fuel irradiated up to high burn-up is an option which was not yet exploited. Since the experimental data concerning the dislocations in irradiated UO_2 fuels do not provide the information needed to analyze well defined dislocation configurations, a tool which enables to analyse the stress distributions associated with all types of periodic dislocation configurations has been developed. This is based on Kröner's theory of discrete dislocations in a continuum in which the plastic incompatibilities are adjusted in a purely elastic way. I have become acquainted with this formalism that was finally successfully applied to several well-known dislocation configurations: an analytical solution of the stress function has been calculated in each case, the stress field has been derived and compared to existing solutions, if any. Finally, the elastic energy in a defined unit cell has been calculated and a comparison between the different configurations established.

Thanks to the on-going development and first exploitation of the tool presented in this thesis, the perspectives are numerous. One of them is related to the possibility of applying this tool to more complex 3D-structures, like the honeycomb network of dislocations. This problem has already been launched and is presented in appendix B. The solutions of the stress function tensor have been calculated and a numerical treatment is needed in order to obtain results in terms of elastic energy at any point of the medium. This will complete the list of dislocation configurations studied in this work, as the honeycomb network of dislocations is one of the

possible configurations observed in the HBS.

Future development of this tool concerns its extension to a more representative medium, in order to acquire a more realistic description of the internal stresses in irradiated nuclear fuels. A potential anisotropy of irradiated UO_2 may appear due to the accumulation of radiation damage and/or fission products dissolved in the lattice. The case of an anisotropic medium in the theory of discrete dislocations in a contimuun has already been proposed by Kröner [50]. Its application to the basic dislocation configurations in UO_2 material would provide with an effect of anisotropy on the stress distribution around the dislocation structure. In the same way, the route towards a limited medium is an interesting challenge as well. The internal stress problem is initially developed in an infinite medium, i.e. a monocrystal, and its extension to polycrystals will give a closer representation of the UO_2 polycrystalline material, and would enable to assess theoretically the effect of the grain size on the HBS formation mechanisms. For this purpose, several steps need to be solved. The passage to a bi-crystal seems easily possible since the representation of a grain-boundary (edge dislocation wall, or symmetrical tilt-boundary) is known. However, the calculations performed in the case of the bi-crystal can not be directly transposed to the polycrystal. An intermediate step for the study of the role of three-grain junctions (grain edge) is needed before any generalization to a polycrystalline description of internal stresses. Some guidelines have been proposed by Rey in [110].

An extension of the tool to include interactions with precipitates and pores is also of great interest. The latter have been observed in the HBS of nuclear fuels, and are therefore mandatory for the theoretical analysis of the micro-polygonisaton of the restructured area in nuclear fuels. Extended defects like precipitates can be considered in two differents ways. The first one consists of translating the presence of strains induced by the precipitates into an equivalent tensor of dislocation density. This is besides one of the advantages of the theory of discrete dislocations which has provided a unified way of representing and calculating the internal stresses with a plastic origin. Problems of elastic inclusion, of magneto-elasticity, or thermal stresses can therefore be translated to a problem of stress field induced by an adequate distribution of dislocations.
In case the first possibility leads to too complex calculations, it is possible to study the presence of precipitates by directly superposing the stress field of a given dislocation distribution to the one of an inclusion whose solution is well-known (see below).

A comparison of the tool with experimental results is also needed. For this purpose, the dislocation configurations have to be characterised as a function of burn-up, which is the parameter setting the accumulation of defects, before and after the formation of the HBS in irradiated fuels. A statistical approach has to be adopted in order to provide the model with reliable input. However, only a few facilities in the world are able to perform such investigations and the handling of highly radioactive materials limits the accuracy of the TEM observation. This is a recurring problem in this work. Nevertheless, there is no doubt that such experimental results would be a benefit for the tool itself, but also for the overall understanding of the HBS formation mechanisms.

Beyond the development and use of the present tool, an analysis of the possible sources of dis-

locations should also be attempted. The origin of dislocations in UO_2, except those produced during the pellet fabrication, are up to now not clarified. Various possibilities can be considered. The stresses due to the pellet-cladding mechanical interaction as well as the thermal gradient in the pellet could have been the required source. However, the HBS having been also observed in the irradiated HBRP fuel discs (low radial temperature gradient in a section of the fuel disc, as well as unconstrained axially and radially), a search of the dislocation source in the pellet volume itself would rather be investigated. The sources considered are the different precipitates, gas bubbles and pores. Two possibilities of dislocation production arise that have been recently proposed in [130].

The first one considers the direct production of dislocation loops due to the mismatch between the precipitates (or over-pressurized gas bubbles) and the UO_2 matrix. Consider a spherical particle, of radius R, made up of an elastic material (any of the solid fission products which have formed precipitates) that is fitted into a smaller hole in an infinite matrix (UO_2 fuel) such that the radial misfit is δR. The latter can be calculated by considering the difference in the coefficient of thermal expansion $\delta\alpha$ between the matrix and the particle. By knowing the temperature history of the fuel, the mismatch strain $\delta\varepsilon$ between the particle and the matrix is deduced from:

$$\delta\varepsilon = \delta\alpha\,\Delta T$$

where $\Delta T = T(t) - T_0$ is the temperature variation. The radial misfit δR is therefore:

$$\delta R = R\,\delta\varepsilon$$

The stress field in spherical coordinates generated in the matrix due to such a situation has been calculated by Eshelby [27] has a function of the radial misfit δR.

This calculation may subsequently show that the stress field at the precipitate surface can exceed the Von Mises yield criterion, hence a plastified zone can appear and develop, characterised by the production of dislocation loops. The number of dislocations produced to accommodate the mismatch strain due to the difference in the thermal expansion coefficients is a function of the precipitate size and temperature change. Furthermore, it is well known that the difference in crystallographic structures between the precipitates and the matrix can also be a source of dislocations. In that case, the dislocations are produced at the interface in order to accommodate this difference (epitaxy mismatch).

A second possibility for the dislocation production is related to the activation of the Frank-Read sources due to the spatial distribution of precipitates in the matrix. Within the population of precipitates which is observed by means of TEM in the fuel before the HBS formation, the following condition,

$$\tau = \frac{\mu\, b}{\pi L}$$

may be locally satisfied, where b is the module of Burgers vector, τ the shear stress and L is the mean free path corresponding to the average distance between the precipitates which can be deduced from TEM micrographs. The shear stress has to be determined as a function of the external or internal conditions.

If the precipitates do not play a role in the production of dislocations, an alternative possibility would be to consider the initial grain-boundaries as a source of dislocations, as proposed by Priester [98].

In any case, a detailed analysis of the possible sources of dislocations would give precious information on the possible scenario of the HBS formation.

Growth mechanisms of interstitial loops in α-doped UO_2 samples

Since sub-microscopical characterisation of irradiated fuel is very complex, a simpler system reproducing some of the features observed in the HBS, was chosen in the form of UO_2 sintered pellets, doped with $\sim$10 wt% ^{238}Pu and stored for different times, during which α-damage resulting from the decay of ^{238}Pu was produced. By this way, the single effect of interstitial-type dislocation loops can be studied, as these loops are directly formed by precipitation of interstitials, produced by the self-irradiation. The experimental loop size distributions were obtained by means of transmission electron microscopy and image analysis for this sample stored during 4 and 7 years. The initial set of equations proposed by Hayns [34] has been extended to the doped materials and to take into account additional phenomena, i.e. the re-solution of interstitials from the loops due to the impact with the ^{234}U recoil atom and the coalescence of diffusing dislocation loops. The latter mechanisms are known to play a role in the distribution of fission gas bubbles in irradiated UO_2 fuels and it was here proposed to study their effects on the growth mechanism of interstitial loops. A sensitivity analysis has been also performed, showing the important effects of the uranium interstitial diffusion and uranium Frenkel pair recombination coefficients, whereas the depth value of the recoil atom has a small influence on the simulated loop size distributions. It is also shown that the re-solution and coalescence processes alone have an important and positive effect on the loop size histograms. The former enables to reach steady-state and is in competition with a growth mechanism purely based on trapping interstitials. The latter enables to simulate a tail oriented towards larger loop sizes, which is typical of the present coarsening mechanism and similar to the one observed on the experimental histogram.

As a logical continuation of the present analysis, the global system, i.e. the one consisting of the re-solution and coalescence processes, has to be solved. This is an important step but there is no doubt that numerical problems and even longer computation times will arise from this coupling between these two mechanisms. A first task may consist in adopting a more robust integration method, like an implicit method which will allow to use larger time steps. However, the handling of very large matrices to be decomposed and inversed, especially in our case where the number of equations increases with time, can be very difficult. Particular attention will be put on the matrix coefficients which may differ for several orders of magnitude, due to very sensitive coefficients in the proposed set of equations.

Another improvement of the present model regards the geometry of loops resulting from the coalescence mechanism. Indeed, in the present model, no geometric consideration of the loop interaction is taken into account accurately: two colliding cylindrical loops results in a cylindrical loop. In the case the resulting loop is not cylindrical or does not lie in a single cristallographic plane, the capture volume of interstitials may be larger.

Heterogeneous nucleation of interstitial loops should be also discussed. So far, the nucleation

implememted in the model was assumed to be homogeneous. This nucleation mode was guided from the previous models on which this work is based. However, it is possible to exploit further the analogy with the fission gas bubbles where bubbles are considered to nucleate along the fission spike [120, 121]. However, like in the case of the heterogeneous nucleation of fission gas bubbles, an important parameter will be the number of nucleated interstitial loops per α-decay of ^{238}Pu. This parameter has never been determined, both experimentally nor by use of molecular dynamics techniques. A sensitivity analysis as the one performed in this work would nevertheless provide an indication whether this nucleation mode is realistic or not in our case.

In parallel with the on-going analysis of the mechanisms involved in the interstitial loop population in α-doped UO_2 with the present model, ab initio and molecular dynamics calculations could be used in order to verify some assumptions. For instance, ab initio calculations could provide the present model with a more accurate value for the uranium interstitial migration energy, and a surface diffusion coefficient of interstitial loops in the temperature range considered. Molecular dynamics computations could help in quantifying the parameters of the re-solution process of interstitial dislocation loops due to recoil atoms, to be compared with the results of the TRIM calculation, or could be applied to simulate heterogenous nucleation of di-interstitials.

Together with the theoretical work, more accurate experimental data are needed. Firstly, statistical observations of the doped materials should confirm the shape of the loop size distribution. Only one observation has been performed by means of TEM at two different storage times, whereas an observation compaign at a given storage time would have been necessary. Secondly, the uncertainty itself has to be better determined. In this work, an uncertainty of about 30% has been applied, due to a non-constant thickness of the sample induced by the preparation procedure. Moreover, the experimental determination of the dislocation loop population itself is prone to some errors. Indeed, some loops are not necessarily visualised, depending on their orientation: the handling of radioactive samples was limiting the tilting in the microscope. This error is sometimes compensated by using the "factor 3" rule: among the real dislocation loop population, only one third may be observed. However, this results in much too large experimental uncertainties.

Once the model has been totally analysed, its application to irradiated UO_2 fuel seems to be the obvious next step. Despite the problem of statistical observations is inherent in the case of nuclear materials, this would be a very innovative contribution. A further step would be the coupling with the model of Rest and Hofman [109] in which the interactions of interstitial loops with dislocation lines, but also with vacancy clusters and bubbles will have to be taken into account. Here again, numerical problems will arise of such a coupling. An ultimate step of this mechanistic approach would be to model the HBS formation in irradiated UO_2 fuels.

Appendices

Appendix A: Resolution method of a 2D-biharmonic equation

We propose to solve the following biharmonic equation:

$$\nabla^4 \psi' (\underline{x}) = \sum_{n=-\infty}^{\infty} b\, \delta (x_1 - nh)\, \delta' (x_2) \tag{A.1}$$

One possible way to solve this equation consists of applying a Fourier Transform. Several definitions of the Fourier Transform exist, but the most widespread is the following:

$$F\left(\underline{\xi}\right) = \int_{-\infty}^{\infty} f (\underline{x}) \exp\left(-i\underline{\xi}.\underline{x}\right) d\underline{x} \tag{A.2}$$

where $i = \sqrt{-1}$ and $\underline{\xi}.\underline{x} = \xi_1 x_1 + \xi_2 x_2 + \xi_3 x_3$.

The inverse Fourier Transform is obtained with the following equation:

$$f (\underline{x}) = (2\pi)^{-3} \int_{-\infty}^{\infty} F\left(\underline{\xi}\right) \exp\left(i\underline{\xi}.\underline{x}\right) d\underline{\xi} \tag{A.3}$$

As the source term in Eq. A.1 is independent of x_3, the solution $\psi' (\underline{x})$ will only depend of x_1 and x_2. The problem is thus two-dimensional and Eq. A.2 is therefore reduced to a 2D transform.

Before applying the 2D Fourier Transform, it is useful to express the periodic part of the source term which appears in Eq. A.1 under the form of a Fourier Serie. A function $f (x_1)$ can be written as a complex Fourier serie as follows:

$$f (x_1) = \sum_{k=-\infty}^{\infty} C_k \exp\left(\frac{2\pi i k x_1}{h}\right) \quad \text{with} \quad C_k = \frac{1}{h} \int_{-h/2}^{h/2} f (x_1) \exp\left(-\frac{2\pi i k x_1}{h}\right) dx_1 \tag{A.4}$$

where h is the period of the source term. The Fourier serie coefficients C_k then read:

$$C_k = \frac{b}{h} \int_{-h/2}^{h/2} \sum_{n=-\infty}^{\infty} \delta (x_1 - nh) \exp\left(-\frac{2\pi i k x_1}{h}\right) dx_1 \tag{A.5}$$

$$C_k = \frac{b}{h} \sum_{n=-\infty}^{\infty} \int_{-h/2}^{h/2} \delta (x_1 - nh) \exp\left(-\frac{2\pi i k x_1}{h}\right) dx_1 \tag{A.6}$$

As $-h/2 < x_1 < h/2$, the only non-zero integral term is for n=0, which gives:

$$C_k = \frac{b}{h} \tag{A.7}$$

Eq. A.1 can now be expressed under the form of a Fourier serie:

$$\nabla^4\psi'\left(\underline{x}\right) = \frac{b}{h}\sum_{k=-\infty}^{\infty}\exp\left(\frac{2\pi ikx_2}{h}\right)\delta'\left(x_2\right) \tag{A.8}$$

The Fourier Transform is performed to Eq. A.8:

$$\int_{-\infty}^{\infty}\nabla^4\psi'\left(\underline{x}\right)\exp\left(-i\underline{\xi}.\underline{x}\right)d\underline{x} = \frac{b}{h}\int_{-\infty}^{\infty}\sum_{k=-\infty}^{\infty}\exp\left(\frac{2\pi ikx_1}{h}\right)\delta'\left(x_2\right)\exp\left(-i\underline{\xi}.\underline{x}\right)d\underline{x} \tag{A.9}$$

Let $S\left(\xi_1,\xi_2\right)$ be the right-hand-side term of Eq. A.9:

$$S\left(\xi_1,\xi_2\right) = \frac{b}{h}\sum_{k=-\infty}^{\infty}\int_{-\infty}^{\infty}\exp\left(\frac{2\pi ikx_1}{h}\right)\delta'\left(x_2\right)\exp\left(-i\underline{\xi}.\underline{x}\right)d\underline{x} \tag{A.10}$$

The latter equation is simplified by using the properties of the Dirac delta function:

$$S\left(\xi_1,\xi_2\right) = \frac{b}{h}\sum_{k=-\infty}^{\infty}2\pi\delta\left(\xi_1-\frac{2\pi k}{h}\right)i\xi_2 \tag{A.11}$$

In cartesian coordinates, the bi-Laplacian $\Delta^2 = \nabla^4$ of a real function f is expressed by:

$$\nabla^4 f\left(x_1,x_2\right) = \frac{\partial^4 f}{\partial x_1^4}+\frac{\partial^4 f}{\partial x_2^4}+2\frac{\partial^4 f}{\partial x_1^2\partial x_2^2} \tag{A.12}$$

The Fourier transform of the n^{th}-derivative over x of a function f is used to simplify the latter equation. If F_x denotes the Fourier Transform on the x-variable, this relation is written:

$$F_x\left\{f^{(n)}\left(x\right)\right\}\left(\xi\right) = \left(i\xi\right)^n F_x\left\{f\left(x\right)\right\}\left(\xi\right) \tag{A.13}$$

By applying Eq. A.13 to Eq. A.12, the left-hand side term of Eq. A.9 reads:

$$\int_{-\infty}^{\infty}\nabla^4\psi'\left(\underline{x}\right)\exp\left(-i\underline{\xi}.\underline{x}\right)d\underline{x} = \left\{\left(i\xi_1\right)^4+\left(i\xi_2\right)^4+2\left(i\xi_1\right)^2\left(i\xi_2\right)^2\right\}\psi'\left(\xi_1,\xi_2\right) \tag{A.14}$$

and Eq. A.9 becomes:

$$\left(\xi_1^2+\xi_2^2\right)^2\psi'\left(\underline{\xi}\right) = \frac{b}{h}i\xi_2\sum_{k=-\infty}^{\infty}2\pi\delta\left(\xi_1-\frac{2\pi k}{h}\right) \tag{A.15}$$

$\psi'\left(\underline{\xi}\right)$ has to be inversed in order to obtain $\psi'\left(\underline{x}\right)$:

$$\psi'\left(\xi_1,\xi_2\right) = \frac{b}{h}i\xi_2\sum_{k=-\infty}^{\infty}\frac{2\pi\delta\left(\xi_1-\frac{2\pi k}{h}\right)}{\left(\xi_1^2+\xi_2^2\right)^2} \tag{A.16}$$

The first inversion on ξ_1 is simple:

$$\psi'(x_1,\xi_2) = \frac{b}{h} i \sum_{k=-\infty}^{\infty} \frac{\xi_2 \exp\left(\frac{2\pi i k}{h} x_1\right)}{\left(\left(\frac{2\pi k}{h}\right)^2 + \xi_2^2\right)^2} \tag{A.17}$$

For the second inversion on ξ_2, the following result is exploited:

$$F_x^{-1}\left(\frac{\xi_2}{\left(\alpha^2+\xi_2^2\right)^2}\right) = \frac{1}{4}\frac{i x_2}{\alpha}\left\{H(x_2)\, e^{-\alpha x_2} + H(-x_2)\, e^{\alpha x_2}\right\} \qquad \text{if } \alpha > 0 \tag{A.18}$$

and

$$F_x^{-1}\left(\frac{\xi_2}{\left(\alpha^2+\xi_2^2\right)^2}\right) = -\frac{1}{4}\frac{i x_2}{\alpha}\left\{H(x_2)\, e^{\alpha x_2} + H(-x_2)\, e^{-\alpha x_2}\right\} \qquad \text{if } \alpha < 0 \tag{A.19}$$

where H(x) is the Heaviside Step function.

By noticing that:

$$H(x)\, e^{-|\alpha| x} + H(-x)\, e^{|\alpha| x} = e^{-|\alpha x|} \tag{A.20}$$

we finally obtain:

$$F_x^{-1}\left(\frac{\xi_2}{\left(\alpha^2+\xi_2^2\right)^2}\right) = \frac{1}{4} i \frac{x_2}{\mid \alpha \mid} e^{-|\alpha x_2|} \qquad , \forall \alpha \neq 0 \tag{A.21}$$

For α=0, the inversion is different and is given by:

$$F_x^{-1}\left(\frac{1}{\xi^3}\right) = \frac{1}{4} i x_2^2 \left(1 - 2H(x_2)\right) \qquad , \alpha = 0 \tag{A.22}$$

By applying this result to Eq. A.17, we have the result:

$$\psi'(x_1,x_2) = -\frac{b}{4} \sum_{k=-\infty \, and \neq 0}^{\infty} \frac{x_2}{2\pi \mid k \mid} \exp\left(\frac{2\pi i k x_1}{h}\right) \exp\left(-\frac{2\pi \mid k \mid \mid x_2 \mid}{h}\right) - \frac{b}{h}\frac{x_2^2}{4}\left(1 - 2H(x_2)\right)$$

which can be simplified if we make advantage of the following expression:

$$\begin{aligned} \sum_{k=-\infty \, and \neq 0}^{\infty} \exp\left(\frac{2\pi i k x_1}{h}\right) &= \sum_{k=1}^{\infty}\left(\exp\left(\frac{2\pi i k x_1}{h}\right) + \exp\left(-\frac{2\pi i k x_1}{h}\right)\right) \\ &= \sum_{k=1}^{\infty} 2\cos\left(\frac{2\pi k x_1}{h}\right) \end{aligned} \tag{A.23}$$

Moreover, H(x) is defined through the *sign* function by:

$$H(x) = \frac{1}{2}\left(1 + sign(x)\right) \tag{A.24}$$

The solution of Eq. A.1 is finally given by:

$$\psi'(\underline{x}) = -\frac{b}{4\pi}\sum_{k=1}^{\infty}\frac{x_2}{k}\cos\left(\frac{2\pi k x_1}{h}\right)\exp\left(-\frac{2\pi k \mid x_2 \mid}{h}\right) + \frac{b}{h}\frac{x_2^2}{4}sign(x_2) \tag{A.25}$$

which gives the stress function $\psi'(\underline{x})$ of an infinite edge dislocation pile-up.

Appendix B: Application of Kröner's theory to the honeycomb network of screw dislocations

In this appendix, we propose to give the results regarding the hexagonal network of dislocations, also known as honeycomb network. As seen below, three sets of dislocations are necessary to build-up this network. It is therefore possible to build various networks with different combinations of edge or screw dislocations. In the following, the honeycomb network was chosen to be made of screw dislocations exclusively.

A first build-up of a honeycomb network of dislocations (Fig. XIV.12) was proposed by Mura [87] who calculated the total stress field by directly superposing the stress fields of the three sets of dislocations. Each stress field was calculated as a function of an edge- and a screw-type component, under the assumption that no dislocation had a component in the x_3-direction (i.e. normal to the network plan). In this condition, the stress field could be calculated. However, only the total normal stress σ_{33} was provided, because of its relative simplicity. In addition to tedious cyclic permutations of subscripts in order to obtain all the stress components, the solution was given under the form of Fourier series, as it is done here as well, but with complex coefficients.

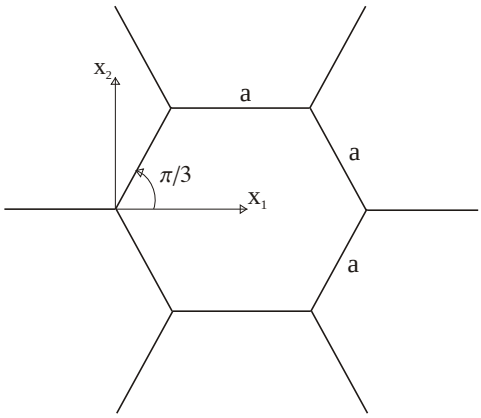

Figure XIV.12: Part of a honeycomb network

Later, Rey and Saada [111] proposed to determine the total dislocation density tensor. For that purpose, they started from a unit cell of dislocation as shown in Fig. XIV.13. However, the final expression of the dislocation density tensor, provided in the Fourier space, can not be directly computed, hence the stress field neither.

The approach used to solve the internal stress problem of a honeycomb network of screw dislocations is somewhat similar to the one proposed by Mura [87]. We clearly make use of

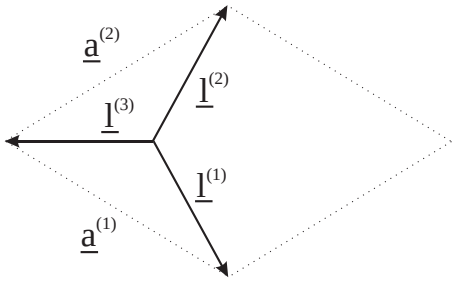

Figure XIV.13: Unit cell as defined by Rey and Saada [111]

the tensor of dislocation density, but we also take advantage of using Kröner's theory and extending the resolution method of appendix A to a 3D-problem.

The steps presented here are successively:

- Geometrical build-up of the network, under the condition that the three Burgers vectors obey the node law at each dislocation knot:

$$\sum_{i=1}^{3} \underline{b_i} = 0$$

- Definition of the incompatibility tensor: the tensor of dislocation density is first written in a relative basis for only one set of screw dislocations (since all sets of dislocations are screw-type).

- Calculation of the stress function tensor corresponding to previous dislocation density tensor. The total stress function of the network is then obtained by adding the contributions from the other two rotated sets of screw dislocations.

- Calculation of the total stress function tensor and stress field

The last step is not entirely complete.

Geometrical build-up of the dislocation network

Fig. XIV.14 shows the illustration of the network. It consists of an initial set of dislocations (red vectors in Fig. XIV.14). Because the network is assumed to be infinite in an infinite medium, the other two sets can be obtained simply by a rotation of $\pm 2\pi/3$. The length of the regular hexagon is taken as h.

It can be seen that at every dislocation knot, the sum of the three Burgers vectors is zero, whether the three vectors are converging to a knot or starting from a knot. This condition has always to be respected when considering dislocation networks.

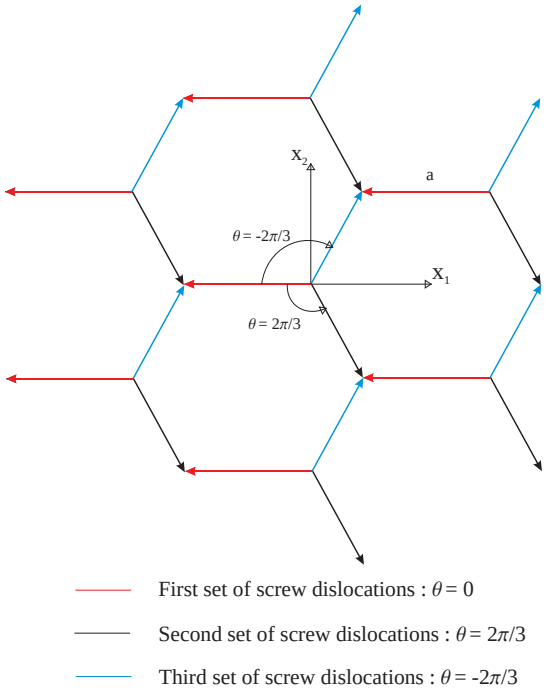

Figure XIV.14: Illustration of honeycomb network of dislocations, indicating the three sets of screw dislocations and their Burgers vector.

The incompatibility tensor

The second step of the method consists of writing the dislocation density tensor of the first dislocation set. The first Airy stress function is then deduced. The two other stress functions are calculated by performing rotations from the first dislocation set. This approach is mathematically correct if the following expression is fulfilled:

$$\underline{\underline{R}}^t . \left(\underline{\underline{\alpha}}\right)_{sym} . \underline{\underline{R}} = \left(\underline{\underline{R}}^t . \underline{\underline{\alpha}} . \underline{\underline{R}}\right)_{sym} \tag{B.1}$$

where $\underline{\underline{R}}$ is the rotation tensor in order to obtain the two other sets of dislocations from the first one, the superscript "t" holds for the tensor transposition and the subscript "sym" for the tensor symmetrisation. Eq. B.1 means that we can either consider a single dislocation density tensor which is then rotated to give the total incompatibility tensor, hence stress function tensor, or consider the single dislocation density tensor from which the single incompatibility tensor is deduced, hence the single stress function tensor, which is rotated to give the total stress function tensor. The latter possibility is kept in the following. It is easily shown that Eq. B.1 is respected.

The tensor of dislocation density for the first set of screw dislocations is reduced to a single component, and can be expressed in terms of Dirac delta functions and Heaviside step

functions, as follows:

$$\begin{aligned}\alpha_{11} &= b\sum_{n=-\infty}^{\infty}\left[H\left(x_1'-(3n-1)h\right)-H\left(x_1'-3nh\right)\right]\times\sum_{m=-\infty}^{\infty}\delta\left(x_2'-mh\sqrt{3}\right)\times\delta\left(x_3\right)\\ &\quad+b\sum_{n=-\infty}^{\infty}\left[H\left(x_1'-(3n+\frac{1}{2})h\right)-H\left(x_1'-3(n+\frac{1}{2})h\right)\right]\\ &\quad\times\sum_{n=-\infty}^{\infty}\delta\left(x_2'-\frac{1}{2}(2m+1)h\sqrt{3}\right)\times\delta\left(x_3\right)\end{aligned}\tag{B.2}$$

from which the incompatibility tensor $\underline{\underline{\eta}}$ is derived:

$$\eta_{il}=\left(e_{ijk}\,\alpha_{lj,k}\right)_{sym}\tag{B.3}$$

The latter equation gives:

$$\underline{\underline{\eta}}=\left[\begin{array}{ccc}0&\frac{-\alpha_{11,3}}{2}&\frac{\alpha_{11,2}}{2}\\ \frac{-\alpha_{11,3}}{2}&0&0\\ \frac{\alpha_{11,2}}{2}&0&0\end{array}\right]_R\tag{B.4}$$

Calculation of the stress function tensor associated to the first set of screw dislocations

For a given incompatibility tensor $\underline{\underline{\eta}}$, the stress function tensor is obtained by solving the following bi-harmonic equation as shown by Kröner [50]:

$$\nabla^4\psi_{ij}'=\eta_{ij}\tag{B.5}$$

Because the four latter equations are uncoupled, the solution of the stress function tensor will be given under the following form:

$$\underline{\underline{\psi}}'\left(\underline{x}'\right)=\left[\begin{array}{ccc}0&\psi_{12}'\left(\underline{x}'\right)&\psi_{13}'\left(\underline{x}'\right)\\ \psi_{12}'\left(\underline{x}'\right)&0&0\\ \psi_{13}'\left(\underline{x}'\right)&0&0\end{array}\right]\tag{B.6}$$

According to the different terms in Eq. B.2 and the derivatives which need to be calculated in Eq. B.4, it is seen that several bi-potential equations have to be solved. The first kind of equation is under the following form:

$$\nabla^4\psi'\left(\underline{x}\right)=\frac{b}{2}\sum_{n=-\infty}^{\infty}\left[H\left(x_1-(3n-1)h\right)-H\left(x_1-3nh\right)\right]\times\sum_{m=-\infty}^{\infty}\delta'\left(x_2-mh\sqrt{3}\right)\times\delta\left(x_3\right)\tag{B.7}$$

The solution of the latter equation is given by:

$$\begin{aligned}\psi'(\underline{x}) &= \frac{b}{2}\sum_{l=1}^{\infty}\left[\sum_{k=1}^{\infty}-\frac{l}{3kh^2}\sin\left(\frac{2\pi l}{h\sqrt{3}}x_2\right)\left[\sin\left(\frac{2\pi k}{3h}(x_1+h)\right)-\sin\left(\frac{2\pi k}{3h}x_1\right)\right]\right.\\ &\times\frac{\left(1+\mid x_3\mid\sqrt{\left(\frac{2\pi k}{3h}\right)^2+\left(\frac{2\pi l}{h\sqrt{3}}\right)^2}\right)\exp\left(-\mid x_3\mid\sqrt{\left(\frac{2\pi k}{3h}\right)^2+\left(\frac{2\pi l}{h\sqrt{3}}\right)^2}\right)}{\left[\left(\frac{2\pi k}{3h}\right)^2+\left(\frac{2\pi l}{h\sqrt{3}}\right)^2\right]^{3/2}}\\ &\left.-\frac{\pi l}{9h^2}\sin\left(\frac{2\pi l}{h\sqrt{3}}x_2\right)\frac{\left(1+\frac{2\pi l}{h\sqrt{3}}\mid x_3\mid\right)\exp\left(-\frac{2\pi l}{h\sqrt{3}}\mid x_3\mid\right)}{\left(\frac{2\pi l}{h\sqrt{3}}\right)^3}\right]\end{aligned}\tag{B.8}$$

The second left-hand side term in Eq. B.2 leads to solve the second kind of equation:

$$\nabla^4\psi'(\underline{x})=\frac{b}{2}\sum_{n=-\infty}^{\infty}\left[H\left(x_1-(3n-1)h\right)-H\left(x_1-3nh\right)\right]\times\sum_{m=-\infty}^{\infty}\delta\left(x_2-mh\sqrt{3}\right)\times\delta'(x_3)\tag{B.9}$$

which solution is:

$$\begin{aligned}\psi'(\underline{x}) &= b\left[-\sum_{l=1}^{\infty}\sum_{k=1}^{\infty}\frac{1}{4h\sqrt{3}\pi k}\left[\sin\left(\frac{2\pi k}{3h}(x_1+h)+\frac{2\pi l}{h\sqrt{3}}x_2\right)+\sin\left(\frac{2\pi k}{3h}(x_1+h)-\frac{2\pi l}{h\sqrt{3}}x_2\right)\right.\right.\\ &\left.-\sin\left(\frac{2\pi k}{3h}x_1-\frac{2\pi l}{h\sqrt{3}}x_2\right)-\sin\left(\frac{2\pi k}{3h}x_1+\frac{2\pi l}{h\sqrt{3}}x_2\right)\right]\frac{x_3\exp\left(-\mid x_3\mid\sqrt{\left(\frac{2\pi k}{3h}\right)^2+\left(\frac{2\pi l}{h\sqrt{3}}\right)^2}\right)}{\sqrt{\left(\frac{2\pi k}{3h}\right)^2+\left(\frac{2\pi l}{h\sqrt{3}}\right)^2}}\\ &-\sum_{k=1}^{\infty}\left[\sin\left(\frac{2\pi k}{3h}(x_1+h)\right)-\sin\left(\frac{2\pi k}{3h}x_1\right)\right]\frac{x_3\exp\left(-\frac{2\pi k}{3h}\mid x_3\mid\right)}{8\pi^2k^2h}\\ &\left.-\sum_{l=1}^{\infty}\cos\left(\frac{2\pi l}{h\sqrt{3}}x_2\right)\frac{x_3\exp\left(-\frac{2\pi l}{h\sqrt{3}}\mid x_3\mid\right)}{12\pi l\sqrt{3}}+\frac{x_3^2}{12h\sqrt{3}}sign\left(x_3\right)\right]\end{aligned}\tag{B.10}$$

Eqs. B.8 and B.10 are then sufficient to calculate the stress function tensor induced by the first set of screw dislocations.

Calculation of the total stress function tensor

The other stress function tensors are determined from the first one by performing a rotation of $\pm 2\pi/3$. As the honeycomb network lies in the plan normale to the x_3-direction, the rotation tensor is defined by:

$$\underline{\underline{R}}_\theta=\begin{bmatrix}\cos\theta & \sin\theta & 0\\ -\sin\theta & \cos\theta & 0\\ 0 & 0 & 1\end{bmatrix}\tag{B.11}$$

The stress function tensor of any of the two other set of screw dislocations is then deduced from the following equation:

$$\underline{\underline{\psi}}'^i=\underline{\underline{R}}_\theta^{-1}.\underline{\underline{\psi}}'.\underline{\underline{R}}_\theta\tag{B.12}$$

in which $\underline{\underline{R}}_\theta$ is an orthogonal matrix and its inverse can therefore be calculated as $\underline{\underline{R}}_\theta^{-1} = \underline{\underline{R}}_\theta^t$. The value of the superscript i in Eq. B.12 corresponds to the different sets of dislocations:

$$\begin{cases} i = 1: & \theta = 0 \\ i = 2: & \theta = \frac{2\pi}{3} \\ i = 3: & \theta = -\frac{2\pi}{3} \end{cases} \tag{B.13}$$

For a given angle, the corresponding stress function is expressed in its relative basis by:

$$\underline{\underline{\psi}}'^i\left(\underline{x}^i\right) = \begin{bmatrix} -2\psi'_{12}\left(\underline{x}^i\right)\cos\theta\sin\theta & \psi'_{12}\left(\underline{x}^i\right)\left(\cos^2\theta - \sin^2\theta\right) & \psi'_{13}\left(\underline{x}^i\right)\cos\theta \\ \psi'_{12}\left(\underline{x}^i\right)\left(\cos^2\theta - \sin^2\theta\right) & 2\psi'_{12}\left(\underline{x}^i\right)\cos\theta\sin\theta & \psi'_{13}\left(\underline{x}^i\right)\sin\theta \\ \psi'_{13}\left(\underline{x}^i\right)\cos\theta & \psi'_{13}\left(\underline{x}^i\right)\sin\theta & 0 \end{bmatrix}_{R^i} \tag{B.14}$$

with $\underline{x}^i$ defined by $\underline{x}^i = \underline{\underline{R}}^i_\theta.\underline{x}$ are the coordinates of a point in the relative basis linked to a given set of dislocations. The relation between the absolute and relative coordinate systems is also obtained from a rotation:

$$\underline{x} = \left(\underline{\underline{R}}^i_\theta\right)^t.\underline{x}^i \tag{B.15}$$

Finally, the total stress function tensor is obtained when considering the contributions from the three sets of dislocations, expressed in the absolute basis:

$$\underline{\underline{\psi}}'\left(\underline{x}\right) = \underline{\underline{\psi}}'^1\left(\underline{x}^1\right) + \underline{\underline{\psi}}'^2\left(\underline{x}^2\right) + \underline{\underline{\psi}}'^3\left(\underline{x}^3\right) \tag{B.16}$$

For the calculation of the total stress field, the last step consists of using Eq. IX.36 given by Kröner, which is here reminded (as Eq. B.17):

$$\sigma_{ij} = 2\mu\left(\Delta\psi'_{ij} - \frac{1}{1-\nu}\left(\psi'_{kk,ij} - \Delta\psi'_{kk}\,\delta_{ij}\right)\right) \tag{B.17}$$

However, a mathematical simplification of Eqs. B.8 and B.10 should be first investigated before any further calculation. This part could not be treated in the present work but is still under consideration as a direct application of Kröner's theory.

Appendix C: FORTRAN program for the calculation of the interstitial loop size distribution in $(U_{0.9},Pu_{0.1})O_2$

This appendix presents the Fortran code used to calculate the size distribution of the interstitial-type dislocation loops in $(U_{0.9},Pu_{0.1})O_2$. At the end of the main program, the subroutines for the re-solution of interstitials from the loops and the coalescence of diffusing loops are provided as well. The code given here initially takes into account the coalescence of loops (subroutine "fonc"), but the user may choose to consider the re-solution process by calling the subroutine "foncresol" instead.

In this example, some parameters are stored in the file "param_coal_5-18_5" and the calculated solutions in the file "result_run_coal_5-18_5". It is also shown how a "restart" was used, in order to increase the number of equations with the computation time: the last iteration is transfered to the file "restart_coal_5-18_5" which is called at the beginning of the next run. For a new run, this part has to be put in comments, and all unknown are initialized to zero.

```
      PROGRAM distribution
c
      IMPLICIT NONE
c
      integer i, j, m, neq
      double precision y, ydot, tmin, tmax, dtout, timp, tout
      double precision tmUO2, den, molw, avn, nav, a, bv, vol,
     &     vol23, zvrho, zirho, nuv, nui, evmUO2, evm, evfUO2, evf,
     &     eimUO2, eim, fden, xi, fn, rg, volg, tk, tm, bolzev, bolzcal,
     &     rgas, rtk, ktk, ktkcal, wov, woi, di, dv, alpha, K, G,
     &     Pi, K1, Kdi, Rha, Lha, ccell
      parameter (neq=5000)
      dimension y(neq), ydot(neq), Rha(neq-1), Lha(neq-1)
c
      write(6,*)
      write(6,*)" ****************************************"
      write(6,*)" Interstitial loop size distribution program"
      write(6,*)" ****************************************"
c
c     Importation of the last calculated distribution
      open(unit=77,file='restart_coal_5-18_5')
      read(77,10) timp
 10   format(e18.8)
      do m=1,3499
```

```
                read(77,*) y(m)
            enddo
            do m=3500,neq-1
                y(m)=y(3499)
            enddo
            read(77,*,end=11) y(neq)
c
  11        close(77)
c
c           timp = 0.0D0
c           interstitials
c           y(1) = 0.0D0
c           di-interstitials
c           y(2) = 0.0D0
c           do m=3,neq-2
c               y(m)= 0.0D0
c           enddo
c           last equation
c           y(neq-1) = 0.0D0
c           vacancies
c           y(neq) = 0.0D0
c
            open(unit=99, file = 'result_run_coal_5-18_5')
            open(unit=88, file = 'param_coal_5-18_5')
c
            Pi = 4.*datan(1.0D0)
c
            tmUO2 = 3123.0D0
            den = 10.96D0
            molw = 270.0D0
            avn = 6.023D23
            nav = (den/molw)*avn
c
            a = 5.47D-8
            bv = dsqrt(2.0D0)*a/2.
c
            vol = 4.2D-23
            vol23 = vol**(2./3.)
c
            zvrho = 1.0D0
            zirho = 1.0005D0
c
            nuv = 5.0D13
            nui = 5.0D12
            evmUO2 = 2.4D0
            evm = evmUO2
            evfUO2 = 3.0D0
            evf = evfUO2
c           ######################## Eim
            eimUO2 = 0.7D0
            eim = eimUO2
c
            fden = 1.0D0
```

```
c
c       ######################## xi
        xi = 0.025D0
        fn = 1.0D0
        rg = 2.16D-8
        volg = (4./3.)*Pi*(rg**3)
c
        tk = 298.0D0
        tm = tmUO2
c
        bolzev = 8.625D-5
        bolzcal = 1.98D0
        rgas = 1.38D-16
        rtk = rgas*tk
        ktk = bolzev*tk
        ktkcal = bolzcal*tk
c
        wov = nuv*dexp(-evm/ktk)
        woi = nui*dexp(-eim/ktk)
        dv = xi*(a**2)*wov
        di = (2.*xi*(a**2)*woi/3.)
c
        alpha = 12.*(wov+woi)
        K = 0.2*9.06D-9
        G = 3.82D11
c
        ccell= 4.599D-8
c
        K1 = 12.*(wov+woi)
        Kdi = dsqrt(2.0D0)*di/(vol23)
        Rha(1)=0.0D0
        Lha(1)=0.0D0
        do m=2,neq-1
                Rha(m)=(2.*Pi/vol)*zirho*di*dsqrt(m*(ccell**2)/Pi)
                Lha(m)=(2.*Pi/vol)*zvrho*dv*dsqrt(m*(ccell**2)/Pi)
        enddo
c
        tmin = timp
        tmax = 2.2D8
c       ###################### deltat
        dtout = 5.0D1
c
        write(88,*) eim, xi, di, dv, alpha, neq, dtout
        close(88)
c
        write (6,120)
  120   format(//' time ci c2i c(n-1)i cni cv'//)
        do tout=tmin, tmax, dtout
                call fonc(neq, y, ydot, K, K1, Kdi, Rha, Lha, di)
                do i=1,neq
                        y(i)=y(i)+ydot(i)*dtout
                enddo
                if (MOD(tout, 1.0D6).eq.0.) then
```

```
                        write(6,140) tout, y(1), y(2), y(neq-2), y(neq-1), y(neq)
 140                    format(d14.5,d14.5,d14.5,d14.5,d14.5,d14.5)
                        write(99,141) tout
 141                    format(d18.8)
                        do j=1,neq
                                write(99,*) y(j)
                        enddo
                endif
        enddo
        close(99)
c
        write(6,*)
        write(6,*)" ********** "
        write(6,*)" Calculation OK ! "
        write(6,*)" ********** "
        END
c
c
c       ////////////////////////////////////////////////////
c       SUBROUTINES
c       ////////////////////////////////////////////////////
c
c       *************************
c       Subroutine for coalescence
c       *************************
c
        subroutine fonc(neq, y, ydot, K, K1, Kdi, Rha, Lha, di)
        implicit none
        integer neq, m, i, j
        double precision y, ydot, K, K1, Kdi, sumR, sumL,
     &          Rha, Lha, coal_plus, coal_minus, Pi, ccell, vol, Dvol,
     &          a, di
        dimension y(neq), ydot(neq), Rha(neq-1), Lha(neq-1),
     &          coal_plus(neq-1), coal_minus(neq-1)
c
        Pi = 4.*atan(1.0D0)
c
        a = 5.47D-8
        vol = 4.2D-23
        ccell = 4.599D-8
c       ############### Dvol
        Dvol = di
c
        sumL=0.0D0
        do m=2,neq-1
                sumL = sumL + Lha(m)*y(m)
        enddo
        sumL = sumL*y(neq)
c
        sumR=0.0D0
        do m=2,neq-2
                sumR = sumR + Rha(m)*y(m)
        enddo
```

```
      sumR = sumR*y(1)
c
      do i=2,neq-1
            coal_plus(i) = 0.0D0
            do j=2,i
                  if ((i-j).gt.0) then
                        coal_plus(i) = coal_plus(i)
     &                        + (dsqrt(dble(j))+dsqrt(dble(i-j)))
     &                        *(1./dsqrt(dble(j))+1./dsqrt(dble(i-j)))*y(j)*y(i-j)
                  endif
            enddo
            coal_plus(i) = (8.*a*Dvol)/(vol*Pi)*coal_plus(i)
            coal_minus(i) = 0.0D0
            do j=2,neq-1
                  coal_minus(i) = coal_minus(i)
     &                  + (dsqrt(dble(i))+dsqrt(dble(j)))
     &                  *(1./dsqrt(dble(i))+1./dsqrt(dble(j)))*y(i)*y(j)
            enddo
            coal_minus(i) = (8.*a*Dvol)/(vol*Pi)*coal_minus(i)
      enddo
c
c     ci
      ydot(1) = K - K1*y(neq)*y(1) - Kdi*y(1)*y(1) - sumR
     &     + Lha(2)*y(2)*y(neq)
c     c2i
      ydot(2) = (1./2.)*Kdi*y(1)*y(1) + Lha(3)*y(3)*y(neq)
     &     - Lha(2)*y(2)*y(neq) - Rha(2)*y(2)*y(1)
     &     + coal_plus(2) - coal_minus(2)
c
      do m=3,neq-2
            ydot(m) = Rha(m-1)*y(m-1)*y(1) + Lha(m+1)*y(m+1)*y(neq)
     &           - Rha(m)*y(m)*y(1) - Lha(m)*y(m)*y(neq)
     &           + coal_plus(m) - coal_minus(m)
      enddo
c     last equation
      ydot(neq-1) = Rha(neq-2)*y(neq-2)*y(1)
c     - Rha(neq-1)*y(neq-1)*y(1)
     &           - Lha(neq-1)*y(neq-1)*y(neq)
     &           + coal_plus(neq-1) - coal_minus(neq-1)
c     vacancies
      ydot(neq) = K - K1*y(neq)*y(1) - sumL
c
      return
      end
c
c     *************************
c     Subroutine for re-solution
c     *************************
c
      subroutine foncresol(neq, y, ydot, K, K1, Kdi, Rha, Lha, di)
      implicit none
      integer neq, m, i, j, imp
      double precision y, ydot, K, K1, Kdi, sumR, sumL,
```

```
     &          Rha, Lha, K3, F, mua, ra, di, a,
     &          Pi, ccell
       dimension y(neq), ydot(neq), Rha(neq-1), Lha(neq-1)
c
       Pi = 4.*datan(1.0D0)
c
       a = 5.47D-8
       F = 3.82D11
       ccell= 4.599D-8
c      ############## mua
       mua = 10.0D-7
c
       ra = dsqrt(4.0135D-20/(Pi*mua))
       imp = floor(Pi*ra**2/ccell**2)+1
c
       sumL=0.0D0
       do m=2,neq-1
            sumL = sumL + Lha(m)*y(m)
       enddo
       sumL = sumL*y(neq)
c
       sumR=0.0D0
       do m=2,neq-2
            sumR = sumR + Rha(m)*y(m)
       enddo
       sumR = sumR*y(1)
c
c      Number of re-soluted interstitials
       K3=0.0D0
       do i=2,neq-1
            K3 = K3 + y(i)*(dble(i))*dble(min(i,imp))
       enddo
       K3 = K3*F*mua*(ccell**2)
c
c      ci
       ydot(1) = K - K1*y(neq)*y(1) - Kdi*y(1)*y(1) - sumR
     &          + Lha(2)*y(2)*y(neq) + K3
c      c2i
       ydot(2) = (1./2.)*Kdi*y(1)*y(1) + Lha(3)*y(3)*y(neq)
     &          - Lha(2)*y(2)*y(neq) - Rha(2)*y(2)*y(1)
     &          + y(2+imp)*F*mua*(dble(2+imp))*(ccell**2)
     &          - y(2)*F*mua*(dble(2))*(ccell**2)
c
       do m=3,neq-2
            if (m.lt.(neq-1-imp)) then
                 ydot(m) = Rha(m-1)*y(m-1)*y(1) + Lha(m+1)*y(m+1)*y(neq)
     &                     - Rha(m)*y(m)*y(1) - Lha(m)*y(m)*y(neq)
     &                     + y(m+imp)*F*mua*(dble(m+imp))*(ccell**2)
     &                     - y(m)*F*mua*(dble(m))*(ccell**2)
            else
                 ydot(m) = Rha(m-1)*y(m-1)*y(1) + Lha(m+1)*y(m+1)*y(neq)
     &                     - Rha(m)*y(m)*y(1) - Lha(m)*y(m)*y(neq)
     &                     - y(m)*F*mua*(dble(m))*(ccell**2)
```

```
                endif
            enddo
c           last equation
            ydot(neq-1) = Rha(neq-2)*y(neq-2)*y(1)
c           - Rha(neq-1)*y(neq-1)*y(1)
           &          - Lha(neq-1)*y(neq-1)*y(neq)
           &          - y(neq-1)*F*mua*(dble(neq-1))*(ccell**2)
c           vacancies
            ydot(neq) = K - K1*y(neq)*y(1) - sumL
c
            return
            end
```

Bibliography

[1] S. Amelinckx, D. van Dyck, and J. van Landuyt. *Handbook of Microscopy: Applications in Materials Science, Solid-State Physics and Chemistry*. 1997.

[2] F. Anselin. The Role of Fission Products in the Swelling of Irradiated UO_2 and (U,Pu)O_2 Fuel. *USAEC Report GEAP-5583*, General Electric Company, January 1969.

[3] K.H.G. Ashbee. Stacking faults in uranium dioxide. *Proceedings of the Royal Society of London*, A280:37–46, 1964.

[4] H. Assmann and R. Manzel. The matrix swelling rate of UO_2. *Journal of Nuclear Materials*, 68:360–364, 1977.

[5] H. Bailly, D. Ménessier, and C. Prunier. *Le combustible nucléaire des réacteurs à eau sous pression et des réacteurs à neutrons rapides. Conception et comportement*, volume Série Synthèses. 1996.

[6] J.O. Barner, M.E. Cunningham, M.D. Freshley, and D.D. Lanning. Relationship between Microstructure and Fission Gas Release in High Burn-up UO_2 Fuel with Emphasis on the Rim Region. *ENS Int. Top. Meeting on LWR Fuel Performance, "Fuel for the 90's"*, pages 538–548, Avignon, France, April 21^{st}-24^{th}, 1991.

[7] J.O. Barner, M.E. Cunningham, M.D. Freshley, and D.O. Lanning. High Burn-up Effects Program Final Report. *HBEP-61*, Battelle Pacific Northwest Laboratories, 1990.

[8] W.K. Barney and B.D. Wemble. Metallography of UO_2-Containing Fuel Elements. *KAPL-1836*, January, 15^{th} 1958.

[9] D. Baron. High burn-up structure observations and modelling. *Int. Workshop on the High Burn-up Structure in Nucl. Fuels*, ITU, Karlsruhe, Germany, June 28^{th}-30^{th}, 2004.

[10] D. Baron. Porosity Buildup in the Fuel Periphery at High Burnup. *HBEP Steering Committee Meeting*, Wengen, Switzerland, June 1986.

[11] D. Baron, B. Hermitte, and J.P. Piron. An attempt to simulate the porosity buildup in the RIM at high burnup. *Technical Committee Meeting on Advances in Pellet Technology for Improved Performance at High Burnup*, IAEA, Tokyo, Japan, Oct. 28^{th} - Nov. 1^{st}, 1996.

[12] D. Baron and J. Spino. Does rim mistructure formation degrade the fuel rod performance. *Technical Committee Meeting on Technical and Economic Limits to Fuel Burnup Extension*, IAEA, San Carlos de Bariloche, Argentina, Nov. 15^{th}-19^{th}, 1999.

[13] J. Belle. Uranium Dioxide: Properties and Nuclear Applications. *Navel Reactors Handbooks*, United States Atomic Energy Commission, 1961.

[14] E. Beltrami. Osservazioni Sulla Nota Precedente. *Atti Accad Nazl Lincei*, 1:141–142, 1892.

[15] B.A. Bilby, R. Bullough, and E. Smith. Continuous distributions of dislocations. a new application of the methods of non-riemannian geometry. *Proceedings of the Royal Society of London*, A263:263, 1955.

[16] M.L. Bleiberg, R.M. Bennan, and B. Lustman. Effects of High Burn-up on Oxide Ceramic Fuels. *Symposium on Radiation Damage in Solids and Reactor Materials*, IAEA, Venice, Italy, May 7^{th}-11^{th}, 1962.

[17] S.D. Borisova and I.I. Naumov. Dislocation pileups: topological features of stresses and strains. *Theoretical and Applied Fracture Mechanics*, 35:237–242, 2001.

[18] A.D. Brailsford and R. Bullough. The rate theory of swelling due to void growth in irradiated metals. *Journal of Nuclear Materials*, 44:121–135, 1972.

[19] R. Brandt and J. Neuer. *Journal of Non-Equilibrium Thermodynamics*, 1:3, 1976.

[20] S. Brémier, R. Manzel, and C.T. Walker. Fission gas release and fuel swelling at burnups higher than 50 MWd/kgU. *Proceedings of International Seminar on Fission Gas Behaviour in Water Reactor Fuels*, pages 93–106, Cadarache, September 2000.

[21] L.M. Brown, A. Kelly, and R.M. Mayer. The influence of Boron on the clustering of radiation damage in Graphite: II. Nucleation of interstitial loops. *Philosophical Magazine*, 19:721–741, 1969.

[22] J.M. Burgers. Some considerations on the fields of stress connected with dislocations in a regular crystal lattice. *Proc. Akad. Sci. Amst.*, 42:293–378, 1939.

[23] V.F. Chkuaseli and Hj. Matzke. Modelling of Microstructure Transformations (RIM Effect) in High Burnup LWR Nuclear Fuels. The Physical Aspects of the RIM Effect in Uranium Dioxide. *Institute for Transuranium Elements, Internal Report*, July, 1996.

[24] J. Cobos, Hj. Matzke, V.V. Rondinella, T. Wiss, and A. Martinez-Esparza. α-Radiolysis effects on UO_2 dissolution. *Proc. of Int. Conf. on Future Nuclear Systems, GLOBAL '99, American Nuclear Society*, Jackson Hole, WY, U.S.A., Aug. 29^{th} - Sept. 3^{rd}, 1999.

[25] A.H. Cottrell. *Dislocations and Plastic Flow in Crystals*. Clarendon Press, Oxford, 1953.

[26] M.E. Cunningham, M.D. Freshley, and D.O. Lanning. Development and characteristics of the rim region in high burnup UO_2 fuel pellets. *Journal of Nuclear Materials*, 188:19–27, 1992.

[27] J.D. Eshelby. The determination of the elastic field of an elliptical inclusion, and related problems. *Proc. Roy. Soc.*, 241A:376396, 1957.

[28] A.G. Evans. *Fracture Mechanics Applied to Brittle Materials*, volume ASTM STP 678, Part 2. S.W. Freiman (American Society for Testing and Materials), 1979.

[29] A.G. Evans and P.L. Pratt. Dislocations in the Fluorite Structure. *Philosophical Magazine*, 20:1213–1237, 1969.

[30] Y. Eyal. *Radiation Waste Management and Environmental Remediation.* Am. Soc. Mech. Eng. R. Baker, S. Slate and G. Benda, 1997.

[31] V.M. Goldschmidt and L. Thomassen. *Cited in Tech. Rept. Ser. Intern. At. Energy*, 39:3–15, 1965.

[32] G.W. Greenwood and M.V. Speight. An analysis of the diffusion of fission gas bubbles and its effect on the behaviour of reactor fuels. *Journal of Nuclear Materials*, 10:140–144, 1963.

[33] N. Hansen and D. Kuhlmann-Wilsdorf. Low Energy Dislocation Structures due to Unidirectional Deformation at Low Temperatures. *Materials Science and Engineering*, 81:141–161, 1986.

[34] M.R. Hayns. The nucleation and early growth of interstitial dislocation loops in irradiated materials. *Journal of Nuclear Materials*, 56:267–274, 1975.

[35] B. Hermitte. Etude et modélisation du rim dans le combustible des crayons REP. Thèse, Université de Provence, Aix-Marseille I, 1996.

[36] K. Hesketh. Advanced fuel designs for existing and future generations of reactors : driving factors from technical and economic points of view. *Nuclear Engineering and Design*, 221:277–292, 2003.

[37] J. Nowotny Hj. Matzke, in: L.C. Dufour. *Surfaces and Interfaces of Ceramics Materials.* Kluwer Academic, Dordrecht, 1989.

[38] J. Jonnet. Towards a better understanding of the role of stress in restructuring of radiation damage. *Proc. of 18^{th} Int. Conf. on Structural Mechanics in Reactor Technology*, pages 606–618, Beijing, China, Aug. 7^{th}-12^{th}, 2005.

[39] J. Jonnet, B. Rémy, and P. Van Uffelen. Stress function determination for dislocation configurations obtained from Kröner's theory. *Theoretical and Applied Fracture Mechanics*, 45:238–251, 2006.

[40] T. Kameyama, T. Matsumura, and M. Kinoshita. Numerical Analysis for Microstructure Change of a Light Water Reactor Fuel Pellet at High Burn-up. *Nuclear Tech.*, 106:334–341, 1994.

[41] M. Kinoshita. Towards the mathematical model of rim structure formation. *Journal of Nuclear Materials*, 248:185–190, 1997.

[42] M. Kinoshita, E. Kolstad, Hj. Matzke, and V.V. Rondinella. High Burnup Rim Project: (V) Complete scope and needs for further study. *Proc. of Enlarged Halden Program Group Meeting*, Loen, Norway, May 24^{th}-29^{th}, 1999.

[43] M. Kinoshita, T. Sonoda, S. Kitajima, A. Sasahara, E. Kolstad, Hj. Matzke, V.V. Rondinella, A.D. Stalios, C.T. Walker, I.L.F. Ray, M. Sheindlin, D. Halton, and C. Ronchi. High Burn-up Rim Project, (II) Irradiation and examination to investigate rim-structured fuel. *Proc. Int. ANS Top. Meet. on LWR Fuel Perf.*, Park City, Utah, USA, April 2000.

[44] H. Kleykamp. The chemical state of the fission products in oxide fuels. *Journal of Nuclear Materials*, 131:221–246, 1985.

[45] S. Koizumi, H. Umehara, and Y. Wakashima. *Proc. IAEA Technical Committee Meeting on Fuel Performance at High Burnup for Water Reactors*, Nykoping, 1990.

[46] M.A. Krivoglaz. *X-Ray and Neutron Diffraction in Nonideal Crystals*. Springer, Berlin, 1995.

[47] E. Kröner. *Zeitschrift für Physik*, 141:386, 1955.

[48] E. Kröner. *Zeitschrift für Physik*, 142:463, 1955.

[49] E. Kröner. Die inneren Spannungen und der Inkompatibilitätstensor in der Elastizitätstheorie. *Z. Angew. Phys.*, 7:249–257, 1955.

[50] E. Kröner. *Kontinuumstheorie der Versetzungen und Eigenspannungen*. Springer Verlag, 1958.

[51] E. Kröner. Continuum theory of defects. *Proc. of Physics Summer School: "Physics of Defects"*, pages 282–315, Les Houches, France, July 28^{th} – August 29^{th}, 1980.

[52] E. Kröner. Benefits and shortcomings of the continuous theory of dislocations. *International Journal of Solids and Structures*, 38:1115–1134, 2001.

[53] K. Lassmann, C.T. Walker, J. Van de Laar, and F. Lindström. Modelling the high burn-up UO_2 structure in LWR fuel. *Journal of Nuclear Materials*, 226:1–8, 1995.

[54] J.M. Lefebvre, J. Soullard, R.J. Gaboriaud, and J. Grilhe. Calcul d'énergie de fautes d'empilement dans le dioxyde d'uranium. *Journal of Nuclear Materials*, 60:59–65, 1976.

[55] C. Lemaignan. *Science des matériaux pour le nucléaire*, volume Collection Génie Atomique. EDP Sciences.

[56] S.E. Lemekhov. Computer code ASFAD : status, resent developments and applications. *International Topical Meeting on Light Water Reactor Performance*, pages 162–179, West Palm Beach, Florida, April 17^{th}-21^{st}, 1994.

[57] J.C.M. Li. Some elastic properties of an edge dislocation wall. *Acta Metallurgica*, 8:563, 1960.

[58] A.B. Lidiard. Self-diffusion of Uranium in UO_2. *Journal of Nuclear Materials*, 19:106–108, 1966.

[59] V.V. Likhanskii, O.V. Khoruzhii, and A.A. Sorokin. Physical model development for prediction of rim-layer formation in UO_2 fuel. *Atomic Energy*, 96(2):113, 2004.

[60] V.V. Likhanskii, O.V. Khoruzhii, and A.A. Sorokin. Physical model of rim-layer formation in UO_2 fuel. *Int. Workshop on the High Burn-up Structure in Nucl. Fuels*, ITU, Karlsruhe, Germany, June 28^{th}-30^{th}, 2004.

[61] V.V. Likhanskii and V.G. Zborovskii. On stability of spatial distributions of crystal structure defects in irradiated high burnup UO_2 fuel. *Journal of Nuclear Materials*, 350:1–8, 2006.

[62] N. Lozano. La subdivision d'un solide induite par lévolution de sa composition chimique : Intérêt pour la céramique nucléaire à fort taux d'irradiation. Thesis, Université de Bourgogne, 1998.

[63] N. Lozano, L. Desgranges, D. Aymes, and J.C. Niepce. High magnification SEM observations for two types of granularity in a high burnup PWR fuel rim. *Journal of Nuclear Materials*, 257:78–87, 1998.

[64] P.S. Maiya. Surface diffusion, surface free energy, and grain-boundary free energy of uranium dioxide. *Journal of Nuclear Materials*, 40:57–65, 1971.

[65] R. Manzel and R. Eberle. Fission Gas Release at High Burn-up and the Influence of the Pellet Rim. *ENS Int. Top. Meeting on LWR Fuel Performance, "Fuel for the 90's"*, pages 528–537, Avignon, France, April 21^{st}-24^{th}, 1991.

[66] R. Manzel and C.T. Walker. EPMA and SEM of fuel samples from PWR rods with an average burn-up of around 100 MWd/kgHM. *Journal of Nuclear Materials*, 301:170–182, 2002.

[67] J. Marian, B.D. Wirth, R. Schäublin, G.R. Odette, and J.M. Perlado. MD modeling of defects in Fe and their interactions. *Journal of Nuclear Materials*, 323:181–191, 2003.

[68] J. Marian, B.D. Wirth, R. Schäublin, J.M. Perlado, and T. Diaz de la Rubia. <100>-Loop characterization in α-Fe: comparison between experiments and modeling. *Journal of Nuclear Materials*, 307-311:871–875, 2002.

[69] Hj. Matzke, , J. Ottaviani, D. Pellottiero, and J. Rouault. Oxygen potential of high burn-up fast breeder oxide fuel. *Journal of Nuclear Materials*, 160:142–146, 1988.

[70] Hj. Matzke. Radiation Damage in Crystalline Insulators, Oxides, and Ceramic Nuclear Fuels. *Radiation Effects*, 64:3–33, 1982.

[71] Hj. Matzke. Diffusion process in nuclear fuels. *Journal of Less-Common Metals*, 121:537–564, 1986.

[72] Hj. Matzke. *Fission-product behavior in ceramic oxide fuel.* volume 17 of Advances in Ceramics, I. J. Hastings, 1986.

[73] Hj. Matzke. Atomic transport properties in UO_2 and mixed oxides $(U,Pu)O_2$. *J. Chem. Soc., Faraday Trans. 2*, 83:1121, 1987.

[74] Hj. Matzke. On the rim effect in high burnup UO_2 LWR fuels. *Journal of Nuclear Materials*, 189:141–148, 1992.

[75] Hj. Matzke. Radiation damage in nuclear fuel materials. *Solid State Phenomena*, 30-31:355–366, 1993.

[76] Hj. Matzke. Oxygen potential in the rim region of high burnup UO_2 fuel. *Journal of Nuclear Materials*, 208:18–26, 1994.

[77] Hj. Matzke. Recent studies on the formation of the rim structure and on polygonization in LWR fuel. *Technical Committee Meeting on Technical and Economic Limits to Fuel Burnup Extension*, IAEA, San Carlos de Bariloche, Argentina, Nov. 15^{th}-19^{th}, 1999.

[78] Hj. Matzke. After nearly 50 years of research on fission rare gas diffusion and release from UO_2, what do we know for sure about single gas atom diffusion and what are the problems for the future? *Int. Workshop on the High Burn-up Structure in Nucl. Fuels*, ITU, Karlsruhe, Germany, June 28^{th}-30^{th}, 2004.

[79] Hj. Matzke, H. Blank, M. Coquerelle, K. Lassmann, I.L.F. Ray, C. Ronchi, and C.T. Walker. Oxide fuel transients. *Journal of Nuclear Materials*, 166:165, 1989.

[80] Hj. Matzke and M. Kinoshita. Polygonization and high burnup structure in nuclear fuels. *Journal of Nuclear Materials*, 247:108–115, 1997.

[81] Hj. Matzke and J. Spino. Formation of the rim structure in high burnup fuel. *Journal of Nuclear Materials*, 248:170–179, 1997.

[82] Hj. Matzke and T. Wiss. Radiation Damage in Nuclear Materials. Itu annual report (eur 19812), European Commission, Institute for Transuranium Elements, Karlsruhe, 2000.

[83] J.C. Maxwell. On reciprocal figures, frames and diagrams of forces. *Trans. Roy. Soc. Edinburgh*, 26:1, 1870.

[84] M. Mogensen, J.H. Pearce, and C.T. Walker. Behaviour of fission gas in the rim region of high burn-up UO_2 fuel pellets with particular reference to results from an XRF investigation. *Journal of Nuclear Materials*, 264:99–112, 1999.

[85] N.D. Morelon, D. Ghaleb, J.M. Delaye, and L. Van Brutzel. A new empirical potential for simulating the formation of defects and their mobility in uranium dioxide. *Philosophical Magazine*, 83:1533–1550, 2003.

[86] G. Morera. Soluzioni Generale Delle Equazioni Indefinite Dell'Eguilibrio di un Corpo Continuo. *Atti Accad Nazl Lincei*, 1:137–141, 1892.

[87] T. Mura. Periodic distributions of dislocations. *Proc. Roy. Soc. of London. Series A, Mathematical and Physical Sciences*, 280:528–544, 1964.

[88] S. M. Murphy. A model for segregation in dilute alloys during irradiation. *Journal of Nuclear Materials*, 168:31–42, 1989.

[89] M. Noe and J. Fuger. Self-Radiation Effects on the Lattice Parameter of $^{238}PuO_2$. *Inorganic and Nuclear Chemistry Letters*, 10:7–19, 1974.

[90] K. Nogita and K. Une. Radiation-induced microstructural change in high burnup UO_2 fuel pellets. *Nuclear Instruments and Methods in Physics Research*, B91:301–306, 1994.

[91] K. Nogita and K. Une. Irradiation-induced recrystallization in high burnup UO_2 fuel. *Journal of Nuclear Materials*, 226:302–310, 1995.

[92] J.F. Nye. Some geometrical relations in dislocated crystals. *Acta Metallurgica*, 1:153, 1953.

[93] D. R. Olander. *Fundamental Aspects of Nuclear Reactor Fuel Elements*. Technical Information Center, Energy Research and Development Administration, 1976.

[94] Y. Osetsky. Radiation damage theory I. *Proceedings of International School of Radiation Effects in Solids*, Erice, July 18^{th}-29^{th} 2004.

[95] S.R. Pati and A.M. Garde. Fission Gas Release from PWR Fuel Rods at Extended Burnups. *Proc. Int. ANS Top. Meet. on LWR Fuel Perf.*, Orlando, Florida, USA, April 21^{st}-24^{th} 1985.

[96] G.S. Peace. *Taguchi Methods: A Hands-on Approach*. Addison-Wesley, 1993.

[97] W.H. Press, B.P. Flannery, S.A. Teukolsky, and W.T. Vetterling. *Numerical Recipes in Fortran: The Art of Scientific Computing. Second Edition*. Cambridge University Press, Cambridge, 1989.

[98] L. Priester. Interaction joint de grains - dislocations : les dislocation extrinsèques. *Ecole d'été de Métallurgie Physique: "Les Joints de Grains dans les Matériaux"*, pages 231–260, Carry-Le-Rouet, France, September 20^{th}-28^{th}, 1984.

[99] E.J. Rapperport and A.M. Huntress. Deformation modes of single crystal uranium dioxide from 700°c to 1900°c. *U.S. At. Energy Comm. NMI-1242*, pages 1–29, 1960.

[100] I.L.F Ray, Hj. Matzke, H.A. Thiele, and M. Kinoshita. An electron microscopy study of the RIM structure of a UO_2 fuel with a high burn-up of 7,9% FIMA. *Journal of Nuclear Materials*, 245:115–123, 1997.

[101] J. Rest. Application of a mechanistic model for radiation-induced amorphization and crystallization of uranium silicide to recrystallization of UO_2. *Journal of Nuclear Materials*, 248:180–184, 1997.

[102] J. Rest. A generalized model for irradiation-induced amorphisation and crystallization of U_3Si and U_3Si_2 and recrystallization of UO_2. *Journal of Nuclear Materials*, 240:205–214, 1997.

[103] J. Rest. A model for the influence of microstructure, precipitate pinning and fission gas behavior on irradiation-induced recrystallization of nuclear fuels. *Journal of Nuclear Materials*, 326:175–184, 2004.

[104] J. Rest. A model for the effect of the progression of irradiation-induced recrystallization from initiation to completion on swelling of UO_2 and U-10Mo nuclear fuels. *Journal of Nuclear Materials*, 346:226–232, 2005.

[105] J. Rest. Derivation of analytical expressions for the network dislocation density, change in lattice parameter and for the recrystallized grain size in nuclear fuels. *Journal of Nuclear Materials*, 349:150–159, 2006.

[106] J. Rest and G.L. Hofman. Dynamics of irradiation-induced grain subdivision and swelling in U_3Si_2 and UO_2 fuels. *Journal of Nuclear Materials*, 210:187–202, 1994.

[107] J. Rest and G.L. Hofman. Effect of recrystallization in high-burnup UO_2 on gas release during RIA-type transients. *Journal of Nuclear Materials*, 223:192–195, 1995.

[108] J. Rest and G.L. Hofman. An alternative explanation for evidence that xenon depletion, pore formation, and grain subdivision begin at different local burnups. *Journal of Nuclear Materials*, 277:231–238, 2000.

[109] J. Rest and G.L. Hofman. Irradiation-induced recrystallization of cellular dislocation networks in uranium-molybdenum alloys. *Proc. of the Materials Research Society Meeting*, Symposium R, Volume 650, Boston, 2000.

[110] C. Rey. Transmission des contraintes et des déformations au passage d'un joint de grains. *Ecole d'été de Métallurgie Physique: "Les Joints de Grains dans les Matériaux"*, pages 341–350, Carry-Le-Rouet, France, September 20^{th}-28^{th}, 1984.

[111] C. Rey and G. Saada. The elastic field of periodic dislocation networks. *Philosophical Magazine*, 33:825–841, 1976.

[112] C. Ronchi, M. Sheindlin, D. Staicu, and M. Kinoshita. Effect of burn-up on the thermal conductivity of uranium dioxide up to 100.000 $MWdt^{-1}$. *Journal of Nuclear Materials*, 327:58–76, 2004.

[113] V.V. Rondinella. Physics Properties of Fuels at High Burn-ups. *Proc. of Frédéric Joliot/Otto Hahn Summer School on Nuclear Reactors: "Physics, Fuels and Systems"*, Karlsruhe, Germany, August 24^{th} - September 2^{nd}, 2005.

[114] V.V. Rondinella, Hj. Matzke, J. Cobos, and T. Wiss. α- Radiolysis and α-radiation damage effects on UO_2 dissolution under spent fuel storage conditions. *Materials Research Society*, 556:447–454, 1999.

[115] C. Roy. Thesis, University of London, 1962.

[116] P.T. Sawbridge and E.C. Sykes. Electrostatic charges on dislocations in uranium dioxide. *Journal of Nuclear Materials*, 35:122–125, 1970.

[117] J. Somers, R. Voet, C. Fuchs, H. Hein, C. Boshoven, S. Fourcaudot, N. Modery, and M. Murray-Farthing. Fabrication of UO_2 pellets doped with ^{233}U for α-radiolysis investigations. Technical note, jrc-itu-tpw-2001/12, European Commission, Institute for Transuranium Elements, Karlsruhe, 2001.

[118] T. Sonoda, M. Kinoshita, I.L.F. Ray, T. Wiss, H. Thiele, D. Pellottiero, V.V. Rondinella, and Hj. Matzke. Transmission electron microscopy observation on irradiation-induced microstructural evolution in high burn-up UO_2 disk fuel. *Nuclear Instruments and Methods in Physics Research*, B191:622–628, 2002.

[119] T. Sonoda, Hj. Matzke, and M. Kinoshita. High Burnup Rim Project: (IV) Threshold Burnup of Rim Structure Formation. *Proc. of Enlarged Halden Program Group Meeting*, Loen, Norway, May 24^{th}-29^{th}, 1999.

[120] M.V. Speight. A calculation on the migration of fission gas in material exhibiting precipitation and re-solution of gas atoms under irradiation. *Nuclear Science and Engineering*, 37:180–185, 1969.

[121] M.V. Speight. A calculation on the size distribution of intragranular bubbles in irradiated UO_2. *Journal of Nuclear Materials*, 38:236–238, 1971.

[122] J. Spino. Detailed characterization of the rim structure in PWR-fuels in the burn-up range 40-100 GWd/tM: From porosity evolution to lattice strain recovery and mechanical behaviour. *Int. Workshop on the High Burn-up Structure in Nucl. Fuels*, ITU, Karlsruhe, Germany, June 28^{th}-30^{th}, 2004.

[123] J. Spino, D. Baron, M. Coquerelle, and A.D. Stalios. High burn-up rim structure : evidences that xenon-depletion, pore formation and grain subdivision start at different local burn-ups. *Journal of Nuclear Materials*, 256:189–196, 1998.

[124] J. Spino, J. Cobos-Sabate, and F. Rousseau. Room-temperature microindentation behaviour of LWR-fuels, part 1: fuel microhardness. *Journal of Nuclear Materials*, 322:204–216, 2003.

[125] J. Spino and D. Papaioannou. Lattice parameter changes associated with the rim-structure formation in high burn-up UO_2 fuels by micro X-ray diffraction. *Journal of Nuclear Materials*, 281:146–162, 2000.

[126] J. Spino, D. Papaioannou, and J.-P. Glatz. Comments on the threshold porosity for fission gas release in high burn-up fuels. *Journal of Nuclear Materials*, 328:67–70, 2004.

[127] J. Spino, J. Rest, W. Goll, and C.T. Walker. Matrix swelling rate and cavity volume balance of UO_2 fuels at high burn-up. *Journal of Nuclear Materials*, 346:131–144, 2005.

[128] J. Spino, A.D. Stalios, H. Santa Cruz, and D. Baron. Stereological evolution of the rim structure in PWR-fuels at prolonged irradiation: Dependencies with burn-up and temperature. *Journal of Nuclear Materials*, 354:66–84, 2006.

[129] J. Spino, K. Vennix, and M. Coquerelle. Detailed characterisation of the rim microstructure in PWR fuels in the burn-up range $40 - 67\ GWd/tM$. *Journal of Nuclear Materials*, 231:179–190, 1996.

[130] D. Staicu, V.V. Rondinella, T. Wiss, J. Jonnet, D. Papaioannou, M. Kinoshita, A. Sasahara, T. Sonoda, S. Kitajima, D. Baron, D. Laux, and R. Rahouadj. Evolution of the thermophysical properties of UO_2 fuel as a function of burn-up. *Proc. Int. ENS Meet. on LWR Fuel Perf.: "Nuclear Fuel: Addressing the future"*, Salamanca, Spain, October 22^{nd}-26^{th} 2006.

[131] H. Stehle. Performance of oxide nuclear fuel in water-cooled power reactors. *Journal of Nuclear Materials*, 153:3–15, 1988.

[132] L.E. Thomas, C.E. Beyer, and L.A. Charlot. Microstructural analysis of LWR spent fuels at high burnup. *Journal of Nuclear Materials*, 188:80–89, 1992.

[133] J.A. Turnbull. The distribution of intragranular fission gas bubbles in UO_2 during irradiation. *Journal of Nuclear Materials*, 38:203–212, 1971.

[134] J.A. Turnbull. A comparison between mechanisms for irradiation-induced re-solution of fission gas from bubbles in UO_2. *RD/B/N.1112, Central Electricity Generating Board*, Berkeley Nuclear Laboratories, 1968.

[135] P. Van Uffelen. Contribution to the modelling of fission gas release in light water reactor fuel. Thesis, University of Liege, 2002.

[136] K. Une, M. Hirai, K. Nogita, T. Hosokawa, Y. Suzawa, S. Shimizu, and Y. Etoh. Rim structure formation and high burnup fuel behavior of large-grained UO_2 fuels. *Journal of Nuclear Materials*, 278:54–63, 2000.

[137] K. Une, K. Nogita, S. Kashibe, and M. Imamura. Microstructural Changes and its Influence on Fission Gas Release in High Burn-up UO_2 Fuel. *Journal of Nuclear Materials*, 188:65–72, 1992.

[138] K. Une, K. Nogita, T. Shiratori, and K. Hayashi. Rim structure formation of isothermally irradiated UO_2 fuel discs. *Journal of Nuclear Materials*, 288:20–28, 2001.

[139] M.S. Veshchunov, V.D. Ozrin, S.E. Shestak, V.I. Tarasov, R. Dubourg, and G. Nicaise. Modelling of defect structure evolution in irradiated UO_2 fuel in the MFPR code. *Proc. Int. ANS Top. Meet. on LWR Fuel Perf.*, Orlando, Florida, USA, September 19^{th}-22^{th} 2004.

[140] C.T. Walker. Assessment of the radial extent and completion of recrystallisation in high burn-up UO_2 nuclear fuel by EPMA. *Journal of Nuclear Materials*, 275:56–62, 1999.

[141] C.T. Walker and M. Coquerelle. Correlation between Microstructure and Fission Gas Release in High Burn-up UO_2 and MOX Fuel. *ENS Int. Top. Meeting on LWR Fuel Performance, "Fuel for the 90's"*, pages 506–517, Avignon, France, April 21^{st}-24^{th}, 1991.

[142] C.T. Walker, T. Kameyama, S. Kitajima, and M. Kinoshita. Concerning the microstructure changes that occur at the surface of UO_2 pellets on irradiation to high burnup. *Journal of Nuclear Materials*, 188:73–79, 1992.

[143] C.T. Walker, P. Knappik, and M. Mogensen. Concerning the development of grain face bubbles and fission gas release in UO_2 fuel. *Journal of Nuclear Materials*, 160:10–23, 1988.

[144] C.T. Walker, D. Staicu, M. Sheindlin, D. Papaioannou, W. Goll, and F. Sontheimer. On the thermal conductivity of UO_2 nuclear fuel at a burn-up of around 100 MWd/kgHM. *Journal of Nuclear Materials*, 350:19–39, 2006.

[145] W.J. Weber. Ingrowth of lattice defects in alpha irradiated UO_2 single crystals. *Journal of Nuclear Materials*, 98:206–215, 1981.

[146] T. Wiss. Private communication. August 2006.

[147] H.M. Zbib and T.D. de la Rubia. A multiscale model of plasticity. *International Journal of Plasticity*, 18:1133–1163, 2002.

[148] H.M. Zbib, M. Rhee, and J.P. Hirth. On plastic deformation and the dynamics of 3D dislocations. *International Journal of Mechanical Science*, 40:113–127, 1998.

[149] J.F. Ziegler, J.P. Biersack, and U. Littmark. *The Stopping and Range of Ions in Solids*. Oxford, Pergamon Press, 1985.

INSTITUT NATIONAL
POLYTECHNIQUE
DE LORRAINE

AUTORISATION DE SOUTENANCE DE THESE
DU DOCTORAT DE L'INSTITUT NATIONAL
POLYTECHNIQUE DE LORRAINE

o0o

VU LES RAPPORTS ETABLIS PAR :
Monsieur Michel BEAUVY, Directeur de Recherche, CEA Cadarache, Saint-Paul-lès-Durance

Monsieur Samuel FOREST, Directeur de Recherche, Ecole des Mines de Paris, Evry

Le Président de l'Institut National Polytechnique de Lorraine, autorise :

Monsieur JONNET Jérôme

NANCY BRABOIS
2, AVENUE DE LA
FORET-DE-HAYE
BOITE POSTALE 3
F - 54501
VANDŒUVRE CEDEX

à soutenir devant un jury de l'INSTITUT NATIONAL POLYTECHNIQUE DE LORRAINE, une thèse intitulée :

"Une contribution à la compréhension de la formation de la structure à haut taux de combustion dans les combustibles nucléaires"

en vue de l'obtention du titre de :

DOCTEUR DE L'INSTITUT NATIONAL POLYTECHNIQUE DE LORRAINE

Spécialité : « **Mécanique - énergétique** »

Fait à Vandoeuvre, le 20 décembre 2006
Le Président de l'I.N.P.L.,
L. SCHUFFENECKER

TEL. 33/03.83.59.59.59
FAX. 33/03.83.59.59.55